



UNIVERSITÀ
DEGLI STUDI
DI PADOVA



UNIVERSITA' DEGLI STUDI DI PADOVA
CENTRO INTERDIPARTIMENTALE “*Centro Ricerche Fusione*”
UNIVERSIDADE TÉCNICA DE LISBOA

**JOINT RESEARCH DOCTORATE IN FUSION SCIENCE AND
ENGINEERING**

CYCLE XXIV (2009/2011)

PhD THESIS

**STUDIES, ANALYSES, AVAILABLE MATERIALS AND TECHNOLOGIES FOR PLASMA
FACING COMPONENTS – APPLICATIONS AND FUTURE IMPROVEMENTS FOR
NEGATIVE ION SOURCES OF NEUTRAL BEAM INJECTORS**

Coordinator :

Chiar.mo Prof. Piero MARTIN

Supervisor(s):

Chiar.mo Prof. Piergiorgio SONATO

Dott. Ing. Samuele DAL BELLO

Doctoral Student:

Mauro Pavei

TABLE OF CONTENTS

ACKNOWLEDGMENTS	5
SUMMARY	7
SOMMARIO	9
INTRODUCTION.....	11
1 NEUTRAL BEAM INJECTOR SYSTEMS.....	17
1.1 PRIMA.....	19
1.2 MITICA	21
1.3 SPIDER.....	24
1.4 Negative ion formation	30
2 THE MITICA RF ION SOURCE AND PLASMA DRIVER PLATE.....	33
2.1 The concept of the RF source for the ITER NBIs.....	33
2.2 Overall design requirements, inputs and boundary conditions.....	34
2.2.1 ITER overall requirements	35
2.2.2 IPP inputs	36
2.2.3 Evaluations concerning Back Streaming Positive Ions (BSI+)	36
2.2.4 Evaluations on sputtering	39
2.2.5 Literature survey on molybdenum sputtering and blistering.....	41
2.3 Plasma Driver Plate design and verifications.....	46
2.3.1 General description of the PDP geometry and functions	46
2.3.2 Design of the PDP cooling circuit.....	49
2.3.3 PDP design with thick molybdenum armour layer.....	51
2.4 Design criteria	54
2.4.1 Thermo-hydraulic design criteria	54
2.4.2 Thermo-mechanical design criteria	58
2.5 Thermal design of the PDP	62
2.5.1 Preliminary analytical calculations.....	62
2.6 Finite Elements thermal analyses and verifications	67
2.6.1 FE models description	67
2.6.2 Thermal loads	68
2.6.3 FE analyses of the 5x5mm ² model	71
2.6.4 FE model of the configuration with a 1.0 mm thick molybdenum layer.....	79
2.6.5 FE models of the “half-moon” manifold regions	82
2.7 Finite Elements mechanical analyses and verifications.....	89
2.7.1 FE models description	89
2.7.2 Structural loads.....	89
2.7.3 FE analyses of the 5x5mm ² model	90
2.7.4 FE model of the configuration with a 1.0 mm thick molybdenum layer.....	98
2.7.5 FE models of the “half-moon” manifold regions	100
2.8 FE models simulating the regions not impinged by BSI⁺	105
2.8.1 Loads and boundary conditions.....	106
2.9 Overall results and discussion	107
2.9.1 Analysis results of the CuCrZr solution	108
2.9.2 Analysis results of the solution with 1.0mm thick molybdenum layer	110
3 R&D ACTIVITIES ON THE CU-MO PLASMA DRIVER PLATE.....	111
3.1 Introduction and overview of the R&D activities	111
3.2 Plasma Spray technique	114
3.2.1 Manufactured samples.....	114
3.2.2 Tests on the APS samples.....	115
3.2.3 Conclusions	125
3.3 Explosion Bonding (EB) technique	126
3.3.1 First step of R&D activities	126
3.3.2 Second step of R&D activities	164
3.3.3 Conclusions	189

4 OVERALL CONCLUSIONS.....	191
REFERENCES	193
ANNEXES	197
Annex 1: TECHNICAL SPECIFICATION FOR THE RESEARCH AND DEVELOPMENT ACTIVITIES ON THICK MOLYBDENUM COATING – RFX- MITICA-TN-19 (2010)	197

Acknowledgments

My PhD work would not have been possible without the collaboration of my colleagues in Consorzio RFX, particularly the “Ingegneria del Plasma” group. I would like to thank everybody who have helped and encouraged me during these three years.

Summary

One of the most critical issues for present fusion machines, and even more for next generation ITER and fusion reactor prototypes, is the reliability and fatigue & wearing resistance of plasma facing components. The engineering problem is very challenging and the research in this field requires a number of multidisciplinary competences such as thermo-mechanics, thermo-hydraulics and the knowledge of materials capable of resisting to thermal fatigue cycles under intense irradiation for very long periods in the presence of enhanced creeping and aging phenomena. Wearing estimates need further knowledge on plasma-materials interactions, and on chemical and physical sputtering.

All these issues are particularly important for divertor targets, but are also relevant for some parts of the Radio-Frequency (RF) Ion Sources of Neutral Beam Injectors that are subjected to extremely high and localized peaks of power densities.

The research activities of the candidate have been dedicated in particular to these arguments for the RF ion source and driver back-plates, also considering the present state of the art and next design/material developments for the divertor targets in ITER and DEMO.

Design optimization, numerical models, analyses and technological issues/improvements for the design of the RF source components, with execution of R&D, have been the main goals of this PhD work.

Most of the R&D has been carried out with interactions and strong collaborations with other European Laboratories and private companies. Preliminary samples have been manufactured by explosion bonding and plasma spraying, in collaboration with private companies, for analyzing the possibility of manufacturing 1.0mm thick molybdenum armour layer on copper substrate. These different samples have been tested in order to evaluate the compatibility with vacuum environment and the interface quality; the Explosion Bonding process has eventually been found to be the most promising.

New molybdenum-to-copper explosion-bonded prototypes have then been manufactured, with the most performing parameters, previously defined. The most critical parts of the prototypes have been analyzed and modified; Finite Element models and analyses have been carried out, aiming at reducing the shear stresses in the molybdenum layer during and after the forming of the edge area.

Cut out from the prototypes, some specimens have been produced. These specimens have been thermal-shock and thermal-fatigue tested, under thermal conditions similar to the ones of the RF Ion Source and driver back-plates during the future NBI pulses. The specimens have

been analyzed after the tests: microscopic, XRD and profilometric analyses have been carried out in order to verify the “post mortem” material condition at the interface, after the fatigue test.

The work is continuing towards the full definition of the manufacturing steps, the production of a full scale prototype of the Plasma Driver Plate and a full analysis, study and qualification of the explosion bonding technology for nuclear fusion applications to be submitted to ITER Organization for approval.

Sommario

Uno degli aspetti più critici delle attuali macchine da fusione, e ancor di più di ITER e dei prototipi di reattore della prossima generazione, è l'affidabilità dei materiali esposti al plasma unitamente alla loro resistenza a fatica e all'usura. Il problema ingegneristico da risolvere è una sfida e la ricerca nel campo dei materiali da prima parete richiede competenze multidisciplinari nel campo della termomeccanica e della termoidraulica, nonché la conoscenza di materiali in grado di resistere a cicli di fatica termica quando sottoposti per lungo tempo a forte irraggiamento, e quindi in presenza di fenomeni quali il creep e l'invecchiamento. La stima dell'usura richiede ulteriore conoscenza dell'interazione tra il plasma e i materiali di prima parete, e quindi dei processi di sputtering chimico e fisico.

Tutti questi aspetti sono particolarmente importanti per i pannelli del divertore, ad esempio, ma lo sono anche per alcune parti delle sorgenti di ioni a radiofrequenza degli iniettori di neutri (NBI) che sono soggette a picchi di densità di potenza estremamente elevati e localizzati.

Le attività di ricerca del candidato sono state dedicate in particolare a questi aspetti relativi alla sorgente a radiofrequenza (RF) e ai suoi "driver back-plates" (pareti di contenimento del plasma all'interno della sorgente), considerando lo stato dell'arte e lo sviluppo futuro di materiali per il divertore di ITER e DEMO.

L'ottimizzazione del progetto, i modelli numerici, le analisi e il miglioramento di alcuni aspetti tecnologici del progetto dei componenti della sorgente RF, tramite le attività di ricerca e sviluppo effettuate, sono stati gli obiettivi primari del lavoro di dottorato (PhD).

La maggior parte delle attività di R&D sono state svolte interagendo e collaborando pesantemente con altri laboratori europei e con ditte private. Sono stati infatti realizzati dei campioni mediante le tecniche di "explosion bonding" e "plasma spraying", presso ditte private, con lo scopo di verificare la possibilità di "depositare" uno strato di molibdeno su un substrato di rame. Questi diversi campioni sono stati quindi testati con lo scopo di valutare la compatibilità con il vuoto del materiale depositato e la qualità dell'interfaccia tra i due materiali; alla fine, il processo denominato "explosion bonding" si è rivelato il più promettente.

Si sono quindi realizzati nuovi prototipi aventi uno strato di molibdeno esplosivo su una piastra di rame, tenendo conto dei parametri di esplosione precedentemente identificati che offrivano le migliori prestazioni.

Dai prototipi di piastra realizzati sono stati ricavati alcuni provini. Tali provini sono stati testati a shock termico e fatica termica, sottoponendoli a condizioni di carico simili a quelle stimate per la sorgente RF e per i suoi back plates durante i futuri impulsi dell'iniettore di neutri. Successivamente ai test di fatica, i provini sono stati analizzati al microscopio, con la tecnica

XRD (X-ray Diffraction) e con il profilometro per verificare lo stato del materiale e dell'interfaccia in condizioni "post mortem".

Il lavoro presentato sta attualmente continuando verso la completa definizione dei passi necessari per la costruzione del prototipo in scala reale del "Plasma Driver Plate" e la qualificazione della tecnologia di "explosion bonding" quale processo da sottomettere all'approvazione di ITER (ITER Organization - IO) per applicazioni di fusione nucleare.

Introduction

Nuclear fusion is one of the environmentally acceptable, safe and sustainable energy technologies the researchers from all over the world are working on for the development of the human kind.

Nuclear fusion is the process (see Figure 0.1) that powers the sun and other stars, providing heat and light to sustain life on Earth. While gravity confines the hot plasma in the stars, on earth strong magnetic fields can be used to hold the plasma inside a chamber in a quasi-stable condition; this is the magnetic confinement approach.

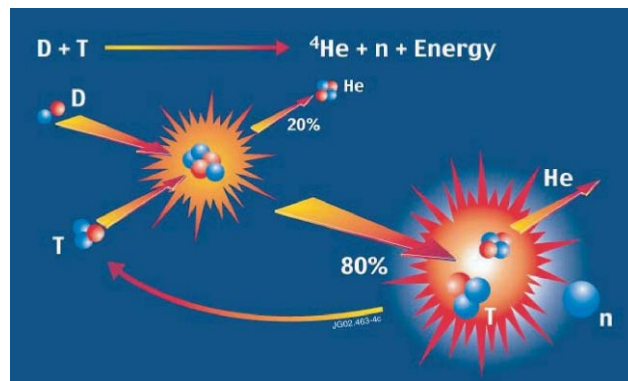


Figure 0.1: The nuclear fusion reaction

To harness fusion power, light nuclei are forced together, undergoing reactions that produce a net energy gain. In order to make fusion happen, the fuel (in plasma state) has to be heated up to very high temperatures (in the order of 100 million degrees).

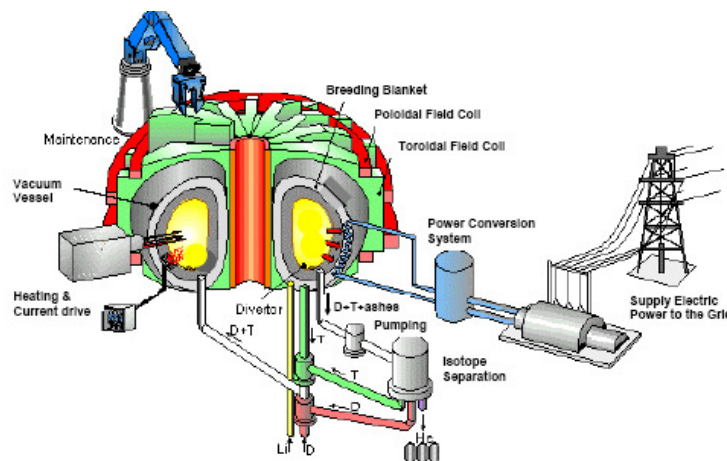


Figure 0.2: Schematic of a future fusion power plant

The “tokamak” has been the most successful concept for confining fusion plasmas up to now: current flows into the plasma along the toroidal direction, with a consequent production of a poloidal magnetic field. Then a stronger toroidal magnetic field is produced by coils in order to

stabilize the configuration. Alternative concepts, like Reversed Field Pinch and Stellarator, are also developed to prepare for fusion power plants.

The primary fuels for nuclear fusion are deuterium and lithium. Deuterium can be extracted from sea water and lithium is abundant in the earth's upper crust. In a power plant lithium is used to breed the tritium which fuses together with deuterium. Only 150 Kg deuterium and 2÷3 tonnes of lithium are needed for a full year of electricity supply for one million persons.

Fusion power plants will be particularly suited for base load energy generation to serve the needs of densely populated areas and industrial zones (see Figure 0.2).

ITER is the next milestone towards the development of a reactor based on the controlled thermonuclear fusion reactions [1]. ITER is an international tokamak research project which is intended to be an experimental step between today's studies of plasma physics and future fusion power plants. It will be built upon research conducted with devices such as DIII-D [2], TFTR [3], JET [4] and JT-60 [5], [6] and will be considerably larger than any of them.

In Figure 0.3 a cutaway of ITER is shown.

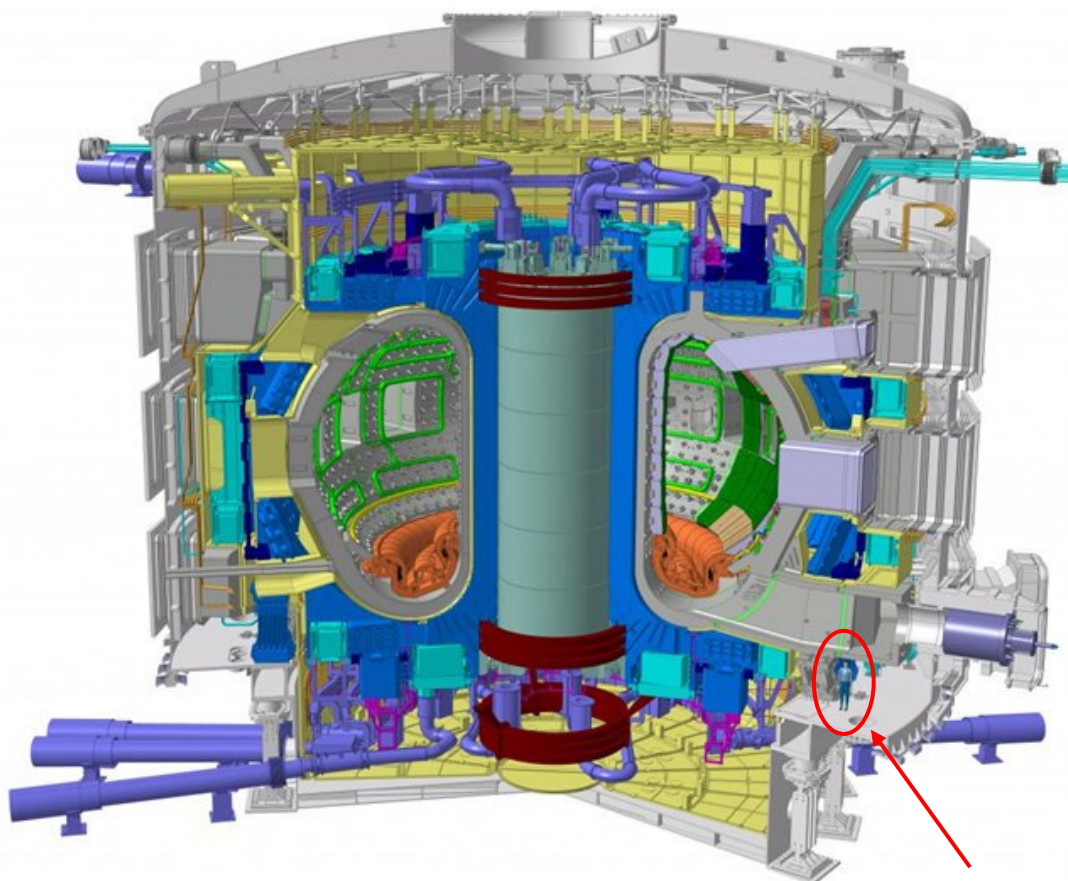


Figure 0.3: Technical cutaway of the ITER Tokamak Torus encasing. Note the human figure for size comparison

On November 21, 2006, European Union, United States of America, Russian Federation, Japan, Republic of Korea, People's Republic of China and India formally agreed to fund the project. The program was anticipated to last for 30 years (10 years for construction, and 20 years of operation) and costs approximately 10 billion Euro, which makes it one of the most expensive modern techno-scientific megaprojects. It will be based in Cadarache, France. It was foreseen to be technically ready to start construction and the first plasma operation is expected in 2016.

In the years the planning has been updated and the first plasma is now foreseen in 2019. The cost of ITER has also been revised and it has been increased of a factor 1.7.

The ITER experiment has the aim of demonstrating the feasibility of the fusion power plant; that means:

- demonstrating the feasibility of creating and maintaining confined a fusion plasma for an indefinite time, in order to extract a continuous flux of energy;
- demonstrating the technical and technological feasibility of the reactor;
- studying the behaviour of the materials, especially the first wall components which directly face the plasma;
- testing all the needed auxiliary plants, including heating and injection components;
- verifying the processes for the recovery and treatment of the nuclear reactor activated materials;
- obtaining a net production of energy: thermal energy obtained from the fusion reaction ≥ 10 times the energy given to the plasma by the auxiliary systems;
- testing the fuel injection and heating systems;
- testing the breeding blanket modules;
- demonstrating the safety of this kind of reactors.

The main goal of ITER is to produce approximately 500 MW of fusion power sustained for at least 300 seconds (compared to JET's peak of 16 MW for less than a second) by the fusion of about 0.5 g of deuterium/tritium mixture in its approximately 840 m³ reactor chamber.

The main ITER parameters are reported in the next table.

Total fusion power	500 MW
Q = Exhausted Fusion Power/Plasma Heating Power	5-10
Specific Power from 14 MeV neutrons on the first wall	>0.5 MW/m²
Discharge duration	>300 s
Major radius of the torus	6.2 m
Mean minor radius of the torus	2 m
Plasma current	15 MA
Toroidal magnetic field strength	5.3 T
Plasma volume	837 m³
Plasma surface	678 m²

Table 0.1 ITER nominal parameters

Within the Tokamak, the changing magnetic fields that are used to control the plasma produce a heating effect. The magnetic fields create a high-intensity electrical current through induction, and as this current travels through the plasma, electrons and ions become energized and collide. Collisions create 'resistance' which results in heat, but, unlike most solid conductors at room temperature, as the temperature of the plasma rises, this resistance - and therefore the heating effect - decreases. Heat transferred through high-intensity current, known as ohmic heating, is limited to a level defined by the balance between energy injection by ohmic heating and energy loss via radiation and particle loss. For this reason the ITER tokamak needs additional heating systems that are also used for regulating the plasma density profile, and suppressing some of the plasma instabilities, aiming at reaching and sustaining the high performance regime (H-mode) [7],[8].

The Heating and Current Drive (H&CD) systems for ITER are an appropriate combination of Neutral Beam Injectors (NBI) and Radio Frequency (RF) H&CD antennas operating at the electron cyclotron (EC), ion cyclotron (IC) and lower hybrid (LH) frequencies (Figure 0.4).

They contribute, together, at providing an active control on all the key phases of the operating scenarios, acting on:

- the plasma temperature,
- the achievement of a steady burn,
- the suppression of instabilities, and
- the achievement of a soft termination.

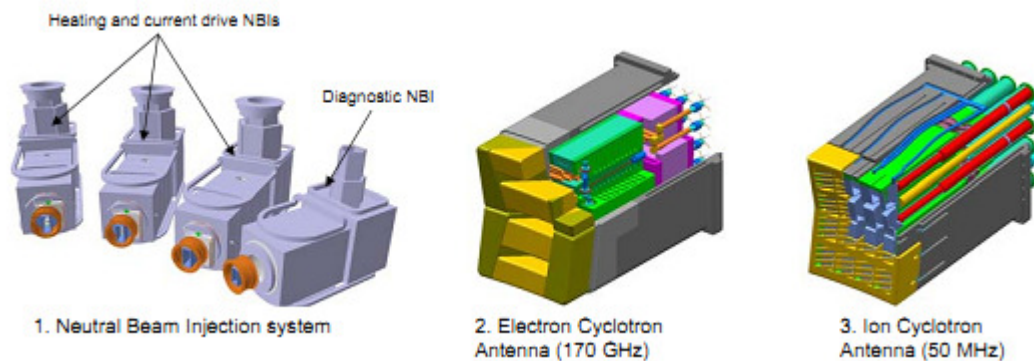


Figure 0.4: Overview of the Heating & Current Drive systems

The neutral beam system design for ITER consists, at present, of two heating and current drive (H&CD) injectors and one diagnostic neutral beam (DNB) injector. Each H&CD injector will deliver a deuterium beam of 16.5 MW (total 33 MW), with energy of 1MeV, and will be able to operate for long pulses (up to 3600 s for steady state operation). A third H&CD NBI is foreseen to be added in a second stage, in order to increase to 50MW the heating power to the ITER plasma [9],[10].

In order to obtain an effective and reliable Neutral Beam Injector (NBI) for ITER, it is required a large amount of research & development (R&D), both on physics and engineering sides. For this reason, a neutral beam test facility is being built in Padova [11]. The facility is named PRIMA (Padova Research on Injector Megavolt Accelerated), it will host both SPIDER (Source for Production of Ion of Deuterium Extracted form Rf-plasma) and MITICA (Megavolt ITER Injector Concept Advanced) test-beds that have the goal to address and solve the main physics and engineering issues related to this system.

This thesis aimed at solving important engineering issues and proposing design solutions of some ion source components for the ITER NBIs and their test-beds.

In **Chapter 1** the ITER NBI basic concepts are presented, describing the main phenomena at the basis of their design. The PRIMA test facility, and the two experiments MITICA and

SPIDER, under development at Consorzio RFX in Padova with the purpose to study the physical and engineering problems of neutral beam injection, are then presented. In particular, a detailed description of the radio frequency beam source of SPIDER and its components is given, since I have been directly and deeply involved on their design. In the final section of the first chapter the physics of the negative ion formation and the effect of caesium seeding in the negative ion sources are described.

In **Chapter 2** the Radio-Frequency ion source for the ITER NBIs are described in more detail, explaining the main scope of its main components. The Plasma Driver Plate (PDP), one of the most critical components, is then introduced, together with all the loads and requirements it shall withstand and fulfil. The design choices of the PDP, the thermo-mechanical analyses and verifications that have been carried out are then presented in detail, as well. The need of investigating the possibility to manufacture a thick armour layer on the plasma facing surface of the PDP is one of the main issues discussed in the last sections of the chapter.

Chapter 3 is instead focused on the Research&Development activities that have been carried out aimed at identifying and qualifying a suitable and reliable technology for producing a 1 millimetre thick armour layer of molybdenum on a copper substrate: this solution being the reference one to be used for the manufacturing of the MITICA Plasma Driver Plate.

Finally, in **Chapter 4** the most important conclusions of the thesis work are summarised; some still open points are also discussed to address next R&D activities that are necessary to finalize the manufacturing procedure of the PDP.

1 Neutral Beam Injector systems

Neutral Beam Injectors (NBI) are used to launch uncharged high-energy particles into the plasma where, by way of collisions, they transfer their energy to the plasma particles.

The beam power deposition in the plasma principally depends on the beam energy and the plasma density and it is necessary to deposit the beam power inside the so-called *H-mode barrier*, which is located between $0.9 < r/a < 1$, where r is the distance from the plasma centre and a is the minor radius of the plasma. For the ITER plasma this means that the D^0 energy has to be >300 keV.

Only atoms with a positive or a negative charge, i.e. ions, can be accelerated by an electric field; for this, atoms have to be transformed into ions. The process must then be reversed before injection into the fusion plasma; otherwise the electrically-charged ions would be deflected by the magnetic field surrounding the plasma. In NBI systems, the ions pass through a cell containing gas where they get neutralized, so they can be injected as fast neutrals into the plasma.

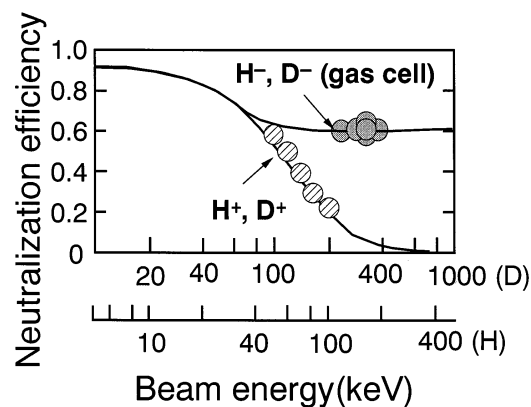


Figure 1.1 Hydrogen ions neutralisation efficiency as a function of energy

The large plasma volume of ITER will impose new requirements on this proven method of injection: the particles must move three to four times faster than in previous systems in order to penetrate far enough into the plasma and at this higher speed the positively-charged ions become difficult to neutralize. At such energies the production of neutral beams by the neutralization of accelerated positive ions becomes in fact very inefficient and the neutralization of accelerated negative ions, D^- , has to be used [12]. The neutralization efficiency measured in negative-ion based NBI for the Japanese Tokamak JT-60U is shown as a function of the beam energy in Figure 1.1 [13].

Although the negative ions are easier to neutralize, they are more challenging to create and to handle than positive ions.

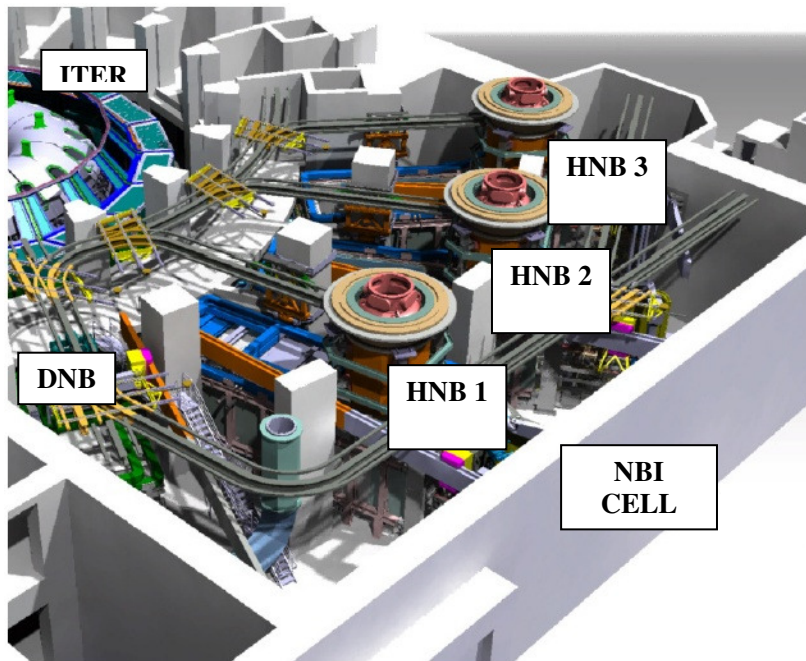


Figure 1.2 ITER and the NBI cell with DNB and 3 HNB

Initially ITER will use two heating neutral beams (HNB) that are designed to inject 33 MW of either 1 MeV deuterium (D^0) or 870 keV Hydrogen (H^0) into the ITER plasma. A third heating beam may be added later, bringing the total D^0 power that may be injected into ITER up to 50 MW. Another different Neutral Beam will be used for diagnostic purposes (DNB). They can be seen in Figure 1.2.

The neutral beam injector technology for the required energy and power is well beyond the present performance reached by similar systems and therefore it is necessary to create a new experimental facility addressing all the current issues, to fill up all the residual technical and scientific gaps.

The realization of this laboratory, with the financial support of ITER, European Union and Italy, has been committed to Consorzio RFX in Padova. The experimental devices hosted in the facility will be realised with the contribution of important European research institutes (from France, Germany and United Kingdom) and the contribution of international ITER partners, Japan and India.

Some of these contributions are limited to the design phase, others will extend to the supply, installation and commissioning of components and services. At the end this facility will be available to all ITER parties for the exploitation and the development of the high energy neutral beam injectors for plasma heating and current drive based on negative ions.

1.1 PRIMA

Padova Research on Injector Megavolt Accelerated (PRIMA) identifies all the R&D facilities that will be realised and hosted at Consorzio RFX in Padova in the framework of international agreements with all the different actors: ITER Organization, Europe and the Host, Consorzio RFX, with contributions from the other ITER Parties, Japan and India, directly involved in the neutral beam systems procurements. The PRIMA activities foresee the design, construction, installation and exploitation of two experimental devices in a new building whose construction is going to start soon.

The laboratory that will host the prototype experimental injector, for the technical and scientific development of the injectors to be installed in ITER, will be erected in the site of the National Research Council (C.N.R.) of Padova in Corso Stait Uniti, 4. The facility will be built in the South side of the research C.N.R. area, next to the 400 kV power station that supplies energy to the existing RFX device and that will also supply energy to the experimental plants hosted by PRIMA.

The facility will host two experimental devices: MITICA (described in Section 1.2) and SPIDER (described in Section 1.3), all the experimental service plants and the control rooms necessary for the operation of the two devices. The buildings will be built on a surface of approximately 17500 m², whereas the area covered by buildings is of approximately 7000 m². The tallest building will reach 26 m in height. A cutaway view can be seen in Figure 1.3.



Figure 1.3: PRIMA experimental hall cutaway view

Figure 1.4 shows the buildings layout. The main building is subdivided in two bodies having different height, but the same length of 110 m. The main single-span building (1) will host the mechanical parts of the two devices; it will cover a surface of 3000 m² and is 26 m high. A single crane having a total capacity of 50 tons and covering the whole building area will allow

the manoeuvring and placing of all components to be installed in the experimental devices. The second body (2) is adjacent to the first one and has a surface of 2100 m²; it is partially divided into rooms that are disposed along in two floors. The whole height of the building is 18 m. The body is divided in two spans to host on the roof some of the experimental apparatuses. In particular some components of the cooling and of the cryogenic plants will be housed here. To move the components inside the buildings, two cranes (10 tons maximum weight to be moved) have been foreseen for each span in the single floor rooms. A second body of buildings is composed of two rooms; the first one (3) with a surface of about 800 m² and a height of 26 m will host a -1MV shielded deck, containing power supply systems and other devices set at -1 MV voltage to ground. The second room (4) having a surface of 400 m² and 17 m height has two floors; it will host other power supply systems and utility devices. A final building (5), connecting the previous ones, will host two experiment control rooms; computers, network devices and data storage systems. In the external area, other systems and components necessary for the experimental plant operation can be seen: the MITICA acceleration grid power supply, hosting five secondary 200 kV transformers series-connected in order to reach the voltage value of -1 MV (6), the underground -1MV transmission line (7) and three underground water basins which serve as cooling system heat capacity (8).

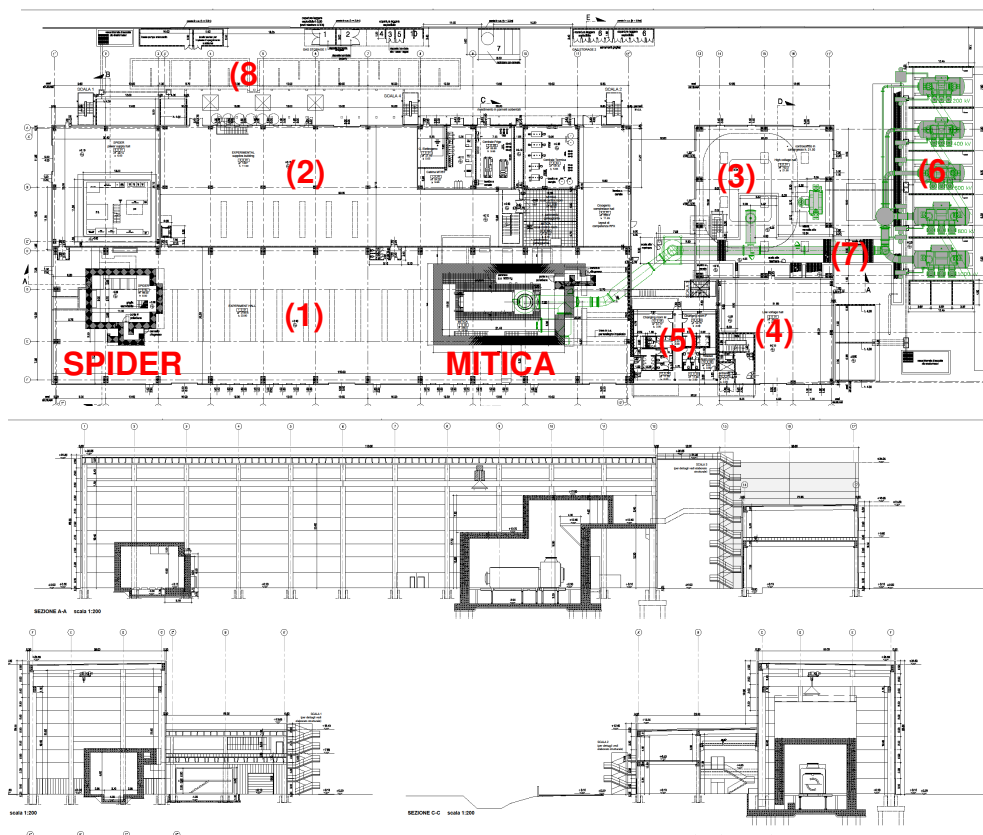


Figure 1.4: PRIMA buildings, layout and side views

1.2 MITICA

The Megavolt ITER Injector & Concept Advancement (MITICA) is the first of the two experiments which will be hosted on the premises of the new laboratory. MITICA is the prototype of the injectors which will be realised and installed in ITER. Figure 1.5 shows the injector with its main dimensions in the experimental hall. The 1.8 m thick concrete bio-shield has been partially removed to show the injector.

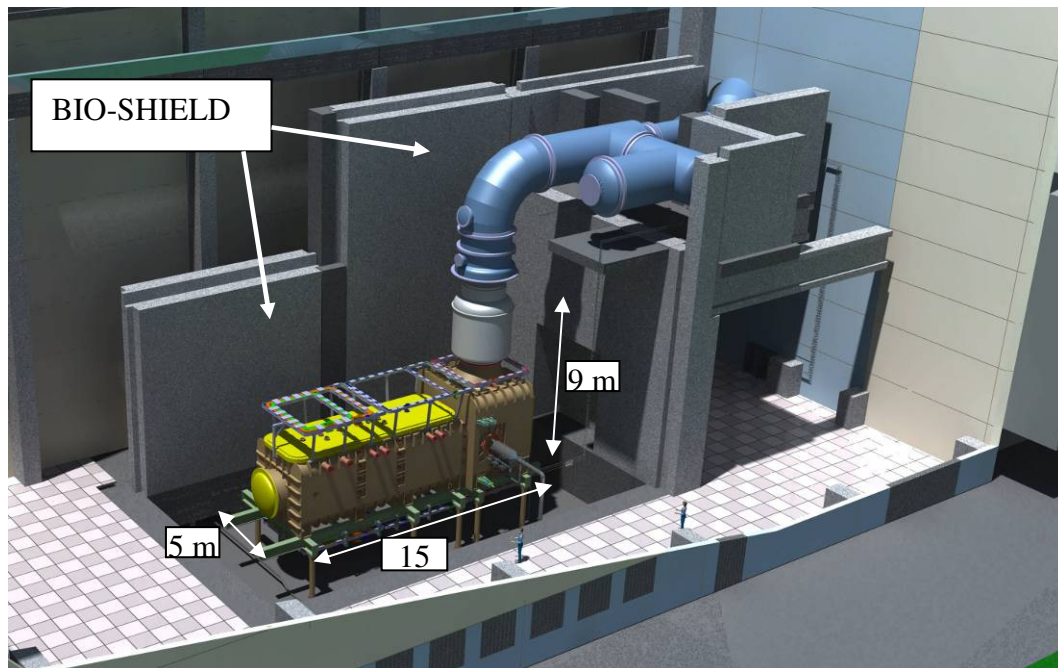


Figure 1.5: MITICA experiment external view

The injector is being designed in order to be able to produce a beam of neutral particles of deuterium, accelerated up to the energy of 1 MeV by means of an electrostatic accelerator with an acceleration voltage of 1 MV. The beam shall be able to transfer a power of 16.5 MW to the plasma for 3600 s, continuously. The process for the production of deuterium neutral particles originates from a deuterium (D) plasma produced by means of 8 inductive radiofrequency generators (1 MHz) in a chamber 1.8 m high, 0.6 m wide and 0.2 m deep. The chamber (PLASMA SOURCE) faces a surface (PLASMA GRID) having 1280 holes, with a diameter of about 12 mm, previously covered with a caesium layer [14]. Deuterium – caesium surface interaction can generate a deuterium ion having an additional electron, i.e. a negative deuterium ion (D^-). The D^- is created either by reactions within the plasma or by surface reactions involving the bombardment of ions and atoms. There are many processes that lead to the destruction of D^- , which exacerbates the difficulties of producing high extracted current densities. The choice for ITER of 1 MeV is a compromise between the foreseen difficulties of developing higher energy, high power, power supplies and accelerators and the difficulty in

making and accelerating high D^- currents [12]. A cutaway view of MITICA is shown in Figure 1.6 and a brief description of its main components is given hereafter.

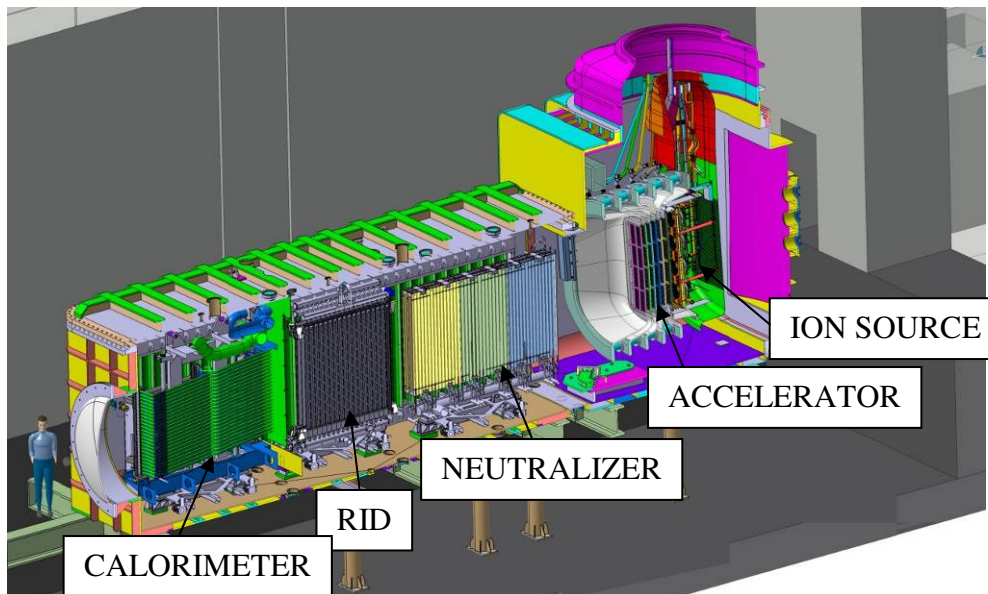


Figure 1.6: MITICA components cutaway view

The ion source is held at -1 MV and the D^- ions are accelerated up to ground potential by a system of 5 grids (ACCELERATOR) set at different potentials, by steps of 200 kV, applied to each couple of grids. At the end of the accelerating grid system, a beam of negative deuterium ions accelerated to an energy of 1MeV will be obtained and a current of 40 A will be extracted. The composition of the ion source and the accelerator is called BEAM SOURCE. The beam will then pass through a cloud of deuterium gas where the negative ions get neutralised by a charge exchange process (NEUTRALIZER), in order to generate a neutral beam. During the passage through the neutralizer, collisions of the D^- with the D_2 injected into the neutralizer leads to formation of D^0 by simple stripping of the outer electron from the D^- , and double stripping creates D^+ . D^+ is also created by re-ionization of the D^0 resulting from D^- .

At the exit of the neutralizer, the beam will pass through an electrostatic field (RESIDUAL ION DUMP, RID). The electric field deflects the charged particles of the beam onto a set of plates, leaving the neutral beam to impinge onto the CALORIMETER located just downstream of the residual ion dump. The two panels making up the calorimeter form a V with the open end of the V facing the RID. In this configuration the injector can be commissioned and the neutral power dumped onto the calorimeter can be measured. In the ITER NBI, the V calorimeter will be opened and the neutralized deuterium beam of 16.5 MW power will flow along the duct until the ITER plasma is reached.

Large cryopumps are placed on each side of the beam path and the beamline components (neutralizer, RID and calorimeter) inside the injector to reduce the pressure downstream of the accelerator and downstream of the neutralizer exit to the required values. The pressure downstream of the accelerator must be low in order to minimize losses in the accelerator due to stripping. The pressure downstream of the neutralizer must be low in order to minimize re-ionization of the D^0 by collision with the background D_2 . The nominal parameters of the MITICA injector are reported in Table 1.1.

MITICA	Unit	H	D
Neutral beam power	MW	16.5	16.5
Beam energy	keV	870	1000
Acceleration current	A	49	40
Maximum Beam Source pressure	Pa	<0.3	<0.3
Beamlet divergence	mrad	≤ 7	≤ 7
Beam-ON time	s	3600	3600
Co-extracted electron fraction (e^-/H^- or e^-/D^-)		<0.5	<1

Table 1.1 MITICA nominal parameters

1.3 SPIDER

The Source for Production of Ion of Deuterium Extracted from Rf plasma (SPIDER) is the second experiment that will be hosted in the premises of the new laboratory [15]. SPIDER is an experiment which will allow to develop the knowledge on negative ions and to optimize the uniformity of negative ion production, up to the ITER requirement, before MITICA enters into operation (indicatively 2.5 years before) and then in parallel to MITICA operation. SPIDER will be equipped with a source for negative ion production that, once optimized, will be duplicated for MITICA. Figure 1.7 shows the SPIDER experiment in the experimental hall. The 1.2 m thick concrete bio-shield has been partially removed to show the device. The high voltage deck (in yellow colour) and the squared cross-section transmission line can be seen.

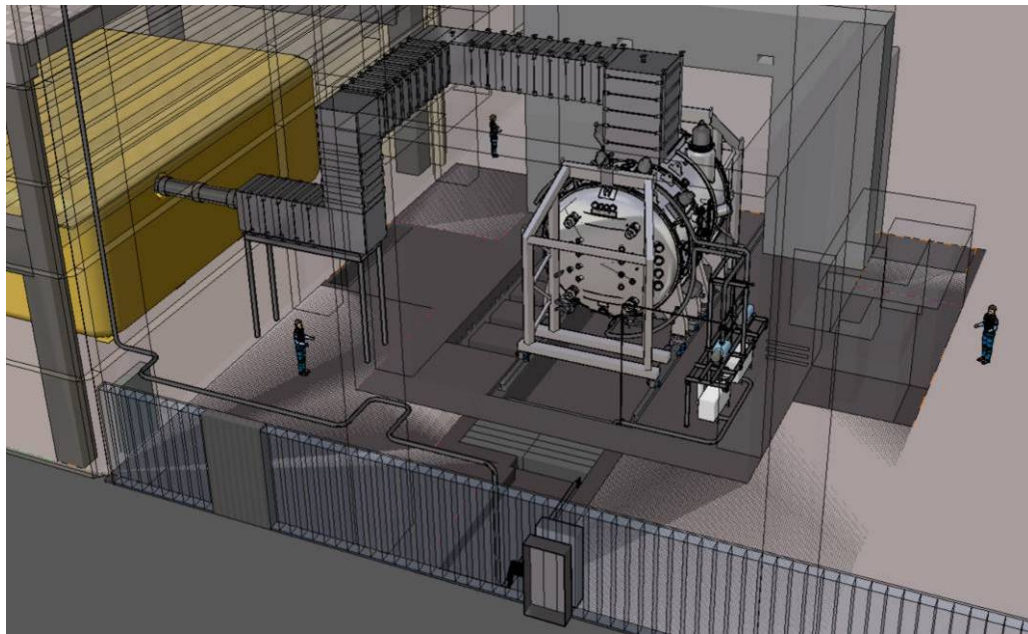


Figure 1.7 SPIDER experiment external view

The SPIDER beam source will be characterised by a lower acceleration voltage (100 kV) than the MITICA one (1 MV). This is due to the fact that SPIDER will focus on the optimization of the negative ion beam creation process. The full acceleration and neutralization processes will be the scope of MITICA injector that will be the prototype of the ITER neutral beam injector. Thus, the mission of the SPIDER experiment is developing the ion source to guarantee on a large extraction surface of $1.52 \times 0.56 \text{ m}^2$ the following parameters:

- the necessary ion current density;
- the lowest possible pressure;
- the required uniformity;
- the lowest percentage of co-extracted electrons.

The SPIDER nominal parameters are reported in Table 1.2 and an overall picture of the whole experiment can be seen in Figure 1.8.

SPIDER	Unit	H	D
Beam energy	keV	100	100
Maximum Beam Source pressure	Pa	<0.3	<0.3
Uniformity	%	±10	±10
Extracted current density	A/m²	>350	>290
Beam-ON time	s	3600	3600
Co-extracted electron fraction (e⁻/H⁺ or e⁻/D⁺)		<0.5	<1

Table 1.2 SPIDER nominal parameters

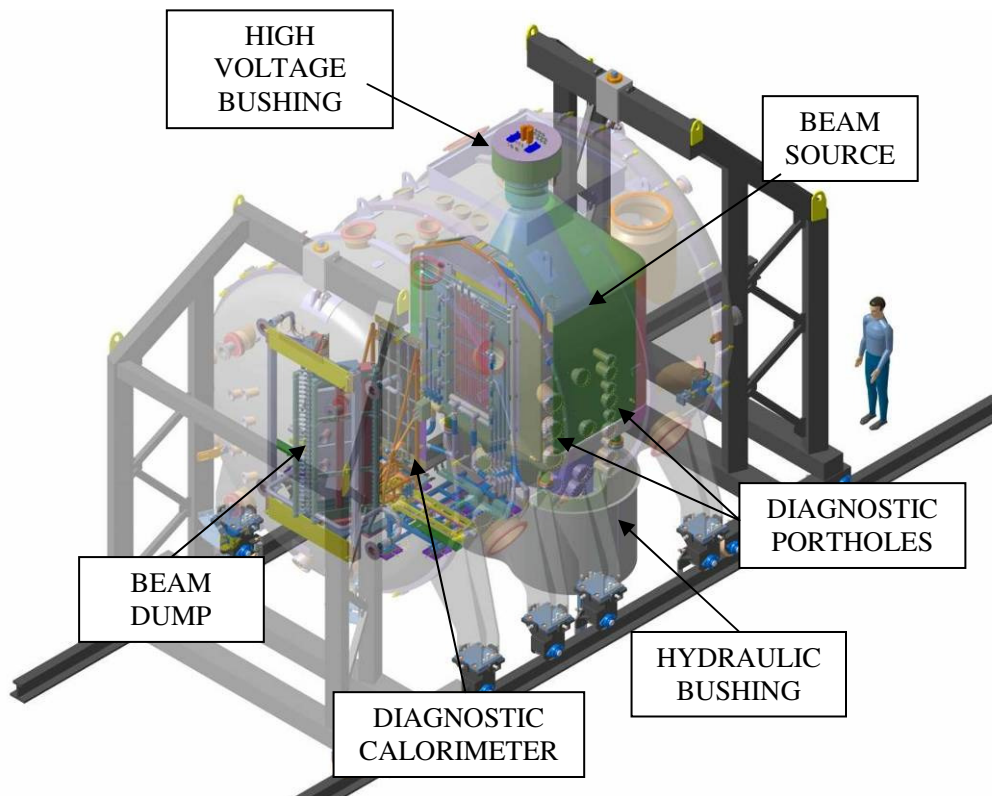


Figure 1.8 SPIDER experiment with transparent vessel

The most important component of the SPIDER experiment is of course the beam source (Figure 1.9), nevertheless, the experiment would be useless without dedicated diagnostic systems which are able to measure the beam parameters (Figure 1.8). In particular, inside the vacuum vessel a special diagnostic calorimeter called STRIKE (Short-Time Retractable Instrumented Kalorimeter Experiment) is hosted. STRIKE is made of 16 Carbon Fibre Composite (CFC) tiles that intercept the beam. The CFC tiles are one dimensional (1D) with the

fibres oriented in the thickness. In this application the carbon fibres have the aim to fast conduct the heat deposited on the front side to the back side of the tile. In this way the thermal image of the impinging beam is transferred to the back where it is acquired by thermal cameras. From the data collected with STRIKE, measurements of the beam uniformity and divergence will be possible. Nevertheless, since STRIKE is passively cooled, it can tolerate the beam power for not more than 10 seconds and can open to let the beam pass through. Thus, a beam dump composed of actively cooled panels is also present to exhaust the beam power during the full length pulse of 3600 s. Many other optical diagnostics are present on the outside of the vacuum vessel. They diagnose the beam through dedicated aperture rows (portholes) around the vessel.

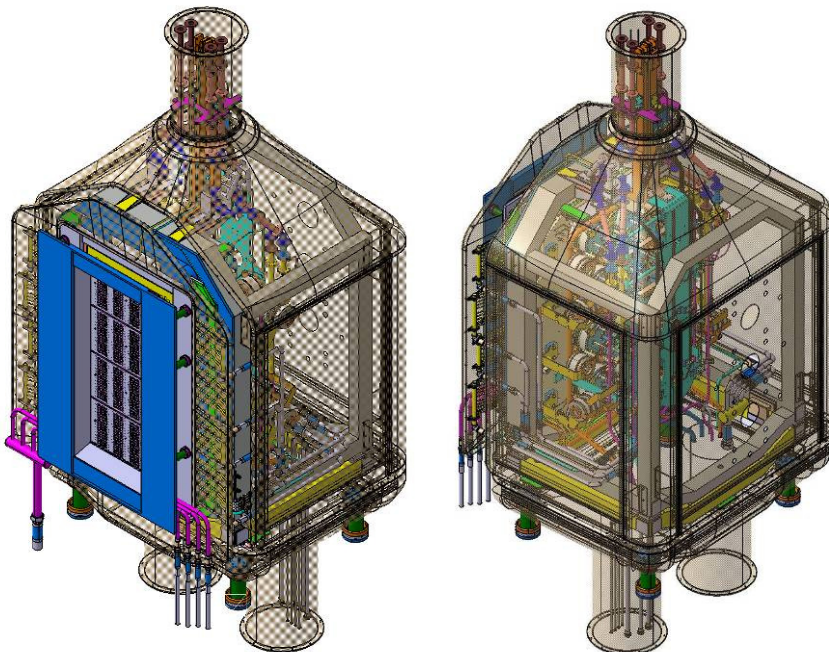


Figure 1.9 SPIDER Beam Source: frontal view (left) and rear view (right)

MITICA and SPIDER share the same Plasma Source and also the Bias Plate, the Plasma Grid and the Extraction Grid are coincident, that is they share the same ion source [14]. What differs among the two sources is essentially the presence of demountable hydraulic connections in SPIDER, not used in MITICA, to allow a higher flexibility to modifications, and the presence of a different accelerating grid system of the extracted beam. In fact, as the aim of SPIDER is the production of an ion beam satisfying the ITER NBI requirements, the ion beam extracted is accelerated up to a lower energy (only 100 keV instead of 1 MeV) through just one accelerating grid placed at zero potential [16].

The SPIDER grid system is composed as follows:

- Bias Plate (for controlling the potential close to the PG)
- Plasma Grid (for negative ion production)
- Extraction Grid (for negative ion extraction and dumping of co-extracted electrons)
- Grounded Grid (for negative ion acceleration)

As the last accelerating grid (grounded grid) is placed at zero potential, the accelerating voltage is 100 kV and another 12 kV is needed for the ion extraction between the extraction grid and the plasma grid, the SPIDER source is at -112 kV potential with respect to the zero potential reference. This potential configuration leads to a specific isolating system design and to a specific design of the source electric and hydraulic service feedthroughs. An exploded view of the SPIDER beam source is given in Figure 1.10.

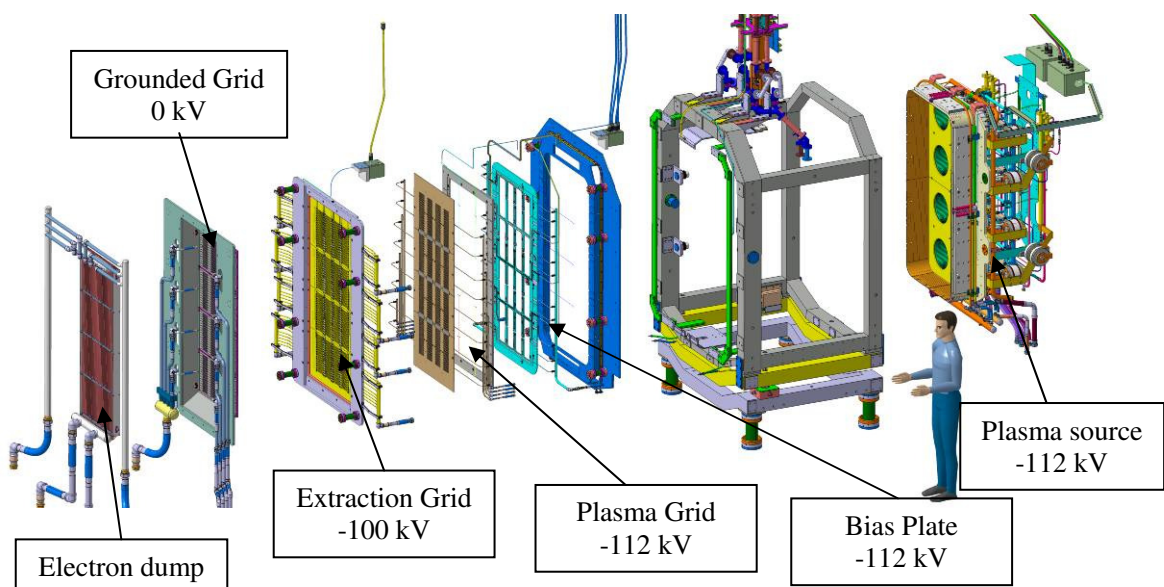


Figure 1.10 SPIDER Beam Source: exploded view

The electrons that are present in the source plasma in a great quantity can be dangerous because, once they are extracted and accelerated, they can be easily steered by magnetic fields (much more than ions since their mass is much lower) so focusing and hitting other components. This happens because electrons are negatively charged and thus they feel the electric field in the same way as negative ions. Consequently, their extraction is unavoidable (the electron to deuterium ion extraction ratio is required to be kept <1) and co-extracted electrons are one of the major sources of heat loads on the Extraction Grid; suitable magnets are in fact embedded in the Extraction Grid itself with the specific purpose of deflecting and collect the co-extracted electrons. The other main source of thermal loads on the grids is given by impinging electrons

created by stripping (see Figure 1.11). The electrons that exit from the Grounded Grid are collected in the Electron Dump to avoid they hit downstream components or the vacuum vessel.

Since the grids are loaded by very high and localized heating power, they feature many cooling channels inside the grids themselves. This guarantees the proper cooling of the components that otherwise could not survive in a steady state regime, as that required for the ITER NBIs. Magnets to steer the electrons, before they are fully accelerated, are also embedded in dedicated grooves into the grids. A detail view of the grids and of their features is given in Figure 1.12.

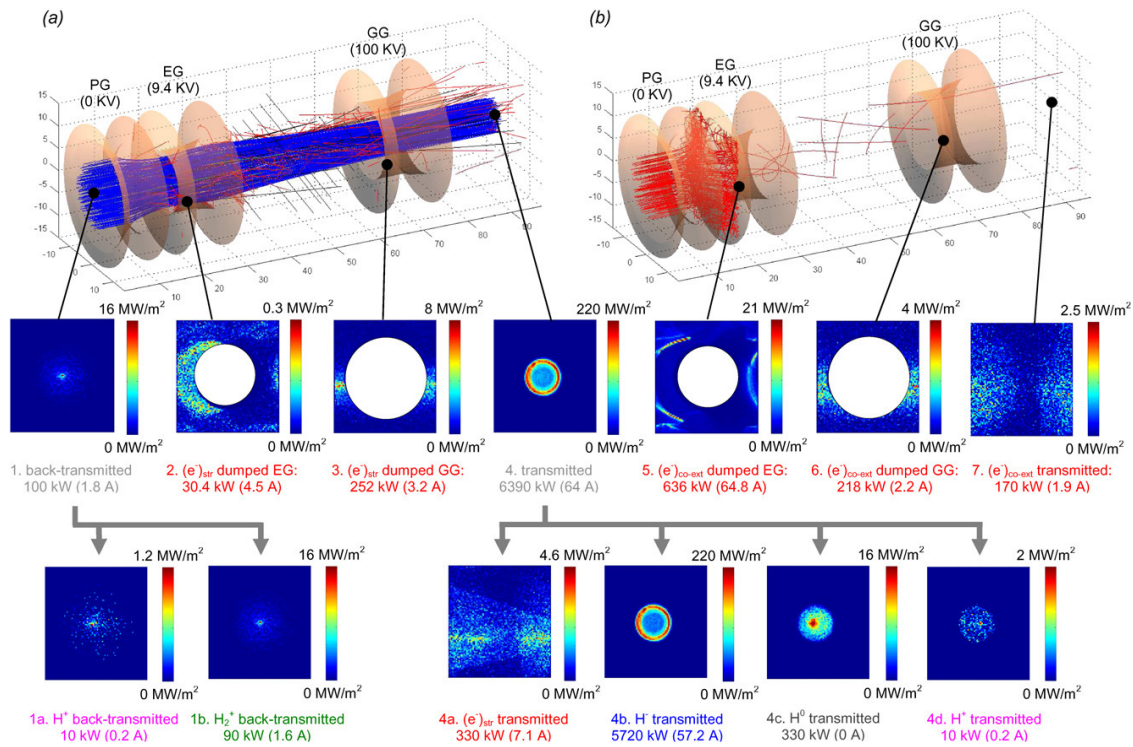


Figure 1.11 Simulation (a) of a negative ion beamlet and (b) of the co-extracted electrons in the SPIDER accelerator. The power loads and currents corresponding to the whole accelerator (1280 beamlets) are reported [17]

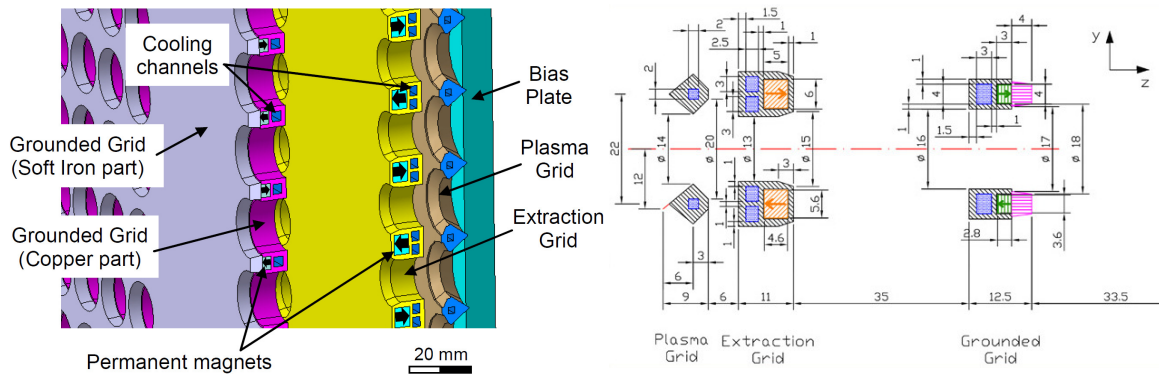


Figure 1.12 SPIDER grid system

In Figure 1.13 the SPIDER plasma source can be seen. The plasma source is mainly a box (chamber) open on the front side, having 1.8 m high, 0.9 m long and 0.2 m wide prism shape. Eight inductive radiofrequency sources, called Drivers, are placed on the rear edge of the chamber. Each driver is composed of a ceramic cylinder, made of alumina, around which electric coils, where a Radio Frequency (RF) current at 1 MHz is induced, are wound. The driver is the component where the plasma is produced by radiofrequency electromagnetic fields. Thus, in order to protect the ceramic from the plasma, the driver inner part is constituted of an actively cooled copper protection shield and permanent magnet systems for plasma confinement are installed too. On the rear of the source three caesium ovens are connected; their aim is to feed the Caesium into the source chamber in order to enhance the negative ion production. On the rear of the source also the load adaptation capacitors for the RF circuit are installed. Also all the hydraulic connections for the source component cooling water, coming from the hydraulic bushing, are routed there. The source lateral walls and the bottom of the plasma chamber (the Plasma Driver Plate), are actively cooled as well and the former also houses other permanent magnet systems for magnetic plasma confinement of the main chamber. Finally, the plasma source chamber is open on the front, where the plasma grid is located.

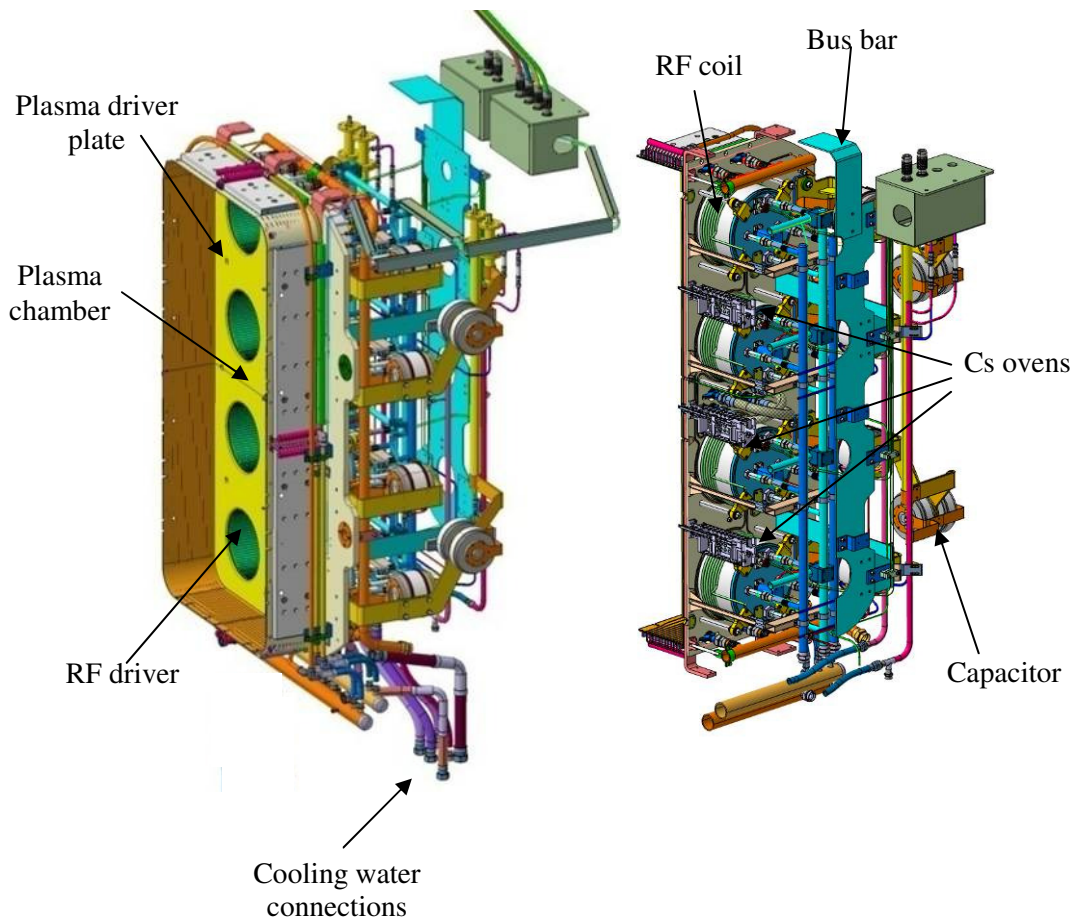
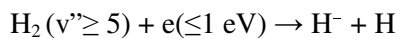


Figure 1.13 SPIDER plasma source views

1.4 Negative ion formation

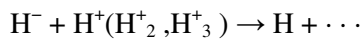
While positive hydrogen ions can be extracted directly from the plasma boundary, the physics of production, transport and extraction of negative ions is much more complex. The development of modern negative ion sources started in the '70s with the discovery of two important negative hydrogen ion formation processes: the surface and the volume production.

The philosophy on which the operation of volume production negative ion sources relies is based on the consideration of production and destruction processes. The main negative hydrogen ion formation process in pure hydrogen plasma is dissociative electron attachment (DA) to highly rovibrationally excited molecules:

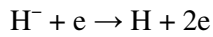


Dissociative electron attachment to vibrationally cold $\text{H}_2(v'' = 0)$ molecules is known to have a very small cross section, the DA cross section increases by five orders of magnitude when the hydrogen molecules are vibrationally excited from $v'' = 0$ to $v'' = 5$ and stays constant at higher v'' [18].

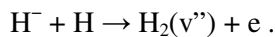
The three main volume destruction processes are: mutual neutralization (MN) in collision with positive ions (the most important)



electron detachment (ED) in collision with electrons:



and associative detachment (AD) in collision with atoms:



The other negative hydrogen ion formation process, the surface production, was discovered in the 80s [19]. Two types of H^- ion emissions from a surface are considered: thermodynamic equilibrium surface ionization and non-thermodynamic equilibrium surface ionization, or secondary negative ion formation processes. In the case of thermodynamic equilibrium surface ionization, atoms impinging on a hot metal surface may be emitted as atoms or ions in subsequent evaporation processes after mean residence times long enough for the establishment of equilibrium. In this case the probability of leaving the hot surface as a negative ion depends on the difference between the electron affinity A_e and the work function, ϕ , of the surface, i.e. $(A_e - \phi)$ and is given by the Langmuir–Saha relation.

$$Y\left(\frac{\text{H}^-}{\text{H}}\right) \propto \exp\left(\frac{A_e - \phi}{kT}\right)$$

The electron work function ϕ is a measure of the minimum energy required to extract an electron from the surface of a solid. In general, ϕ differs for each face of a monocrystalline sample. Since ϕ is dependent on the cleanliness of the surface (presence of impurities), measurements reported in the literature often cover a considerable range [20].

A low work function surface is required for negative ion formation.

However the H^- ion emission from surfaces in surface plasma sources is the result of the interaction of a fast particle with the surface and is a non-equilibrium one and may be obtained even from a surface with comparatively high work function. However no investigations of H^- emission as a function of neutral particle or H^+ velocity towards a surface with high work function were reported. An important value of H^- emission from a surface with high work function is very doubtful.

The enhanced efficiency of H/D^- ion generation in the discharge with the caesium additive [19] is caused by a substantial increase in the secondary emission of negative ions from the electrode bombarded by plasma particles.

2 The MITICA RF ion source and Plasma Driver Plate

2.1 The concept of the RF source for the ITER NBIs

The RF ion source for the ITER NBI is the component where the negative ions, that will be extracted and accelerated by the accelerator towards the ITER plasma, are generated.

The RF source utilizes the oscillating electric field, induced by a RF coil, for ionizing the Hydrogen/Deuterium gas in order to create the source plasma. The frequency adopted for the RF source is 1 MHz, and the typical RF power is around 100 kW [21]. RF sources have many advantages over the arc sources, such as:

- long lifetime due to the absence of filaments suffering of strong consumption during operation,
- better control, during beam modulation, of the extracted ion current due to the direct response of the ion density in the source to changes of the RF input power; this makes active beam current control possible;
- the simplicity of the source (less electrical connections compared to arc sources), making remote handling easier.

The source is a complex chamber, featuring a main space, enclosed in a structure called source case and facing the plasma grid, on whose surface most of negative ions are generated, and eight rear smaller chambers called drivers, where the gas is injected (hydrogen or deuterium).

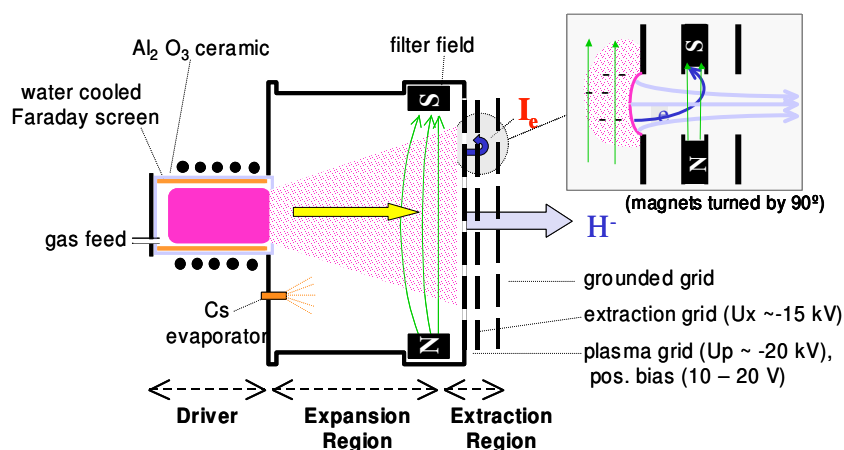


Figure 2.1: Scheme of a RF ion source

RF coils wound around the lateral wall of the drivers, and connected to a 1MHz oscillator, transfer the RF power and ionize the gas: the resulting plasma flows then into the main chamber,

where the additional presence of caesium enhances the number of negative ions generated on the surface of the plasma grid [22]. An internal water-cooled copper Faraday screen protects the driver alumina cylinder from the plasma. In Figure 2.1 a schematic of the RF source is shown.

The RF ion source also includes a series of auxiliary systems: the electric circuit for power input, the cooling circuits for heated components, the gas supply system, three ovens to dispense the caesium inside the source, starter filaments to initiate the plasma and several diagnostic sensors to monitor and control the source behaviour.

For optimum performance, i.e. high negative ions current density and a low amount of co-extracted electrons, Cs evaporation into the source is mandatory in order to lower the surface work function. The underlying process of the RF sources is, in fact, the “surface negative ion production” [22].

Due to the short survival length of the negative ions (some cm) in the plasma [23], [24], only ions created at the plasma grid can be accelerated. The evaporated caesium covers the plasma grid with a thin layer, which reduces the work function depending on the thickness of the Cs layer. The latter can be controlled (somewhat) by heating the plasma grid to temperatures in the range of 150÷200 °C. A further reduction of the amount of co-extracted electrons is achieved by biasing the plasma grid with 10÷20 V against the source body together with a sufficient filter field across the plasma grid [25]. The so called “filter field”, applied inside the RF source, in front of the plasma grid surface, is in fact necessary in order to keep the “free” electrons, which are generated by the RF and have energies of about 8 eV, away from the extraction region, where electron temperatures below 2÷3 eV are necessary for minimizing the destruction rate of the negative hydrogen ions by electron collisions; then mutual neutralization with positive ions takes over being the dominant destruction process. This magnetic field is created by the current flowing along the plasma grid and can be increased by mounting on the source side walls a set of permanent magnets.

2.2 Overall design requirements, inputs and boundary conditions

Several requirements and inputs had to be taken into account for the design of the RF ion source, starting from the initial ones stated in the ITER Design Description Document 5.3 and finishing with the continuous update received from the IPP colleagues:

- in section 2.2.1 functional requirements for the ITER NBI ion source, mainly derived from DDD5.3, are reported.

- in section 2.2.2 some fundamental contribution came from IPP are reported, regarding experience on test beds experimental campaigns (RADI, BATMAN, MANITU), ongoing designs of the new ELISE test bed and considerations of several design issues.
- further requirements have been identified during the design progress itself, due to the R&D results obtained in the meanwhile and due to the continuous development of physical models and analyses carried out at Consorzio RFX. These are presented in Section 2.2.3 and 2.2.4.
- in Section 2.2.5 a literature survey on sputtering and other effects on molybdenum surfaces after Hydrogen bombardment is presented.

2.2.1 ITER overall requirements

The starting point for the design of a new RF source for ITER NB injector was the set of requirements for the negative ions source that are stated in the DDD 5.3 and hereafter reported in Table 2.1.

<u>Parameter</u>	<u>ITER Requirement</u>
Beam energy	1 MeV (D ⁻) / 800 keV (H ⁻)
Beam current	40 A
Beamlet divergence	< 7 mrad
Calorimetric Current Density	20 mA/cm ² D ⁻ 28 mA/cm ² H ⁻
Extraction Voltage	9 kV
Source Pressure	0.3 Pa
Electron Content (j _e /j _H)	1
Pulse Length	3600 s
Source Dimension	1.5 x 0.6 m ²
Extraction Area	2000 cm ²
Uniformity	± 10%

Table 2.1 : ITER main requirements for the ion source [26]

These parameters actually refer to the beam source functional requirement, intended as assembly of ion source plus accelerator.

Part of this list have impact mainly on the accelerator design (energy, divergence, voltages), while some other characteristics have a large influence on the ion source design (dimensions, current density, source pressure, pulse length, uniformity).

2.2.2 IPP inputs

Several meetings, videoconferences and communications were held throughout the SPIDER source design phase with IPP colleagues.

The design of the new IPP test bed, ELISE, was ongoing in parallel to the SPIDER one and several issues have been shared and discussed, in order to evaluate whether to adopt the same design solutions for both, or not.

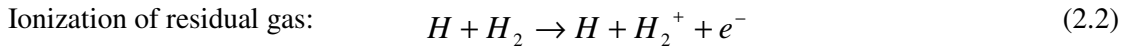
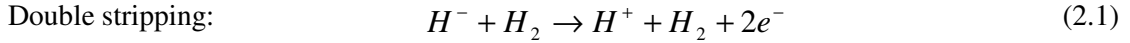
Drivers in ELISE are different from RADI ones (basis for the preliminary outline design carried out in 2007): size and inter-axis have been increased in ELISE, in order to optimize source parameters, homogeneity in particular. The same choice was done for the SPIDER RF source.

Tungsten or molybdenum coating was decided on the inside of the Faraday shield to reduce the sputtering of the copper surface due to the interaction with plasma. The presence of copper in the plasma has a pollution effect and could compromise the source functionality. A thin PVD (Physical Vapour Deposition) coating of molybdenum, of some microns (1-3 μ m) was successfully tested in BATMAN test bed faraday shield, prior to decide the adoption of this solution in the ELISE, SPIDER and MITICA RF sources, as well [27].

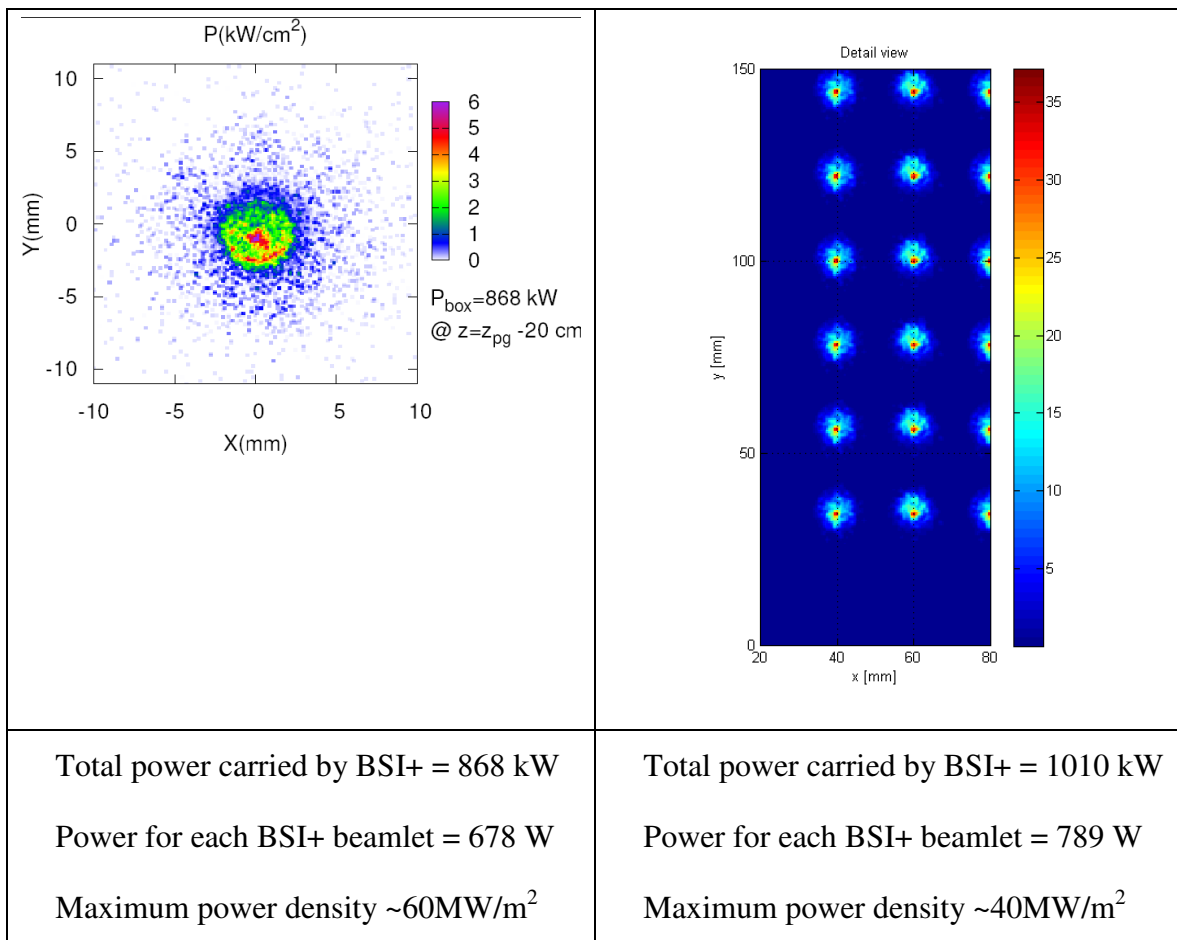
2.2.3 Evaluations concerning Back Streaming Positive Ions (BSI+)

During the last years, Consorzio RFX has been deeply involved in the development of the NBIs for ITER, both from the technical and physical points of view. Strong efforts have been spent on studying and modelling the ion extraction phenomena and the accelerator. Large improvement has been obtained with continuous update and inputs for the design, in particular on the heat loads within the accelerator and on the down-stream and back-stream components.

The so called “Back-Streaming positive Ions” (BSI+) are generated within the accelerator volume by stripping losses or by ionisation of the background gas. A significant fraction of the negative ions can, in fact, be stripped in the accelerator, losing one or two electrons by collisions with the neutral gas; when two electrons are lost, a positive ion remains. Positive ions are also created by ionisation due to collision of the beam particles with the background gas. The main stripping and ionisation reactions, causing the formation of positive ions within the accelerator, are the following:



The double stripping reaction creates a positive ion having about the same energy as the negative one from which it is generated, whilst, in the case of ionization of residual gas particles, the newly born positive ion has energy of some eV [28]. The positive ions created within the accelerator volume feel an electric field that back-accelerates them, towards the RF source; from this, the name “Back-Streaming” positive ions. As a consequence, the energy of the BSI+ depends both on the position inside the accelerator where the positive ions are created, and on the generating reaction.



a – Results of analyses done in 2006 [28]; single beamlet

b – Current data (2011) [29]; one fourth of a beamlet group

Figure 2.2: Contour plots of the power density of BSI+ calculated for the MITICA MAMuG accelerator; the total heat power associated to BSI+ is also given

The energy gained by the BSI+, due to the back-acceleration, is transferred to the exposed surface of the rear of the RF source chamber, causing physical sputtering and heat power deposition.

The first calculations on the expected BSI+ generation within the ITER NBI accelerator and the consequent heat loads transferred to the rear vertical components of the source were published in 2008 [28]. The results of this work yielded additional, strong new inputs for the mechanical design of the affected components, that are the Plasma Driver Plate (PDP) and the Faraday Shield Back Plate (FSBP), making them the most critical items of the RF ion source.

Since then, Consorzio RFX has developed the necessary qualified competences in the study of the physical processes happening within the beam source, and, in particular, in the accelerator. After the first study on the BSI+, other detailed analyses have been carried out internally on this aspect (with continuous updating in synergy with the advancement of the design) confirming the very high additional heat power load carried by the BSI+.

In Figure 2.2 the total heat power and the power density contour plot of the BSI+ are shown, comparing the results of the first study (for one beamlet), partially presented in [28], (a) with the last calculations made at RFX (for a quarter of beamlet group), based on the current design of the MITICA beam source (b) [29]. In the last calculations the total power on the back plates is higher than what initially calculated of about 16%, but the maximum power density is lower by a factor 2.

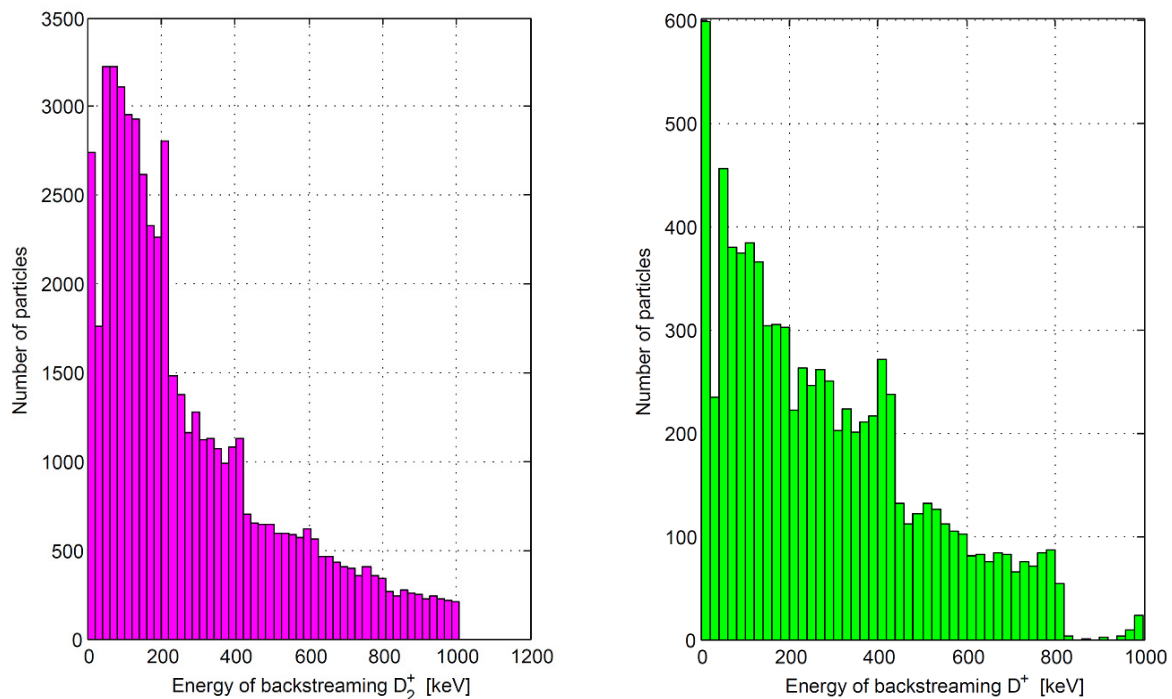


Figure 2.3: Energy spectra of the BSI+, based on the current MITICA accelerator design

The energy spectrum of the BSI+ is a function of the pressure distribution within the accelerator, in fact the higher the gas pressure, the higher the amount of stripping loss reactions (2.1) and (2.2). In Figure 2.3 the energy spectrum of the BSI+ calculated on the current MITICA accelerator design is shown: since the background gas pressure is quite high in the extractor

region (due to the relatively high pressure inside the source chamber, that is 0.3 Pa), whilst it decreases rapidly along the downstream beam direction, it can be noticed that most of the BSI+ are concentrated in the energy range 10÷200 keV (Figure 2.3).

The energy spectra of the BSI+ are very important for the evaluation of the sputtering rate, as it is described in Paragraph 2.2.4.

2.2.4 Evaluations on sputtering

If a solid surface is exposed to energetic particles bombardment, these particles can penetrate the solid and cause electron excitation and nuclear collisions. The latter generate the sputter process: if the transfer of energy is sufficient (threshold energy) to overcome the surface potential, the solid atom can be extracted from the lattice.

The sputtering yield is then defined as the average number of atoms (neutral or ionized) ejected from a surface by the impact of an ion.

In these processes it can be observed that the charge state of the impinging particles do not affect the sputter processes; the sputtered particles are mainly neutrals, the mass of the projectile is important: light particles can transfer lower energy and the sputtering yield decreases with respect to collision with heavy particles; the target temperature can influence the sputtering, in particular for incident heavy ions [30].

In parallel to the SPIDER source design, an internal technical note was written (in close collaboration between RFX and IPP colleagues), reporting the first evaluations on sputtering expected on the rear vertical plates of the RF source, hit by the BSI+ coming from the accelerator (see Paragraph 2.2.3), raising a strong issue, especially for the choice of materials. The conclusion of this analysis is shown in Table 2.2, where the last column quantifies the hours of operation of the NBI, at nominal conditions in ITER, in which the BSI+ “erode”, by physical sputtering, a 1µm thick layer of different materials. The hypothesis on which the calculations were based are:

- BSI+ composition: 86% D_2^+ / 14% D^+ (conservatively assumed 100% D_2^+)
- impinging flux: $\Phi_{D_2^+} = \frac{0.011 \text{ A/cm}^2}{e} = 6.9 \cdot 10^{16} \frac{\text{ions}}{\text{cm}^2 \cdot \text{s}}$
(equivalent to $\Phi_{D^+} = 2 \cdot \Phi_{D_2^+} = 13.8 \cdot 10^{16} \frac{\text{ions}}{\text{cm}^2 \cdot \text{s}}$)
- impinging D_2^+ energy: 540 keV (equivalent to a half energy =270 keV for a double flux Φ_{D^+} of D^+)

The preference for molybdenum or tungsten with respect to copper as plasma facing material is confirmed, since copper is sputtered 4 times faster.

From a quantitative point of view, the outcome of this study is that a thin coating of some microns of Mo, or W (for example produced by Physical Vapour Deposition – PVD, as in the IPP sources [27]) is not sufficient in the areas hit by the BSI+.

	ρ	M	ρ_{AT}	σ_{AT}	ML	SY	Φ_{sp}	$t_{\mu m}$
	Density	Atomic mass	Atomic volum. density	Atomic surface density	Monolayer thickness	Sputtering yield for D ⁺ ions	Sputtered atoms flux	Beam-on time to remove 1 μm
	[g/cm ³]	[g/mol]	[atoms/cm ³]	[atoms/cm ²]	[nm]	/	[atoms/(cm ² ·s)]	[hours]
Cu	8.9	63.54	$8.4 \cdot 10^{22}$	$1.9 \cdot 10^{15}$	0.23	0.006	$8.3 \cdot 10^{14}$	2.8
W	19.3	183.85	$6.2 \cdot 10^{22}$	$1.58 \cdot 10^{15}$	0.25	0.001	$1.4 \cdot 10^{13}$	12.6
Mo	10.28	95.94	$6.4 \cdot 10^{22}$	$1.60 \cdot 10^{15}$	0.25	0.001	$1.4 \cdot 10^{13}$	12.9

Table 2.2 : calculations on sputtering caused by the BSI+ impinging the RF source rear surfaces [31]

Each component of the RF source has to be designed for a lifetime at least comparable with the ITER one, that is 20 years. The actual operation time of the ITER H&CD NBI at nominal parameters, cannot be easily estimated, but it is larger than the 35-40 hours calculated for eroding the 3 microns thick layer of Mo (or W) [27]. Considering that the ITER NBI is foreseen to have a total beam-on time of about 5500 hours [31], the thicknesses of material removed from the hot spots can be estimated as:

$$tk_{Cu} = \frac{5500 \text{ h}}{2.8 \text{ h}/\mu\text{m}} = 1964 \mu\text{m} = 1.964 \text{ mm} \quad \text{with a copper surface,}$$

$$tk_{W} = \frac{5500 \text{ h}}{12.6 \text{ h}/\mu\text{m}} = 436 \mu\text{m} = 0.436 \text{ mm} \quad \text{with a tungsten surface,}$$

$$tk_{Mo} = \frac{5500 \text{ h}}{12.9 \text{ h}/\mu\text{m}} = 426 \mu\text{m} = 0.426 \text{ mm} \quad \text{with a molybdenum surface.}$$

The conclusion of this analysis is that a 1.0 mm thick armour layer of molybdenum or tungsten is necessary on the surfaces of the RF source hit by the BSI+.

2.2.5 Literature survey on molybdenum sputtering and blistering

In order to investigate the behaviour of molybdenum when exposed to a positive Hydrogen ion beam, a test campaign is foreseen to be carried out in a suitable facility. These tests are expected to characterize the thick molybdenum explosion-bonded back plate (see Chapter 3) from the physical sputtering point of view, being the latter caused by the back-streaming positive ions impinging the rear vertical plates of the ITER NBI RF source.

In order to obtain meaningful results, the tests shall replicate the experimental conditions expected during ITER HNB accelerator operation. The beam characteristics should be known and comparable, in terms of ion energy and heat power density, to the ones expected to be back accelerated toward plasma source during operation of ITER HNB.

Contacts with IPP colleagues have already been established in order to define and organize these tests at GLADIS facility [32] [33]. The tests campaign is expected to be carried out at the beginning of 2012.

In the meanwhile a specific investigation of the results collected in literature regarding molybdenum physical sputtering has been carried out in order to have basic information supporting the setting of significant tests and also to have a basis for the comparison of future results.

The sputtering of molybdenum by H^+/H_2^+ is well assessed in literature. Due to its high melting temperature, high thermal conductivity and high threshold energy for physical sputtering, molybdenum can be considered one of the most suitable plasma-facing materials in fusion reactors. Microanalyses on Hydrogen ions irradiated molybdenum films have been carried out and discussed in [34]. Samples constituted by a 200 nm molybdenum film deposited on a stainless steel substrate have been analyzed after being exposed to a Hydrogen ions beam with an energy level of 10 keV reaching an overall dose of 10^{20} ions·m⁻². The main conclusion coming from analyses by Scanning Electron Microscopy has been that the surfaces of molybdenum films were still dense and complete after Hydrogen ion irradiation while the degree of the crystallization was decreased due to Hydrogen ion irradiation. No visible erosion was experienced.

Furthermore theoretical formulas have been developed in order to predict the sputtering yield. Bohdanský formula [35] can be applied for all projectile-target combination from threshold energy to about 100 keV.

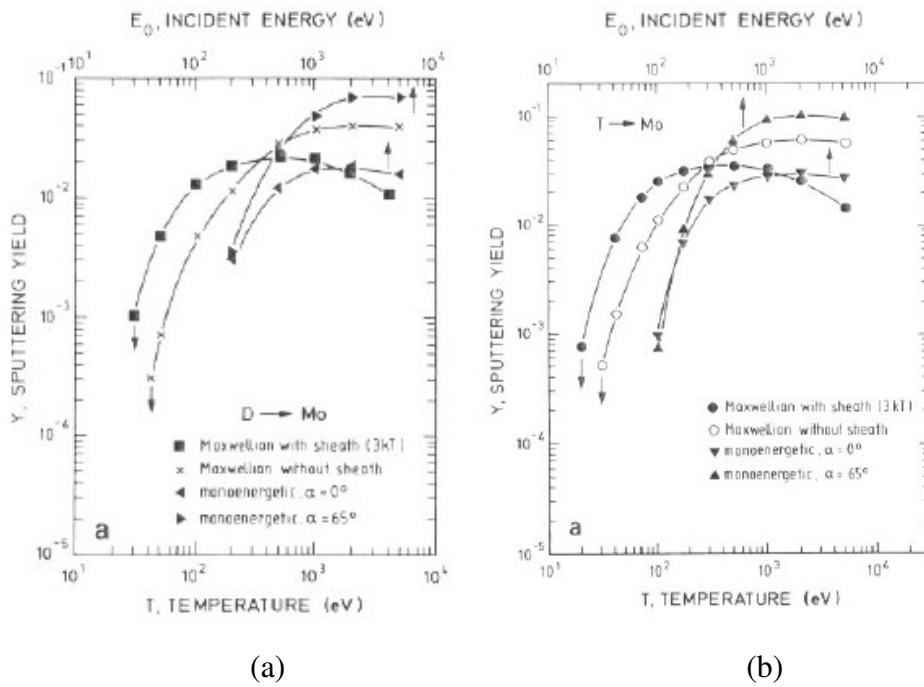


Figure 2.4: Sputtering yield of Mo versus incident energy due to deuterium (a) and tritium (b) bombardment

Computer simulations performed by W. Eckstein and J. László in [36] give the sputtering yield for molybdenum irradiated with deuterium and tritium. The sputtering yield is defined as the average number of atoms ejected from the target per incident ion. The results are shown in Figure 2.4.

Considering the expected beam-on time of about 5500 hours of ITER HNB accelerator [31], Eckstein results seem to support the choice of 1 mm thick molybdenum coating.

Nevertheless, information about deep erosion on molybdenum came from Yu. I. Belchenko at Budker Institute of Nuclear Physics of SB RAS, Novosibirsk, Russia [37]. Rapid erosion of thick pure molybdenum has been experienced during tests on Negative Ion Sources at BINP. The main characteristics of the tests (and the related equipment) performed by Dr. Belchenko are summarized below:

- the back-streaming flux was composed by a mixture of hydrogen, cesium and molybdenum positive ions. The amount of Cs and Mo impurities was not measured. The erosion was increased in the case of increased Cs leak. Most of back-streaming ions have the energy of 4÷5 keV, current density up to 10 mA/cm^2 . Part of the ions had the full acceleration energy of 25 keV.
- the anode was machined from a single piece of vacuum-melted molybdenum with a low level of impurities. Molybdenum electrode average temperature (not the surface) was about 500°C during the 5 hours run.

- the strong erosion for the 3 mm in diameter hole was exactly due to sputtering by heavy ions components.
- flakes of deposited molybdenum, produced due to cathode sputtering by 10A/80 V H₂+ Cs discharge and due to anode sputtering by back-streaming ions. These flakes were a problem for the source long-term runs.
- caesium is essential for negative ions production. Cs was fed to discharge through the hollow cathode in this case. Cs ions are blocked by discharge plasma and by negative ions extraction voltage, but there was still a small Cs leak (5 mg/hour) through the 3 mm emission hole.

The molybdenum erosion is shown in Figure 2.5.

From what experienced in the above mentioned tests, it seems that the main cause of molybdenum deep erosion is due to heavy ions like cesium ions impinging on molybdenum anode. The presence of high energy cesium ions in the back-streaming ions flux could lead to a higher sputtering yield and, consequently, to a larger and rapid erosion of molybdenum.

This hypothesis seems to be confirmed also in [38], where it is found that electrons and H⁺ beam induced ionization of Hydrogen gas and cesium vapour. Back-streaming heavy cesium ions, hitting the molybdenum target at a very concentrated point, caused large sputtering and a visible damage.



Figure 2.5: Three millimeters erosion area of Mo target during tests performed at BINP.

Also in [39] cesium ions seems to be responsible for molybdenum flaking.

For a molybdenum-cesium system a sputtering yield of 1.8 atoms/ion at 5 keV has been reported in [40]. The target temperature dependency is shown in the Figure 2.6.

Furthermore, investigations on molybdenum blistering have been carried out by T. Hoshihira in [41]. Two main mechanisms of blisters formation on Hydrogen irradiated molybdenum have been identified. One is blistering due to bubble coalescence accompanying plastic deformation of the blister skins. Another is exfoliation or fracture of a grain caused by mechanical cracking started at the grain boundaries and/or defect clusters. In this case, internal stress given by retained Hydrogen in grains and accumulated Hydrogen at grain boundaries weaken the binding force between the grains and makes crack penetration easier.

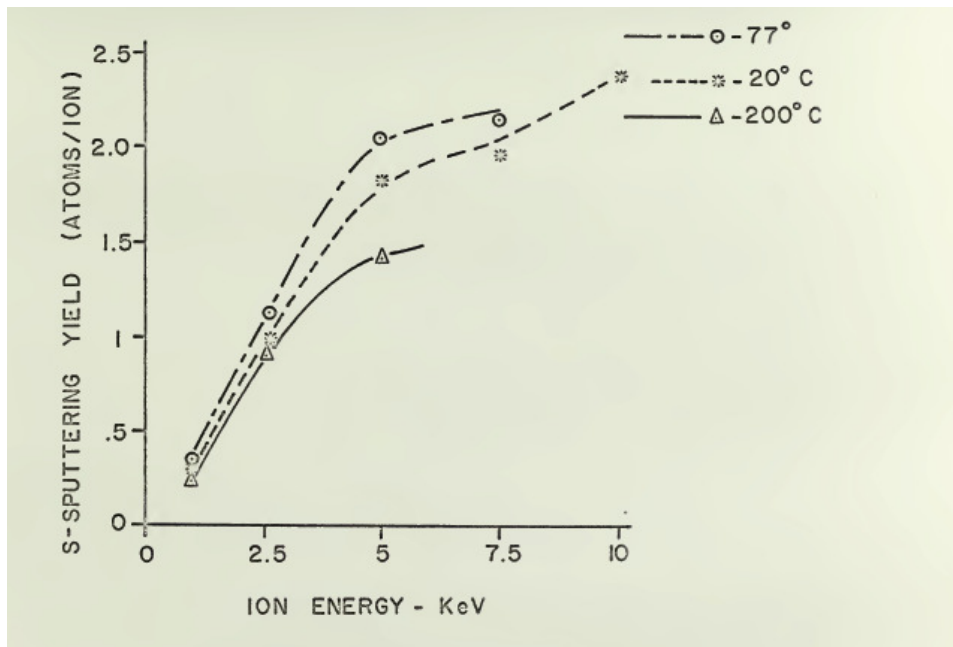


Figure 2.6: Sputtering yield versus incident ion energy for 1-10 keV Cesium ion bombardment of monocrystalline Molybdenum at 77 K, 20 °C and 200 °C with the ion beam normal to the surface.

As a conclusion of this investigation on the results collected in literature about experiences concerning effects on Molybdenum surfaces exposed to energetic ions, no severe damage has been found in case of light impinging ions. The Molybdenum sputtering yield commonly experienced when irradiated with Hydrogen or Deuterium is acceptable since the impinging particles are not so heavy to induce large erosion during long term operations.

This conclusion is coherent with the experiences of other research institutes such as IPP, where slight molybdenum sputtering yields have been found during various experimental tests

with Hydrogen ions. Also in LHD no damage due to large sputtering on the copper rear plate of the ion source chamber has been reported.

On the other hand deep molybdenum erosion has been experienced with heavy ion irradiation such as high energy cesium ions. For this reason the source conditioning with cesium assumes a great importance since even small Cs leakages through the Plasma Grid could bring to unacceptable erosion of the molybdenum back-plates due to back-accelerated Cs ions.

Anyway, the results found in literature refer to very specific tests performed with parameters not always exactly comparable to the expected ITER HNB accelerator operating conditions. In other cases the results came from computer simulations not always cross-checked with experimental results. For these reasons further investigations with the performing of dedicated tests are strongly advisable in order to assess the actual behavior of the 1 mm thick explosion-bonded molybdenum back-plates.

The expected back-streaming positive ions heat power deposition during ITER HNB accelerator operation has a maximum (calculated) power density of $\sim 40 \text{ MW/m}^2$. Furthermore the energy of the large part of impinging particles ranges between 0 and 200 keV.

Tests could be carried out at IPP GLADIS facility aiming to verify the molybdenum sputtering rate under specific controlled conditions, replicating the expected operating parameters for ITER HNB accelerator. The power density will range between 20 and 40 MW/m^2 ; the irradiation will be performed with H^+ and H_2^+ with a particle flux of $4 \cdot 10^{21} \text{ ions/(m}^2 \text{ s)}$ and a total exposure of $1 \cdot 10^{25} \text{ ions/m}^2$ [42].

These tests, together with the other results collected in literature, will assess the correct choice of an armour layer, 1.0 mm thick, of molybdenum as sputtering-resistant materials for the back-plates under ITER HNB accelerator operating conditions.

2.3 Plasma Driver Plate design and verifications

2.3.1 General description of the PDP geometry and functions

The source case of the RF source mainly consists of a main plate (or flange) and a lateral wall in stainless steel, as shown in Figure 2.7: the flange is called “drivers plate”. Both of them are described in detail in the following paragraphs.

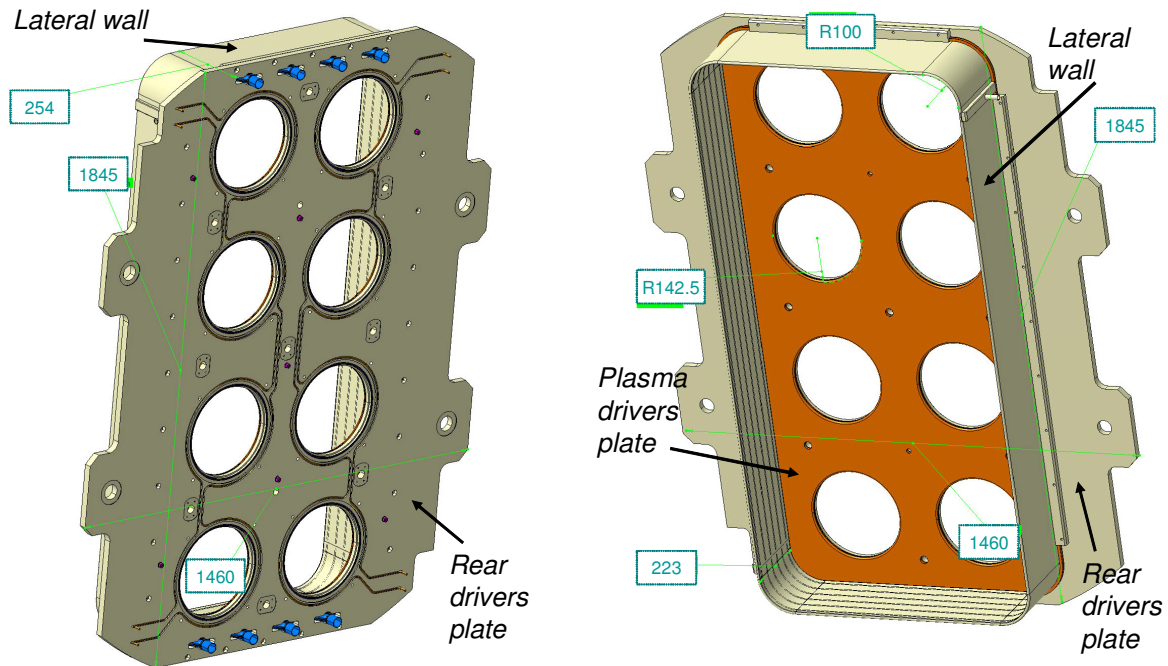


Figure 2.7: Views of the RF source case (main dimensions in dark green colour [mm])

Two different technical solutions were initially identified and studied for the PDP design, since there was no experience on the BSI+ effects and the evaluations reported in Paragraph 2.2.4 were not immediately adopted as functional and technical requirements for the design of the RF source components, since ITER had to formally evaluate and approve them.

As indicated in Figure 2.7, the so-called “driver plate” is made of 2 different plates: a first stainless steel plate, named “rear drivers plate”, acts as support for the drivers and all other components (Cs ovens, diagnostics, etc.), whereas a second plate, made of copper or copper alloys, called “plasma drivers plate”, is bolted to the previous one by means calibrated pin-screws that allow their relative differential thermal expansion.

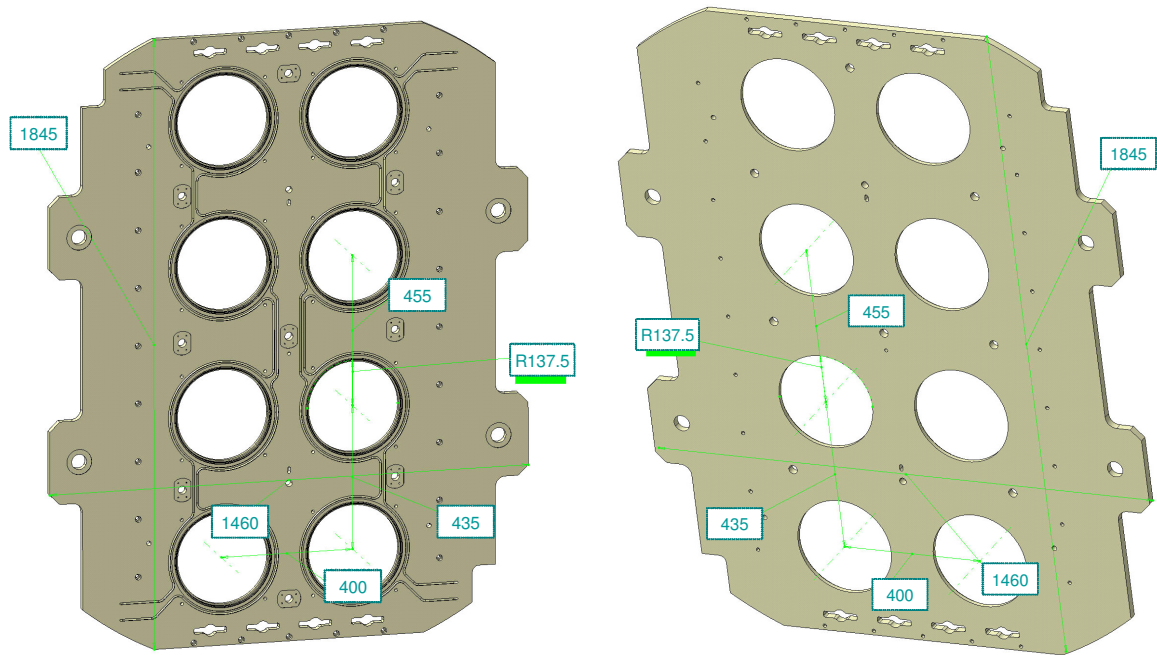


Figure 2.8: Views of rear drivers plate (main dimensions in dark green colour [mm])

The rear drivers plate (Figure 2.8) is made of AISI 316L(N)-IG, has 4 drilled “ears” for the ion source support, it is 20 mm thick and it is machined in order to:

- support the Plasma Driver Plate. The PDP is equipped with pin-screws that go through slots milled on the RDP (see Figure 2.9 - top-right view).
- support the lateral wall. The later wall has 4 drilled brackets in order to be bolted to the rear drivers plate and keeps the PDP in position (see Figure 2.9 - bottom-right view and Figure 2.7).
- support the drivers
- support the Cs ovens
- seat the shaped brazed pipes that cool the plate. The eddy currents due to the RF coils generate an internal heat load on the RDP that must be exhausted, so a dedicated cooling circuit had to be foreseen.
- allow the integration and support of diagnostics.

The PDP (Figure 2.9 – left view) was made of CuCrZr in the first stage of the design and the solution with the 1.0 mm thick armour layer was, initially, just an alternative solution, since the calculations on the expected sputtering were not already done.

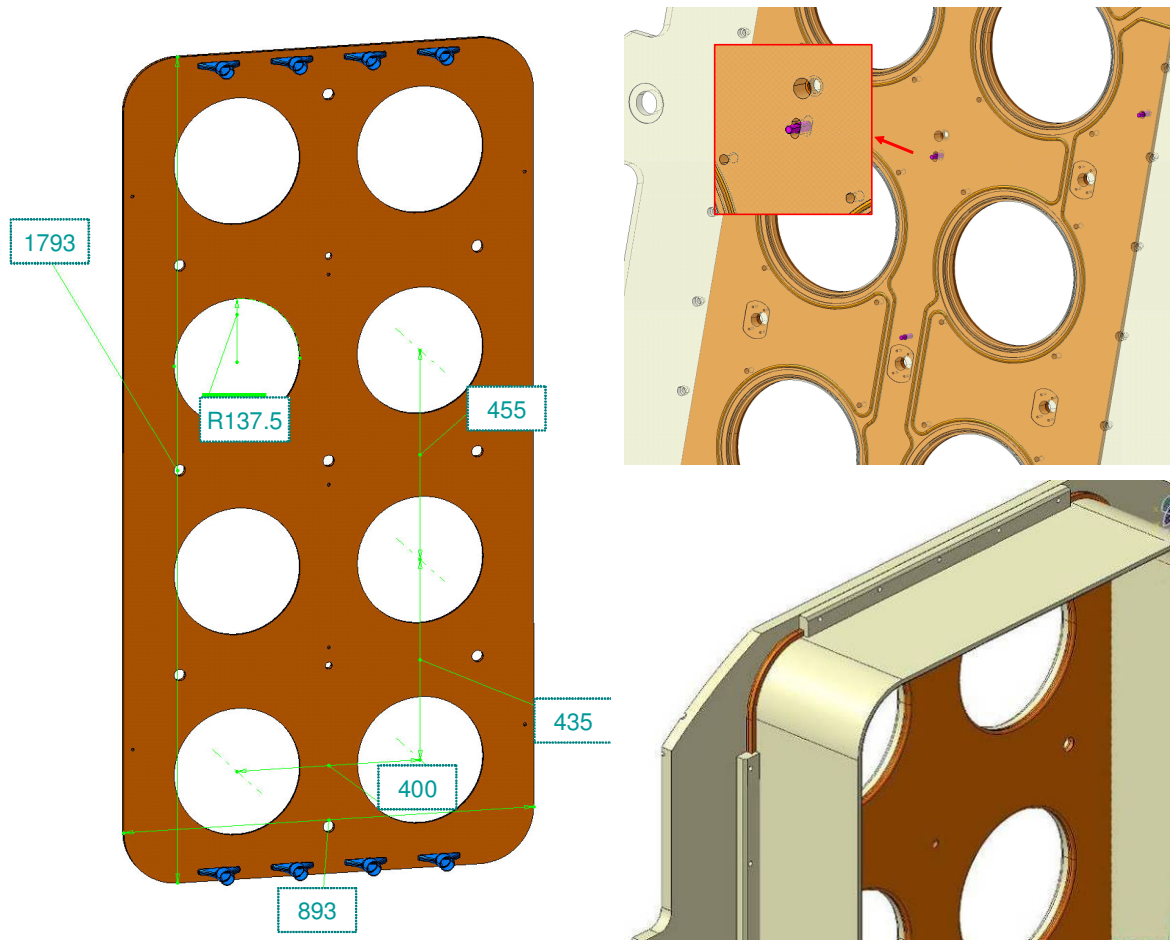


Figure 2.9: Views of the Plasma Driver Plate and its fixing systems

The reason why the RDP and the PDP are two distinguished plate is that the RDP is the main supporting component of the whole RF plasma source, whilst the PDP has the main goal of exhausting the thermal power due to the interactions with the generated plasma and carried by the BSI+ (see 2.2.3). The cooling channels of the PDP are realized by milling (a complex path of) channels and “manifolds” on the 8.5mm thick plate, on the rear side; by means of copper electro-deposition these cavities are then closed with a 3.0 mm thick copper layer.

This design allowed:

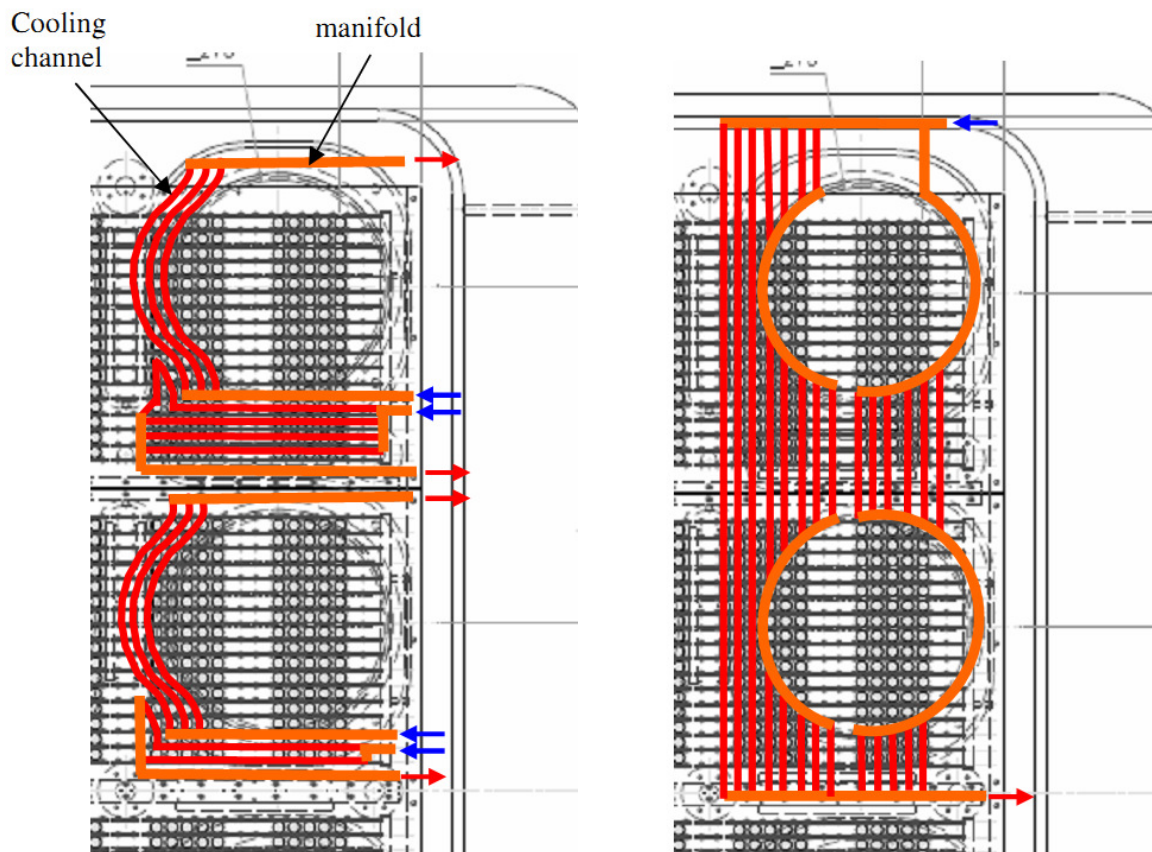
- having CuCrZr facing plasma and hit by BSI+: the CuCrZr is a copper alloy, containing less than 1% of Chromium and less than 0.1% of Zirconium; in comparison to the pure copper, the CuCrZr alloy has, after Precipitation Hardening, much higher mechanical properties, but same thermal conductivity [43].
- maximizing the heat exhaustion.
- to optimize the cooling circuit geometry and the path of the channels.

As the rear drivers plate, the plasma drivers plate has holes for drivers, diagnostics, Cs ovens and gas supply.

In line with what is foreseen for the Faraday Shield [27], a thin layer of molybdenum was prescribed on the internal surfaces of the SPIDER source chamber, in order to prevent possible sputtering of the copper surface from interaction with plasma particles.

2.3.2 Design of the PDP cooling circuit

Various solutions were considered for the cooling system of the ITER NBI and MITICA PDP, in order to withstand the loads carried by the back-streaming ions (Paragraph 2.2.4). The most significant are here below summarized and shown in Figure 2.10.



a – Solution 1: independent driver holes

b – Solution 2: division in 4 quarters

Figure 2.10: Schematics of two possible solutions for the cooling circuit of the Plasma Driver Plate

Solution 1 : independent sub-circuits for each driver hole

The first considered solution (Figure 2.10-a) foresees a number of little cooling channels bended around each driver hole. The channels are embedded inside the back plate and made by milling/electro-deposition technique. A number of inlet/outlet manifolds feed these cooling channels.

This solution has the following:

- Advantages
 - cooling efficiency
- Disadvantages
 - complicated cooling scheme, difficulty to reach all the most heated zones.
 - lack of space for the manifolding.

Solution 2: subdivision of the PDP cooling circuit in 4 quarters

The second considered solution (Figure 2.10-b) foresees vertical cooling channels running along the hot spots columns, feed by "half moon" manifolds that run around the drivers holes. The PDP cooling system is in this case subdivided in 4 quarters. The channels are embedded inside the back plate and made by milling/electrodeposition technique.

This solution has the following:

- Advantages
 - simpler cooling scheme
- Disadvantages
 - the pressure drop inside the "half moon" manifolds could cause disuniformity of the water flow (hence of cooling efficiency) in the vertical channels

Finally the “solution 2” was adopted: the PDP was subdivided in 4 quarters, as shown in Figure 2.11, with large advantages for the manufacturing and for the satisfaction of the mechanical tolerances and requirements.



Figure 2.11: Front and rear isometric views of the MITICA Plasma Drivers Plate

2.3.3 PDP design with thick molybdenum armour layer

The sputtering calculations, due to the BSI+ impinging on the PDP, highlighted that a thin PVD coating is not enough in MITICA (and the ITER NBIs). Another solution, later assumed as the reference one, was identified and then analyzed, even if it was not known how could be possible to manufacture a 1.0 thick molybdenum armour layer on the copper sub-plate.

The thickness eroded by sputtering during ITER life was in fact estimated in about 2 mm on copper surfaces and about 0.5mm on Mo or W surfaces (see section 2.2.4).

This solution with the armour layer is similar to the CuCrZr one, in terms of overall dimensions (thickness included), with the difference that the first millimetre facing the plasma is molybdenum and the “baseplate” is made of Oxygen Free High Conductivity copper, instead of CuCrZr.

From the manufacturing point of view, it was not clear how to produce this thick armour layer on the copper baseplate; consequently it was not known the manufacturing process of the PDP with this solution.

The advantages of this design are:

- less plasma pollution: impurity within the plasma due to less sputtering on Mo than on CuCrZr.
- molybdenum has a better interaction with Cs in the surface mechanism of negative ions generation rather than copper and this is the reason why the plasma grid of the RF sources are molybdenum coated [22]. Adopting molybdenum (instead of Tungsten) as armour material of the PDP, the atoms of the surface that are worn away by sputtering from the PDP, that consequently flow in the plasma and then comes to the PG surface, do not reduce the negative ions generation, by surface mechanism, as copper atoms do.

These relevant advantages clash with an engineer issue that is generated by the high difference in thermo-mechanical properties of Mo and Cu: this causes, in fact, very high stresses at the interface between the two materials that are crucial for the fatigue life mechanical verification. The problem of the interface stresses has been studied with FEM analyses and presented in Paragraph 2.7.

Some literature search was carried out investigating the possible techniques to reduce the interface stress between different materials by means of interlayer of other materials. The plasma-spray technology allows also the manufacturing of a smooth transition between the two metals by changing gradually the composition of the powder during the spraying process, for thick coating. This solution has been tested for W-Cu interfaces [44]. Similar studies have been carried out for Mo-Cu interfaces in France [45].

The thermal and mechanical verifications have been carried out calculating the main design parameters with preliminary analytical evaluations; these results have been then applied to the Finite Element (FE) numerical models in order to perform the thermal and mechanical analyses and to perform the engineeristic verifications.

The Driver Plate is cooled by two parallel cooling circuits: the first one is realized in the SS Rear Driver Plate (RDP) and it is designed to exhaust the thermal loads due to the Joule effect of the eddy currents induced by the RF coils; the second one is machined in the copper Plasma Driver Plate (PDP) and it exhausts the thermal loads generated into the source chamber and due to the BSI+.

The cooling circuit of the RDP consists of wound copper tubes running around the driver seats. These copper tubes are brazed into grooves machined on the rear surface of the RDP.

The thermal loads that have to be exhausted by this cooling circuit are actually unknown, then the copper tubes have been preliminarily designed with inner diameter 6 mm. However the water mass flow rate needed for the cooling is negligible as respect to the other components, because the heat power is low.

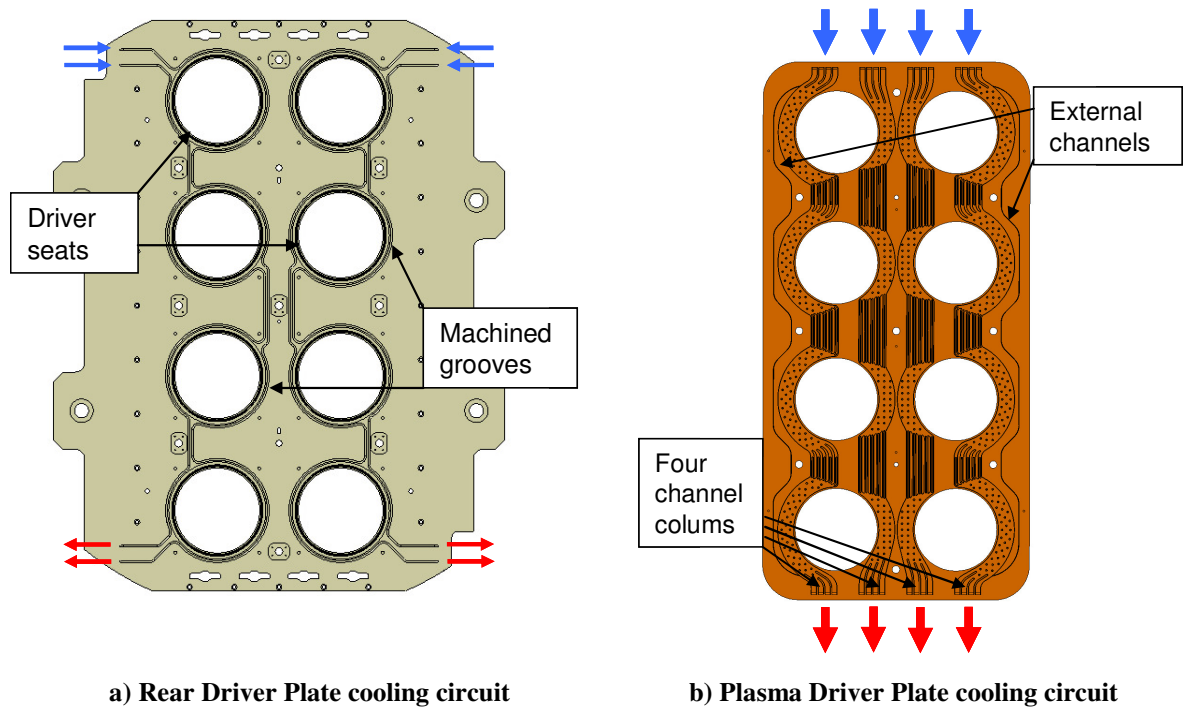


Figure 2.12: Back and front views of the 3D Driver Plate CAD model

2.4 Design criteria

The performance and the reliability required to a complex system, as the RF ion source is, can be guaranteed only if the functional and system requirements are considered since the beginning of the design phase. The requirements are analysed and developed obtaining engineering, physical, and technological issues that influence and determine the design of the system; in particular the thermomechanical design of the RF source shall consider:

- thermomechanical strength of the components (verifications of stress and strain limits, thermal fatigue and creep damages, maximum material temperature)
- material erosion due to ions sputtering
- thermal control of the source chamber (inner wall temperature around $\sim 50^{\circ}\text{C}$).

Thermo-hydraulic and thermo-mechanical numerical FE and analytical calculations have been carried out to verify the compliance with the above criteria and to reduce the need for realising three-dimensional mock-ups to prove system performance. The local heat transfer conditions for thermal control are evaluated carrying out coupled nonlinear thermo-hydraulic analyses with local calculation of the Convective Heat Transfer (CHT) coefficient during the transient analyses. The nonlinear thermo-mechanical analyses have been carried out implementing the elasto-plastic stress-strain curves of the materials, in particular the cyclic stress-strain curves for fatigue verification.

2.4.1 Thermo-hydraulic design criteria

The following main criteria have been adopted to develop the cooling circuits of the RF ion source:

- limit in the maximum material temperature at the inner channel surface, that has to be below the local water saturation temperature to avoid boiling conditions (otherwise special active cooling devices such as swirl tube elements or hypervaportrons should be used)
- subcooled water flow even if local boiling conditions could occur at the inner channel wall
- limit in the mean water velocity inside cooling channels: $v_{cc} < 10 \text{ m/s}$
- limit in the mean water velocity inside manifolds: $v_m < 6.0 \text{ m/s}$.

The suitable calculations of the convective heat transfer coefficient and pressure drops are very important for the design, optimization and thermal control of thermomechanical

components. The correlations used for analytical calculations and implemented in the FE models for local evaluations are:

- Sieder-Tate for the calculation of the convective heat transfer coefficient at the wetted surfaces [46]
- Colebrook-White for the calculation of the friction coefficient for distributed pressure drops along cooling channels [47].

Proper evaluations of the hydraulic diameter for each circuit, allow using the above correlations. Nonlinear formulations have been implemented for water thermo-physical properties considering the temperature dependence.

The components of the RF ion source have specific functional requirements referable to the inlet coolant temperatures and to the mean surface/material temperatures. The fulfilment of the functional requirements is controlled adjusting the flow rates and the inlet water temperatures of the components (see Table 2.3). The flow rate adjustments are performed by means of regulating valves at the outlet of the cooling circuits. The water inlet temperature is regulated by adjusting the flow rates at the heat exchangers and by arranging special heaters as specified by the NB Injector cooling system.

Component	Functional requirement	Inlet coolant temperature
RF coils	$T \leq 40 \text{ }^\circ\text{C}$ (to keep high electrical resistivity of water and low electrical resistivity of copper)	$T_{inlet} \approx 40 \text{ }^\circ\text{C}$
Drivers	$T \approx 50 \text{ }^\circ\text{C}$ (heat removal)	$40 \text{ }^\circ\text{C} < T_{inlet} < 80 \text{ }^\circ\text{C}$
Source case	$T \approx 50 \text{ }^\circ\text{C}$ (ions production and heat removal)	$40 \text{ }^\circ\text{C} < T_{inlet} < 80 \text{ }^\circ\text{C}$

Table 2.3 : Components functional requirements and inlet water temperature control and adjustment

2.4.1.1 Convective Heat Transfer coefficient

The RF ion source components subjected to high thermal loads are actively cooled with specific cooling circuits that have been designed considering the thermal loads and the operating conditions of each component. The coolant is demineralized water that is treated in the primary cooling water system of the test facilities.

The heat transfer between the cooling channels inner surface and the water bulk occurs by forced convection in single-phase flow. The heat flux q is proportional to the heat transfer coefficient α and the difference between the channel inner wall temperature T_w and the bulk fluid temperature T_b :

$$q(T_w) = \alpha(T_w - T_b) \quad (2.3)$$

The Sieder-Tate correlation (valid for forced convection in single-phase flow) is used to calculate the heat transfer coefficient from the Nusselt number Nu [46]:

$$\alpha = Nu \cdot \frac{\lambda}{D_h} \quad (2.4)$$

$$Nu = 0.027 \cdot Re^{0.8} \cdot Pr^{1/3} \cdot \left(\frac{\mu_b}{\mu_w} \right)^{0.14} \quad (2.5)$$

where:

- λ is the water thermal conductivity
- μ_b is the local dynamic viscosity in the water bulk
- μ_w is the local dynamic viscosity at the channel inner wall
- D_h is the equivalent hydraulic diameter of the cooling channel
- $Re = \frac{\rho \cdot v \cdot D_h}{\mu_b}$ is the Reynolds number (v is the water velocity and μ is the water dynamic viscosity)
- $Pr = \frac{c_p \cdot \mu_b}{\lambda}$ is the Prandtl number (c is the water specific heat at constant pressure)
- ρ is the water mass density
- c_p is the water specific heat at constant pressure

The ranges of validity of the Sieder-Tate correlation are: $0.70 < Pr < 160$, $Re > 10^4$, channel length/inner diameter > 60 .

The term $\frac{\mu_b}{\mu_w}$ is the diabatic correction factor known as the Sieder-Tate parameter, in which $\mu_b = \mu(T_b)$ and $\mu_w = \mu(T_w)$ are respectively the water local dynamic viscosity in the bulk and at the tube inner wall flow.

Most of the RF source cooling channels have non circular cross-section. A literature research has been carried out in RFX and the result is that there are no standard specific equations for the heat transfer coefficient in these cases.

For turbulent flow in noncircular channels/pipes, heat transfer coefficients can be determined from the usual equations (Sieder-Tate) by substituting the hydraulic diameter D_h for the pipe diameter:

$$D_h = \frac{4 \cdot A}{P} \quad (2.6)$$

Most of the thermal flow resistance is concentrated in the viscous sub-layer near the wall for turbulent flow, and the temperature and velocity profiles are relatively flat over most of the cross section. Hence, provided that there are no sharp corners, the influence of the channel shape in turbulent flow is not as great as that in laminar flow. Hence, it is generally an accepted fact that the hydraulic diameter correlates Nu and the friction coefficient f for fully developed turbulent flow in circular and noncircular ducts. This is true for the results to be accurate within $\pm 15\%$ for most non-circular ducts except for those having sharp or acute-angled corners in the flow passage. In these cases the values of Nu and f factors could be more than 15% lower than the values for the circular tube [48].

In the RF source, for technical reasons, the most channels have cross-section with rectangular shape.

In [48] (table 7.7) more accurate results for turbulent flow also for rectangular section are presented. For uniform heating on the walls it is suggested to use circular duct Nu correlation for an accuracy of $\pm 9\%$ for $0.5 \leq Pr \leq 100$ and $10^4 \leq Re \leq 10^6$. With equal heating at two long walls it is suggested to use circular duct correlation for an accuracy of $\pm 10\%$ for $0.5 < Pr \leq 10$ and $10^4 \leq Re \leq 10^5$. With heating at one long wall only, it is suggested to use circular duct correlation to get approximate Nu value for $0.5 < Pr < 10$ and $10^4 \leq Re \leq 10^6$. These calculated values may be up to 20% higher than the actual experimental values.

2.4.1.2 Pressure drops

The correlations for the calculation of the friction factor f are obtained in literature by regression fit of experimental data. For turbulent flow, the correlation of Colebrook-White [47] is used for the calculation of the friction factor along cooling channels:

$$\frac{1}{\sqrt{4f}} = -2 \log_{10} \left(\frac{2.51}{Re \cdot \sqrt{4f}} + \frac{\varepsilon_r}{3.71} \right) \quad (2.7)$$

where $\varepsilon_r = \varepsilon / D_h$ is the reduced roughness which is a dimensionless quantity. Equation (2.7) can be solved for f using a convenient numerical method like bisection or Newton-Raphson.

The pressure drop Δp along a cooling channel of length L is then calculated with the correlation:

$$\Delta p = 4f \cdot \frac{L}{D_h} \cdot \rho \cdot \frac{v^2}{2} \quad (2.8)$$

The maximum absolute roughness for copper tubes $\varepsilon = 0.01$ mm has been considered for the analyses. This is a conservative value since a lower roughness would cause smaller pressure drops along the cooling channels.

The inlet/outlet localized pressure drops are estimated with the ratios 0.5/1.0 of the kinetic load.

2.4.2 Thermo-mechanical design criteria

The ion source components are subjected to thermal cycles due to plasma standard operation mode of the NB Injector in ITER (beam injection pulses up to 3600 s at full power) and commissioning/conditioning mode (the NB Injector power is dumped onto the calorimeter). Three types of load cycles are considered, applying a procedure [49] for combination of cycles, during the load history of the NB Injector system: beam-on/beam-off, breakdown cycles and plasma-on/plasma-off. Then, the thermal fatigue of the ion source components is due to the effects of three types of thermal cycles:

- cycles associated with each of the beam-on/beam-off pulses at full power;
- cycles associated with the breakdowns in the beam source occurring during the duration of each pulse;
- cycles related to the on/off cycles of the ions source (plasma-on/plasma-off cycles).

The first type of cycles implies a full thermal excursion from coolant temperature or the plasma-on temperature to the maximum surface temperature, while the second type (having duration typically shorter than the thermal time constant of the high heat flux elements) produces only a partial temperature decrease. The strain range associated with the second type of cycles derives from the transient power load starting from steady state at full power, then no power during a pause of 50 ms, then linear power ramp up to full power in 80 ms. Therefore the breakdown strain range is smaller than the first one due to beam-on/beam-off cycles. In general a breakdown frequency of 1 breakdown every 50 s is assumed. Only for commissioning/conditioning, during short pulses (up to 50 s duration) a breakdown frequency of 1 breakdown every 5 s is assumed [50].

Total beam-on time [s]	Total number of pulses	Total number of breakdowns
$1.98 \cdot 10^7$	$5.0 \cdot 10^4$	$4.5 \cdot 10^5$

Table 2.4 : Duration and design cycles for the fatigue life assessment of the RF source components

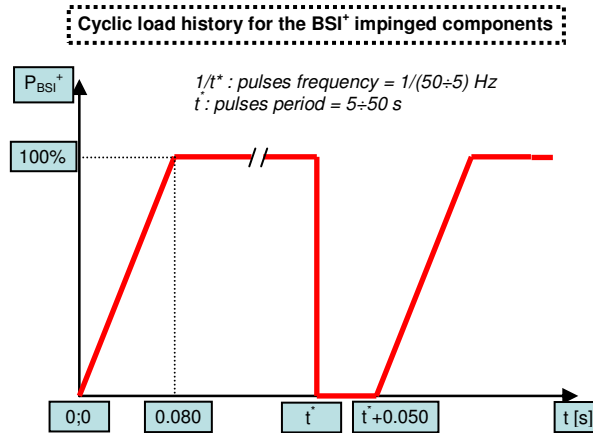


Figure 2.13: Transient PD applied during breakdown cycles with 50 ms breakdown pause, 80 ms linear power ramp up to full PD

The number of plasma-on/plasma-off cycles has not been established, but it will be less than the beam-on/beam-off cycles considering the operation of the RF source in the ITER NB Injector. Then, this cyclic load is considered to carry out the fatigue verification of components that not experience other cyclic loads. The fatigue verifications with plasma-on/plasma-off cycles have been carried out considering the beam-on/beam-off cycles: $5.0 \cdot 10^4$.

The envisaged damage for the RF ion source components are monotonic type (M-type) damage, that denotes damage in a structure which can result from the application of constant loads, and cyclic type (C-type) damage, that denotes damage that results from repeated application of loads (ratcheting and fatigue). The results of thermomechanical analyses are post-processed applying the verification criteria for prevention of C-type damages [51]. M-type verifications have been also satisfied in compliance with International Codes [49], [50], [52] but they are much less critical being C-type structural verifications caused by high thermal loads variations.

The verifications that have been carried out are associated with the normal operation of the ITER NB Injector for Heating & Current Drive and they are classified as level A (the aim of level A criteria is to protect the component against damage) [49], [50]. The RF source components must maintain the specified service function under level A loads.

The following rules are aimed at providing sufficient safety margins with regard to C-type damages [49] and are applicable only if the rules for the prevention of M-type damage have

been satisfied. The way in which the operating periods are combined depends on the specific limits being evaluated [49].

To account for the usual fatigue results dispersion and size effects [49], a safety margin has been adopted, with respect to the average curve, considering:

- division by 2 of the strain range,
- division by 20 of the number of cycles.

A statistical approach could be applied on the fatigue endurance data sets to account for the results dispersion and size effects. Precise values of these statistical coefficients could be calculated for strain range and number of cycles, and then the design curve could be depurated from assumptions and further safety coefficients. Moreover, the fatigue design curve could be obtained parametrically in temperature on the basis of data collected at different test temperatures. Actually, the fatigue design curve is modified considering the effects of local stress and strain components, the mean stress, local temperature, hold periods for the creep-fatigue combine effects.

The strain range for the fatigue life assessment has been calculated in each node of the FE model with the octahedral shear (or Von Mises) strain range rule defined as follows [49] [50]:

$$\overline{\Delta\epsilon} = \frac{\sqrt{2}}{3} \cdot \sqrt{(\Delta\epsilon_x - \Delta\epsilon_y)^2 + (\Delta\epsilon_y - \Delta\epsilon_z)^2 + (\Delta\epsilon_z - \Delta\epsilon_x)^2 + \frac{3}{2} \cdot (\Delta\epsilon_{xy}^2 + \Delta\epsilon_{yz}^2 + \Delta\epsilon_{zx}^2)} \quad (2.9)$$

The local equivalent strain range is calculated combining the strain ranges that are maximized in the time range and are expressed in a fixed Cartesian coordinate system.

The effect of mean stresses may be considered in strain controlled fatigue modifying the Manson-Coffin relationship [51]:

$$\Delta\epsilon_{ax} = \left(1 - \frac{\sigma_m}{S_u}\right) \cdot C_{el} \cdot N^{n_{el}} + C_{pl} \cdot N^{n_{pl}} \quad (2.10)$$

The experimental fatigue curves are obtained with uniaxial load condition ($\Delta\epsilon_{ax} = \Delta\epsilon_{el} + \Delta\epsilon_{pl}$) in which the plastic strain range component is not changed since $\nu_{pl} = 0.5$, but the elastic strain range component has to be multiplied by $(1 + \nu)/(1 + 0.5)$ [49], [51].

The fully reversed multiaxial fatigue curve $\overline{\Delta\epsilon} - N$ for CuCrZr-IG in the range of cycles $10^3 \leq N \leq 10^7$ and in the temperature range of $20 \div 350$ °C (with high temperature fatigue tests conducted in vacuum or in an inert gas environment) is [43], [51]:

$$\overline{\Delta\varepsilon} = \frac{1+\nu}{1+0.5} \cdot \left(1 - \frac{\sigma_m}{S_u}\right) \cdot C_{el} \cdot N^{n_{el}} + C_{pl} \cdot N^{n_{pl}} = \frac{1+0.33}{1+0.5} \cdot \left(1 - \frac{\sigma_m}{S_u}\right) \cdot 0.00828 \cdot N^{-0.06} + 0.20 \cdot N^{-0.54} \quad (2.11)$$

The fully reversed multiaxial fatigue curve $\overline{\Delta\varepsilon} - N$ for unirradiated OFHC copper in the range of cycles $11 \leq N \leq 1.4 \cdot 10^{10}$ and in the temperature range of $20 \div 300$ °C (with high temperature fatigue tests conducted in vacuum or in an inert gas environment) is [43], [51]:

$$\overline{\Delta\varepsilon} = \frac{1+\nu}{1+0.5} \cdot \left(1 - \frac{\sigma_m}{S_u}\right) \cdot C_{el} \cdot N^{n_{el}} + C_{pl} \cdot N^{n_{pl}} = \frac{1+0.33}{1+0.5} \cdot 0.0040 \cdot N^{-0.075} + 0.4989 \cdot N^{-0.56} \quad (2.12)$$

The design curves for fully reversed multiaxial fatigue are obtained translating the above equations by the factor 2 along the axis of strain ranges and 20 along the axis of cycles.

2.5 Thermal design of the PDP

Preliminary analytical calculations have been carried out in order to estimate the water temperature rise and the Convective Heat Transfer (CHT) coefficient to be applied to the FE model.

Thermal transient and thermo-mechanical nonlinear analyses have been carried out using finite element numerical models.

The geometry of the whole Plasma Driver Plate would require a very large model for the analysis with a sufficient mesh refinement.

The cyclic conditions along the vertical and horizontal directions, due to the hot spot periodicity, and the hypothesis of isostatic constraints for the whole plate, allowed the study of a group of smaller and detailed finite element models, developed for specific aims with suitable assumptions, as explained below.

The critical heat conditions for the component are in fact localized in a high number (1280) of very small areas. This induce to analyze the plate just in correspondence to these points, allowing significant time and resource saving.

The models allow the evaluation and verification of the thermo-hydraulic design parameters, heat transfer conditions, temperature profiles, thermal deformations and stress on the plate

2.5.1 Preliminary analytical calculations

Cooling circuit engineering design

The reference inlet water temperature for these analyses was assumed to be 55°C, as foreseen in ITER (even if the inlet temperature has been then revised and changed more than once, in the last years, and it is now 35-45°C for the RF source components in MITICA). This value is specified as boundary condition at the inlet manifold.

The water bulk temperature rise has been analytically estimated, so the local bulk temperature of 68°C has been assumed and imposed for the local FE model analyses.

By counting the number of hot spots that impinge the PDP, that is 608, it is possible to calculate the total power due to BSI+ on the PDP and on the FS (see Figure 2.14).

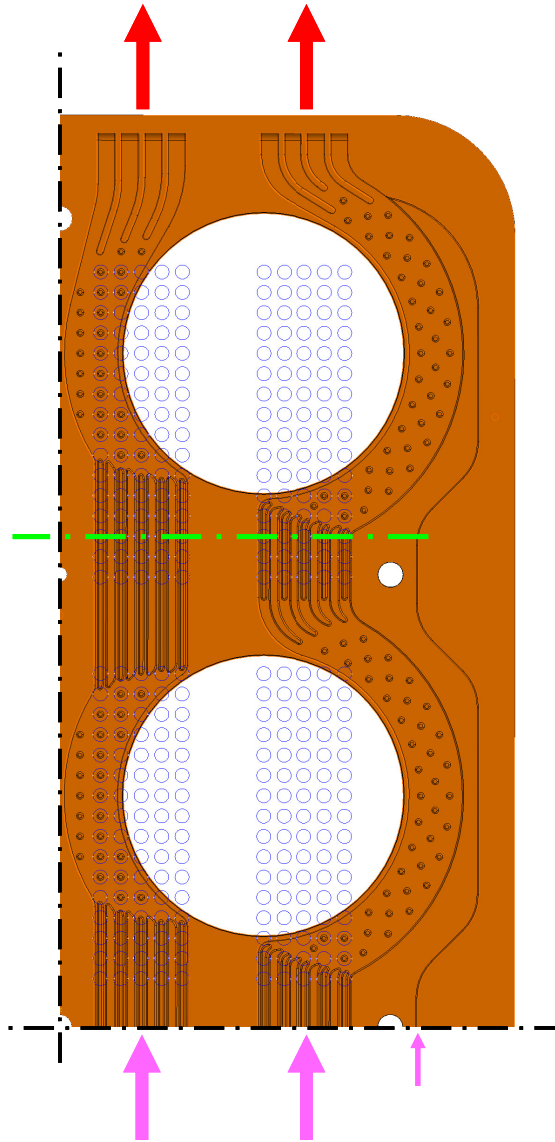


Figure 2.14: Plasma Driver Plate cooling circuit (for symmetry reasons just a quarter of PDP is shown)

The ratio between the number of hot spots gives the ratio between the power applied to the Plasma Driver Plate $P_{BSI^+}^{PDP}$ and to the Faraday Shield Back Plate $P_{BSI^+}^{FS}$:

$$\frac{P_{BSI^+}^{PDP}}{P_{BSI^+}^{FS}} = \frac{608}{672} = 0.475 \quad (2.13)$$

$$P_{BSI^+}^{PDP} = 0.475 \cdot 868 \cong 412kW \quad (2.14)$$

$$P_{BSI^+}^{FS} = (1 - 0.475) \cdot 868 \cong 456kW \quad (2.15)$$

The power on the PDP due to the 20kW/m^2 uniform distributed power density is:

$$P_{PD}^{PDP} = PD \cdot A_{PDP} \cong 21\text{kW} \quad (2.16)$$

The total power that must be exhausted by the Plasma Driver Plate cooling circuit is:

$$P_{tot}^{PDP} = P_{BSI+}^{PDP} + P_{PD}^{PDP} \cong 433\text{kW} \quad (2.17)$$

The water mass flow rate is set to 9 kg/s (8.8 kg/s for BSI+ plus 0.2 kg/s for the two lateral channels (see Figure 2.14) due to the very high power density applied in each hot spot. The water velocity in the cooling channels is $\sim 9\text{ m/s}$ and, consequently, a high CHT coefficient is guaranteed. Furthermore, a margin of about 10% is kept, on the maximum water velocity of 10 m/s inside the cooling channels, fixed by the design.

The bulk water temperature rise results as follows:

$$\Delta T_{bulk}^{water} = \frac{P_{tot}^{PDP}}{\dot{m} \cdot c_p} \cong 12^\circ\text{C} \quad (2.18)$$

that is a reasonable value of ΔT , since it keeps safety margin against overloads.

The mean water temperature at the outlet manifold is $55 + 12 = 67^\circ\text{C}$, but the non equal distribution of the hot spot onto the central and the external cooling channels columns cause a larger water temperature rise in the central cooling channels. The different values of pressure drops into the central and external columns are not considered in these analyses, so the same mass flow rate has been assumed for each of the four columns of channels.

	Central	External	Total
Hot spots number per column	214	90	608
Power [kW]	301	132	433
m' [kg/s]	4.4	4.4	8.8
Coolant inlet [°C]	55	55	55
ΔT_{med} [°C]	16.3	7.2	11.8
Coolant outlet [°C]	71.3	62.2	66.8
Coolant average [°C]	63.2	58.6	66.8
T (3/4 plate) [°C]	68.0	61.2	

Table 2.5 : PDP cooling circuit temperature rises

At the section highlighted in green dashed line in Figure 2.14, the most significant for the analyses, because it is localized at the end of the cooling channel, the water bulk temperature is 68°C (Table 2.5) and this is the value adopted in the FE analyses.

The water temperature rise of 12°C is not so high and it could be possible to think to use a lower water mass flow rate; the main problem is that a high value of water flow rate is needed in order to guarantee a high CHT coefficient.

Convective heat transfer coefficient evaluation and modelling

The heat exchange between the plate wetted surfaces and water depends on the CHT coefficient and influences the temperature of the plate. Accordingly to the Sieder-Tate formula [46], the CHT coefficient has been calculated for the 5x5mm² channel section, as explained in Paragraph 2.4.1.1:

$$\alpha = \frac{Nu \cdot \lambda}{D_i} \quad (2.19)$$

where Nu is calculated as follows:

$$Nu = 0.027 \cdot Re^{0.8} \cdot Pr^{0.33} \cdot \left(\frac{\mu_{T,bulk}}{\mu_{T,wall}} \right)^{0.14} \quad (2.20)$$

The hydraulic diameter of the channel has been calculated as prescribed by most of the heat exchanger handbooks, for non circular channels:

$$D_i = \frac{4 \cdot A}{P} \quad (2.21)$$

In order consider the diabatic factor $\left(\frac{\mu_{T,bulk}}{\mu_{T,wall}} \right)^{0.14}$ in the FE analyses, the CHT coefficient

has been analytically calculated in advance for each channel with the simplified formula:

$$Nu = 0.027 \cdot Re^{0.8} \cdot Pr^{0.33} \quad (2.22)$$

The diabatic factor has been then introduced by varying the wall temperature in the calculation, maintaining constant to 68°C the reference water bulk temperature. The data have been fitted, obtaining an equation of the second order for the CHT coefficient, much simpler to be implemented in the FE simulations than the original Sieder-Tate one, as function of the wall temperature.

The afore described equations have been used in the FE analyses to apply the CHT coefficient to the channel wall surface, by selecting the nodes and applying to them the CHT coefficient, with intervals of 2°C. The procedure required the adoption of an iterative solving procedure, re-application of the CHT coefficient, till reaching the convergence. This procedure

was necessary, since the wall temperature resulted quite high and the diabatic factor could not be neglected (see Paragraph 2.6.3.1).

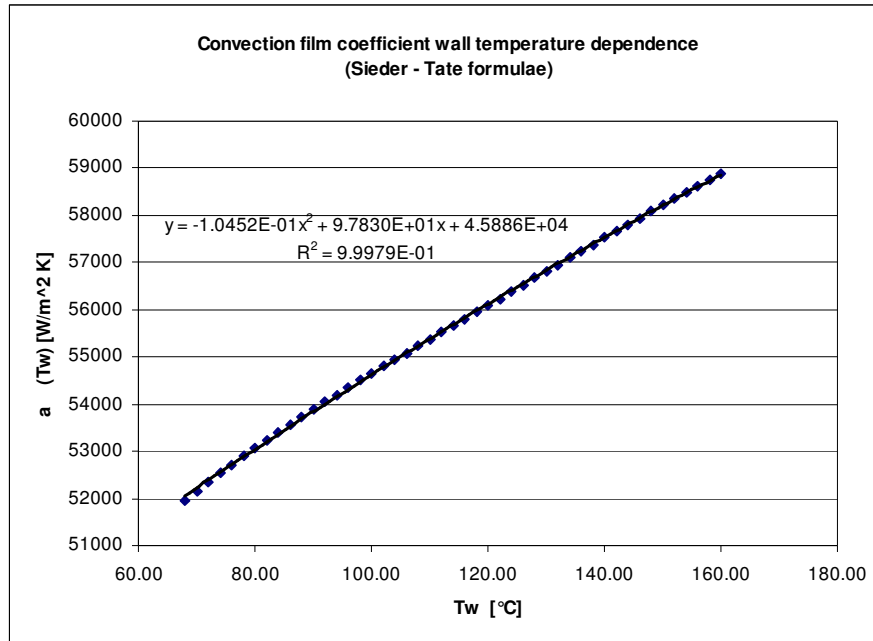


Figure 2.15: Graphic of the forced convective heat transfer coefficient as function of the channel wall temperature for 5x5 mm² cooling channels

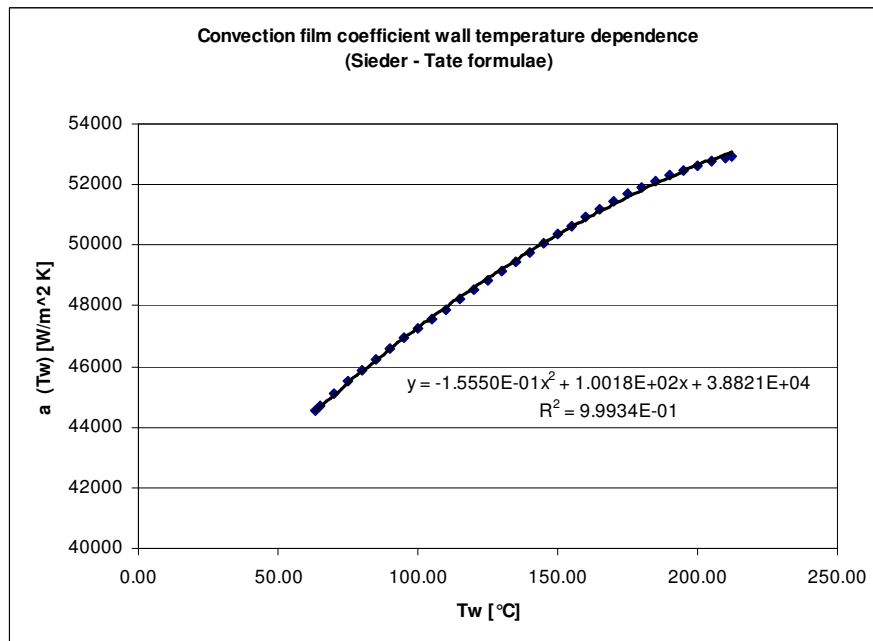


Figure 2.16: Graphic of the forced convective heat transfer coefficient as function of the channel wall temperature for the 50x5 mm² cooling channels

2.6 Finite Elements thermal analyses and verifications

The high complexity of the PDP geometry, the very high and localized power density carried by the BSI+, and the related thermal and mechanical issues, make the development of a unique large FE model of the whole plate a very difficult task.

2.6.1 FE models description

In order to study the behaviour of the whole PDP with a good detail but with reasonable resources, the two most relevant sections/portions of it have been modelled and analyzed.

Figure 2.17 shows an image of the PDP and the two main models, here named “5x5 mm² channels FE model” and “half-moon manifold pillar FE model”.

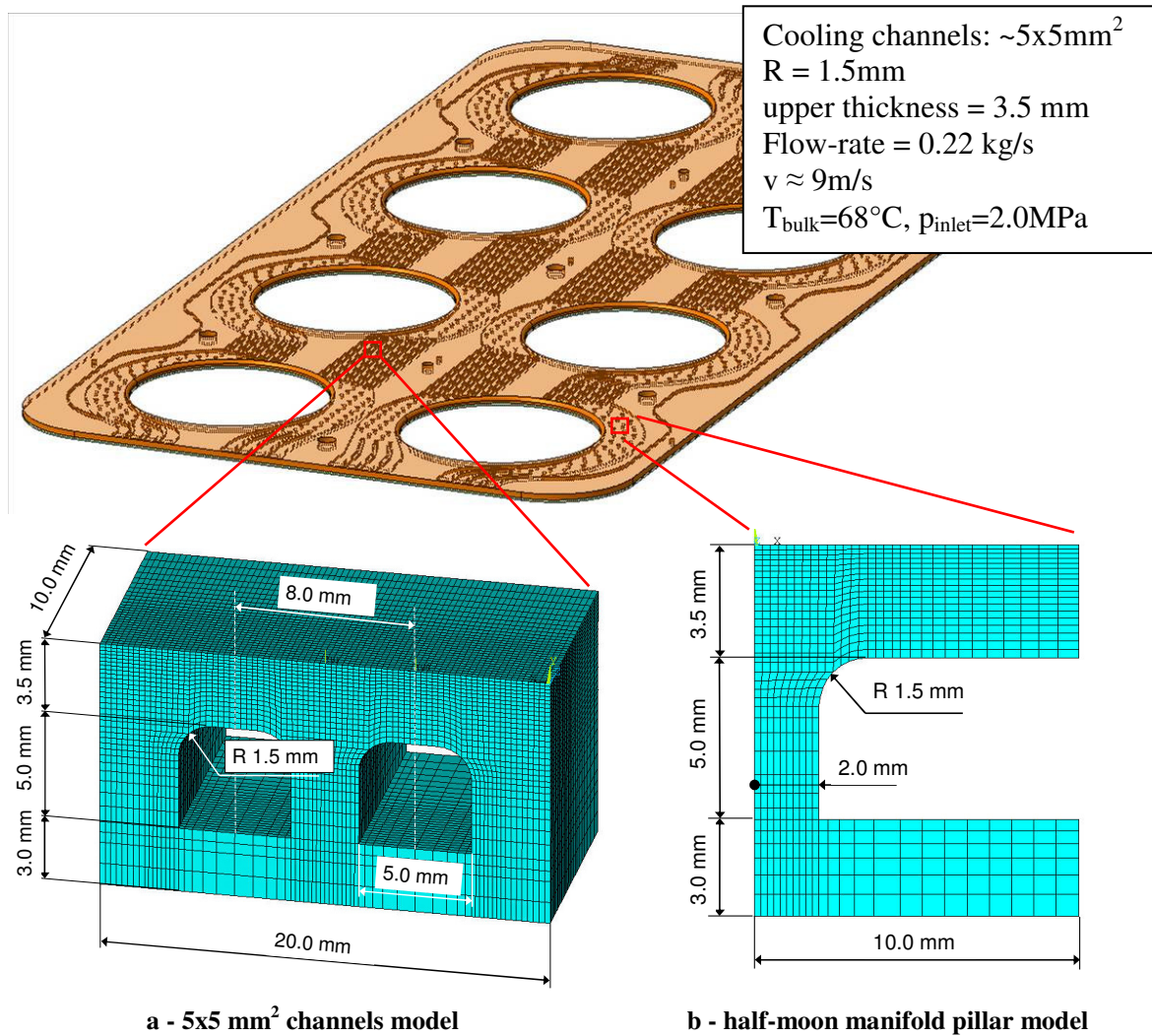


Figure 2.17: FE models of the PDP cooling channels

2.6.2 Thermal loads

The Driver Plate has to withstand cyclic thermal loads and constant pressure, inside the channels, due to the pressurized water flowing into its cooling circuit.

Analytical calculations and numerical analyses have been carried out in order to estimate the heat loads due to the BSI+ on the source case, as reported in Paragraph 2.2.3.

The power density for each one of the 1280 “hot spots”, corresponding to the position of the PDP, used as loading condition for the analyses is shown in Figure 2.2. The total heat load, given by the BSI+ on the source, is 868 kW (see Figure 2.2).

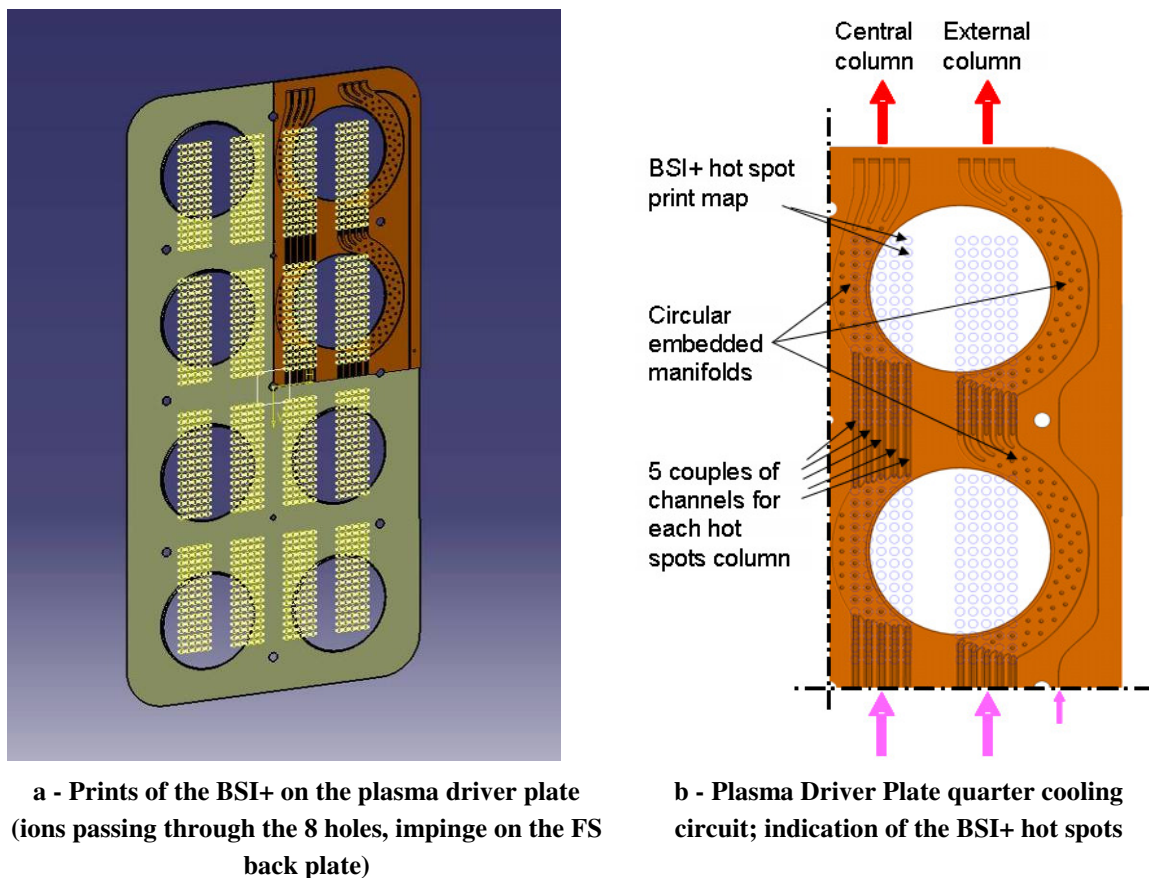


Figure 2.18: View of the Plasma Drive Plate with BSI+ impinging point map

Not all the BSI+ beamlets hit the PDP, since some of them pass in the driver holes and impinge on the Faraday Shield Back Plate. Since the grids have 1280 apertures in total, and only 608 of them are in correspondence of the PDP (see Figure 2.18), it is possible to calculate the heat power (P_{DP}) due to BSI+ on the Plasma Driver Plate:

$$P_{DP} = \frac{608}{1280} \cdot 868 \cong 412kW \quad (2.23)$$

This heat load given by the BSI+ is not stable, because the electric breakdowns between the accelerator grids cause periodic falls in the down-stream acceleration of negative ions and in the up-stream acceleration of the BSI+, as well.

Since 450000 breakdowns and 50000 beam-on/off cycles are foreseen for the ITER life-time, the heat load due to the BSI+ has a cyclic behaviour, as shown in Figure 2.13 and it was necessary to perform the fatigue verification of the impinged components, accordingly to the design criteria explained in section 2.4.2.

Beam-ON heat load

In order to determine the suitable power density distribution to be applied to the FE model in correspondence of each hot spot, a sinusoidal curve has been adopted as axi-symmetric power density profile. It has been fixed to 60MW/m^2 the maximum power density (PD^{max}), by analyzing the power density contour plot of Figure 2.2-a, and the maximum radius of the sinusoidal “bell” (R_{eq}) has been then calculated by fixing the total power per hot spot ($P^{\text{BSI+}}_{\text{,HS}}$), that is given by

$$P^{\text{BSI+}}_{\text{,HS}} = \frac{868\text{kW}}{1280} \cong 678\text{ W} \quad (2.24)$$

This assumption was necessary since no more data was available on the power density distribution per hot spot apart from the contour plot.

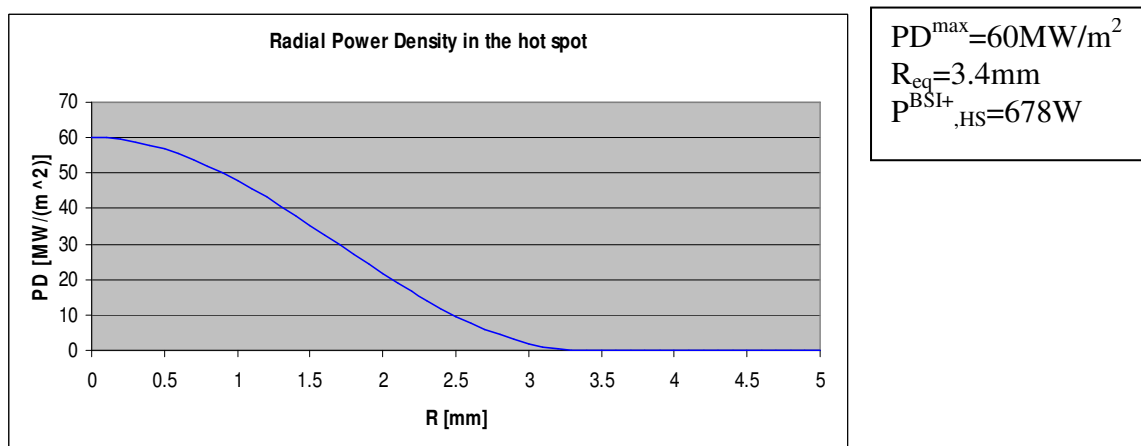


Figure 2.19: Power density profile applied on the models

By comparing the plots in Figure 2.20 it is possible to note that the model-load is a bit more critical than the one of Figure 2.2-a: in fact, the higher and larger the power density in the middle of the print, the higher the resulting thermal gradients.

This gives to the simulation some safety margin on results (not easily quantifiable) since the critical factor in this condition is the high thermal gradient on the plate, that induces high localized mechanical stress in the materials.

A further uniformly distributed heat load of 20kW/m^2 [14] has been considered all over the PDP, due to the interaction with the plasma in the source chamber. It is represented by the blue contour in Figure 2.20-a.

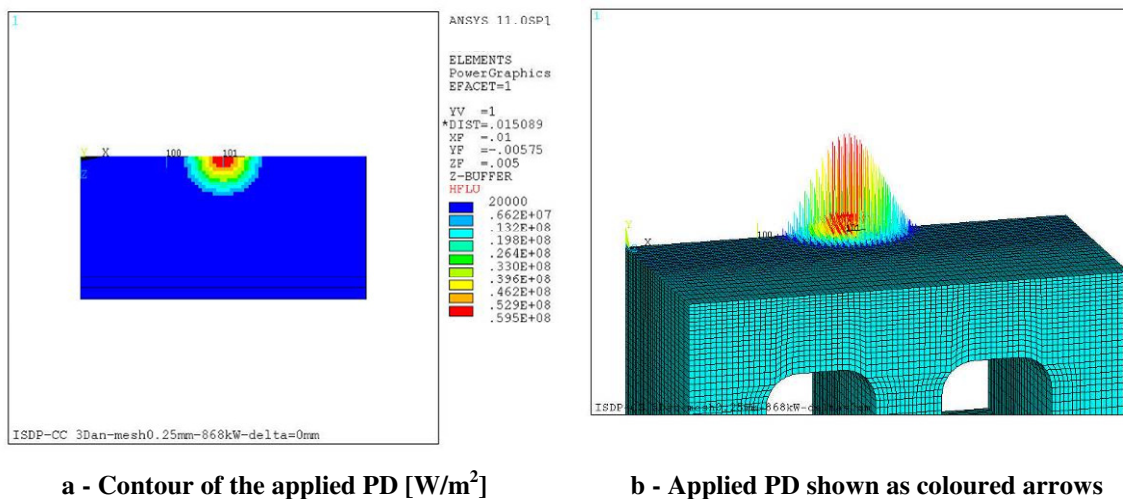


Figure 2.20: Power density (PD) applied on the FE models during beam-on conditions

Beam-OFF heat load

The beam-ON/OFF determine the thermal cycles of the Driver Plate structure with thermal excursion from the maximum temperature reached during the beam-ON to the lower temperature reached at the end of the breakdown pause when the component is exposed only to the uniform PD of 20 kW/m^2 due to the plasma interaction (see relative load case of Figure 2.21).

The breakdowns imply thermal cycles with smaller temperature excursion than the beam-ON/OFF due to the short duration of the breakdown pause.

The Power Densities has been applied to the FE model nodes (with an automatic procedure), following the sinusoidal distribution shown in Figure 2.19 by imposing the agreement between

the single hot spot integrated power and the total value of the heat power given by the BSI+, divided by the 1280 PG apertures.

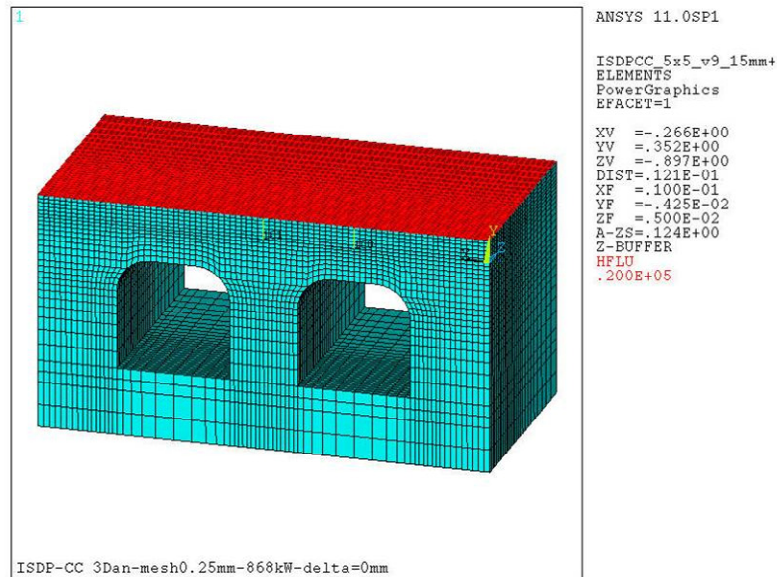


Figure 2.21: Power density [W/m²] applied to the FE models during beam-off and breakdown pause

2.6.3 FE analyses of the 5x5mm² model

The three dimensional solid models have been created in ANSYS® with the bottom-up technique and dragging the lowest-order entities along the channels axis direction. The global coordinate systems are placed with X and Z coordinates in the Driver Plate plane and Y as beam axis. A fine mesh of solid elements with 0.25 mm width, 0.25 mm length is modeled (values at the surface where the heat loads are applied). The thickness of these elements is about 0.15 mm for the CuCrZr (reference) model.

Models with different cooling channels geometry has been developed and analyzed, taking into account both maximum reached temperatures, foreseen total pressure drops and sputtering phenomena. By means of successive improvements, the configuration and its relative model shown in Figure 2.17-a has been selected, as the best one. The cross section of each channel is 5mm by 5 mm, with round corners on the top, in order to reduce the thermally-induced stress concentrations. The pitch between the coupled channels is 8 mm; the channels are in fact “coupled” in correspondence of the impinging BSI+ column in order to double the heat exchange surface, minimize the path of the heat flux and reduce the maximum temperature variation caused by possible changes in the hot spots position. Each couple of channels is then

reproduced with a pitch of 20 mm, that is the horizontal pitch of the holes on the grids. This design, with the PDP made in CuCrZr, was initially taken as reference solution [53].

The analyses of the model with an upper 1.0 mm thick Mo armour layer, are presented in Paragraph 2.6.4.

2.6.3.1 Convective Heat Transfer coefficient

The CHT coefficient to be applied to the model is a 2nd degree function of the wall temperature and it is calculated for each node by iterative solutions.

Figure 2.22 shows the applied CHT coefficients to the model. It is in the range 52600÷56800 W/(m² K).

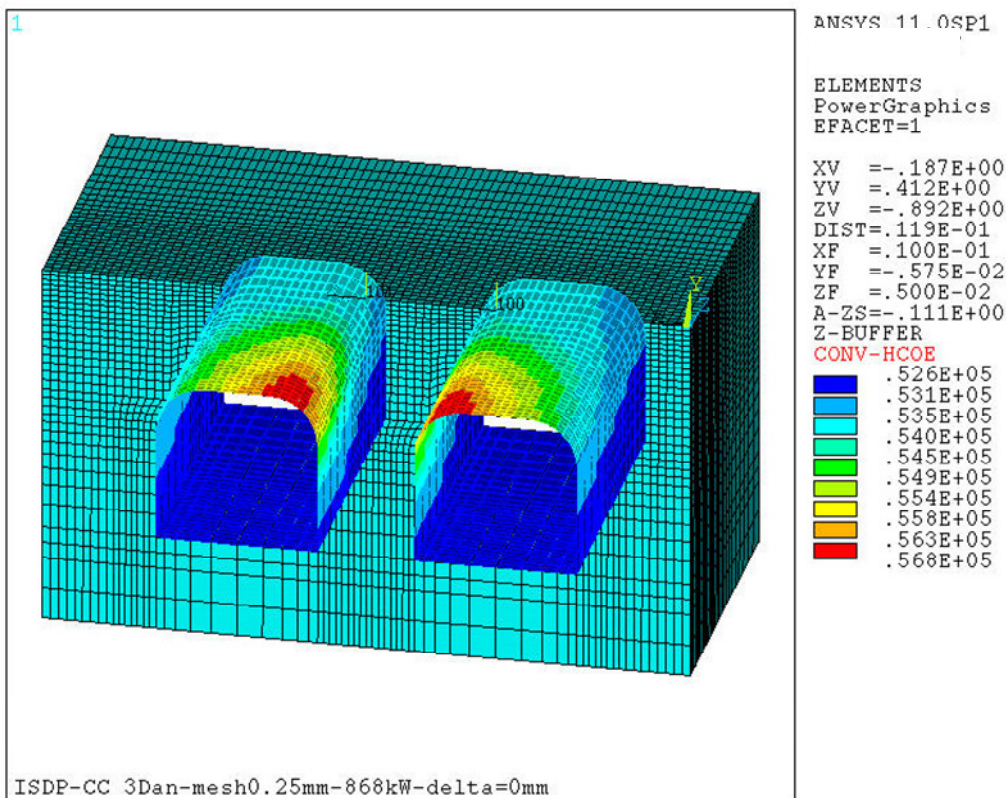


Figure 2.22: Convective heat transfer coefficient [W/(m² K)] applied to the 5x5 mm² CuCrZr model

2.6.3.2 Boundary conditions

Adiabatic conditions on all the boundary surfaces of the Plasma Driver Plate are considered a good approximation to simulate the thermal behaviour of the plate: radiation and conduction through contacting surfaces were neglected. Nodes at the lateral surfaces of the model (referred to X direction) with same y and z in plane coordinates are coupled in temperature degree of

freedom. This constraint is useful only for the load cases in which the hot spot is not centred on the model (nominal position) and then the symmetry conditions fall, as discussed in Paragraph 2.6.3.3.1.

2.6.3.3 FE nonlinear thermal analyses

The results of the analyses are presented in terms of temperature distribution, thermal fluxes and thermal gradients.

The results of thermal analyses allow:

- the verification of the operating temperature range;
- the application of the thermal results on the structural model to carry out the mechanical structural analyses and verification.

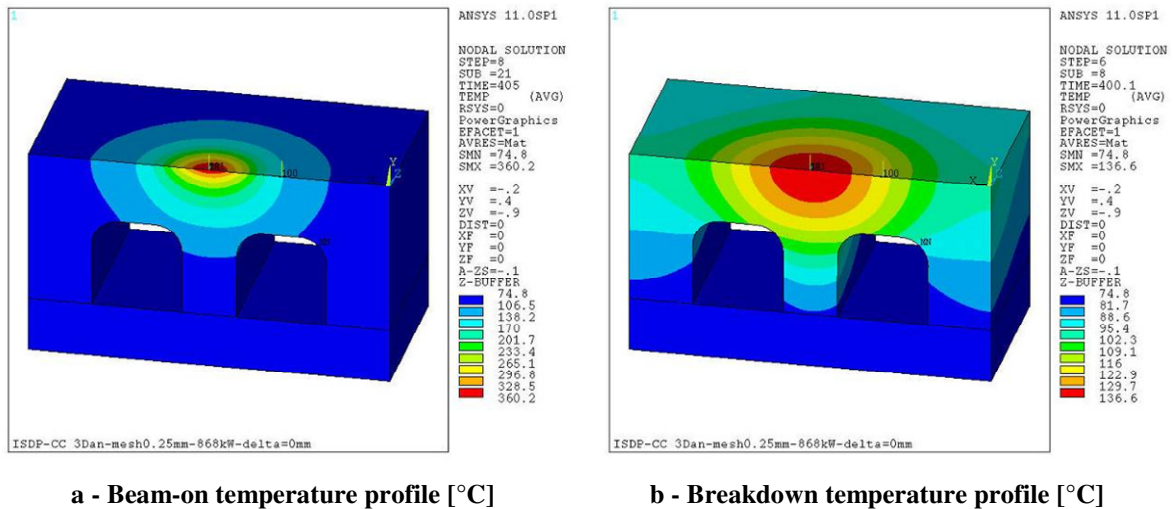


Figure 2.23: Beam-on / Beak-downs temperature [°C] profiles

Figure 2.23 shows the temperature distribution on the CuCrZr PDP 5x5mm² model, assuming the hydraulic parameters corresponding to the reference operating conditions (9m/s coolant water velocity, the correspondent CHT coefficient, 68°C coolant bulk temperature).

The hottest area of the model during beam-on condition is localized just in a very small volume where the BSI+ beamlet impinges the plate: there is a spherical cup of about 2.5 mm diameter and less than 0.5mm depth with temperatures over 300°C and just a surface node that achieve 360°C.

Such temperatures are high for CuCrZr alloy, over the safe limit (of 350°C) of about 10°C. This condition could however been accepted in this analysis because:

1. the exceeding of the temperature is very limited: the aging of the material is very slow at 360°C;
2. the volume interested by temperature higher than 350°C is of some tenth of cubic millimetre or less;
3. the heat power load applied on the model is very high and concentrated, and more critical than what was calculated [28].

For these considerations the design was considered acceptable.

The very high heat fluxes in the heat sink cause large temperature decrease during the breakdown pause: $\Delta T=223^\circ\text{C}$ during 50 ms (Figure 2.23-b).

These very high, fast and localized excursions in temperature cause high local stress on the material.

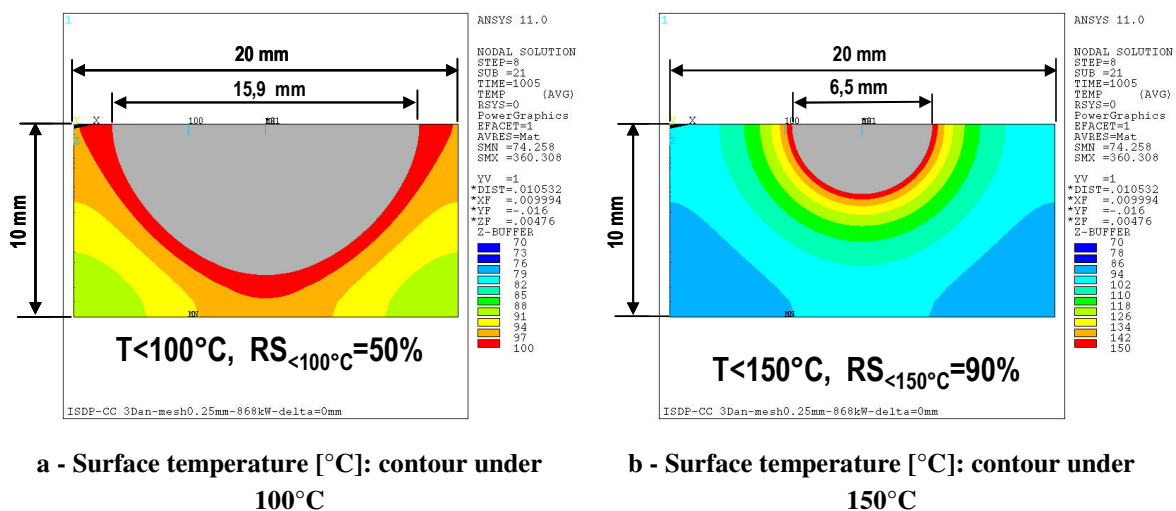


Figure 2.24: Plasma surface temperature [$^\circ\text{C}$] of the model under beam-on conditions

It is important to note (Figure 2.24) that the 50% of the surface material facing the plasma has temperature under 100°C, as required for an optimum management of the caesium, and the 90% is under 150°C.

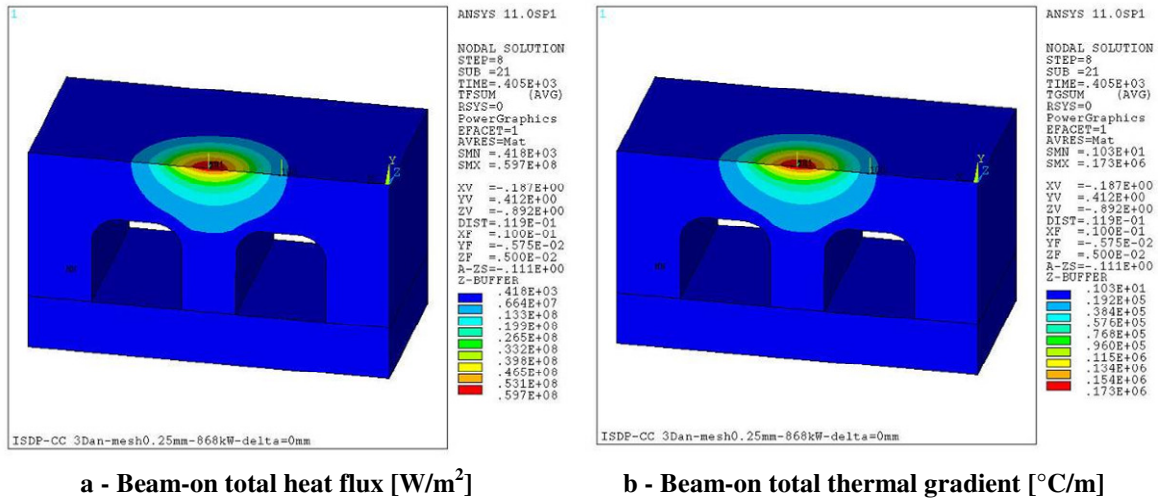


Figure 2.25: Beam-on total heat flux and thermal gradient

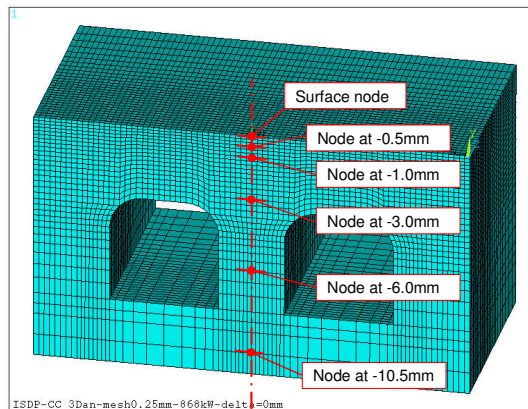


Figure 2.26: Scheme of the nodes of which time dependent temperatures are plotted

The charts in Figure 2.27 show the time dependent temperature of 6 nodes positioned in the beamlet axis direction and respectively on the surface and at 0.5, 1, 3, 6 and 10.5 mm deeper in the plate, as shown in Figure 2.26.

From Figure 2.27 it is possible to note how the temperature excursion due to the breakdown pause is higher at the surface and it decreases going deeper in the material. In particular it halves from the surface down to 1 mm of depth.

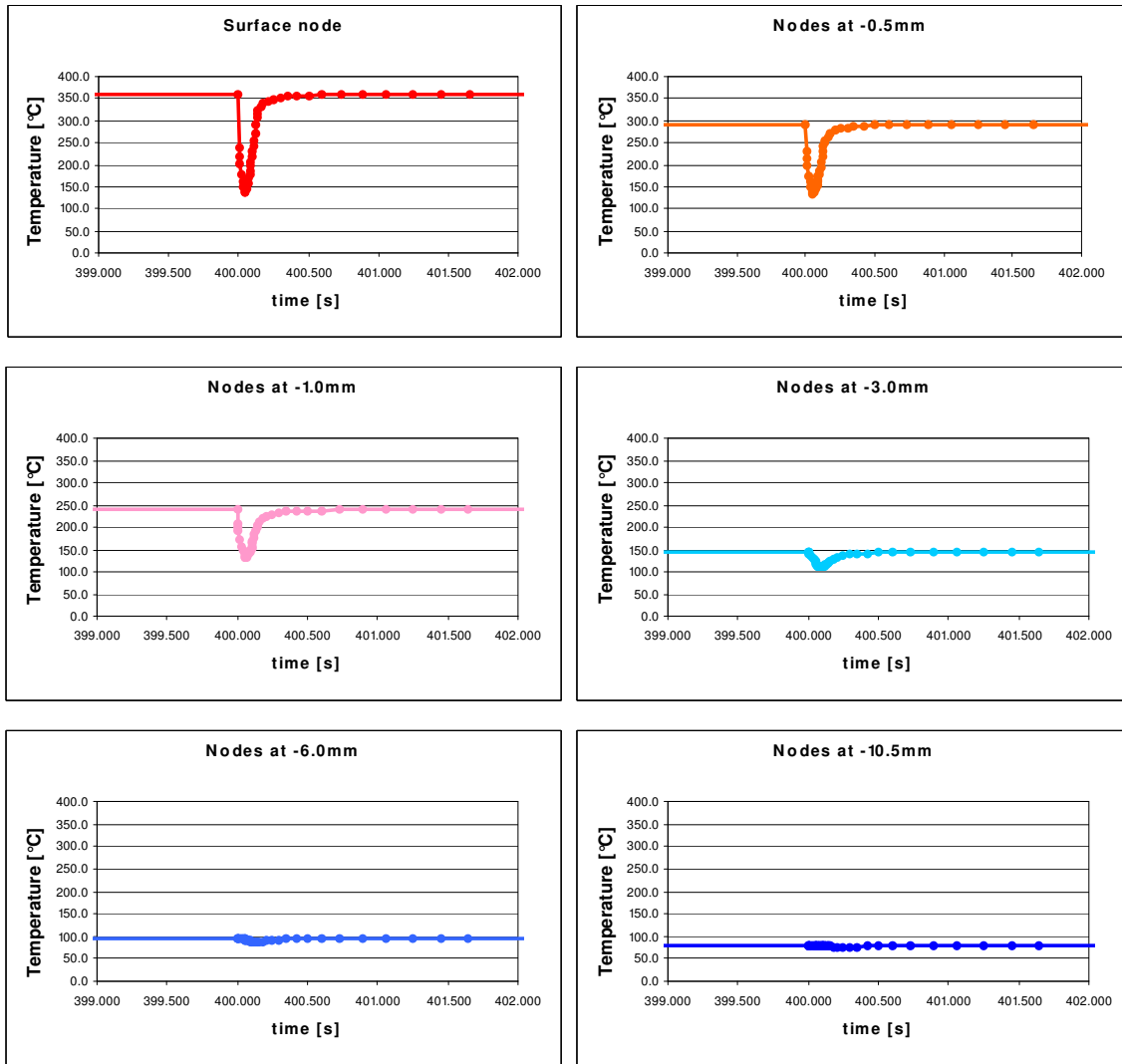


Figure 2.27: Time dependent temperature for the nodes shown in figure 4.2.9

2.6.3.3.1 5 mm displacement of the hot spot

On the same model further analyses have been carried out considering a possible (maximum) displacement of 5 mm of the BSI+ beamlet, causing an asymmetric heat load on the FE model. In this case it was necessary to couple the temperature degree of freedom of the nodes at the lateral surfaces of the model (referred to X direction) with same y and z in plane coordinates in order to guarantee the periodicity of the results.

The value of 5mm should be considered overestimated, in fact the BSI+ beamlets are well focused, due to the optics, so the possible displacement can only depends on a the thermal expansion of mechanical misalignment of the grids (the latter required to be smaller than 0.2 mm) and the thermal expansion of the RF source.

Figure 4.2.11 shows the FE model loaded with the BSI+ beamlet power density, displaced of 5.0 mm.

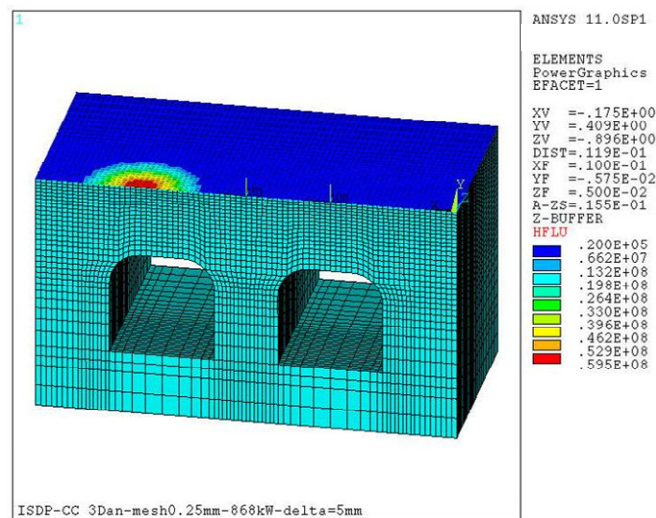


Figure 2.28: 5x5 mm² CuCrZr model with 5 mm displaced heat load [W/m²]

As shown in Figure 2.29 the maximum reached temperature is comparable to the one reached in the model under nominal heat conditions. The thermal gradients obtained from the analysis (Figure 2.30) are quite the same to those of the on-axis loading condition. This relevant datum suggests that the cooling channels geometry assure that the thermal behavior of the material under the impinging beamlet is scarcely dependent on the hot spot position in a range of misalignment 0-5 mm.

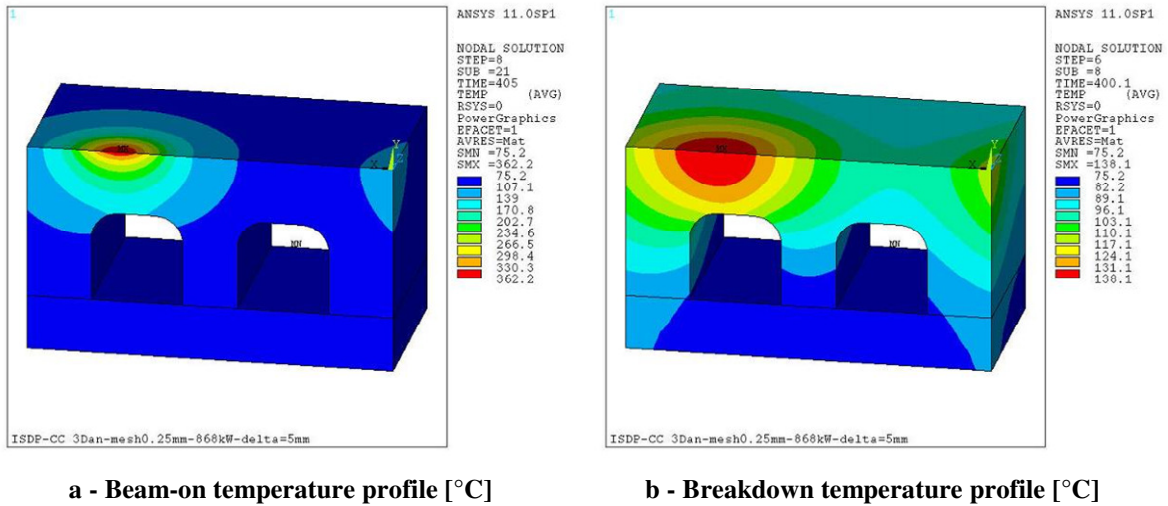


Figure 2.29: Beam-on / Break-downs temperature profiles [°C] with 5 mm displaced heat load

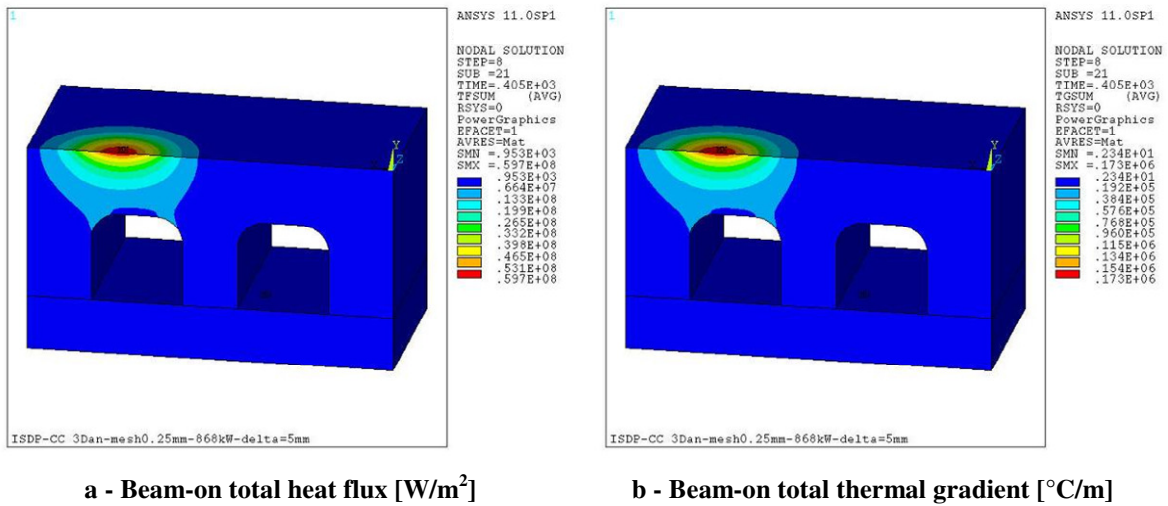


Figure 2.30: Beam-on total heat flux and thermal gradient with 5 mm displaced heat load

2.6.4 FE model of the configuration with a 1.0 mm thick molybdenum layer

In order to withstand the sputtering phenomenon on the plate described in 2.2.4 an alternative solution (later become the reference and the adopted one) was taken into account and analyzed: it foresees the presence of a 1mm thick Mo layer facing the plasma on a OFHC copper base plate.

The model geometry, with the changed dimensions, is shown in Figure 2.31.

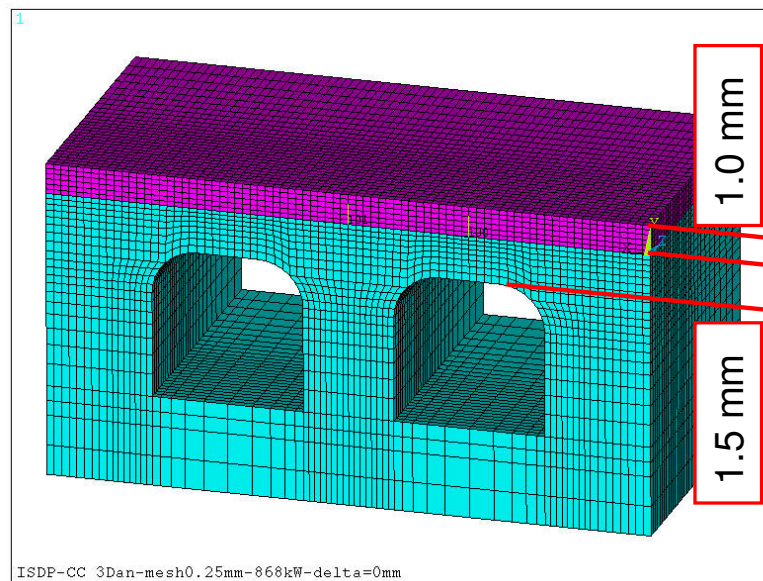


Figure 2.31: FE model of the configuration with a 1.0 mm thick molybdenum armour layer

The applied heat loads and boundary conditions are the same as the reference model.

The contour plot of the temperatures is shown in Figure 2.32 the maximum of the temperature is very high (almost 600°C), due to the low thermal conductivity of molybdenum in comparison to copper, combined with the severe power density. The contour of temperature just on the molybdenum layer is represented in Figure 2.32-c and -d.

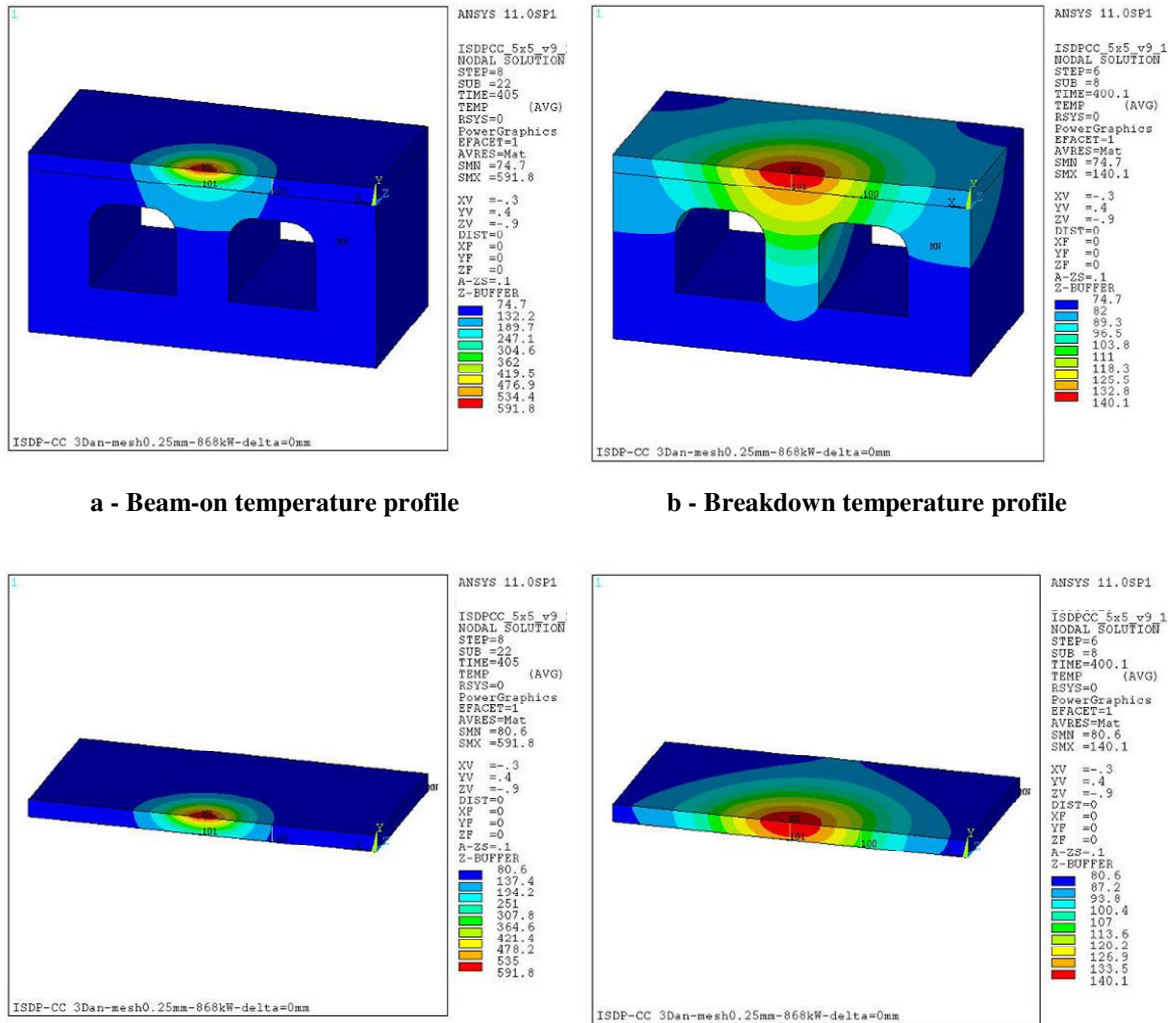
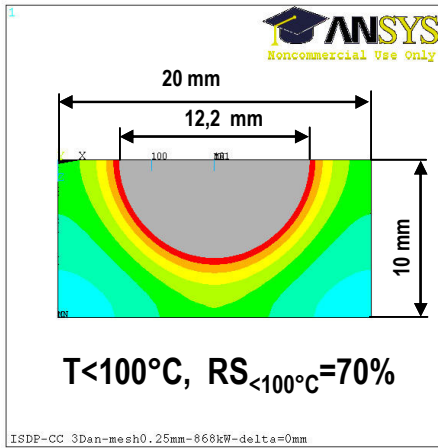


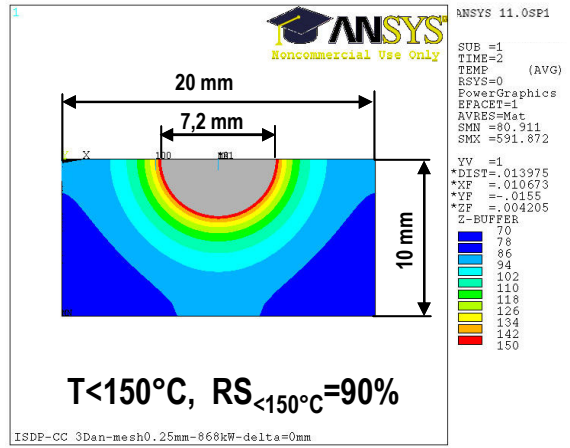
Figure 2.32: Beam-on / Breakdowns temperature profiles [°C] on the model with 1.0 mm thick molybdenum armour layer

The surface temperature contour plots in Figure 2.33 show that about the 70% of the surface is under 100°C and about the 90% is under 150°C.

In the following Figure 2.34 the thermal flux and thermal gradient are shown: in this case the maximum gradient is quite higher than in the CuCrZr solution, causing higher secondary stresses, in particular in the molybdenum and at the interface between the two metals.

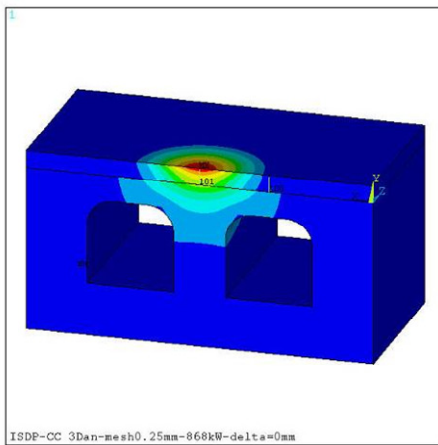


a - Surface temperature < 100°C

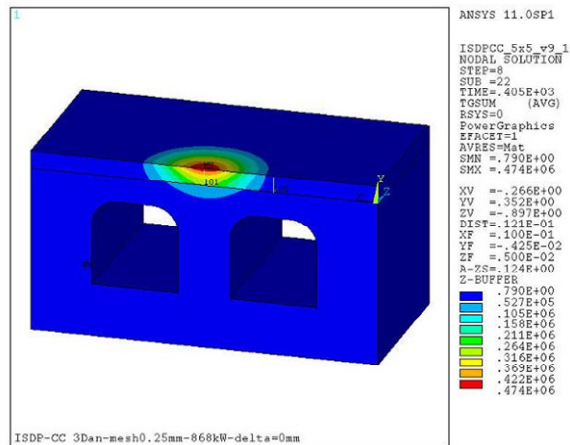


b - Surface temperature < 150°C

Figure 2.33: Plasma surface temperature [°C] for the model with 1.0mm thick molybdenum armour layer



a - Beam-on total heat flux [W/m²]



b - Beam-on thermal gradient [°C/m]

Figure 2.34: Beam-on total heat flux and thermal gradient on the model with molybdenum

2.6.5 FE models of the “half-moon” manifold regions

In order to simulate and analyze the regions of the large embedded manifolds around the driver holes, in correspondence of the BSI+ beamlets impinging points, another FE model has been developed.

Due to lack of space the “half-moon” manifold geometry has been adopted, instead of multiple cooling channels, around the driver holes of the PDP. The design choice was to place reinforcing cylindrical elements inside the unique 50 mm large channel (the “half-moon” manifold) in correspondence of the BSI+ beamlets impinging points. These elements, called “pillars”, due to their shape, act as mechanical stiffeners and thermal bridges (see Paragraph 2.3.2). The model that has been developed to simulate the operating conditions of these regions is shown in Figure 2.35-b. It represents, with slight approximation, the minimum repeatable portion of PDP in correspondence of the half-moon manifolds.

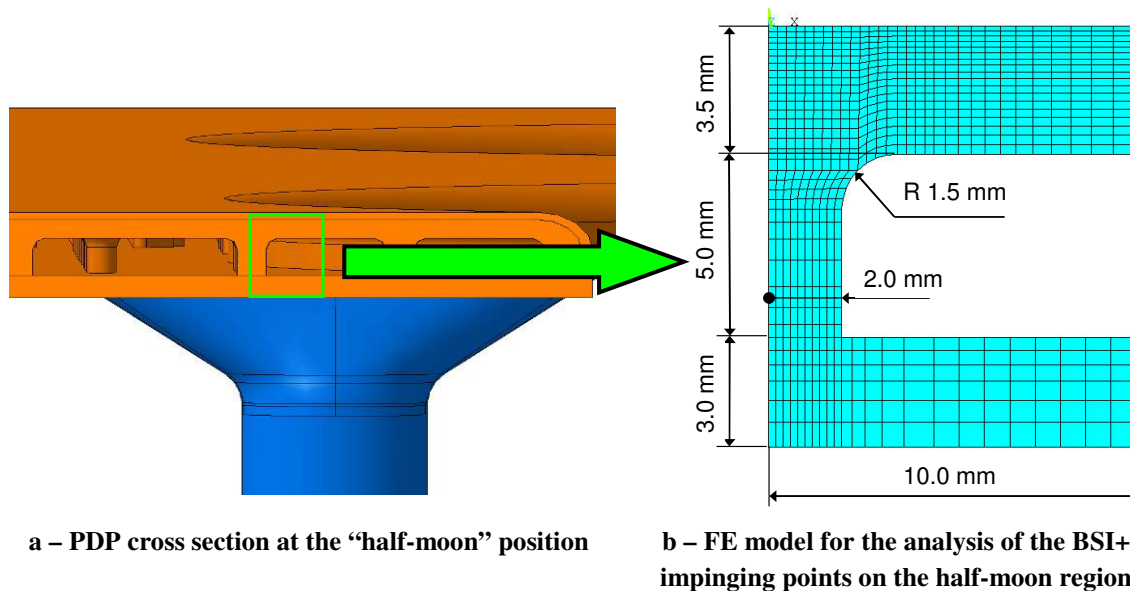


Figure 2.35: FE models of the pillar in the region of the PDP half-moon manifold

The model is axi-symmetric with X radial coordinate in the PDP plane and Y as beam axis in the global coordinate systems. A fine mesh of plane axi-symmetric elements with 0.25 mm length (values at the surface where the heat loads are applied) is modelled. The thickness of these elements is of about ~0.15mm near to the surface, as for the 5x5 cooling channels model.

This choice is justified by the periodicity of the geometry, in fact the pillars are positioned in correspondence of all the impinging BSI+ beamlets in order to enhance locally the heat exhaustion.

The boundary conditions imposed with the assumption of axi-symmetric behaviour are a bit restrictive. The heat exchanging surface correspondent to each periodic square region ($20 \times 20 \text{ mm}^2$) is in fact a bit greater than that one of the analyzed model (inscribed circle of 20 mm diameter). The obtained results are then on the safe side.

2.6.5.1 Power densities

The heat loads have been applied as for the previous models, taking into account the axial-symmetry of the model.

2.6.5.2 Convective Heat Transfer coefficient

The CHT coefficient (α) to be applied to the model is a 2nd degree function of the wall temperature and it is calculated for each node by iterative solutions.

The equation is:

$$\alpha = -1.5550 \cdot 10^{-1} \cdot (T_w)^2 + 1.0018 \cdot 10^2 \cdot T_w + 3.8821 \cdot 10^4 \quad [\text{W}/(\text{m}^2 \text{ K})] \quad (2.25)$$

that represent a 2nd degree regression of the coefficient α , calculated by points, varying T_w in the Sieder-Tate formula (see Paragraph 2.4.1.1).

For this configuration several formulae for the calculation of the forced CHT coefficient have been considered (Sieder-Tate, Gnielinski, Dittus-Boelter, Dittus-Boelter modified). At the end the Sieder-Tate expression has been adopted, because it is the most utilized in the practice and it is the most conservative.

The CHT coefficient applied to the model ranges between 45000 and 49400 $\text{W}/(\text{m}^2 \text{ K})$; it is quite smaller than the ones on the previous models, due to the shape of the crossing area of the manifold and to its dimension. The actual heat transfer coefficient in the half-moon manifolds will be higher because of the high turbulence induced on the water flow by the pillars, but this can not be analytically estimated and would require a fluid-dynamic analysis.

2.6.5.3 Boundary conditions

As for the $5 \times 5 \text{ mm}^2$ cooling channel model, radiation between faced components and conduction through contact surfaces are neglected. The periodicity of the model is guaranteed by the axial-symmetry of the model: all boundaries of the model are adiabatic.

2.6.5.4 Finite elements numerical thermal analyses

Figure 2.36 shows the temperature distribution on the CuCrZr PDP “half-moon” manifold pillar model assuming hydraulic parameters of reference operating conditions.

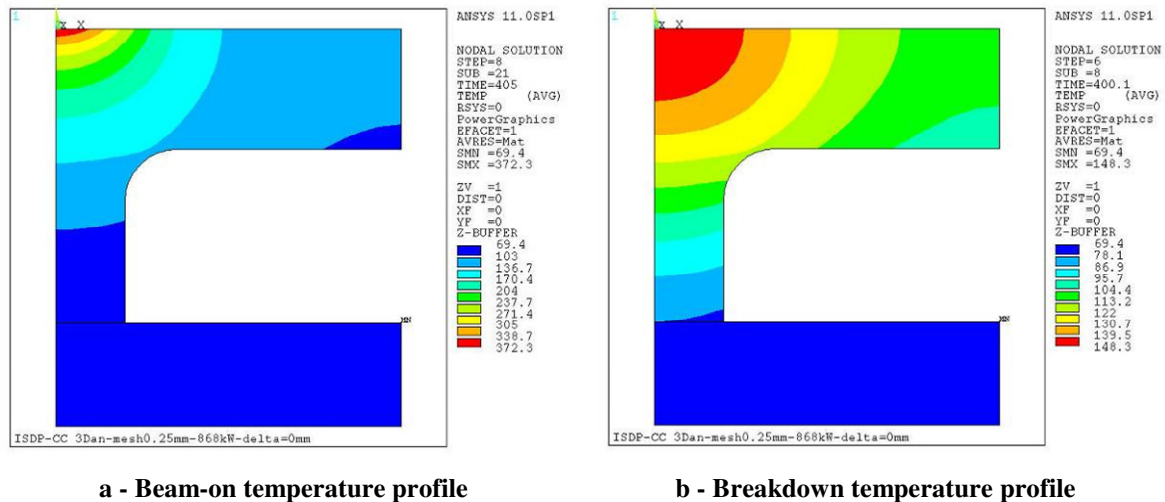


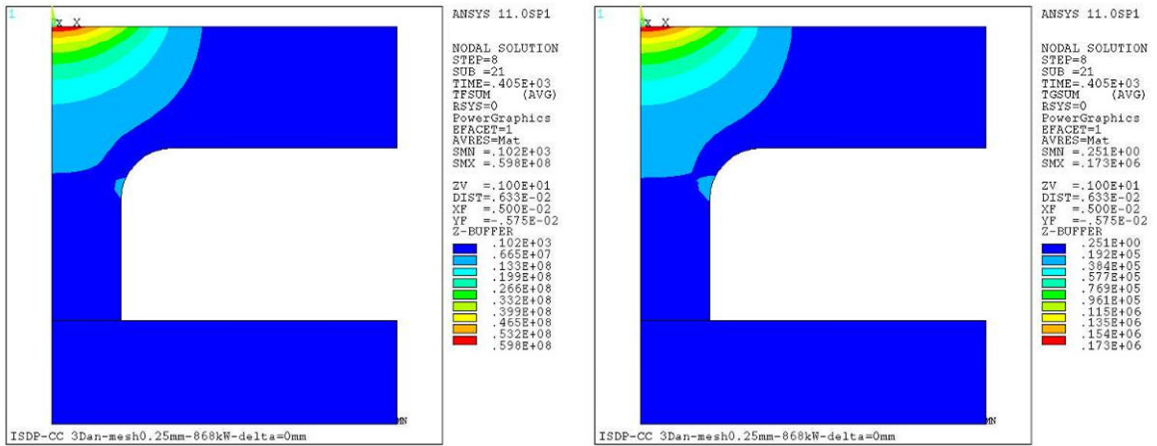
Figure 2.36: Beam-on / Break-downs temperature profiles [°C] on the half-moon manifold model

As for the $5 \times 5 \text{ mm}^2$ cooling channels model, the hottest area of the model during beam-on conditions is localized just in a very small volume, where the beamlet impinges on the plate: there is a spherical cup of about 3 mm diameter and 0.5mm depth that goes over 300°C and just a node that achieve 372°C . The volume that exceeds the temperature of 350°C is a circular surface area of about 1.5 mm diameter and less than 0.15mm deep. For the same consideration made in Paragraph 2.6.3.3, the analyses and obtained results are considered then acceptable.

The maximum ΔT due to the breakdown pauses is of 224°C and it is similar to the value obtained on the $5 \times 5 \text{ mm}^2$ cooling channel model. This high temperature range is caused by the very high heat flux and thermal gradient reached during the beam-on time.

These very high, fast and localized changes in temperature cause high local stresses on the material.

In this case the 100% of the surface facing the plasma has temperature over 100°C , whereas the 87% has temperature lower than 150°C .



a - Beam-on total heat flux [W/m²]

b - Beam-on total thermal gradient [°C/m]

Figure 2.37: Beam-on total heat flux and thermal gradient

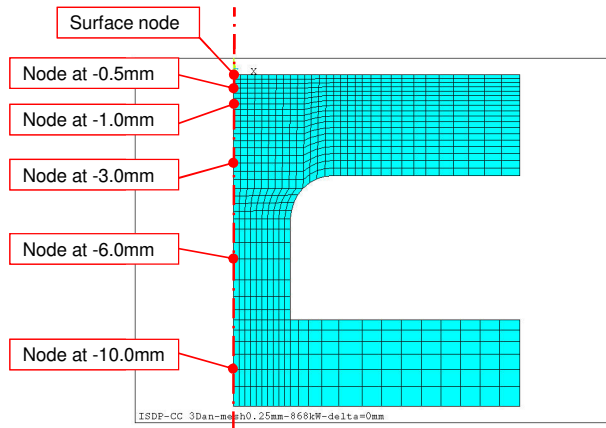


Figure 2.38: Schematic of the nodes of which time dependent temperatures are plotted in following Figure 2.39

Figure 2.39 shows the time dependent temperature of 6 nodes positioned in the beamlet axis direction and respectively on the surface and at 0.5, 1, 3, 6, 10 mm deep in the plate (Figure 2.38).

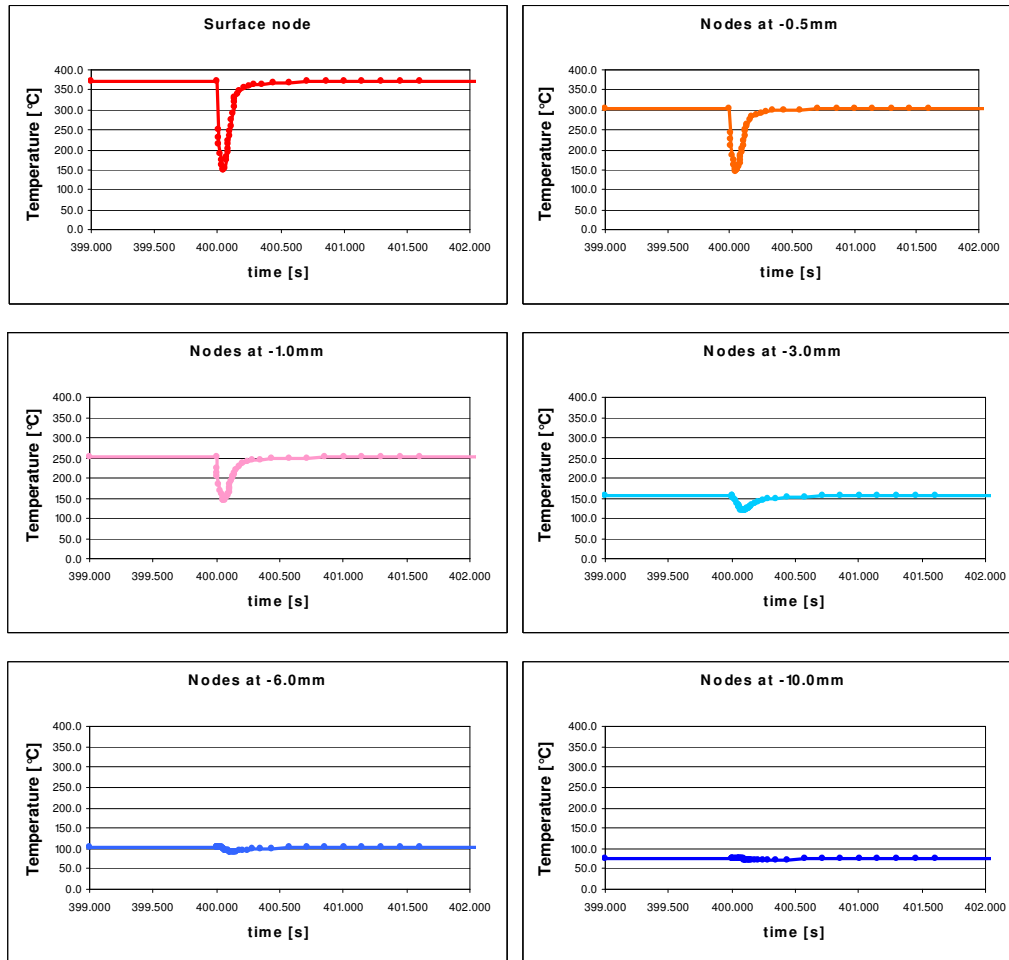


Figure 2.39: Time dependent temperature for the nodes shown in Figure 2.38

2.6.5.4.1 Displacement of the hot spot

As for the previous model, a possible displacement of the impinging BSI+ beamlet, with respect to its nominal position, has been considered.

In particular, the high complexity of the “half-moon” manifold geometry, that does not allow to arrange all the pillars just in correspondence of the beamlet nominal position, suggests to consider as the worst operating condition the case in which a beamlet impinges the PDP just in the centre of one of the squares formed by four adjacent pillars. In Figure 2.40 a) a section of the PDP in correspondence of one half-moon manifold is shown and the picture b) shows the related model.

In order to stay to the safe side and considering the very low thermal effect that the pillar has in such model (being quite far from the impinging point), the pillar has not been modelled and the heat transfer coefficient is applied to the whole lower model surface.

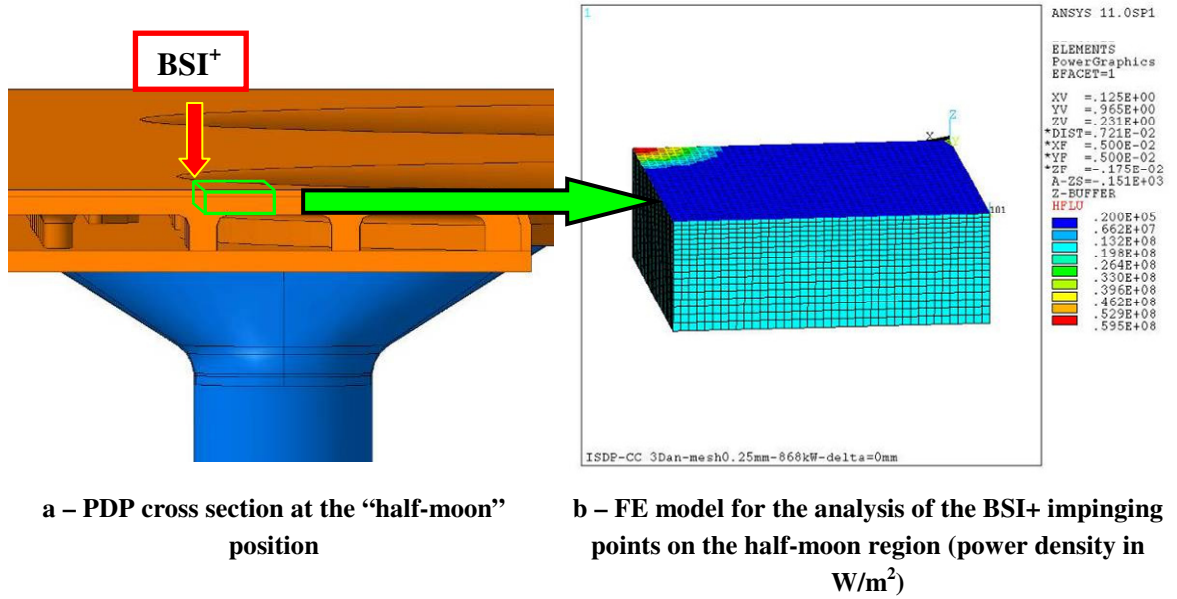


Figure 2.40: FE models of the “half-moon” manifold in the case of BSI+ beamlet impinging far from the reinforcing pillars

In Figure 2.41 a) and b) the beam-on and breakdown temperatures are respectively shown.

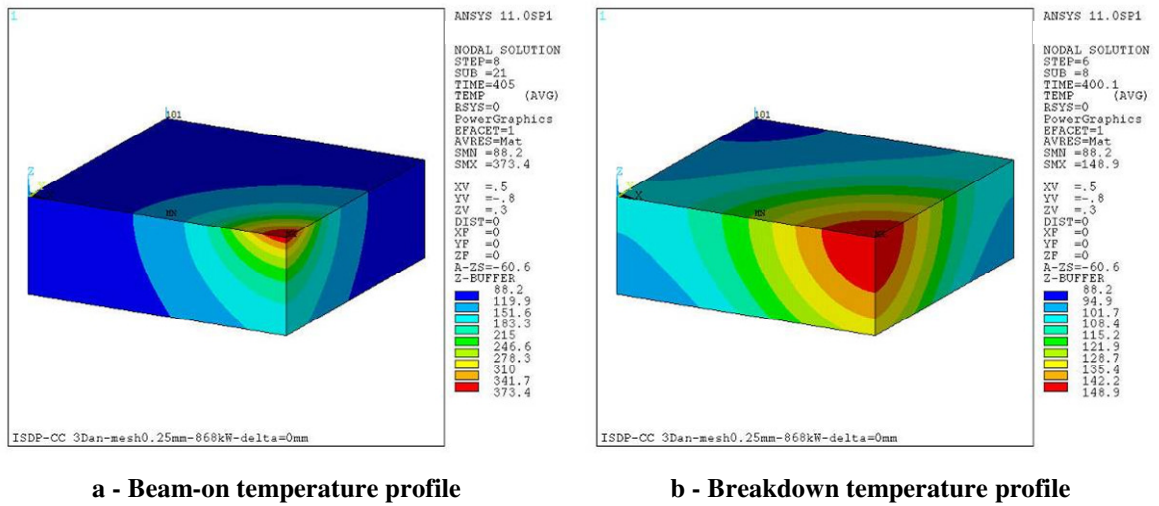
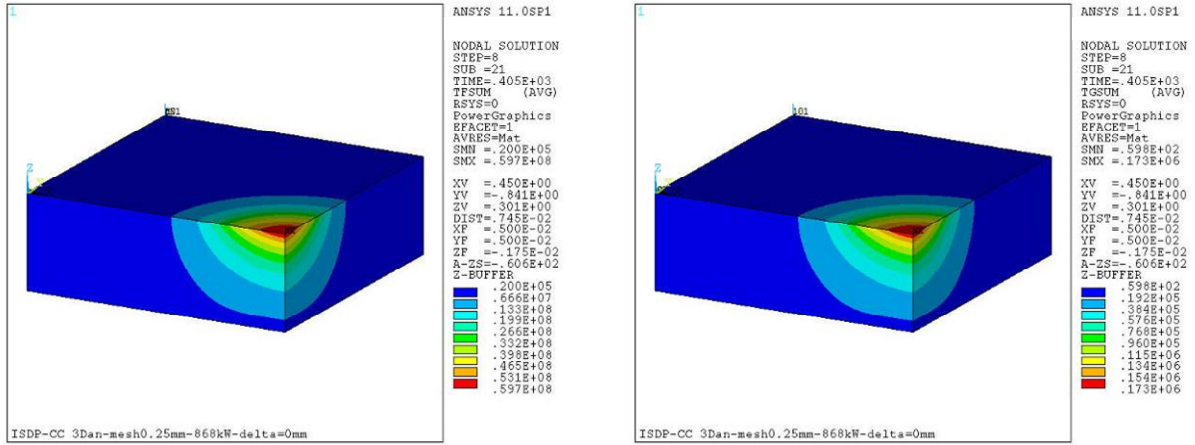


Figure 2.41: Beam-on / Break-downs temperature profiles [°C] on the “half-moon” manifold model with BSI+ beamlet impinging far from the pillars

The temperature results are almost the same obtained with the nominal model, so the design solution can be considered acceptable.

The thermal gradients obtained from the analysis (Figure 2.42) are the same to those of the nominal positioned heat load model; it suggests that the PDP geometry assure a quite uniform thermal behaviour of the material overall its surface.



a - Beam-on total heat flux [W/m²]

b - Beam-on total thermal gradient [°C/m]

Figure 2.42: Beam-on total heat flux and thermal gradient with displaced heat load

2.7 *Finite Elements mechanical analyses and verifications*

2.7.1 FE models description

The models are the same utilized for the thermal analyses, but the element type is substituted to introduce the displacement degree of freedom instead of temperature.

2.7.2 Structural loads

Structural loads are less critical than the thermal loads, in fact there are only constant mechanical stress due to the self-weight and to the coolant water pressure. The expected number of times that the cooling circuit will be pressurized and de-pressurized is, in fact, very low and far from being considered for the fatigue analyses. No fatigue damage accumulation is then considered for this type of load.

The weight of the plate has been neglected.

The inlet water pressure (intended at the component entrance) has been fixed to 2.0 MPa, as prescribed in [54], for each RF source component and it could be considered constant in the cooling circuit for the mechanical analyses, neglecting the pressure drops, taking safety advantage.

The impossibility to have a good estimation of pressure drops along the circuit, due to its complex geometry, and then a precise value of the water pressure at each point of the plate, lead to consider the upper limit as the water pressure in the FE models, being conscious that the real value of pressure will be less than 2MPa. This is a conservative assumption.

However, a rough estimation of the total pressure drop in the PDP can be done analytically using the correlations explained in Paragraph 2.4.1.2.

The Reynolds number in the $5 \times 5 \text{ mm}^2$ cooling channels is $Re=107800$; assuming $\varepsilon = 0.01 \text{ mm}$, the friction factor results: $4f = 0.025$. Adopting an average length of the PDP cooling channels of 0.65m, the distributed pressure drop along the cooling channels is $\Delta p = 0.13 \text{ MPa}$.

The pressure drop due to the flow through the half-moon manifolds, considering $Re=183100$, $4f = 0.022$ for a path length of 1.30m, results $\Delta p = 0.12 \text{ MPa}$.

The total distributed pressure drop is then $\Delta p_{\text{dist}} = 0.25 \text{ MPa}$.

The inlet/outlet localized pressure drops results $\Delta p_{\text{loc}} = 0.32 \text{ MPa}$.

The total pressure drop in the PDP is then of $\Delta p_{\text{tot}} = 0.6 \text{ MPa}$ approximately.

Large uncertainties are typical in the estimation of the pressure drops in such a complex cooling circuit and a Computational Fluid–Dynamic (CFD) analysis is suggested.

2.7.3 FE analyses of the $5 \times 5 \text{mm}^2$ model

2.7.3.1 Boundary conditions

Plane deformation has been assumed for the Plasma Driver Plate.

Reference temperature for the thermal strain calculations is set to Room Temperature $RT=20^\circ\text{C}$.

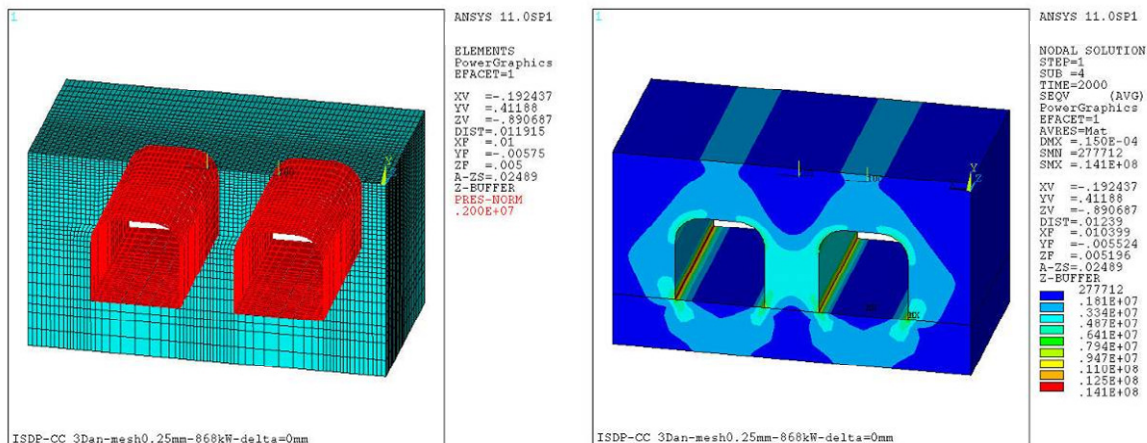
2.7.3.2 Finite elements numerical analyses

2.7.3.2.1 Initial stress

From the mechanical point of view stress on the model are caused by:

1. inner water pressure
2. thermal stress

A first step of analysis has been carried out in order to evaluate the stress induced by the water pressure onto the channel walls. A uniform temperature of 55°C , that was the reference inlet water temperature, and the pressure of 2.0 MPa have been applied to the model (see Figure 2.43).



a – View of the initial structural load (2.0 MPa pressure) applied to the model

b - Von Mises stress [Pa] due to water pressure

Figure 2.43: Static structural load and consequent stress on the $5 \times 5 \text{mm}^2$ model

As shown in Figure 2.43-b the maximum value of the Von Mises stress is of about 14 MPa located on the sharp corners of the channels. This low value of the stress and its localization on the sharp edges of the cooling channels are not significant from a mechanical point of view, since they are largely lower than the material (CuCrZr) admissible stress.

2.7.3.2 Thermo-mechanical analyses

The following Figure 2.44 shows the Von Mises stress contour plots of the 5x5mm² model under beam-on and at the end of the breakdown pause conditions. The maximum value of the equivalent Von Mises stress, during the beam-ON, $\sigma_{eq,max} = 252 \text{ MPa}$, is localized on the surface, due to the high heat power density of the BSI+.

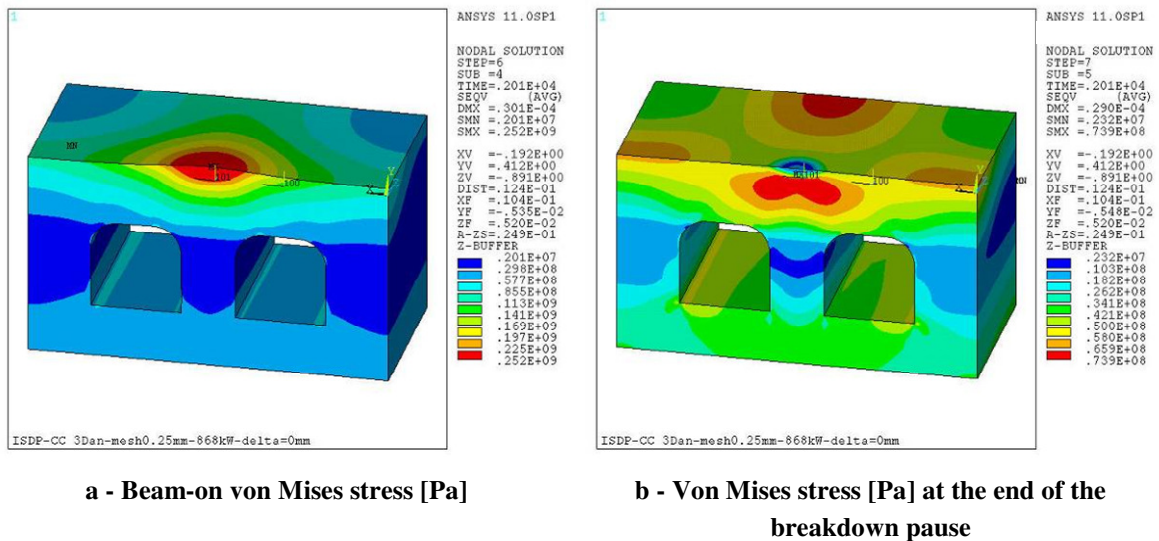


Figure 2.44: Beam-on and breakdown Von Mises equivalent stress

Figure 2.44 helps for better understanding the cyclic stress of the most stressed nodes, in fact, the maximum stress amplitude $\Delta\sigma_{max}$ can be simply estimated by calculating the difference between the maximum first principal stress under breakdown conditions $\sigma_{1,max}^{breakdown}$ and the minimum third principal stress during beam-on $\sigma_{3,min}^{beam-on}$.

$$\Delta\sigma_{max} = \sigma_{1,max}^{breakdown} - \sigma_{3,min}^{beam-on} = 18 - (-252) = 270 \text{ MPa}$$

From the contour plots of the Von Mises stress, it is in fact evident that the stress state is axial-symmetric just around the hot spot axis; this means that $\sigma_1 \approx 0$, $\sigma_2 \approx \sigma_3 = -252 \text{ MPa}$ during

beam-ON and $\sigma_1 \approx \sigma_2 = +18 \text{ MPa}$, $\sigma_3 \approx 0$ at the end of the breakdown pause, consequently:

$$\sigma_{VM,beam-on} \approx |\sigma_3^{beam-on}| \text{ and } \sigma_{VM,breakdown} \approx |\sigma_1^{breakdown}|.$$

The values of the calculated stress range ($\Delta\sigma_{max} = 270 \text{ MPa}$) and of the strains (up to $\epsilon_{eq,tot} = 3.3 \cdot 10^{-3}$) in the CuCrZr are quite high and require a more accurate fatigue life assessment than the classic one based on $\Delta\sigma$, so in next paragraph the fatigue life assessment performed applying the procedure developed inside Consorzio RFX (explained in 2.4.2) is presented.

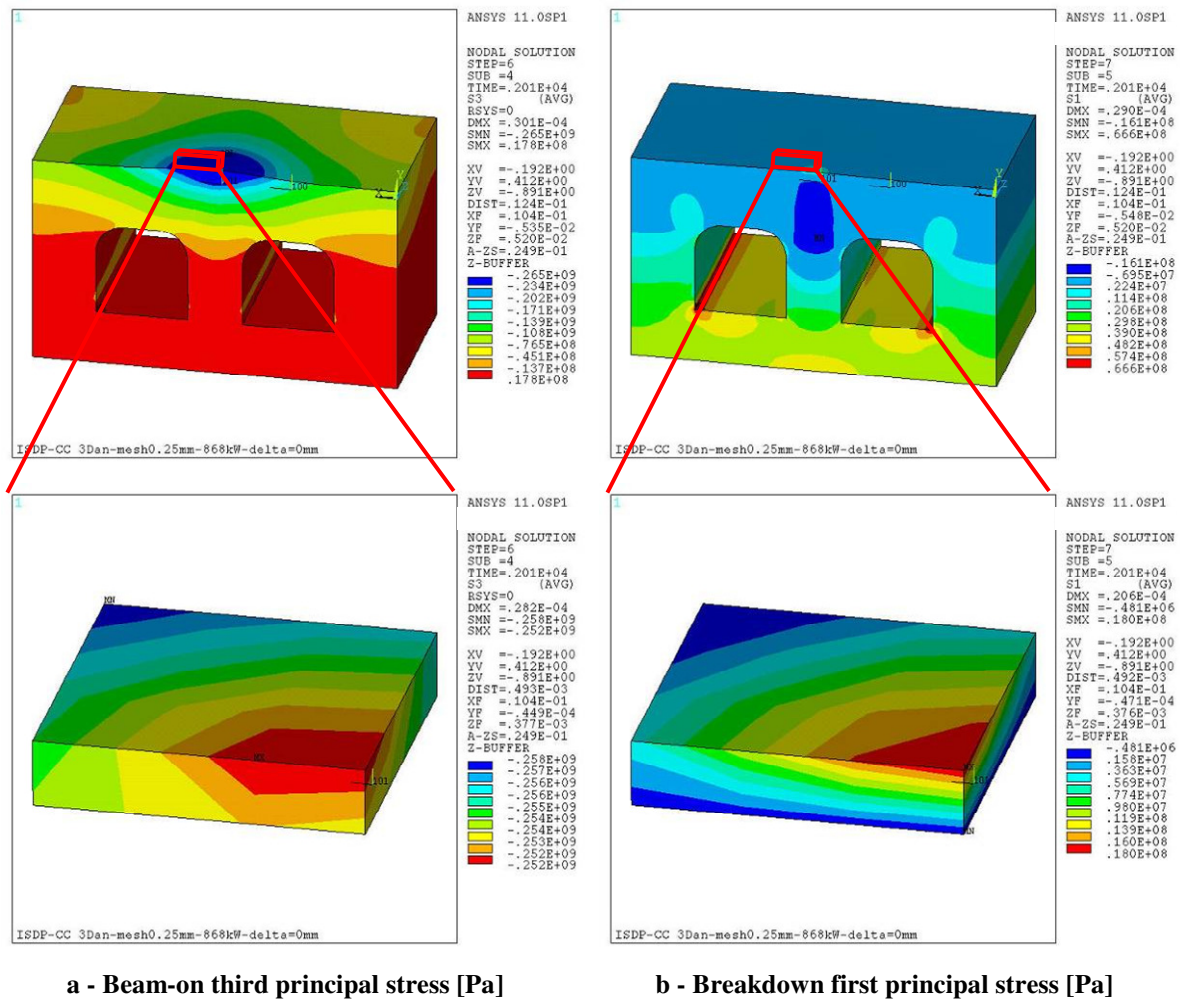


Figure 2.45: Beam-on and breakdown respectively third and first principal stress

2.7.3.2.3 Structural verification

Being the cyclic type damages more critical than the monotonic type, only the fatigue life verification for the creep-fatigue interaction damage has been carried out following the procedure explained in Paragraph 2.4.2.

As already specified in the previous paragraphs, the most damaged nodes are the ones placed around the hot spot axis. Carrying on the mechanical verifications it has been noted that there are a very high gradient in the fatigue damage of the most heated nodes moving from the central one to the others, both on the surface and in depth.

For symmetry reasons the fatigue life assessment has been done on half-size FE model (see Figure 2.46).

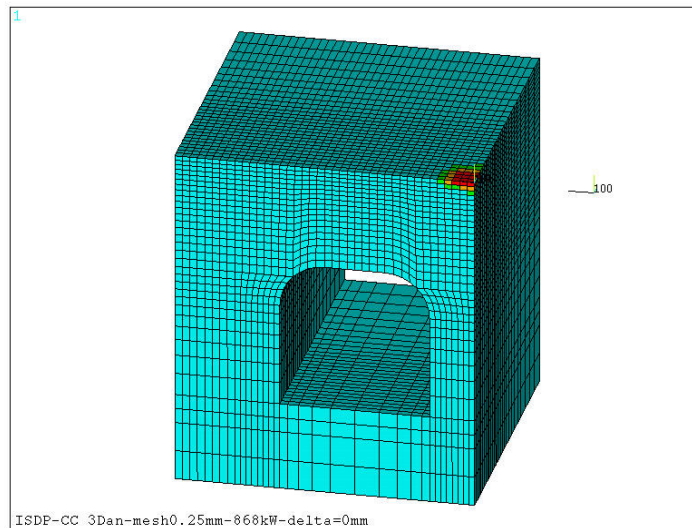


Figure 2.46: Half-size FE 5x5mm² model used for fatigue life assessment

The fatigue verification revealed that there were 9 nodes in a half-size model that have fatigue damage higher than 100%. These nodes are localized in a circular area of about 1.0 ÷ 1.5 mm diameter. The depth of the damaged zone is under 0.15 mm, because all of the mentioned 9 nodes are on the model surface, directly exposed to the BSI+ beamlet, they belong only to the first boundary layer of nodes. Figure 2.47-a shows the model and the circle area in which the nodes are located; Figure 2.47-b shows the half-size model elements attached to nodes with fatigue damage $V > 100\%$.

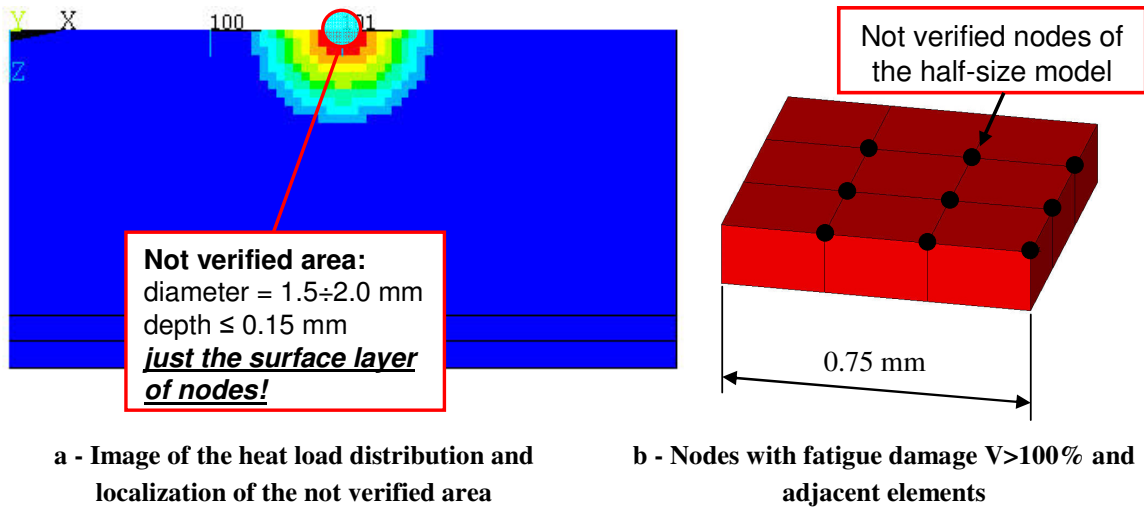


Figure 2.47: Representation of the model nodes resulting in experiencing fatigue damage overcoming the maximum allowed value 100%

An analytical calculation has been performed in order to verify the numerical results about the fatigue damage. As reported in following Table 2.6 the 9 nodes mentioned have a fatigue damage (obtained using their typical equivalent strain range) that is over 100%, as expected.

Type of cycle	$\overline{\Delta\varepsilon_j}$ [%] Typical equivalent strain range	N_j Allowable number of cycles	n_j Required number of cycles	$V_j=n_j/N_j$ [%] Fatigue damage
Beam-on/off main cycles	$\overline{\Delta\varepsilon_j} = 0.25\%$	$5.5 \cdot 10^4$	$5.0 \cdot 10^4$	$V_{\text{beam-on/off}} = 91\%$
Breakdown cycles	$\overline{\Delta\varepsilon_j} = 0.21\%$	$5.7 \cdot 10^5$	$4.5 \cdot 10^5$	$V_{\text{breakdown}} = 79\%$
Total damage				V = 170% Beam-on/off plus breakdown cycles NOT VERIFIED

Table 2.6 : Main results and parameters of the analytical fatigue damage assessment of the most stressed nodes of the CuCrZr Plasma Driver Plate 5x5 mm² channel FE model

Then there are 10 nodes in the half-size model that have fatigue damage between 50% and 100%. These nodes are the nearest to those mentioned before, as shown in Figure 2.48.

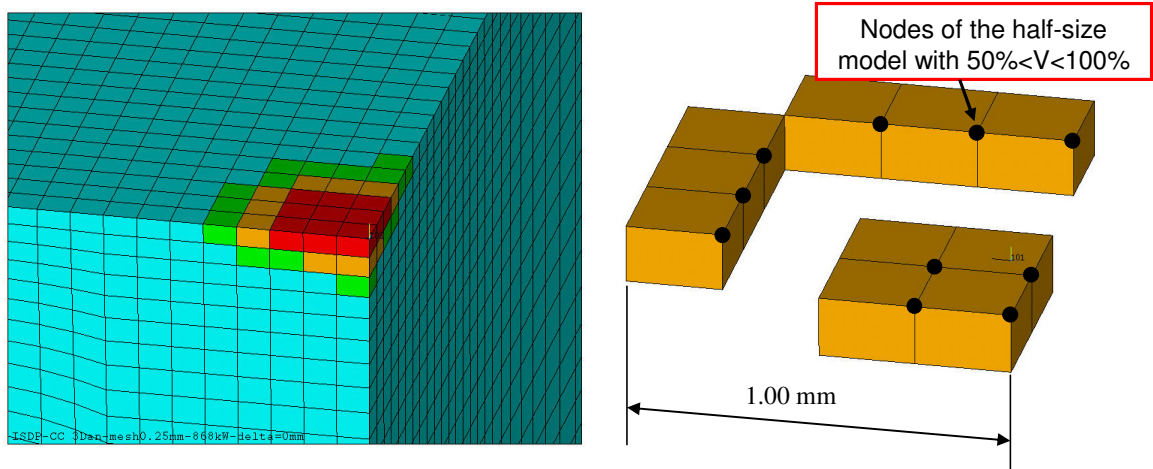


Figure 2.48: Representation of the half-size model nodes and contiguous elements with fatigue damage between 50% and 100%

As previously done, it is possible to carry out an analytical verification of the fatigue damage with reference to the typical equivalent strain range, as shown in table 4.3.2.

Type of cycle	$\overline{\Delta\varepsilon}_j$ [%] Typical equivalent strain range	N_j Allowable number of cycles	n_j Required number of cycles	$V_j = n_j/N_j$ [%] Fatigue damage
Beam-on/off main cycles	$\overline{\Delta\varepsilon}_j = 0.23\%$	$9.2 \cdot 10^4$	$5.0 \cdot 10^4$	$V_{\text{beam-on/off}} = 54\%$
Breakdown cycles	$\overline{\Delta\varepsilon}_j = 0.19\%$	$4.5 \cdot 10^6$	$4.5 \cdot 10^5$	$V_{\text{breakdown}} = 10\%$
Total damage				V = 64% Beam-on/off plus breakdown cycles VERIFIED*

Table 2.7 : Main results and parameters of the analytical fatigue life assessment of the nodes of the CuCrZr Plasma Driver Plate 5x5 mm² channel FE model with fatigue damage in the range 50% < V < 100%

The same considerations have been carried out for nodes (21 in the half-size model) that have fatigue damage between 20% and 50% (see Figure 2.49). The relative table is omitted.

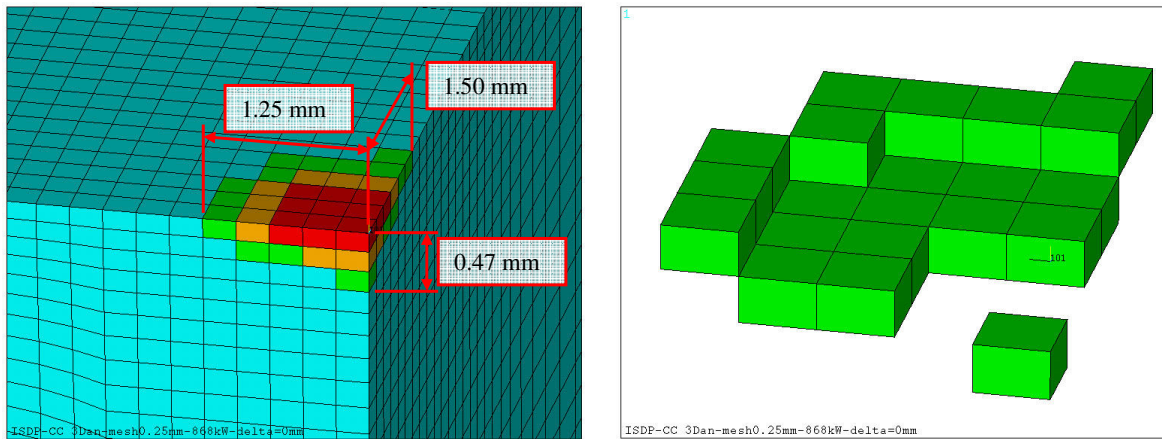


Figure 2.49: Representation of the half-size model nodes and contiguous elements with fatigue damage between 20% and 50%

The following graph of Figure 2.50 shows the fatigue damage, resulting from the calculations, of the nodes placed all around the hot spot axis, in a radius of 2.0 mm, and at different depths. The graph confirms the axial-symmetric trend of the fatigue damage. Figure 2.50 shows that there are just few nodes on the model surface that exceed the threshold of fatigue damage $V=100\%$. All other nodes have fatigue damage smaller than 100%.

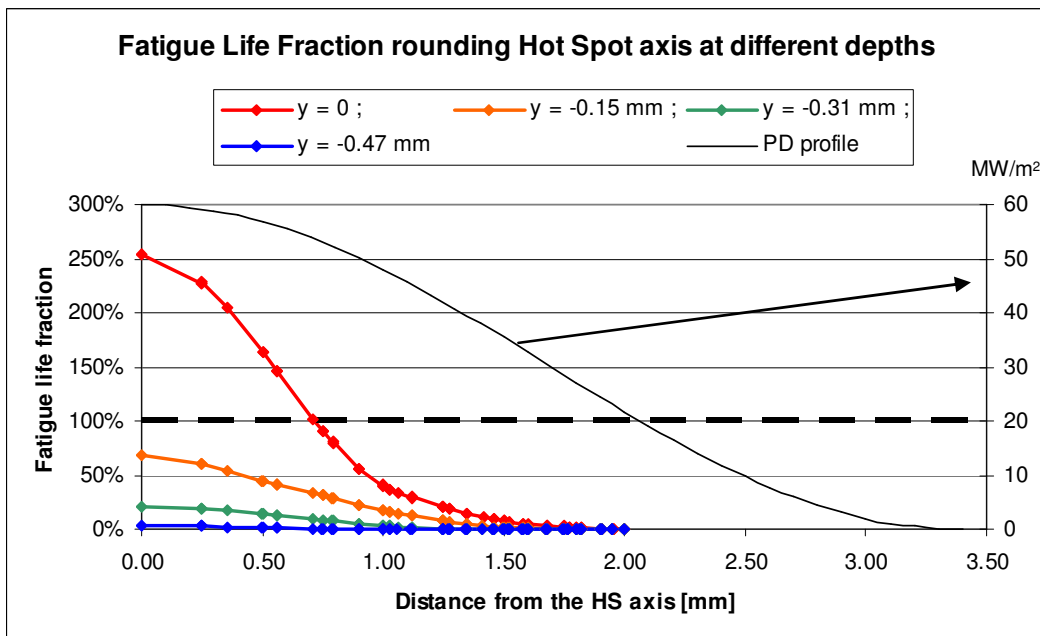


Figure 2.50: Fatigue damage as function of the distance from the hot spot axis for the layers of nodes of the model from the surface till 0.5 mm of depth

2.7.3.3 5 mm displacement of the hot spot on the 5x5 mm² channels model

The thermo mechanical analysis of the model with 5 mm displaced hot spot showed mechanical results that are quite the same as the aligned model (Figure 2.51 and Figure 2.52).

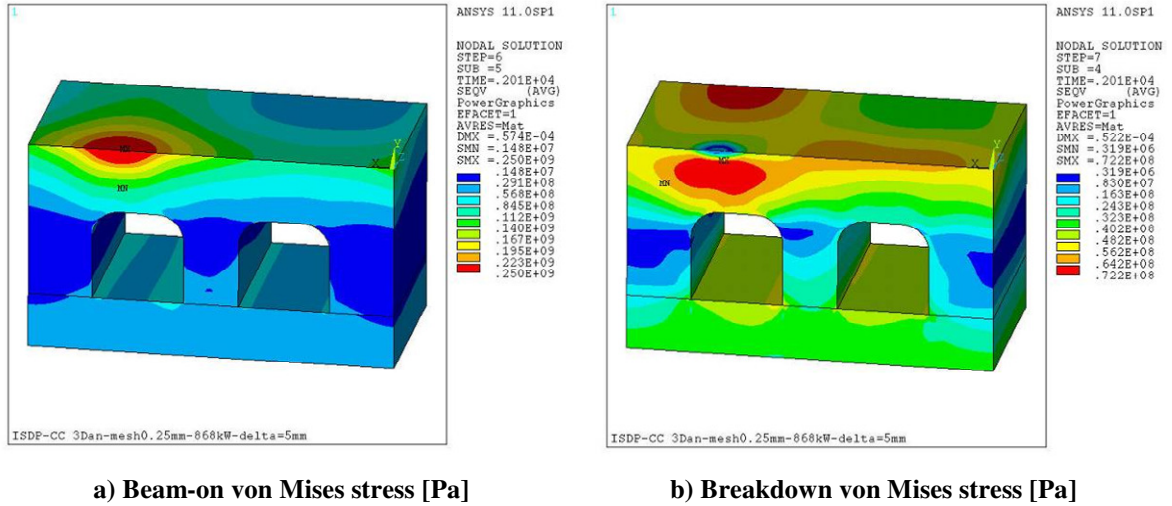


Figure 2.51: Beam-on and breakdown von Mises stress for the model with 5 mm displaced hot spot

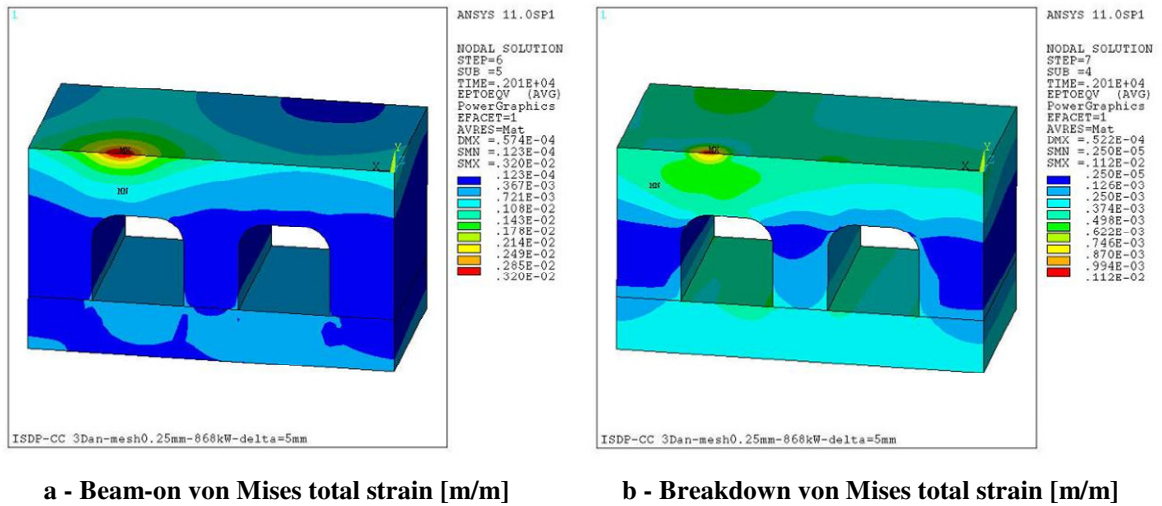


Figure 2.52: Beam-on and breakdown von Mises total strain for the model with 5 mm displaced hot spot

The post-processing fatigue verification has not been performed, in fact the fatigue damage is necessarily similar to (or less than) the reference model because of the quite identical values of the strain ranges (calculated accordingly to [51]).

2.7.4 FE model of the configuration with a 1.0 mm thick molybdenum layer

2.7.4.1 Boundary conditions

The loads and boundary conditions are the same applied to the reference model: plane deformation of the parallel side faces of the model.

2.7.4.2 Finite elements numerical analyses

Figure 2.53 shows the von Mises stress on the model during beam-on and breakdown condition.

Copper and molybdenum have quite different thermal and mechanical properties; as a consequence very high stress resulted at the interface between the two materials that could cause the delamination (detachment) of the molybdenum layer from the copper substrate.

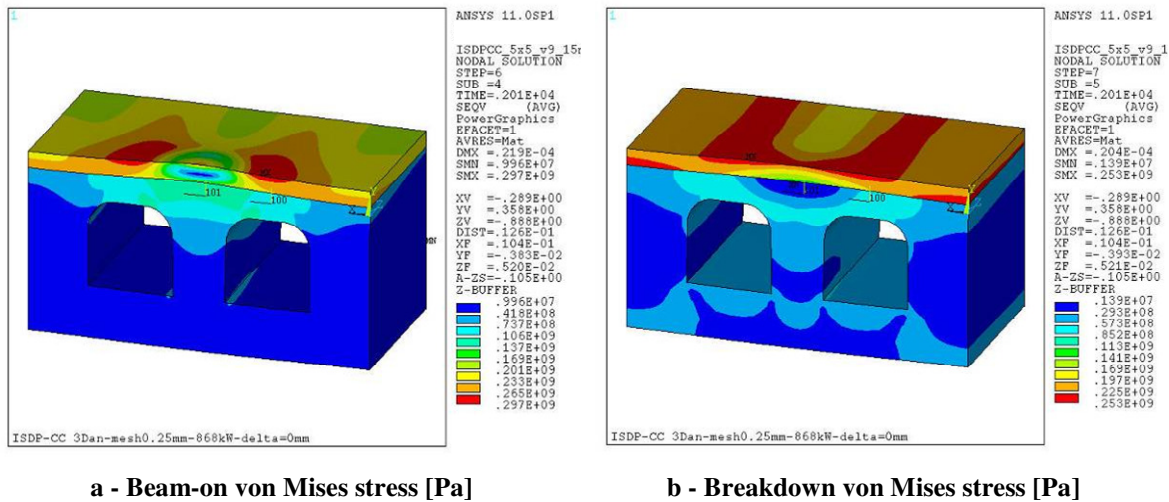
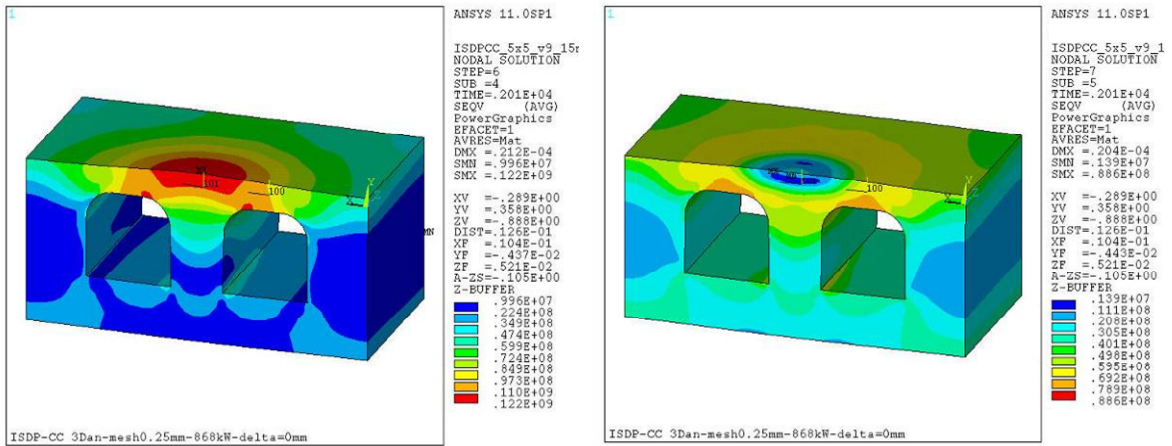


Figure 2.53: Beam-on and breakdown von Mises stress



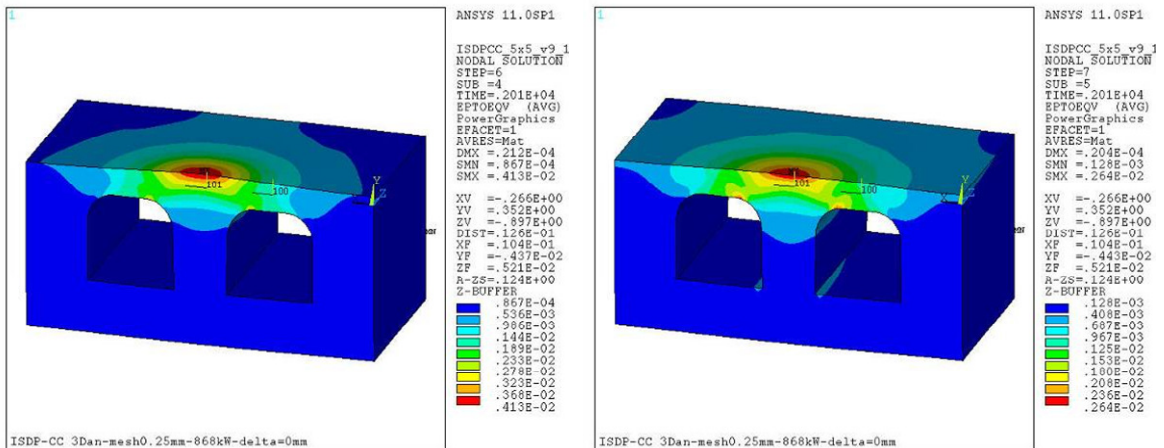
a - Beam-on von Mises stress [Pa] on copper

b - Breakdown von Mises stress [Pa] on copper

Figure 2.54: Beam-on and breakdown von Mises stress of the copper part

The resulting von Mises stress (Figure 2.54) on copper are much lower than that obtained previously for the reference model on CuCrZr; this is due to the fact that copper has a lower yield stress than CuCrZr.

For the same reason the obtained strains for copper are high up to 0.4% in quite a large volume of the model, as shown in Figure 2.55.



a - Beam-on Von Mises total strain [m/m] on copper

b - Breakdown Von Mises total strain [m/m] on copper

Figure 2.55: Beam-on and breakdown equivalent strain of the copper part

For the reasons explained above, the fatigue life verification performed on the copper portion of the model give a large volume (of about 25 mm³) that experiences a fatigue damage higher than V=100% (see Figure 2.56).

In this case the mechanical verification could not been considered successful. Nevertheless there are high uncertainties on the properties of the interface between the two metals. These properties mainly depend on the manufacturing technique used for the production of the armour layer. In these cases only R&D, with production and testing of prototypes can confirm or deny the result of the analyses.

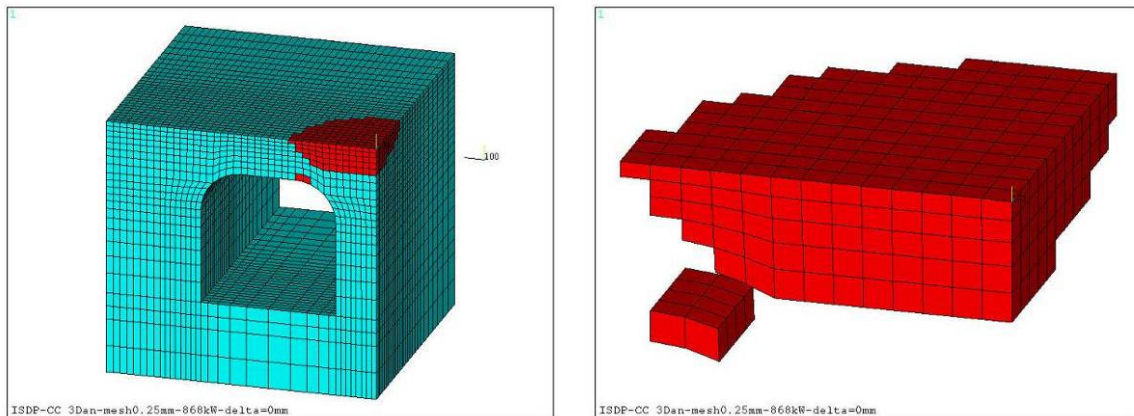


Figure 2.56: Representation of the half-size model nodes and contiguous elements with fatigue damage V larger than 100%

2.7.5 FE models of the “half-moon” manifold regions

2.7.5.1 Boundary conditions

The boundary conditions applied to the plane axial-symmetric model around the pillars of the PDP half-moon manifold are iso-static constraints and plane deformation of the PDP.

2.7.5.2 Finite elements numerical analyses

In Figure 2.57 the von Mises stress during beam-on and ant the end of the breakdown pause are presented. The maximum value, $\sigma_{VM,max} = 261\text{MPa}$, is in this case a bit higher than for the 5x5 cooling channels model ($\sigma_{VM,max} = 252\text{MPa}$).

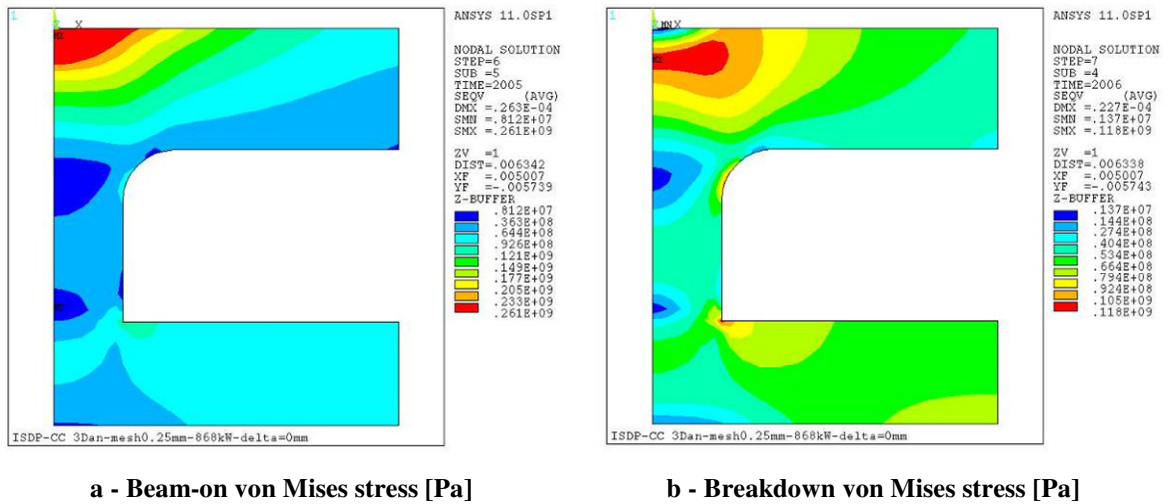


Figure 2.57: Beam-on and breakdown von Mises stress

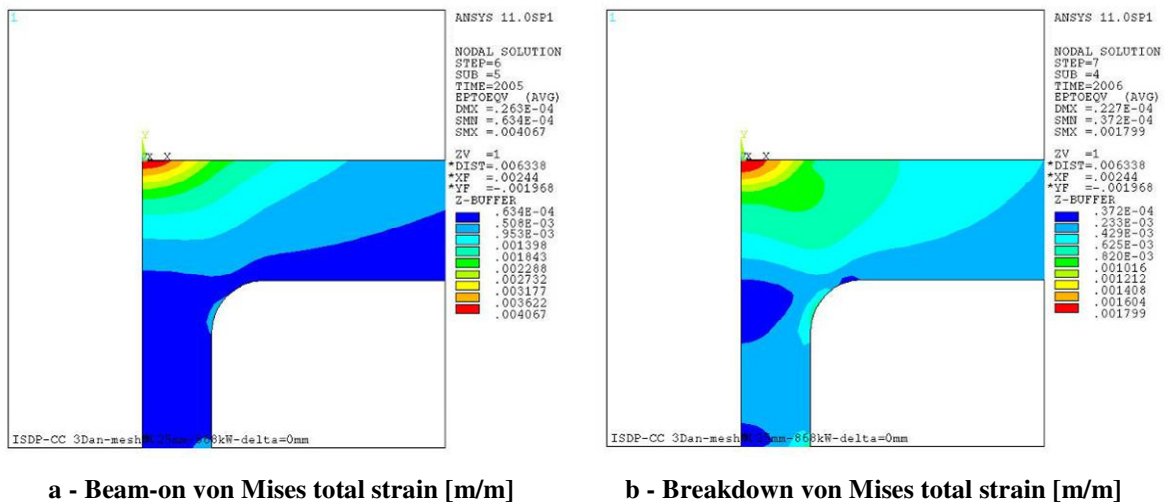


Figure 2.58: Beam-on and breakdown equivalent total strain

Also the total Von Mises strains (Figure 2.58) are higher than in the 5x5 cooling channels model, but the strain ranges are on the same order of magnitude of the other reference models (Figure 2.52).

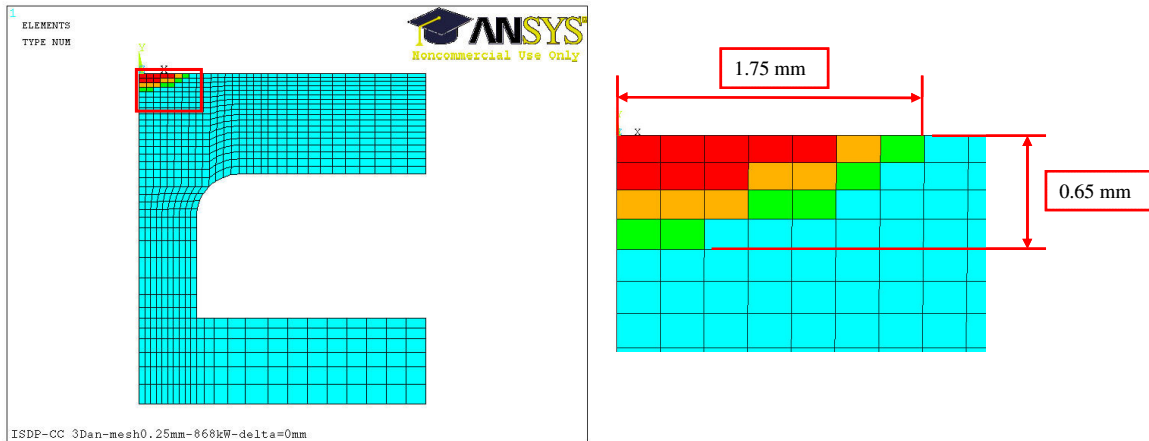


Figure 2.59: Representation of the half-size model with coloured elements having fatigue damage grater than 20%

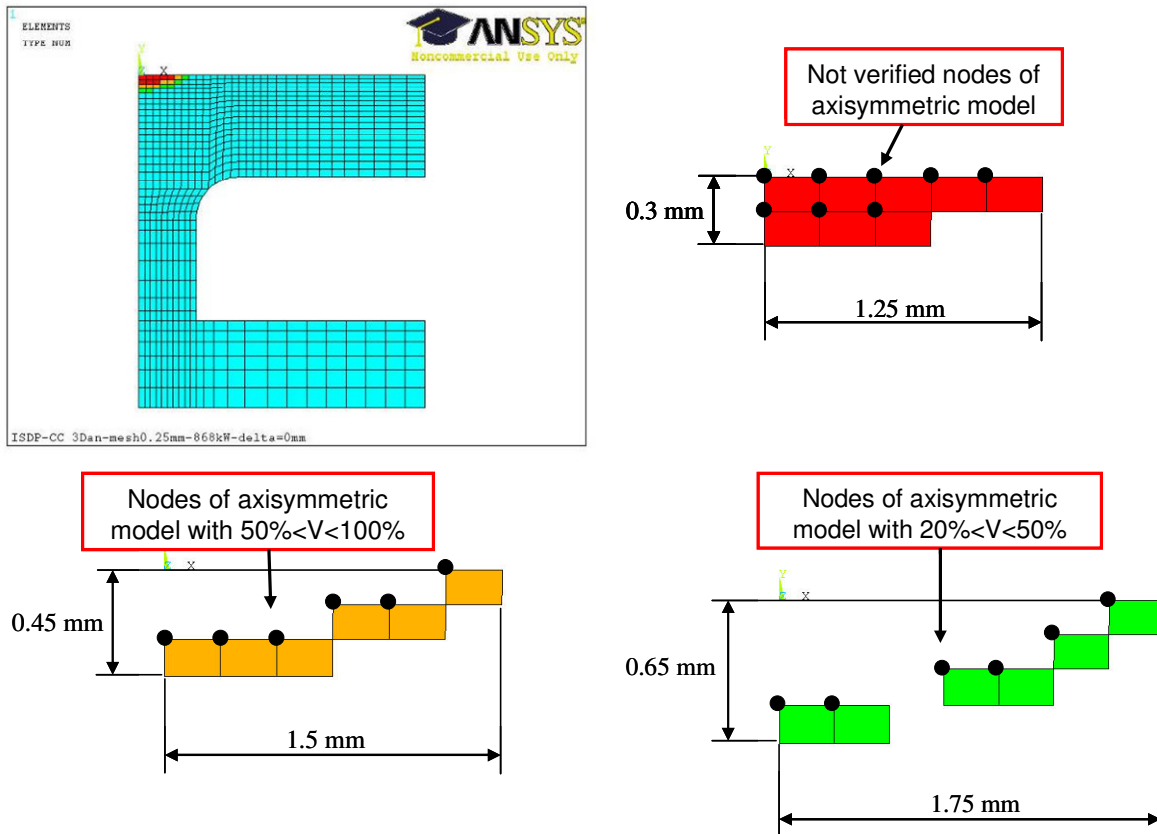


Figure 2.60: Representation of the half-size model nodes and contiguous elements with different values of fatigue damage

The post-processing of the results gave values of the fatigue damage similar to the 5x5 cooling channels model. In fact there is a spherical cup of about 2.5 mm diameter and less than 0.3 mm deep that experiences a fatigue damage higher than $V = 100\%$.

Figure 2.59 shows the elements that experience fatigue damages higher than 100% (red), between 50% and 100% (yellow) and between 20% and 50% (green).

Figure 2.60 shows more in detail the nodes and elements with indication of the related fatigue damage.

The graph in Figure 2.61 shows the fatigue damage of the subsequent layer of nodes rounding the hot spot axis, in a radius of 3.0 mm, at different depths.

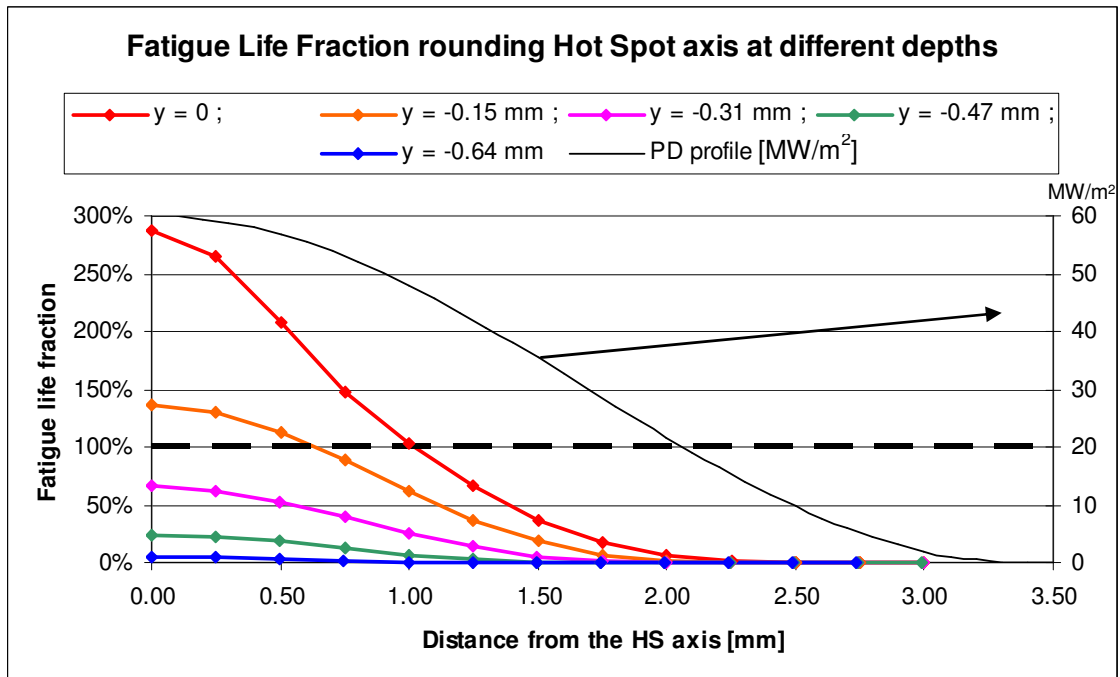


Figure 2.61: Fatigue damage as function of the distance from the hot spot axis for the layers of nodes of the model from the surface till 0.65 mm of depth

It can be noted that the maximum value of the fatigue damage ($V=280\%$) is higher than in the 5x5 cooling channels model ($V=250\%$), that the radius of not verified surface nodes is a bit larger: 1.0 mm instead of 0.75 mm and that, in spite of the results of the 5x5 cooling channels model, in this case there are some nodes at the depth of 0.15mm, within a radius of 0.65 mm, that exceed fatigue life.

2.7.5.2.1 10 mm displacement of the hot spot

The model is the same that has been utilized for the thermal analyses, but the element type has been substituted with the structural one.

Also in this case the boundary conditions have been applied considering plane deformation for the whole PDP, imposing parallelism to the model side faces. The absence of the “pillar” in the FE model, that has structural function, has been avoided by substituting the internal constraints that would have been due to the structural continuity with the pillar with rigid joints. This obviously causes high localized stress concentration just near the edge constrained nodes, but it has negligible effects on the hot spot area results.

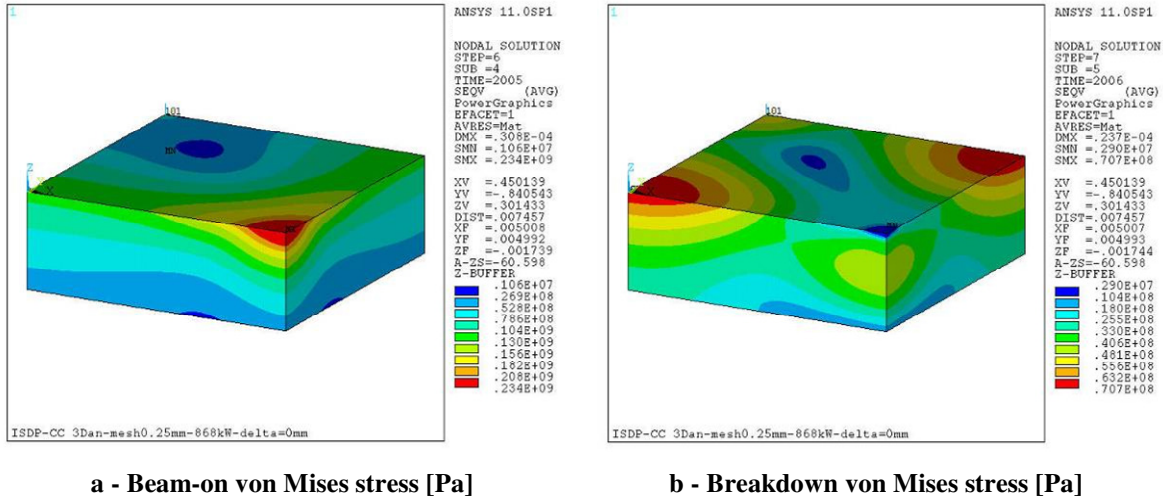


Figure 2.62: Beam-on and breakdown von Mises stresses

In this case the thermo-mechanical analyses give lower values for all mechanical parameters (von Mises stress and total strain in Figure 2.62 and Figure 2.63); this is due to the model shape that assures more deformability and then lower local concentration of stress: the model bends under the high heat power on the surface.

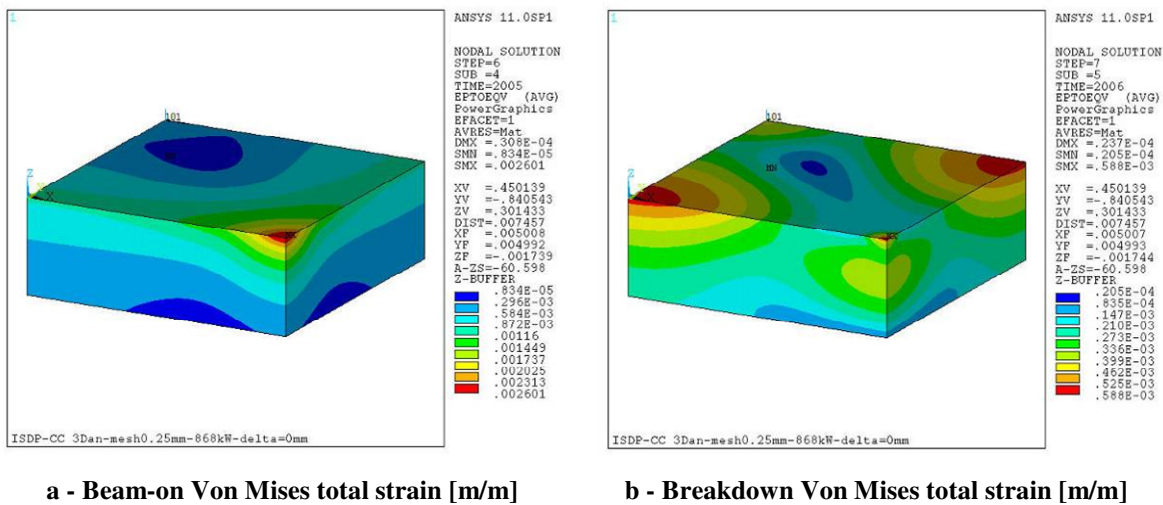


Figure 2.63: Beam-on and breakdown Von Mises total strain

The results of the thermo-mechanical analyses have been post processed in order to perform the fatigue life verification, as for the other models, and the result was that all nodes experienced a fatigue damage lower than $V=76\%$.

The pillars have been located just in correspondence of the nominal position where BSI+ impinge and not between them, because the pillar allows to exhaust a significant portion of the heat load through itself towards the rear wall of the half-moon manifold, reducing the thermal resistance and increasing the heat exchange surface as well. In this way, the efficiency of the heat exhaustion is higher.

2.8 FE models simulating the regions not impinged by BSI*

In order to complete the analyses of the PDP another model that represents the regions between and on the outside of the four columns of cooling channels has been developed. This model is shown in Figure 2.64 -b and represents a characteristic section of the regions without cooling channels, highlighted in blue on the PDP drawing in Figure 2.64 -a. In this case a bi-dimensional simplified model has been considered sufficient for the scope.

The channels are here considered having $5 \times 5 \text{ mm}^2$ section, with sharp corners.

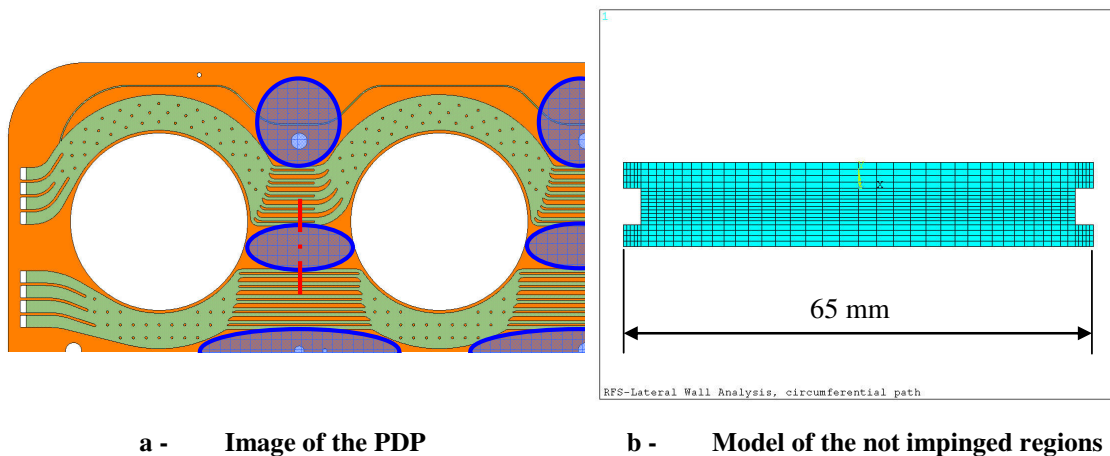


Figure 2.64: FE models of the PDP cooling channels with indication in (a) of the typical areas, highlighted in blue

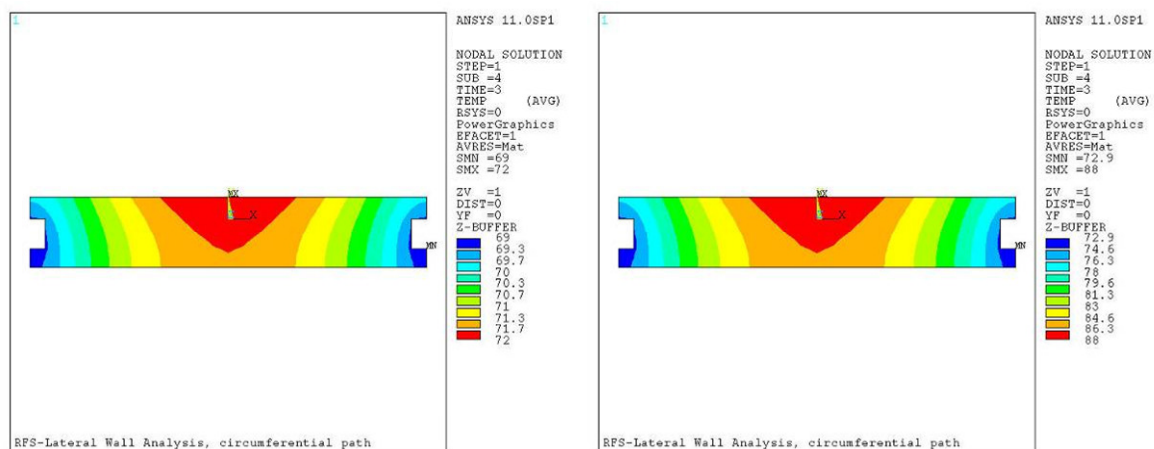
2.8.1 Loads and boundary conditions

The loads are in this case moderate, because there is just a uniformly distributed power density of 20 kW/m^2 applied on the upper surface of the model.

Boundary conditions are given by the application of the CHT coefficient on the inner surface of the two half $5 \times 5 \text{ mm}^2$ cooling channels at the model sides. The value of the heat transfer coefficient has been calculated and applied as explained in Paragraph 2.4.1.1. In first approximation no heat flux has been considered in correspondence to the lateral sides of the model.

Figure 2.65 shows the temperature distribution resulting from the thermal analysis. It is immediate to see that the PDP temperature has a little increase that is of about 4°C and then negligible. This result assures very small thermal stress: the only not negligible mechanical loads on this model are those caused by the water pressure, already analyzed in par. 4.3.2.2.1, so there is enough confidence that no mechanical analysis on this model is necessary.

Further thermal analyses have been carried out considering power densities on the model ranging from 20 to 100 kW/m^2 . In the worst case ($\text{PD} = 100 \text{ kW/m}^2$) material has a temperature rise of 20°C that is still acceptable for a good management of the caesium.



a - Temperature profile with 20 kW/m^2 heat power load b - Temperature profile with 100 kW/m^2 heat power load

Figure 2.65: Temperature contour plot with different loading conditions

2.9 Overall results and discussion

Starting from the overall requirements given by ITER, others coming from the experience of IPP colleagues on their test-beds, and taking into considerations the continuous updates coming from the physical analyses of the ion beam, the design of the RF source for MITICA has been carried out.

Among the RF plasma source components, the so called Plasma Driver Plate (PDP) and the Faraday Shield Back Plate (FSBP) are the most critical components, since they constitute the rear wall of the source and they are impinged by the Back-Streaming positive Ions, that carry a huge amount of energy. These two components experience very strong and localized heat power deposition and sputtering in the 1280 “hot spots” were BSI+ impinge on.

Whereas the FSBP is a plate of about 275 mm in diameter and it has quite a simple geometry, with consequent reduced difficulties for the design of its cooling circuit, the PDP is larger (overall dimensions about 1800mm*900mm*12mm) and it has large holes (called “driver holes”) that “houses” the drivers. As a consequence the PDP component must exhaust a much larger heat load and necessarily have cooling channel length much higher in comparison to the FSBP with consequent higher water mass flow rate and pressure drops. Moreover the cooling channel path is complicated by the presence of the driver holes that prevent the possibility to have straight cooling channels along the plate.

Different configurations of the cooling circuit have been considered; the one with the PDP subdivided in 4 quarters (the PDP quarters) has been finally adopted; analytical calculations of the expected pressure drops and of the main cooling circuit parameters have been carried out on it.

The design of the areas of the PDP where the BSI+ beamlets impinge on has been carefully developed in order to assure the maximum heat exhaustion. Two main “configurations” of cooling channels have been identified in the PDP: the one with couples of parallel channels having about $5*5\text{mm}^2$ of cross section area and the so called “half-moon” manifold, around the driver holes, having cross section of about $50*5\text{mm}^2$. Finite Element (FE) analyses have been carried out on models reproducing significant portions of these two different configurations of the cooling circuit, both present in the PDP quarter.

The FE analyses have been carried out considering also possible displacement of the BSI+ beamlets with respect to their expected position.

Two different concepts for the PDP have been developed and analyzed: a first one, initially taken as the reference solution, in which the PDP was made of CuCrZr alloy, and a second one,

that is now the adopted design and foresees the presence of an armour layer of molybdenum, 1.0 mm thick, facing the plasma and the BSI+ impinging beamlets.

Thermal and related thermo-mechanical FE analyses have been carried out on the described models; the results have then been post-processed in order to perform the fatigue verification, on the basis of the total beam ON/OFF and breakdowns expected for the ITER NBIs (node by node of the model), accordingly to a suitable procedure developed internally to Consorzio RFX [51].

2.9.1 Analysis results of the CuCrZr solution

As explained in details in [51], a safety factor, that is the major between 2 on the total strain range and 20 on the allowable number of cycles, has been adopted to draw the design curve, starting from the experimental fatigue curve for CuCrZr. This means that all nodes that are been calculated to experience a fatigue damage $V < 100\%$ are verified with the mentioned safety margin.

The fatigue verifications evidence that the nodes of the $5 \times 5 \text{ mm}^2$ cooling channels model in CuCrZr experiencing fatigue damage over 100% are localized just on the surface of the model in a very small circular area of about 1.5 mm in diameter. Nodes 0.5mm deep in the material, just below the loaded surface, experience a maximum fatigue damage of $V = 68\%$, so the conclusion is that the volume of the CuCrZr solution that presents a fatigue damage $V > 100\%$ is a spherical cup of 1.5mm diameter and 0.5mm deep maximum localized under the centre of each BSI+ hot spot. Due to the very high focalization of the heat power deposition, the fatigue damage experienced by a very small volume of material is not strongly affected by the geometry of the cooling circuit under the BSI+ impinging point.

The very small volume that results in experiencing fatigue damage over the limit of 100% is sufficient, accordingly to the classical mechanical theory, to generate a crack and consequently to cause the fatigue failure of the component.

Nevertheless, there are uncertainties due to the following aspects:

- the heat power density, at the centre of each BSI+ beamlet is very high; such a strong focalization of the beamlets is considered unrealistic even by the physicist specialized in this kind of processes;
- fluctuations of the BSI+ beamlets around their theoretical impinging points are expected: the plasma in the chamber, with its own large energy sources, will most probably cause variations of the heat power deposition points and distributions;

- the heat power density distribution over the hot spot is actually unknown and a little change of its profile has strong influence on the stresses that it induces in the material, and consequently on the total fatigue damage;
- the impact of the hydrogen and deuterium positive ions (the BSI+) causes strong interaction with the impacted material, on an atomic scale (sputtering, blistering, etc), but it is unknown how this interacts with the process that leads to the formation of cracks.
- the most stressed nodes of the models experience negative (compressive) stresses, both in average and peak values, that are less critical than the positive ones.

For the reasons explained above it is not possible to reliably conclude whether the component can actually survive for the whole life time of the ITER NBIs or not.

Due to physical sputtering, an erosion of about 2.0 mm has been estimated on the copper surface impinged by the BSI+, based on the whole ITER NBI+ life. Considering that CuCrZr is a copper alloy with 99% of copper, it has been reasonably assumed the same sputtering rate on CuCrZr, as for copper.

Trying to superposing the two main effects, we can calculate say that the thickness of CuCrZr experiencing fatigue damage lower than 70% is of about 0.30 mm; such a thickness will be locally “eroded” by BSI+ in:

$$t_{0.15mm} = t_{\mu m} \cdot 300 = 0.56 \frac{h}{\mu m} \cdot 300 \mu m = 168 h$$

The number of heating/cooling cycles experienced by the PDP in 168 hours of operation (considering that 450000 breakdowns and 50000 beam-on/off cycles are expected in total, over the 5500 hours of ITER NBIs life) is:

$$n_{breakdown} = \frac{168h}{5500h} \cdot 450000 = 13744 \quad \text{breakdown cycles}$$

$$n_{beam-on/off} = \frac{168h}{5500h} \cdot 50000 = 1527 \quad \text{beam-on/off cycles}$$

The consequent fatigue damage accumulated by the material in 168 hours by 1527 beam-on/off and 13744 breakdown cycles is $V=8.8\%$ for the most stressed node.

We can conclude that, within the cited hypotheses (superposition of effects of the fatigue phenomenon with the sputtering one), the erosion caused by sputtering removes the material with a rate that is higher than the one leading the same material to failure, due to fatigue.

2.9.2 Analysis results of the solution with 1.0mm thick molybdenum layer

The same fatigue verification has been performed for the solution with 1.0mm thick molybdenum armour layer, limited to the copper-subplate, since the fatigue curves for the molybdenum were not known.

Due to the large mismatch between the copper and molybdenum thermal and mechanical properties, the FE models showed a relatively large volume of copper, at the interface, experiencing fatigue damage over the threshold of 100%. In this case, the results show also plastic deformations of the copper at the interface (strains up to 0.4%).

Since the properties at the interface between the two metals strongly depend on the technology used for the production of the joint, and it is impossible to predict and simulate the properties in the FE analyses, the only way to establish whether a 1.0mm molybdenum armour layer on copper substrate is a feasible and reliable solution or not for the ITER NBI RF ion source components is to perform dedicated R&D activities.

3 R&D activities on the Cu-Mo Plasma Driver Plate

3.1 Introduction and overview of the R&D activities

On the basis of the calculations on BSI+ and related sputtering on the hit surfaces (see Paragraphs 2.2.3 and 2.2.4), ITER decided to start R&D activities in order to explore if and which, among the available technology, were suitable for the production of a thick (in the order of 1.0 mm) armour layer of molybdenum or tungsten for the rear vertical plasma facing components of the MITICA and ITER NBIs RF sources. The activities, not yet concluded, eventually aim at qualify (at least) one technology for the scope.

On the basis of the general requirements, the first activity has been the assessment of the detailed requirements and of the strategy to be followed for the whole R&D program.

In Table 3.1 the first list of specific identified requirements is shown. The content of this list has been then revised considering costs, available time, and on the basis of the partial results obtained step by step.

RFX APPROVAL	Main requirements	
ok	i	To investigate different technologies available for the production of thick Mo coatings for the PDP
ok	ii	To qualify the successful ones
ok	iii	To select the best one for the future manufacturing of the PDP quarters and FSBPs (selection based on tests)
Strategy:		
ok	1	R&D focused on relevant prototypes, not on the PDP quarters (cost saving). The Suppliers are requested to guarantee that the results obtained on the prototypes are reproducible on the PDP quarters.
ok Mo for armour. No CuCrZr, but copper for the heat sink	2	Identification of molybdenum as reference armour material since the plasma grid is molybdenum PVD coated.
ok	3	Consorzio RFX identifies a set of companies (holding specific technology) to ask for the manufacturing of 1 and 3 prototypes each one
	4	Technologies to be investigated:
ok. Priority 1	a	Explosion bonding
ok. Priority 2	b	Plasma Spraying (vacuum, atmospheric, low pressure, ...?)
ok. Priority 3 (later stage)	c	Hot Hydrostatic Pressing

ok. Priority 4 (later stage)		d	Brazing
ok	5		The explicit quotation of each of a set of destructive and non destructive tests to be required to the companies
ok	6		In parallel Consorzio RFX evaluates the costs of doing the same tests on all the prototypes together (at Consorzio RFX and/or at specialized companies).
based on the quotations	7		Cost management strategy:
ok		a	definition of the budget;
ok		b	to assign an order of priority to each technology to be tested;
based on the quotations		c	to assign an order of priority to each non destructive and destructive test;
ok		d	to organize the contracts by steps (quotation for each step and to proceed step by step under written approval of Consorzio RFX)
Detailed requirements / specifications:			
ok	1		design of the relevant prototype
ok (the company can propose alternatives)	2		overall prototype dimensions: 300mm x 300mm x 11,5mm (reproducing also a part of the driver's hole).
ok	3		pure molybdenum layer nominal thickness: 1,0 mm
ok	4		high vacuum compatibility
To request quotation for 1 and for 3 prototype(s)	5		number of prototypes (requested to each company): 3
	6		Non destructive tests:
ok (as applicable)		a	Ultrasonic examinations
ok		b	Radiographic examinations
ok		c	Surface examinations
in house (to be assessed)		d	Infrared thermography
To be further investigated		e	HR(B or C) of CuCrZr as function of the distance from the interface
ok		f	Micrography of the section
	7		Destructive tests (on samples cut from the prototypes)
ok		a	tensile test
ok		b	bending
ok		c	shear test at the interface
in house	8		Thermal shock(s) (to be done at Consorzio RFX or at dedicated test-facility)
in house - to be further investigated	9		Thermal fatigue (to be done at Consorzio RFX or at dedicated test-facility)

Table 3.1 : list of the detailed requirements and strategy for the R&D activities identified at the beginning

According to the priority assigned to the different technology to be investigated (see point 4 of Table 3.1), based on a literature research on the pros and cons of each one, the following possible suppliers were identified:

- explosion bonding/welding
 - EXPLOFORM – 3D Metal Forming B.V. -Kolkweg 6, Postbus 2192, 8203 AD LELYSTAD; www.exploform.com
- plasma spraying:
 - PLANSEE SE - 6600 Reutte – Austria; www.plansee.com
 - Sulzer Metco AG (Switzerland) - Rigackerstrasse 16, 5610 Wohlen, Switzerland; www.sulzermetco.com

Since the budget was limited, the Hot Hydrostatic Pressing and the Brazing technologies have not been investigated since the beginning.

A technical specification document has been prepared and sent to the selected companies (with slight modifications in order to adapt the requirements to the specific required technology) in order to receive quotations for the R&D activities to be carried out (this technical specification document is reported in Annex 1).

3.2 Plasma Spray technique

Plasma spraying is a widely used technique in the nuclear fusion field for producing coatings. Two leading companies were selected for testing the plasma spraying technology for the manufacturing of copper prototypes with 1.0mm thick molybdenum coating layer.

PLANSEE read and studied the technical specifications (Annex 1) and did not make any quotation. After a telephone call in which the application, use and requirements for the final components to be used in MITICA and ITER NBIs were deeply discussed, the Manager of the Nuclear Fusion Division at PLANSEE declared that PLANSEE was not able to produce thick coatings respecting the requirements stated in the technical specification document (Annex 1).

3.2.1 Manufactured samples

After receiving the technical specification document, SULZER Metco proposed to start with the production of few scouting samples in order to evaluate the possibility to manufacture the requested 1.0 thick molybdenum coating on copper, since the company was not able to assure the result.

Small samples have been manufactured (see Figure 3.1): 1.0mm thick molybdenum coating was deposited onto 3 copper disks ($\text{Ø}=25\text{mm}$, $h=10\text{mm}$) and 2 rectangular plates (50mmx20mmx2mm) by Atmospheric Plasma Spraying (APS).

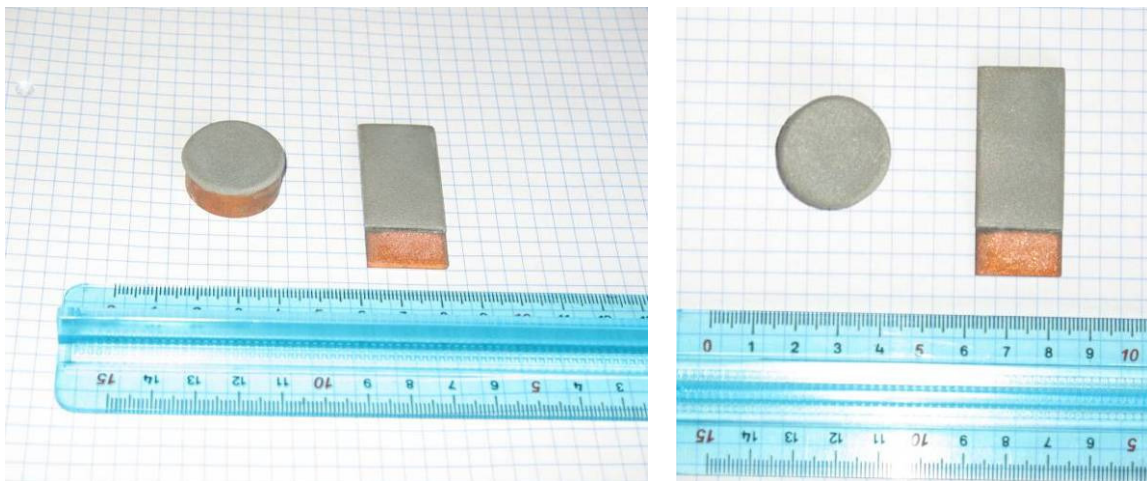


Figure 3.1: Photos of the scouting samples manufactured by APS

The molybdenum powder used for the manufacturing of the coating is the SULZER Amdry 313x. Figure 3.2 shows the composition and the characteristics of the Amdry 313x.

AMDRY 313X

Chemistry:	Mo 99.5%
Particle Size:	-90 +37 μm (-170 +400 mesh)
Morphology:	Spheroidal, Agglomerated and Densified
Specifications:	Canada Pratt Whitney CPW 213 Amend. 1 Pratt Whitney PWA 1313 Rolls-Royce Allison EMS 56705
	CFM International CP 6019 Rolls-Royce MSRR 9507/19

Tough and hard, with excellent sliding properties and galling resistance; good emergency running properties. Fret resistant. Resistant to electric arc erosion. High-density coatings are possible. In oxidizing or atmospheric conditions, Mo should not be used above 340°C (650°F). Used for pump parts, diesel engine fuel injectors piston rings, synchronizing rings, press fits, valves, gears, cam followers and similar applications. Bonds well to steel.

Figure 3.2: Data sheet of the Amdry 313x Molybdenum based powder used for the APS coating deposition

3.2.2 Tests on the APS samples

After the manufacturing of the samples some tests were carried out on them in order to investigate the characteristics of both the coating and of the interface. The analyses carried out are here after reported.

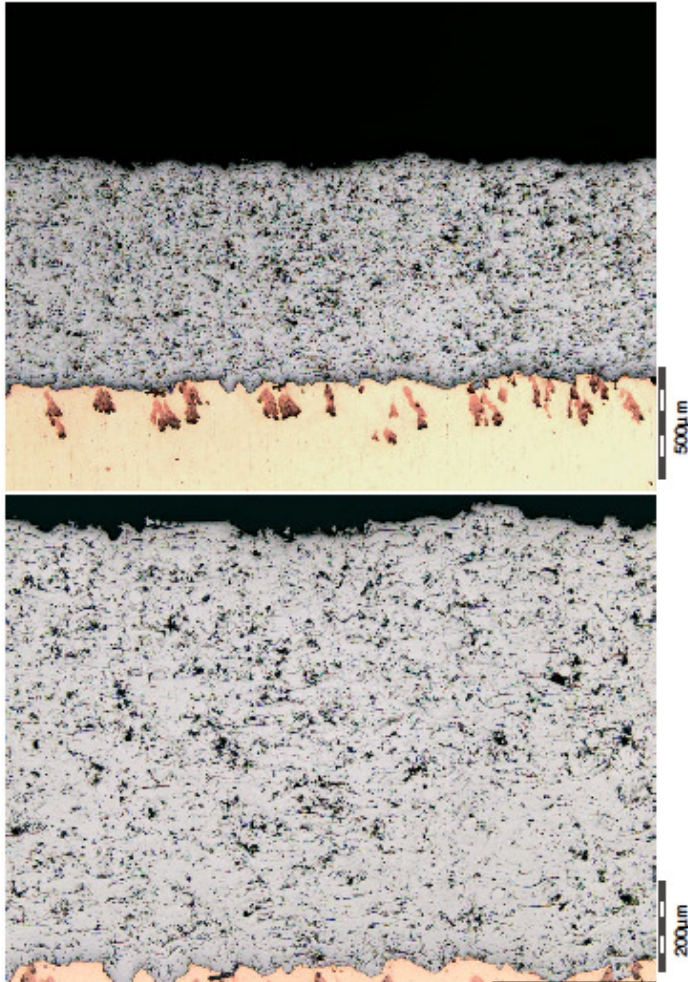
3.2.2.1 Porosity measurement

The measurement of the porosity of the coating layer was required to the manufacturer, in order to make a qualitative estimation of the expected outgassing rate. Figure 3.3 shows the micrographic test-report made by SULZER, in which the porosity is declared to be 4.5% (in volume) and the coating thickness is 0.9mm.

SULZER

Sulzer Metco

Run No.: 10C0314 Process: APS Customer: Consorzio RFX
Project No.: CSC10_227 Gun: F4-MB



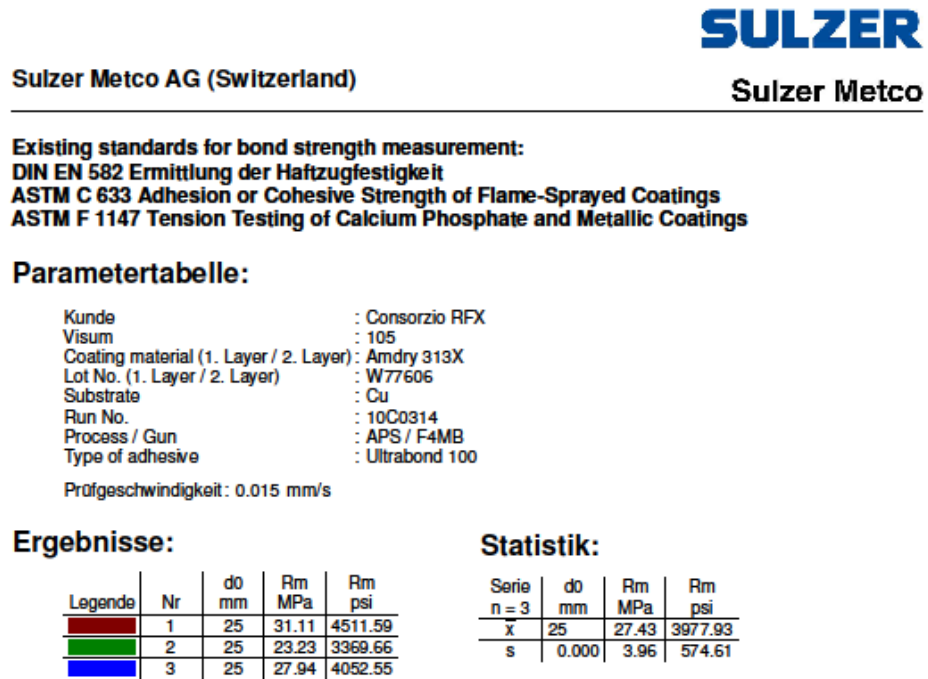
Coating material: Amdry 313X
Coating thickness: 900 µm
Porosity: 4.5 %

Remarks: -

Figure 3.3: Micrographic test report on the scouting samples

3.2.2.2 Interface bond strength measurement

In Figure 3.4 the report of the interface bond strength is shown, reporting a mean value of 27 MPa. This value is quite low, largely under the required value, that was 50 MPa, as specified in Annex 1



Seriengrafik:

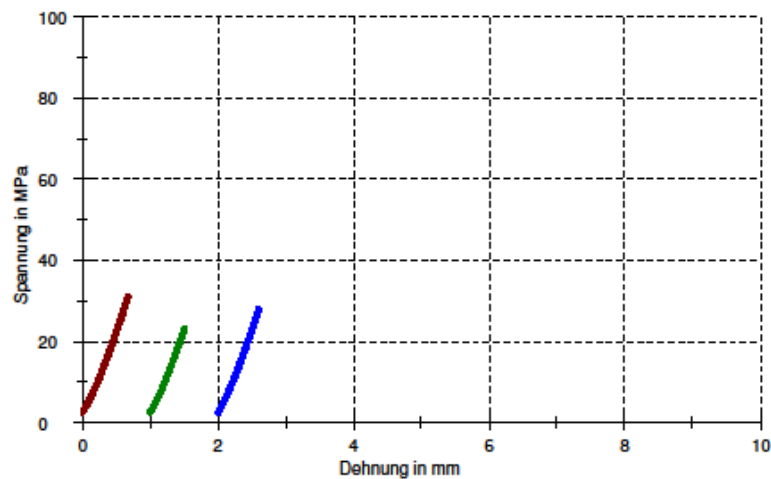


Figure 3.4: Bond strength test report on the scouting samples

3.2.2.3 Surface roughness measurement

The typical value of the roughness of the APS coatings is around $5\mu\text{m}$. The surface roughness required for the plasma facing surfaces inside the MITICA RF source is $R_a 0.8\mu\text{m}$. This value is required in order to make easier (or even possible) the cleaning of the source from the caesium compounds that unavoidably form when the source is vented. In order to verify whether such a low value of roughness is reachable on an APS coating, with relatively high porosity (4.5%), one of the cylindrical scouting samples has been grinded. Figure 3.5 shows the roughness measurement report made by SULZER Metco: the value $R_a=0,2\mu\text{m}$ was obtained.

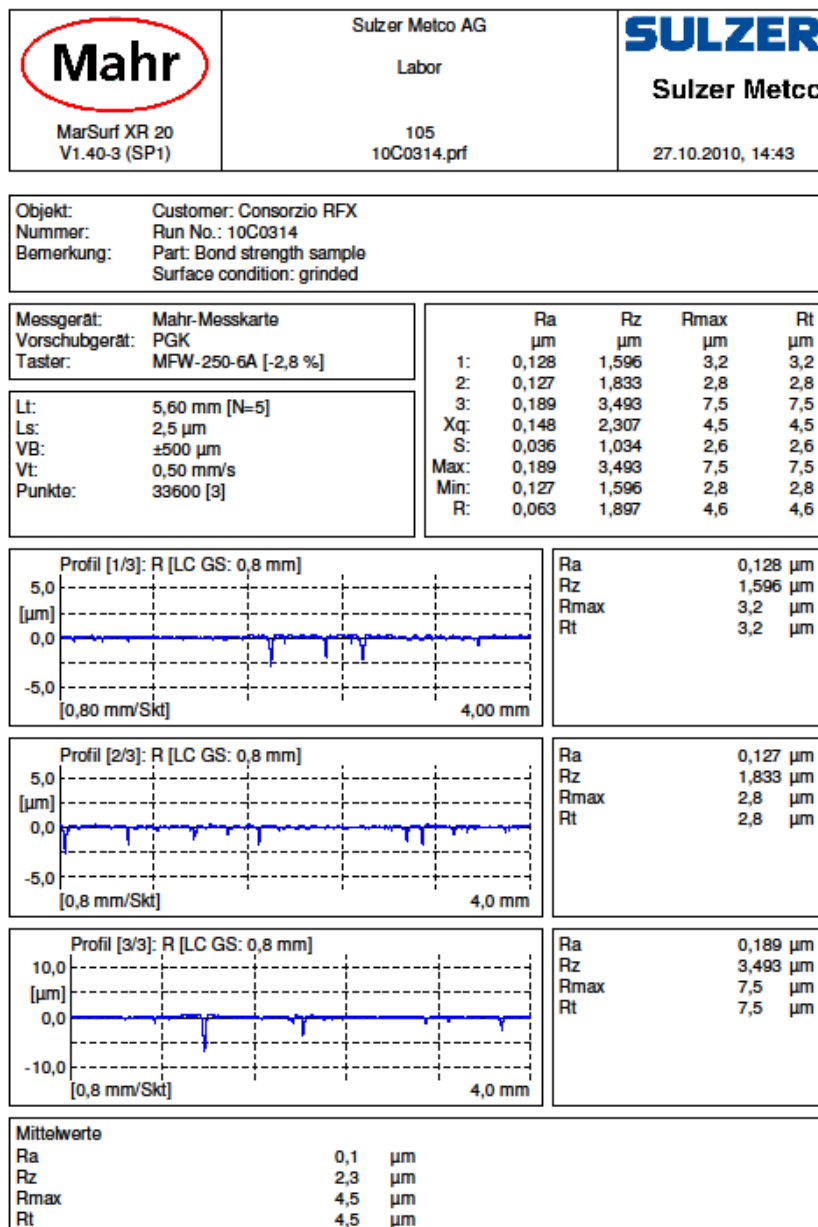


Figure 3.5: Roughness measurement report on the grinded cylindrical scouting sample

3.2.2.4 Outgassing rate measurement

Since the porosity of the coating layer is 4.5%, it was decided to investigate further its compatibility with vacuum applications; an outgassing test was performed on two of the cylindrical samples coated by APS. The samples copper substrate was 25mm in diameter, 10mm thick; the molybdenum coatings had instead diameter in the range 26.5 - 7 mm, and thickness ~0.9 mm.

The outgassing measurement was done on the grinded sample (labelled with “B”) and on one of the others, not grinded (labelled with “A”). The samples have been cleaned in acetone bath, then ethylene ultrasonic bath, and finally dried at 50°C for 30 minutes.

Experimental Setup and Procedures

The measurements were carried out on a UHV vacuum bench equipped with a high sensitivity Quadrupole Mass Spectrometer (QMS), as schematically shown in Figure 3.6.

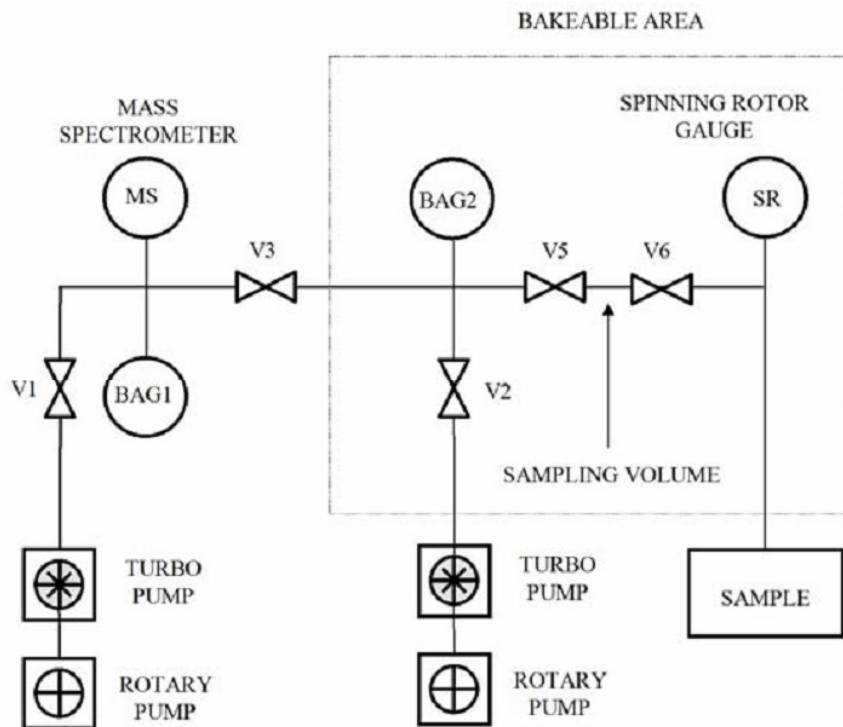


Figure 3.6: Layout of the experimental apparatus for the static outgassing measurements

The samples were mounted in a metallic cage (contained inside a Pyrex bulb), which can be heated using a RF coil, while the temperature was monitored using a thermocouple (Figure 3.7). The outgassing test was performed in static conditions, i.e. isolating the sample area from the pumping system and accumulating the released gases during the thermal treatment.

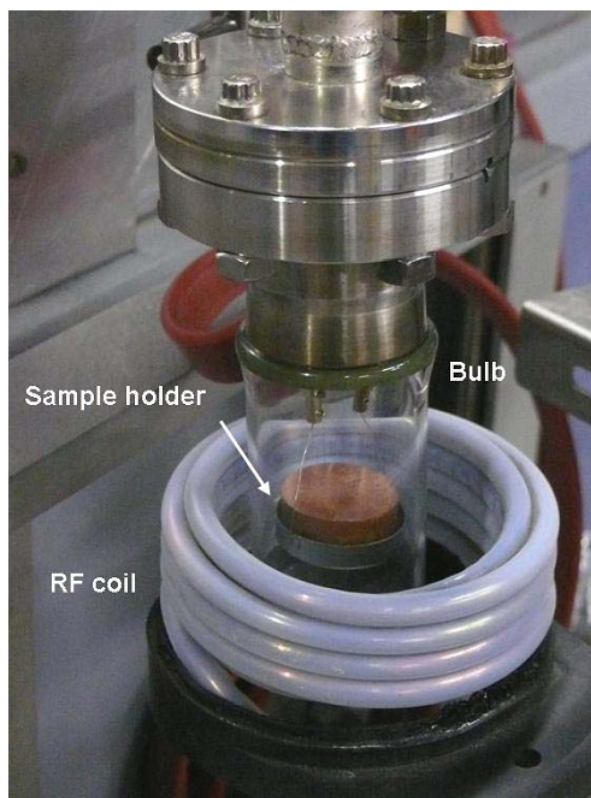


Figure 3.7: Image of a copper sample mounted for the analysis

At specified time intervals, a small part of the atmosphere was collected in the sampling volume (defined by valves V5-V6) and analyzed with the QMS. Such gas quantity is then taken into account when calculating the results of the next analysis. The QMS is calibrated for the main gas species using a certified gauge, so that the acquired current signal is converted into a partial pressure value. An accurate knowledge of the volumes of the different parts of the bench allows determining the amount of gas analyzed. After mounting the sample, the bench bakeout was performed to achieve a base pressure in the low 10^{-9} mbar range (the volume of the QMS is not exposed to air). In order to evaluate the contribution of the Mo film alone, we performed a blank run with a bare copper substrate and we subtracted it to the results of the experiments with the coated samples. Two different thermal ramps were used for the polished and unpolished samples, as shown in Figure 3.8. The outgassing properties of the unpolished sample (A) were studied at 50, 100 and 200°C (one hour for each step), while the polished one (B) was subjected to a longer test at 50°C. The samples were rinsed in acetone before shipping and then underwent ultrasonic ethylene bath before being mounted in the experimental apparatus. The samples were baked at 200°C for one hour and then exposed to air for 30 minutes before the analysis in order to simulate the expected exposure to air of the components, during the assembly in the RF source.

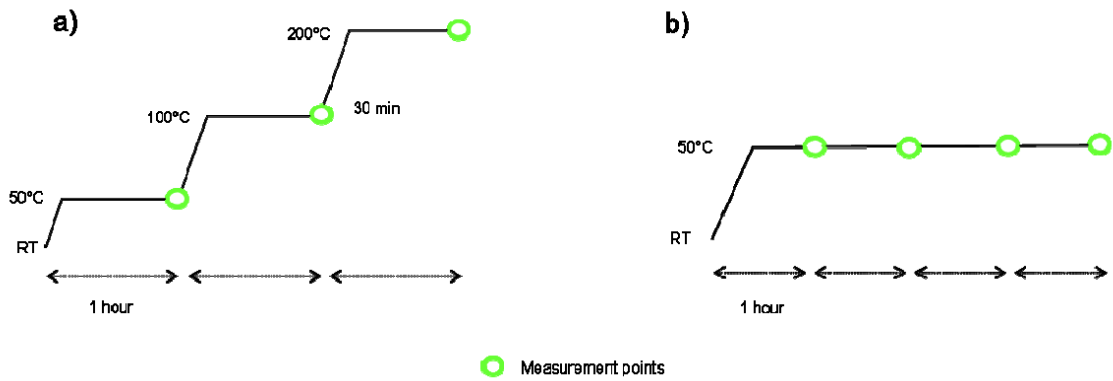


Figure 3.8: Temperature ramps applied to the unpolished “A” (a) and polished “B” (b) samples

Results and discussion

The following Table 3.2 reports the gas quantity released during the experiments (total amount and total amount per unit area). Data are cumulative, i.e. the values shown for a specific step include the gas released during the previous ones. Whenever the signal was very close to the one given by the copper substrate alone, only an upper limit for the gas quantity is indicated.

CO, N₂, and CH₄ are the main gases desorbed by sample A at 50°C. Also H₂ desorption is in the 10⁻⁵ cc·mbar range. Raising the temperature to 100°C causes a detectable increase of the H₂O signal. Due to its high sticking factor, water is usually underestimated in all measurements performed with the bench at room temperature. At this temperature, the amount of carbon oxide species increases by more than one order of magnitude. At 200°C the outgassing load increases by several orders of magnitude and CO₂ is the main gas specie, followed by CO and water. The reason for such a step-like behaviour is not completely clear and it may be related to the porous structure of the film, able to retain species and enhance effects related to the chemical properties of the Mo surface.

Sample A (ccmbar)				Sample B (ccmbar)					
Gas	50°C (1h)	100°C (1h)	200°C (1h)	Gas	50°C (1h)	50°C (2h)	50°C (3h)	50°C (4h)	50°C (5h)
H ₂	<1E-4	5,6E-04	1,7E+00	H ₂	<1E-4	2,8E-04	3,2E-04	3,5E-04	3,8E-04
He	<1E-7	5,0E-07	5,0E-04	He	1,5E-07	6,1E-07	1,1E-06	1,2E-06	1,7E-06
CO	5,5E-05	1,1E-03	3,5E+00	CO	6,7E-05	1,4E-04	1,5E-04	2,1E-04	2,5E-04
N ₂	1,2E-04	5,0E-04	1,3E+00	N ₂	9,5E-04	2,0E-03	2,9E-03	4,0E-03	4,7E-03
CH ₄	1,1E-04	1,2E-04	2,2E-01	CH ₄	<5E-5	<5E-5	<5E-5	<1E-4	<1E-4
H ₂ O	0,0E+00	1,2E-04	2,0E+00	H ₂ O	0,0E+00	0,0E+00	0,0E+00	0,0E+00	0,0E+00
O ₂	0,0E+00	0,0E+00	0,0E+00	O ₂	0,0E+00	0,0E+00	0,0E+00	0,0E+00	0,0E+00
C ₂ H ₆	2,2E-05	8,8E-05	2,7E+00	C ₂ H ₆	2,4E-05	3,5E-05	3,7E-05	4,2E-05	4,6E-05
C ₃ H ₈	<1E-5	6,4E-05	1,5E+00	C ₃ H ₈	<1E-5	1,8E-05	2,6E-05	2,9E-05	3,5E-05
Ar	5,3E-06	1,3E-05	3,3E-02	Ar	1,3E-05	3,0E-05	3,9E-05	5,4E-05	6,6E-05
CO ₂	<2E-5	2,4E-04	1,5E+01	CO ₂	1,8E-04	4,2E-04	1,2E-03	1,3E-03	1,6E-03
TOT.	3,1E-04	2,7E-03	2,8E+01	TOT.	1,3E-03	2,9E-03	4,7E-03	6,1E-03	7,1E-03

Sample A (%)				Sample B (%)					
Gas	50°C (1h)	100°C (1h)	200°C (1h)	Gas	50°C (1h)	50°C (2h)	50°C (3h)	50°C (4h)	50°C (5h)
H ₂	22,65%	20,22%	6,10%	H ₂	7,20%	9,59%	6,75%	5,74%	5,37%
He	0,02%	0,02%	0,00%	He	0,01%	0,02%	0,02%	0,02%	0,02%
CO	12,50%	38,48%	12,70%	CO	4,81%	4,84%	3,19%	3,48%	3,52%
N ₂	27,43%	17,91%	4,83%	N ₂	68,23%	66,73%	61,90%	65,51%	65,31%
CH ₄	24,50%	4,46%	0,78%	CH ₄	3,60%	1,69%	1,06%	1,63%	1,40%
H ₂ O	0,00%	4,20%	7,11%	H ₂ O	0,00%	0,00%	0,00%	0,00%	0,00%
O ₂	0,00%	0,00%	0,00%	O ₂	0,00%	0,00%	0,00%	0,00%	0,00%
C ₂ H ₆	4,90%	3,15%	9,79%	C ₂ H ₆	1,74%	1,18%	0,78%	0,69%	0,65%
C ₃ H ₈	2,27%	2,30%	5,40%	C ₃ H ₈	0,72%	0,61%	0,54%	0,47%	0,49%
Ar	1,20%	0,47%	0,12%	Ar	0,92%	1,01%	0,83%	0,88%	0,92%
CO ₂	4,53%	8,79%	53,17%	CO ₂	12,75%	14,32%	24,93%	21,57%	22,32%
TOT.	100,00%	100,00%	100,00%	TOT.	100,00%	100,00%	100,00%	100,00%	100,00%

Sample A (ccmbar/cm ²)				Sample B (ccmbar/cm ²)					
Gas	50°C (1h)	100°C (1h)	200°C (1h)	Gas	50°C (1h)	50°C (2h)	50°C (3h)	50°C (4h)	50°C (5h)
H ₂	1,5E-05	8,3E-05	2,5E-01	H ₂	1,5E-05	4,2E-05	4,7E-05	5,2E-05	5,7E-05
He	1,5E-08	7,4E-08	7,4E-05	He	2,2E-08	8,9E-08	1,6E-07	1,8E-07	2,5E-07
CO	8,1E-06	1,6E-04	5,2E-01	CO	9,8E-06	2,1E-05	2,2E-05	3,1E-05	3,7E-05
N ₂	1,8E-05	7,3E-05	2,0E-01	N ₂	1,4E-04	2,9E-04	4,3E-04	5,9E-04	6,9E-04
CH ₄	1,6E-05	1,8E-05	3,2E-02	CH ₄	7,4E-06	7,4E-06	7,4E-06	1,5E-05	1,5E-05
H ₂ O	0,0E+00	1,7E-05	2,9E-01	H ₂ O	0,0E+00	0,0E+00	0,0E+00	0,0E+00	0,0E+00
O ₂	0,0E+00	0,0E+00	0,0E+00	O ₂	0,0E+00	0,0E+00	0,0E+00	0,0E+00	0,0E+00
C ₂ H ₆	3,2E-06	1,3E-05	4,0E-01	C ₂ H ₆	3,6E-06	5,1E-06	5,4E-06	6,2E-06	6,8E-06
C ₃ H ₈	1,5E-06	9,4E-06	2,2E-01	C ₃ H ₈	1,5E-06	2,7E-06	3,8E-06	4,2E-06	5,1E-06
Ar	7,8E-07	1,9E-06	4,8E-03	Ar	1,9E-06	4,4E-06	5,7E-06	7,9E-06	9,7E-06
CO ₂	2,9E-06	3,6E-05	2,2E+00	CO ₂	2,6E-05	6,2E-05	1,7E-04	1,9E-04	2,3E-04
TOT.	6,5E-05	4,1E-04	4,1E+00	TOT.	2,0E-04	4,3E-04	6,9E-04	9,0E-04	1,1E-03

Table 3.2 : Gas quantity in cm³·mbar desorbed during the experiments. The percentage and the results per unit area have been calculated using the upper outgassing limits, when necessary

Sample B has been characterized accordingly to a different heating schedule, aiming at following the gas evolution at 50°C. Figure 3.9 reports a plot of the results. Nitrogen is the main desorbed species, followed by carbon dioxide and, below 10%, H₂ and CO.

N₂ and Ar pressures grow with rather constant rate and the ratio N₂/Ar ranges from 65 to 75: such behaviour suggests that the porous structure of the film may trap air, which is then slowly released in vacuum. Oxygen was not detected. This is not surprising due to its high reactivity, which considerably lowers the sensitivity for this gas. No clear water signal was observed during the test.

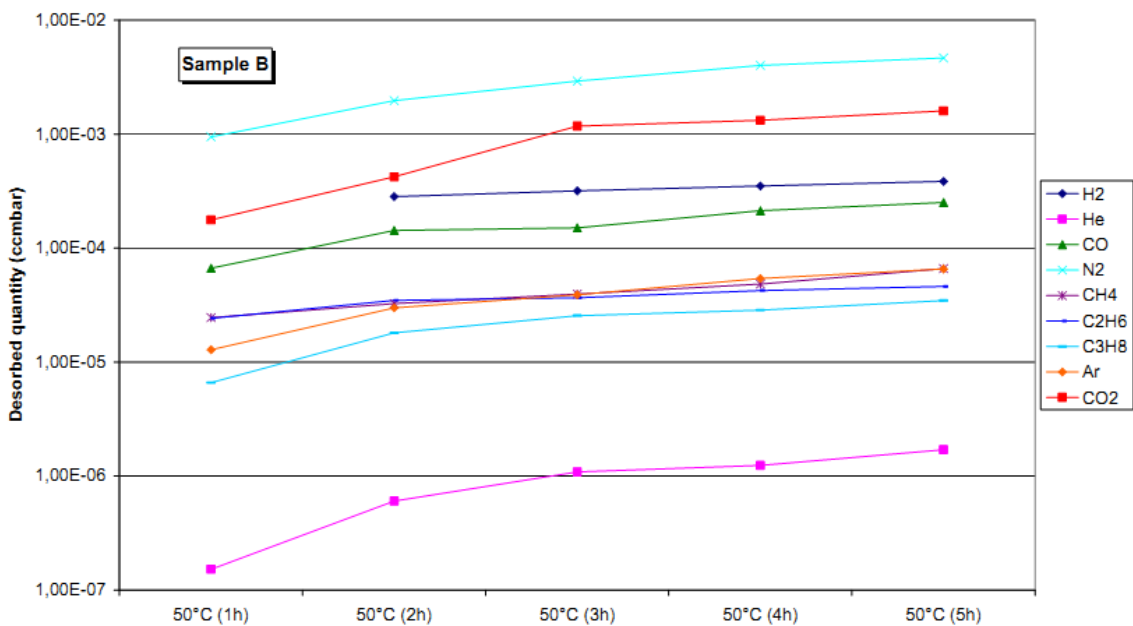


Figure 3.9: Evolution of the desorbed quantities during the outgassing test on sample B (mechanically polished)

Desorbed gases are expected to decrease with time according to a power law, with exponent between 0.5 and 1. This did not happen in the case of carbon oxide/dioxide, suggesting that these gases may require a time much longer than the duration of the experiment (5 hours) to significantly reduce the outgassing rate. Hydrocarbons and hydrogen on the contrary showed a decreasing trend, which anyhow cannot be easily extrapolated. The rather complex morphology of the film seems to have a role in these deviations.

A direct comparison of samples A and B, (with and without mechanical polishing, respectively) was performed using the data collected after one hour at 50°C. As shown in Figure 3.10, sample B released more CO₂, N₂ and Ar and less CH₄ with respect to sample A.

Consequently, the total outgassing load of sample B is about four times higher than for sample A.

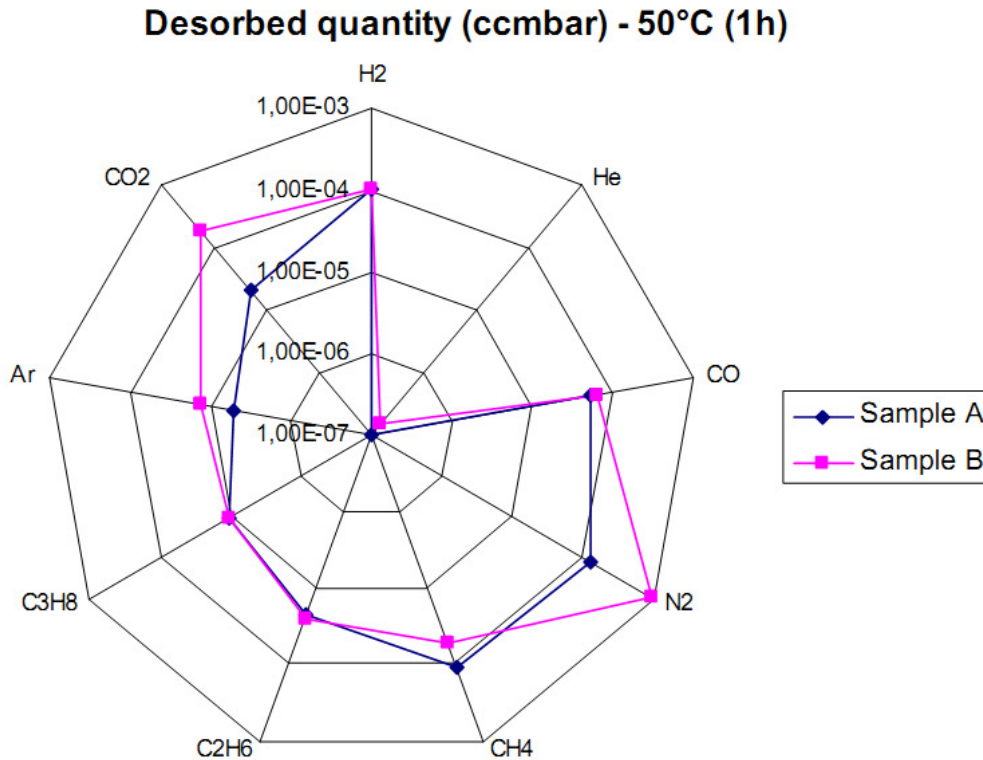


Figure 3.10: Plot of the gas quantity desorbed by the samples after one hour at 50°C, for each species. The upper outgassing limits reported in Table 3.2 have been used when necessary

From the results obtained, it seems possible to apply the mechanically polished Mo films in the ion source. In fact, in spite of the rather large screen area, the total load after a few hours at 50°C was in the range of a few $\text{cm}^3 \cdot \text{mbar}$. Considering the large installed pumping speed in the chamber² the average estimated outgassing is not expected to prevent the achievement of the desired background pressure. During operation of the source, the hydrogen (deuterium) contamination approximately depends on the ratio between the outgassing and inlet fluxes. For example, a total screen outgassing rate in the range of $10^{-3} \text{ cm}^3 \cdot \text{mbar/s}$ (the actual calculation for sample B gives $6 \cdot 10^{-4} \text{ cm}^3 \cdot \text{mbar/s}$), diluted in a $5 \cdot 10^4 \text{ cm}^3 \cdot \text{mbar/s}$ ($=5 \text{ Pa} \cdot \text{m}^3/\text{s}$) H_2 flux [55] would result in 0.02 ppm contamination. Needless to say this is only a first indicative estimation which does not take into account geometric and complex dynamic effects, including, but not limited to, ion bombardment, which occur in the real device. Analysis on more samples would also allow quantifying reproducibility of the degassing properties from sample to sample.

3.2.3 Conclusions

Atmospheric Plasma Spray technique has been investigated for producing 1.0 mm thick molybdenum coating on a copper substrate. One sample has been grinded in order to verify the possibility to reach the required surface roughness ($R_a=0.8\mu\text{m}$). The resulting armour layer showed relatively low bond strength to the substrate (about 30MPa) and quite high porosity (around 5%).

The outgassing properties of the coating have been studied: the main desorbed species at the operating temperature (50°C) are CO_2 and N_2 . The porous structure of the coating seems to have a role in trapping air and other surface contaminants inside the film. The mechanical polishing treatment of the molybdenum coating causes the increase of the outgassed load, which anyway should not represent a problem in order to achieve the desired background pressure in the vessel. In fact, the initial (maximum) outgassing rate is at least seven orders of magnitude lower than the hydrogen flux during source operation, resulting in an expected contamination level <0.1 ppm which is considered an acceptable value.

3.3 Explosion Bonding (EB) technique

The most common explosive metalworking technique is Explosive Bonding (EB), also known as explosive welding or explosive cladding. This metalworking technique uses controlled detonations to force dissimilar metals into a high-quality joint, metallurgically bonded. The process uses in fact the forces of controlled detonations to accelerate one metal plate into another creating an atomic metallic bond. The transition joint has high mechanical strength, is ultra-high vacuum tight and can withstand drastic thermal excursions.

Typical uses of the Explosion bonding technique include ultra-high vacuum joints between aluminium, copper and stainless steel, corrosion resistant claddings on mild steel substrates, and alloy aluminium joined to low-expansion rate metals for electronic packages.

The Explosion Bonding can be used, in principle, for joining every type of metal.

The interface between the two metals is typically not flat, it usually presents wavy profile and this increases the interface area, enhancing the adhesion strength.

Even if some trials have been carried out in the past, explosion bonding molybdenum to copper [56], the joining of these two metals is not industrially experienced and required to be further investigated.

3.3.1 First step of R&D activities

EXPLOFORM – 3D Metal Forming B.V. (EXPLOFORM) made a quotation for the production of the prototypes, accordingly to the requirements specified in Annex 1 that was too expensive. As consequence the goal of the supply was reduced and a new technical specification document, was prepared; its main content is presented in next paragraph.

3.3.1.1 Main goals

The final goal of the “first step of R&D activities” was to manufacture preliminary prototypes reproducing, in scale, the part of the Plasma Driver Plate around one of the driver holes (see Figure 3.11) and to carry out tests aiming to analyze the interface quality and strength (micrography, tensile test, chisel test, etc).

The detailed aiming of the first step is summarized in the following list:

1. identification of the parameters for a successful explosion bonding of a 1.0 mm thick molybdenum sheet onto a copper sub-plate;

2. forming of the clad plate in correspondence to the driver hole rim, aiming to obtain the final PDP local required shape (see Annex 1);
3. analyses of the interface (by means of conventional tests and analyses);
4. testing of the interface under strong localized heat deposition (thermal shock and thermal fatigue tests).

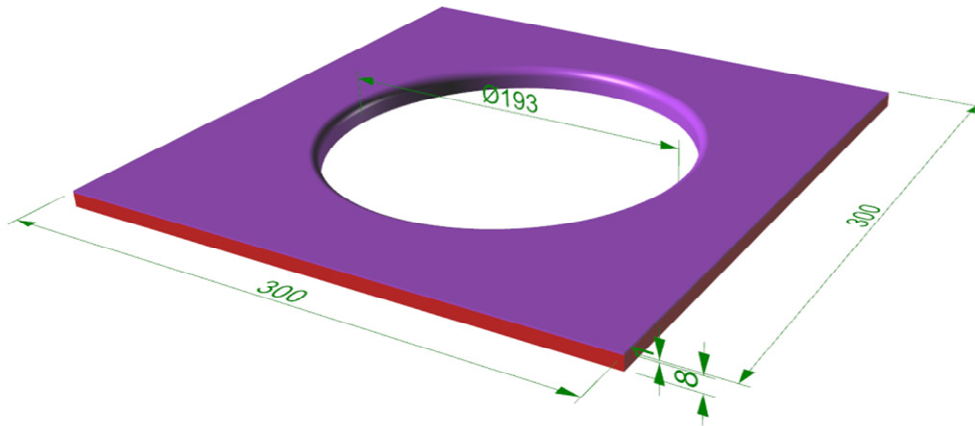


Figure 3.11: Picture with the main dimensions of the prototypes to be manufactured within the “first step of R&D activities” by explosion bonding

3.3.1.2 Manufacturing of the prototypes

The research was initially focused on the identification of the parameters for explosive bonding molybdenum to copper. Tests were performed with plates of 200x50 mm.

Secondly plates of about 300x300 were clad. A hole was cut in these plates and the hole edge was formed. The obtained prototype shape is shown in Figure 3.11.

In Figure 3.12 the geometry of the driver hole rim (before and after its forming) is shown: the ‘finger’ in the picture on the left is 10 mm long and 3 mm thick (2 mm Cu + 1 mm Mo). The ‘overhanging’ is the extra depth of the flange that is needed for achieving the required total thickness of 11.5 mm of the PDP.

The molybdenum was purchased at Plansee (Austria) and the copper at Artyomovsk (Ukraine). The certificates of the materials are shown in Figure 3.13.

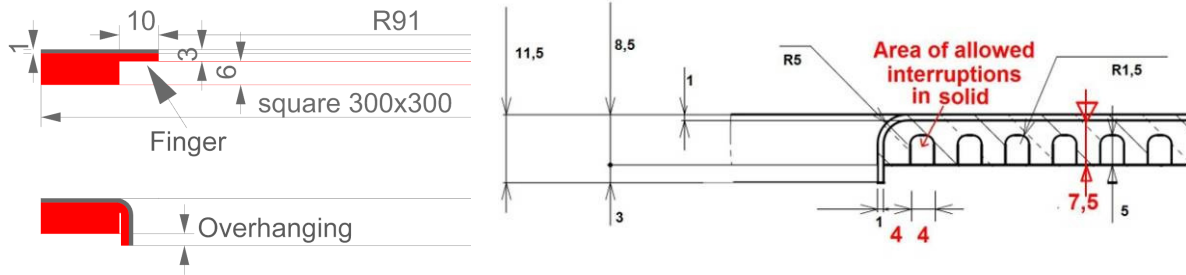


Figure 3.12: Shapes (axial-symmetric section) before and after forming with ‘finger’ and ‘overhanging’ (left) and final required shape of the PDP driver hole rim (right)

RoHS QUALIFIED
QCS
SYSTEM CERTIFIED
ISO 9001:2008 NR. 021751
ISO 14001:2004 NR. 010311
OHSAS 18001:2007 NR. 003511

Test-Report
acc. to EN 10204 - 2.2

Report No.: 87311765000010
Date: 04.10.2010
Customer: 3D-Metal Forming B.V. / NL
PLANSEE-Order No./Item No.: 8002991 / 10
PLANSEE-Material-No.: Z257249
PLANSEE-Segment / PoC. / / Luke /
Customer Order No.: O20100812 dated 17.09.2010
PLANSEE-Specification: PS-GF013

Material / Product: MO / Mo Sheet 1,0 x 600 x 1000mm
Condition of material / Quality: /

Dimensions:
Customer-Material-No.: /
Quantity / Weight: 6,040 KG / KG
Batch(es): 0090667629 6,040 KG 6,040 KG

GUARANTEED MECHANICAL REQUIREMENTS:
Yield Strength EN ISO 6892-1/Methode B: >590 MPa
Tensile Strength EN ISO 6892-1/Methode B: >680 MPa
Elongation EN ISO 6892-1/Methode B: >10,0 %
Hardness HV EN ISO 6507-1: 250 - 280

GUARANTEED CHEMICAL ANALYSIS: acc. to PAG-Spec. A001

Mo	min. 99,97 %*	Al	max. 10 µg/g	As	max. 5 µg/g
Ag	max. 10 µg/g	Ca	max. 20 µg/g	Cd	max. 5 µg/g
Ba	max. 5 µg/g	Cr	max. 20 µg/g	Cu	max. 20 µg/g
Co	max. 10 µg/g	K	max. 10 µg/g	Mg	max. 10 µg/g
Fe	max. 60 µg/g	Na	max. 10 µg/g	Nb	max. 10 µg/g
Mn	max. 2 µg/g	Pb	max. 10 µg/g	Ta	max. 20 µg/g
Ni	max. 10 µg/g	Zn	max. 10 µg/g	Zr	max. 10 µg/g
Ti	max. 10 µg/g				
W	max. 250 µg/g				
C	max. 30 µg/g	H	max. 10 µg/g	N	max. 5 µg/g
O	max. 40 µg/g	P	max. 20 µg/g	S	max. 10 µg/g
Si	max. 30 µg/g				

* metallic purity without W

СЕРТИФИКАТ № 469 ОТ « М. » 08 2002 Г.

№ заказа № 469 изделие 11002
ГОСТ, ТУ, ТТ 469-82 марка сплава 1100 размер (мм) 8.000.1000
состояние 11001 партия № 469 вес 450 кг.

РЕЗУЛЬТАТЫ ИСПЫТАНИЙ

№ партии	Механические свойства			
	Предел прочности при растяж. МПа (кг/мм²), не менее	Относительное удлинение, % не менее	Глубина выдвигания по Эриксену в мм	Удельное электросопротивление Ом мм²/м
469	470	46,5	47,5	

На основании осмотра поверхности, обмера и проведенных испытаний в соответствии с вышеуказанным УСТом, партия принята УП и СТП.
Химический состав соответствует ДСТУ ГОСТ 469-82 ТУ. У

Контролер продукции цветной металлургии склада плоского проката (подпись)

Штамп контролера продукции цветной металлургии склада плоского проката

Certified that the supplies/services detailed hereon have been inspected and tested in accordance with the conditions and requirements of the contract or purchase order and unless otherwise noted below, conform in all respects to the specification(s), drawing(s) relevant thereto.

This certificate has been generated by computer and need not to be signed for validity according to EN 10204.

PLANSEE Metall GmbH -
High Performance Materials
QM - Certificates

Figure 3.13: Certificates of the molybdenum (left) and of the copper (right)

Translation from Ukrainian manufacturer: OJSC “Artyomovsk non-ferrous metal processing plant”, Ukraine.

Alloy grade: M2. State: soft UTS = 230...234 MPa Elongation = 46.5...47.5%

Chemical composition is in accordance with GOST 859-2003: Cu ≥ 99.7%, Bi = 0.002%, Fe = 0.05, Ni = 0.2%, Sn = 0.05%, Sb = 0.005%, As = 0.01%, Pb = 0.01%, S = 0.01%, O = 0.07%.

The molybdenum plate was laser cut in accordance with the cutting scheme of Figure 3.14.

The standard settings for cutting pure molybdenum were applied in the settings of the laser cutting machine and the cut lines had a straight, flat and clean appearance.

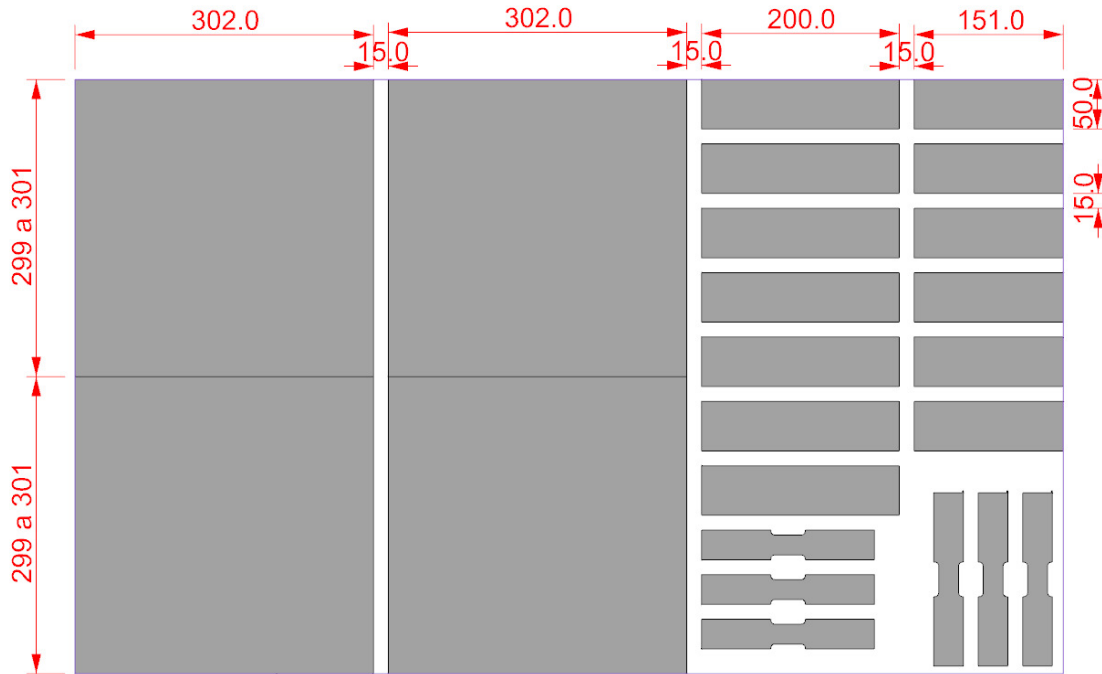


Figure 3.14: Cutting scheme of the molybdenum sheet. The rolling (longitudinal) direction is horizontal one, in the picture

The molybdenum was not provided with a mechanical test certificate, only with guaranteed minimum values. Therefore 3 specimens were cut in the rolling (longitudinal) direction and 3 specimens in transverse direction of the purchased sheet and tensile tested, see Figure 3.15.

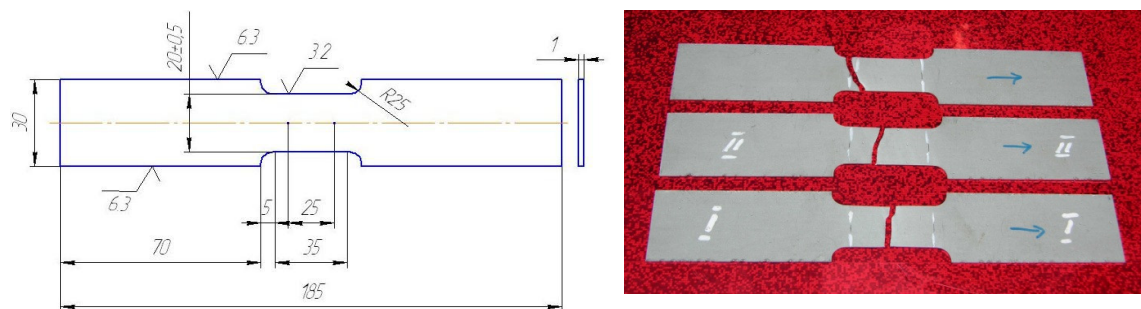


Figure 3.15: Dimensions and pictures of specimens for tensile test of the molybdenum sheet

The values obtained from the tensile tests on the molybdenum specimens are shown in Table 3.3.

Specimen label	Yield Strength (MPa)	Ultimate Tensile Strength (MPa)	Elongation (%)
Longitudinal-1	721,2	806,3	24,6
Longitudinal-2	744,5	784,5	27,1
Longitudinal-3	762,5	792,6	20,8
Transverse-1	755,4	811,7	18,3
Transverse-2	739,3	809,0	8,3
Transverse-3	721,2	789,9	24,2

Table 3.3 : Tensile test results on the purchased molybdenum sheet

The explosive welding parameters (mixture of explosives; height of explosive; temperature of molybdenum plate) were first checked on molybdenum plates of 200x50 mm. After a few tests the suitable explosives mixture, height and pre-heating temperature were determined and applied on plates of about 300x300 mm.

The molybdenum plate was heated by electric infrared radiators. The temperature of the molybdenum sheet was of about 200 °C at the explosion ignition. Since the heaters must be removed once the molybdenum reaches the required temperature, and then the explosive can be placed on it, a wide tolerance of $200 \pm 50^\circ\text{C}$ had to be accepted on the Molybdenum temperature. Further developments are possible for a better control of the temperature of the molybdenum sheet.

The 300x300mm plates were fixed by means of suitable equipment and milled in order to obtain the driver hole, with the required shape of the finger (see Figure 3.12)

The prototypes were formed by conventional pressing at $200 \pm 50^\circ\text{C}$. Figure 3.16 shows an axial-symmetric section of the press tooling and a picture of the formed part (cross section).

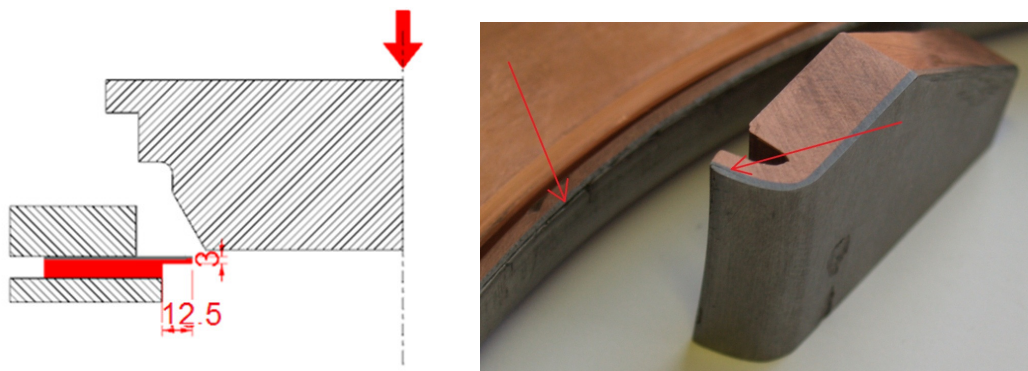


Figure 3.16: Press tooling used for forming the edge of the driver hole accordingly to the design of the Plasma Driver Plate (left) and picture of the formed part (right)

Delamination was found in the Mo layer, at the end of the overhanging, see the right picture in Figure 3.16. This was caused by cracks that were introduced during the machining process prior to forming.

Each formed plate was then flattened by pressing it in the 150 tons press. The flatness was measured and resulted to be lower than 2 mm.

It should be noted, that the elastic stresses will become out of balance when the grooves for the cooling channel will be machined. This has to be taken into account during the design of the whole manufacturing cycle of the PDP quarters.

The outer edges were finally cut (about 1 cm).

In Figure 3.17 the manufactured prototypes and samples during the first step of R&D activities are shown.

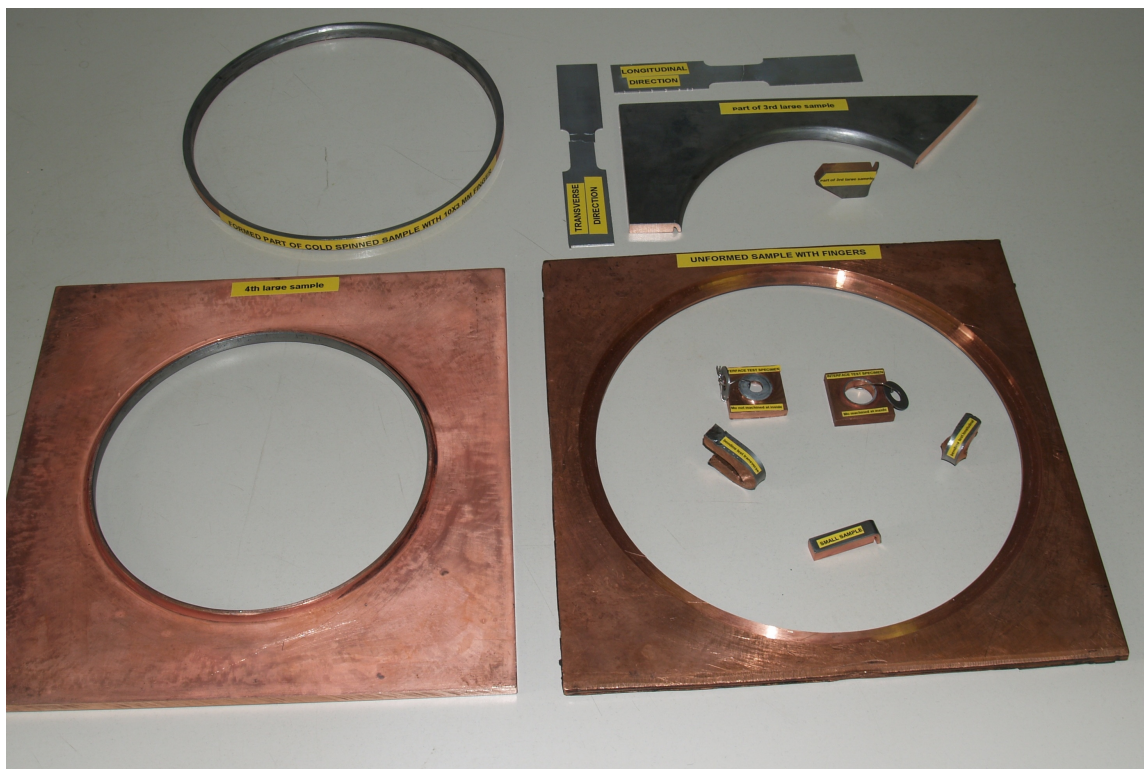


Figure 3.17: Picture of the Explosion Bonding manufactured prototypes and samples

3.3.1.3 Conventional tests on the EB samples

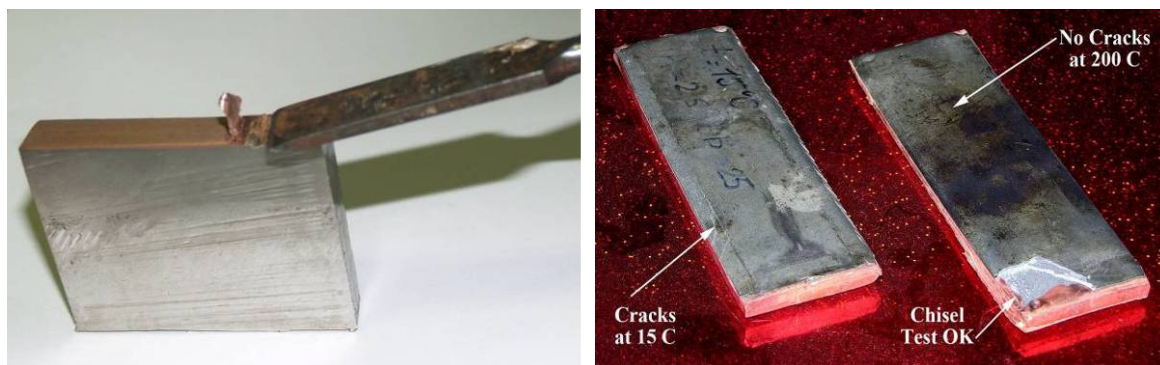
In order to investigate the quality of the interface between molybdenum and copper, a series of conventional test has been carried out on the manufactured samples; they are reported here after.

3.3.1.3.1 Chisel test

A so-called “Chisel Test” was performed for checking the quality of the bond. The test is accepted if the sample fails in one of the metals and not at the interface.

The chisel test was performed on a small sample (at room temperature) after each tentative of explosion bonding during the first stage of the activities, aiming at identifying the correct parameters for a successful cladding.

In Figure 3.18-a a picture explaining the chisel test is shown on the left; Figure 3.18-b shows a picture of the chisel test specimens as performed after bonding at 15 °C (left) and at 200 °C (right). From this test was possible to identify the temperature of the molybdenum sheet for a successful explosion bonding (200°C).



a – chisel test example

b - Picture of the chisel test specimens as performed after bonding at 15 °C (left) and at 200 °C (right)

Figure 3.18: Chisel test

3.3.1.3.2 Visual examination for cracks

The 300x300 mm bonded plates were inspected visually on the surface for cracks.

Figure 3.19 shows the plate with the rough appearance of the surface immediately after the explosion.

The appearance is from dirt that was removed. No cracks were found.

Cracks were instead visible on the specimen of Figure 3.18 (right) that was bonded with the molybdenum sheet at 15 °C.



Figure 3.19: Explosive bonded prototype. Note the unbounded center; this was the ignition point. The ‘flower-like’ appearance is from detonation products and was removed by cleaning

3.3.1.3.3 Bend test

Strips about 80 mm long and 8 mm wide were cut from explosive bonded samples in both longitudinal and transverse direction of the bare molybdenum.



Figure 3.20: Bend tests - the samples were 150° bent, without cracking.

A crack appeared in the transverse sample (right) after further bending, up to 180°

The strips were bent over a rod with a radius of 15 mm with the molybdenum on the outside. There were no cracks after bending 150°. After further bending, up to closure, a crack appeared in the sample with transverse direction, but not in longitudinal direction.

In Figure 3.20 the picture of the 2 strips, after the bend test are shown.

3.3.1.3.4 Microscopic examination

The shape of the interface indicates if the bonding is good. Figure 3.21 shows microscope picture of 3 samples that were explosive bonded under different process parameters.

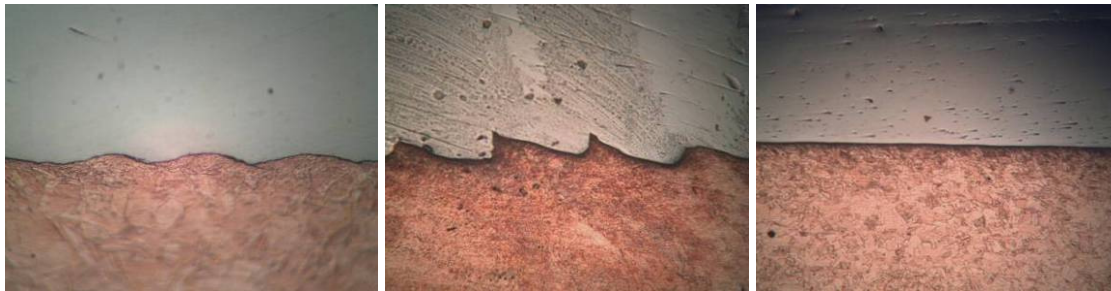


Figure 3.21: Microscope pictures of samples that were explosive bonded with different process parameters

Normally, the waves from the picture in the centre are optimal: waves with sharp tops but no vortices. Then the process parameters of this sample are applied to the plates of 300x300 mm. However, the shape appeared to be not critical because all 3 wave configurations passed the chisel test.

3.3.1.3.5 Interface tensile test

The company that produced the EB prototypes uses its own Interface Tensile Test method for quantify the interface bond strength. This method has already been used by the same company in the framework of other activities carried out for ITER.

In Figure 3.22 the schematic of the Interface Tensile Test method is shown. The (ultimate) tensile strength can be determined with the formula:

$$UTS = \frac{4 \cdot F}{\pi \cdot (D_o^2 - D_i^2)}$$

where D_o is the outer diameter at interface; D_i is the inner diameter at interface and F is the force applied to the specimen.

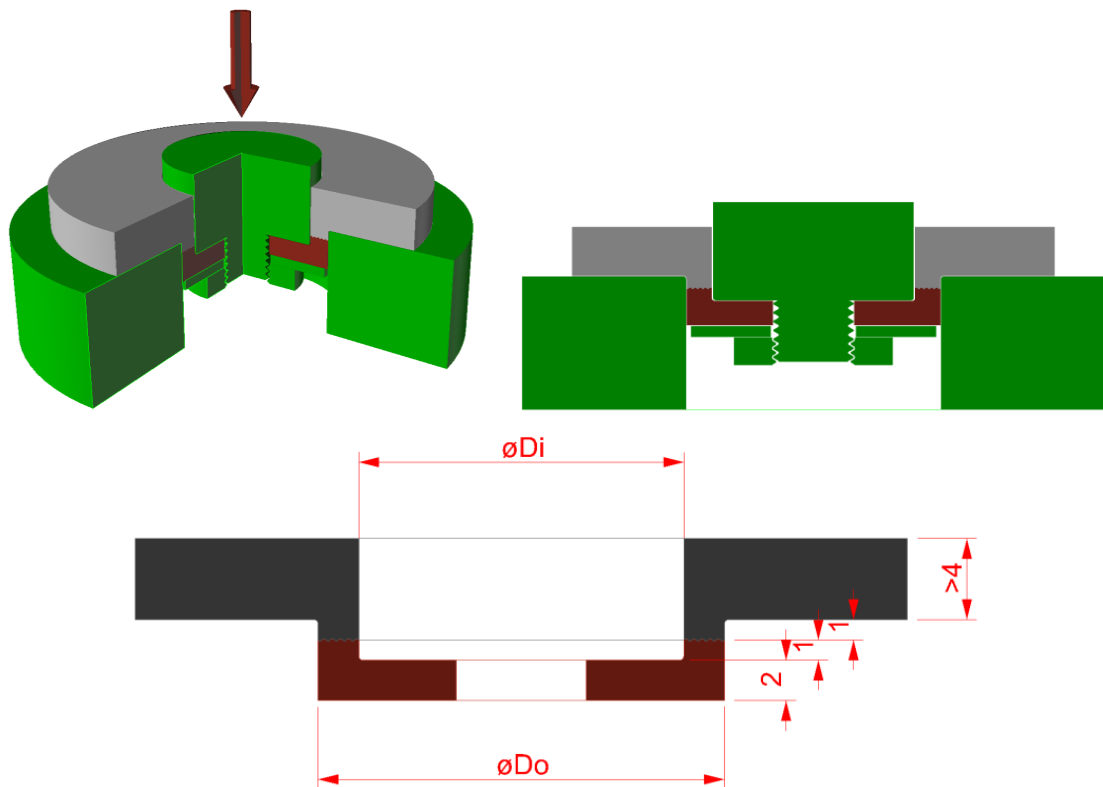


Figure 3.22: Schematic of the Interface Tensile Test method with main dimensions of the specimen

The tests were performed in 3 runs; the results of the tests are shown in Table 3.4

Run nr.	specimens	Ultimate Tensile Strength (MPa)	remarks
1	2	47,5 and 81,3 MPa	Cracks initiated due to machining
2	2	197 and 167 MPa	Copper not fully machined for avoiding crack initiation
3	1	135 MPa	From delivered sample

Table 3.4 : Results of Interface Tensile Test runs

The results showed a wide spread of values. This is coherent with the results of the tensile tests performed on the purchased molybdenum sheet (see Table 3.3), but it could also be due to the crack initiation, caused by the machining of the specimens; for this reason the specimens of the second and third runs show higher UTS values.

In Figure 3.23 some pictures of the interface tensile test specimens (before and after the test) are shown:

- on the left: 2 samples of the first test run; the copper was fully machined at the inside, up to discover the molybdenum;
- in the centre: one of the 2 samples of the second test run; a thin layer of copper was left on the molybdenum, on the inside, after the machining of the copper, in order to prevent crack initiation in the molybdenum itself;
- on the right: sample of the third run, after the test: the copper inside was machined as for samples of the second run, moreover the cylindrical surface on the outside, across the interface, was polished.

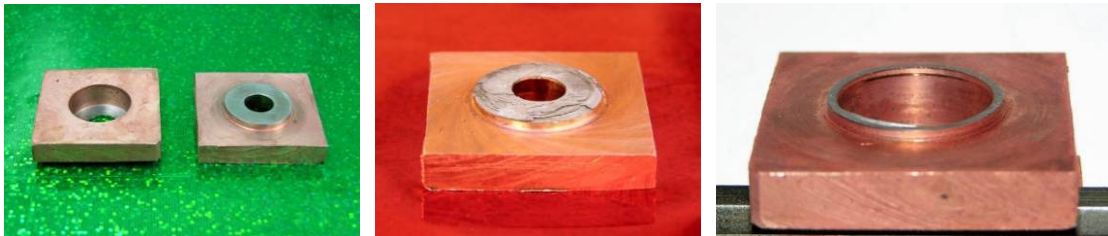


Figure 3.23: Pictures of the samples of the 3 runs of tensile tests

In the picture on the right in Figure 3.23 it is possible to check that the failure of the sample did not happen at the interface between the two metals, but inside the molybdenum, demonstrating that the interface is stronger than the molybdenum itself (at least in its thickness).

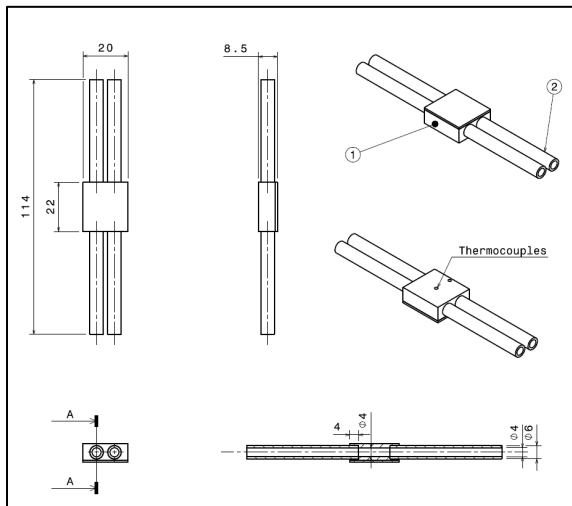
3.3.1.4 Thermal shock and fatigue tests on the EB sample

From the Finite Element (FE) analyses carried out during the design stage of the PDP, aiming to assess the interface stresses between copper and molybdenum, it clearly resulted that the mechanical resistance of the interface is seriously compromised by the highly localized, intense and cyclic heat loads given by the BSI+ (see Paragraphs 2.6.4 and 2.7.4).

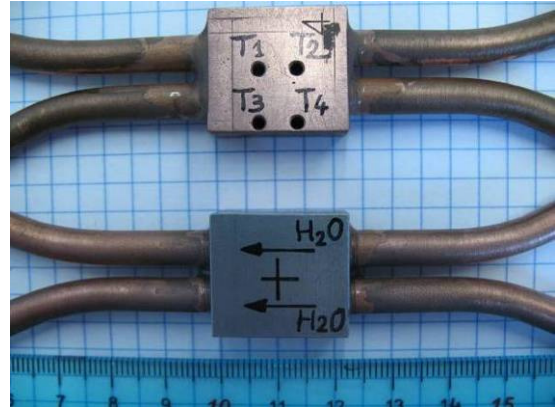
A set of thermal shock and thermal fatigue tests has been carried out on specimens manufactured from the EB samples, aiming at reproducing the MITICA loading and boundary conditions of the PDP in correspondence of one of the BSI+ beamlet impinging points.

3.3.1.4.1 Manufacturing of the test specimens

From one of the sample manufactured by EB during the first step of R&D activities, some pieces have been cut out and machined in order to obtain, at the end, 6 specimens as shown in Figure 3.24.



a – manufacturing drawing



b – photo of the specimens with indication of the water flow and of the temperature measuring points on the specimen

Figure 3.24 – Thermal tests specimens

The specimen dimensions are $22 \times 20 \times 9 \text{ mm}^3$ and they were drilled in order to be actively cooled. The dimensions were chosen in order to reproduce the pitch of the BSI+ impinging matrix: 20 mm horizontally and 22 mm vertically [16] [17].

Each specimen has 4 threaded holes on the back (copper side) for fixing thermocouples and measuring the temperature on the back of the specimen in two points (in between the holes, at the specimen central plane), with redundancy.

The 4 cooling pipes were fixed to the main body by means of a threaded joint and sealed with ARALDITE®.

The specimens were numbered progressively with numbers from 1 to 6.

3.3.1.4.2 Characterization of the TIG welding machine

The heating power, simulating the BSI+ impinging, was applied in the centre of the molybdenum face by means of the torch of a Tungsten Inert Gas (TIG) welding machine. The scope of the thermal shock and fatigue tests was to investigate and qualify the bond strength

between copper and molybdenum. The TIG welding machine was considered suitable for the application of the required heat load on the sample, since the evaluation of the physical and chemical effects of the impinging beam on the molybdenum surface (sputtering, blistering, etc.) was not within the objectives of this specific test. Since each of the 1280 BSI+ beamlets carries a power of about 800 W (see Paragraph 2.2.3, Figure 2.2), a characterization of the TIG machine has been carried out in order to assess the arc current needed for transferring to the target the required thermal load.

An inertial copper calorimeter (see Figure 3.25) has been manufactured and used as target for the mentioned characterization process.

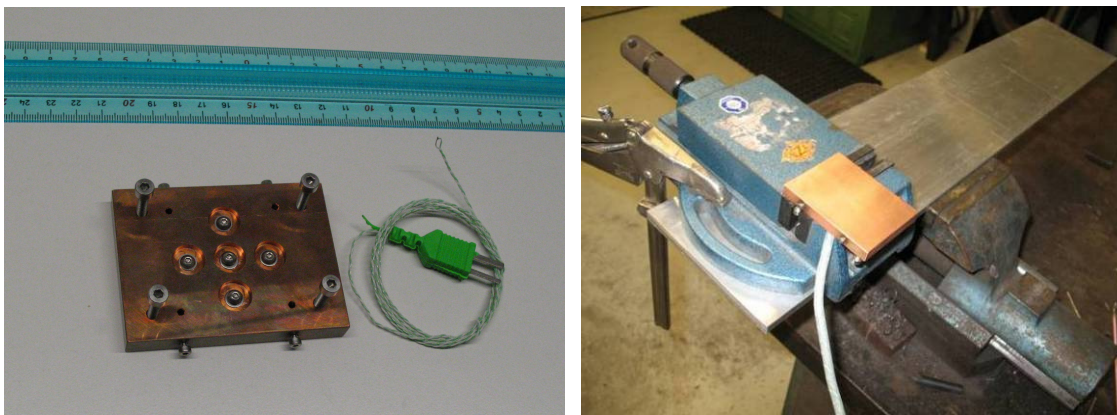


Figure 3.25 – Inertial calorimeter equipment used to characterize the TIG welding machine for tests

The calorimeter was equipped with 9 thermocouples type K. The procedure of characterization consisted in applying the arc to the calorimeter for a time of 30 seconds; in the meanwhile, and for the following 30 seconds, the temperatures measured by the 9 thermocouples were recorded. Since the mass of the calorimeter was known, measuring the stabilized temperatures, before and after each “shot”, and then calculating by difference the temperature growth of the calorimeter, due to the application of power, it was possible to calculate the energy given to the calorimeter. The power was then obtained dividing this energy by the arc application time (20 s). This kind of measurements was repeated for 20 times with arc current varying in the range 70÷150A and the results were plotted together in a graph in order to obtain, by linear interpolation of the data, the relation between the applied current and the resulting heat power transferred to the calorimeter.

The characterization of the welding machine allowed to quantify the total power transferred by the arc to the calorimeter as function of the arc current, but it was not possible to quantify

exactly the maximum of the power density and its distribution. It was not possible, in fact, to calculate, nor measure it.

In Figure 3.26 the plots of the temperatures recorded during one characteristic shot and the final graph, resuming the results of the characterization process are shown.

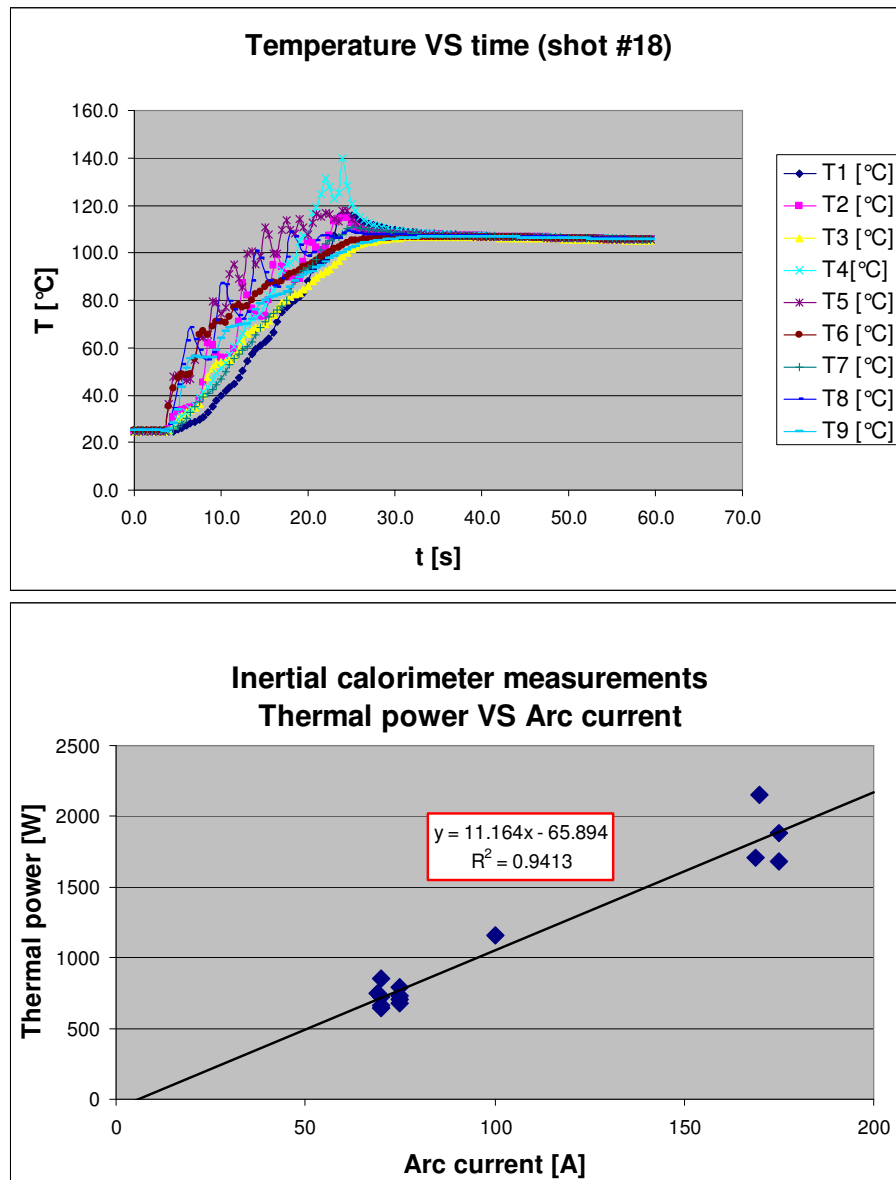


Figure 3.26 – Heat power VS arc current characteristic of the TIG welding machine used for tests

3.3.1.4.3 *The set up of the equipment*

The decision to actively cool the samples during the test came from two main reasons:

1. to guarantee thermal gradients, in particular above the interface zone, similar to the actual ones, in the RF source components, under the BSI+ impinging point;
2. to speed-up the test, in particular for the thermal fatigue test.

The ICE (Insulating Cooling Experiment) [57] plant was considered suitable for circulating the cooling water for the tests. It is equipped with cooling water temperature sensors (thermocouples and PT100 resistance thermometers), an heat exchanger for the regulation of the temperature in the circuit, pumps with inverters for regulating the water mass flow rate and an acquisition system for (up to 10) thermocouples type K that can be applied on the samples under test.

For the thermal fatigue tests, the need to have a remote and automatic control of the TIG welding machine was recognised to be necessary. The system controlling the ICE plant was modified in order to be integrated with the direct control of the welding machine. The machine itself was modified and the command for the arc (ON/OFF) was integrated in the main ICE plant user interface. Another feedback control was added for safety reasons: a current measurement was installed on the TIG torch cables and its measure was integrated in the ICE control system. In this way it was possible to set up a cross-check able to switch off the whole plant in case the arc was commanded, but not detected for 3 consequent times. The same measurement was also used for counting the actual number of successful pulses performed on the sample.

Thanks to this integration, it was finally possible to set the number of pulses (arc ON/OFF) on a desk added to the ICE main user interface and to record the number of actual performed pulses and the temperatures in real-time.

The TIG torch and the sample were kept, during the test, by a structure that was enclosed inside a Plexiglas box; the scope of the box was to assure a proper atmosphere during the test, preventing the oxidation of the molybdenum, and to easy-up the arc ignition. The box was in fact fed with an Argon flux (in addition to the TIG torch one) sufficient to keep it continuously, slightly in overpressure. In Figure 3.27 the equipment that has been set up for the tests and one of the specimens, fixed inside it, are shown.

In order to get a value of the Convective Heat Transfer (CHT) coefficient comparable to the ones within the PDP cooling channels (around $55000 \text{ W}/(\text{m}^2 \cdot \text{K})$), the desired value of the water velocity inside the specimen drilled channels was 9 m/s (see Paragraph 2.3), but, due to the excessive pressure drop within the tubes connecting the specimens to the ICE plant, the water

mass flow rate during tests was set to 0.1kg/s with a consequent water velocity inside the sample channels of 4.0 m/s. Hence, the CHT coefficient in the channels of the specimens was lower, around $22000 \text{ W}/(\text{m}^2\cdot\text{K})$, with a consequent higher temperature on the specimen.

4 thermocouples type K were fixed to the specimen main body during both the thermal shock and thermal fatigue tests by means of TEFLON® M2 screws in the position shown in Figure 3.24b and Figure 3.27b (temperature labels T1÷4). Other 2 thermocouples were fixed on the 2 copper tubes downstream the specimen, with respect to the flowing water direction, for measuring the “mean” water temperature at the exit of the specimen (temperature labels T6 and T7). Another thermocouple was fixed on one of the copper tubes at the entrance side for measuring the inlet water temperature (Figure 3.27b, temperature label T5)

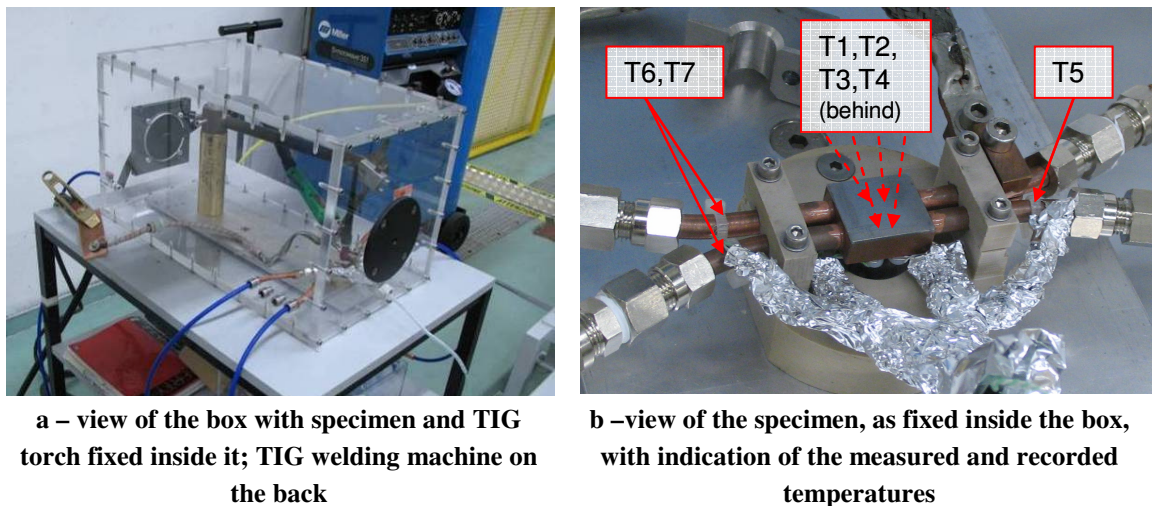
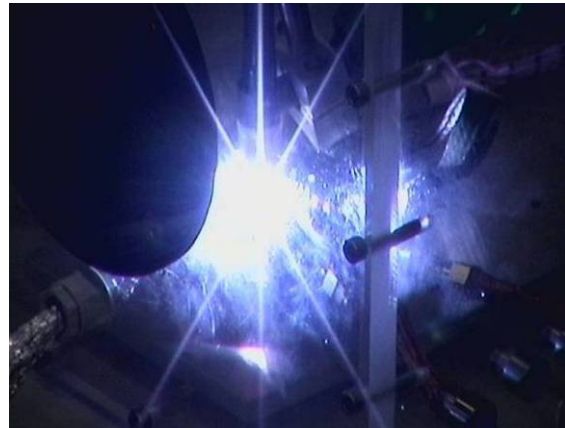


Figure 3.27 – Thermal tests set up equipment

Since the fatigue tests require a long operation time, a remote controllable video-camera was used to have a remote visual control of the operation, via web access. In Figure 3.28 a photo of the camera, installed in the ICE room roof (a) and a screen-shot taken remotely during the tests (b) are shown. Another remote control was possible by checking the main parameters, like temperatures and mass flow rate, in real time, through the “j-Scope” application. In Figure 3.29 a screenshot taken during one of the fatigue tests is shown: if some of the parameters have anomalous behaviour, they can be immediately detected. In the figure the temperatures recorded by the 7 thermocouples applied to the sample are shown, together with the mass flow rate. The time scale is so large in Figure 3.29 that the trends appear as a black band: see Figure 3.34 for having clear understanding of the temperature trends for some shots.



a – view of the video-camera installed on the roof of the ICE room



b –screenshot taken from the monitor

Figure 3.28 – Video-camera used for the remote visual control of the (fatigue) tests

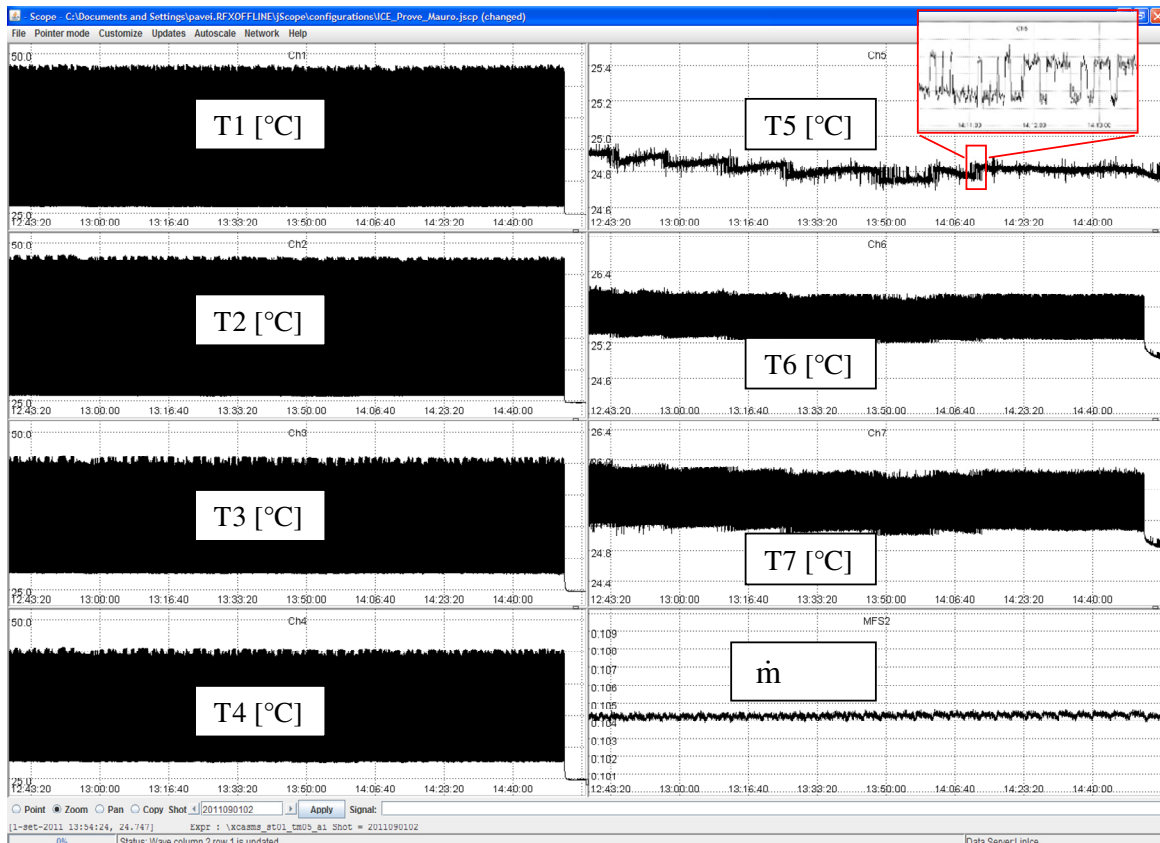


Figure 3.29 – Example of temperatures and mass flow rate recorded during thermal shock tests (see Figure 3.27 for indication of the measuring points on the specimen)

3.3.1.4.4 Issues raised during the set up of the equipment

During the set-up of the facility some issues raised when, for the fatigue tests, on the TIG welding machine the “high frequency mode” was activated. This option allows the arc to initiate between the torch electrode and the piece without the need that two parts come in contact; this is allowed by a high frequency alternate voltage superposed to the continuous nominal one. In order to carry out the fatigue tests, this high-frequency mode was absolutely necessary, but the high frequency caused interferences with the ICE plant electronic equipment and the consequent shutdown of the plant (due to the intervention of the protections). Different possible solutions were tried and the problem was strongly reduced by changing the path of the cables that connected the thermocouples applied to the specimens to the temperature acquisition system, placing them in other cable-trays, in order to separate them from the other ICE signal cables that are instead directly connected to the PLC of ICE. The problem of the interference was however not completely solved in this way and it was finally necessary to exclude the ICE protections.

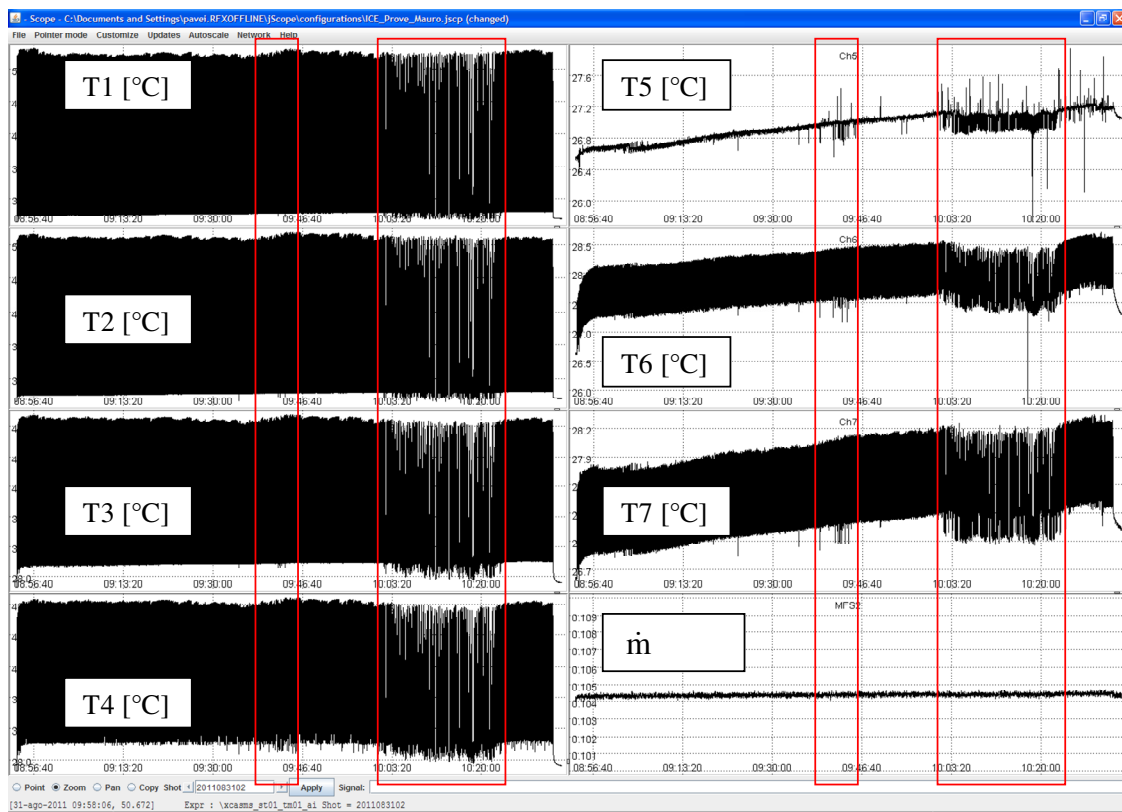


Figure 3.30 – View of one of the shots (1000 pulses, 3s ON / 3s OFF, 75A) showing errors and spikes caused by the use of the high frequency mode of the TIG welding machine during the test

In Figure 3.30 one of the fatigue test shot (of 1000 pulses) that presented the problem of high frequency interferences is shown: the interferences caused random errors, spikes, and small shifts of the temperature trend (like the one highlighted on the top-right corner of Figure 3.29).

The “affected” period is enclosed in the red rectangles. In the figure it can be recognized that all the temperature measurements taken on the specimen are affected by the interferences, but not the mass flow rate measurement.

3.3.1.4.5 The calorimetric measurements performed on the facility

Before starting the tests, calorimetric measurements were repeated, using, this time, the temperature measurements taken:

- on the sample: temperature T5 was taken on one inlet tube (see Figure 3.27b); the thermocouple was fixed using a plastic strap on the outside of the tube at about 10mm from the sample main body; T6 and T7 were taken instead on the exit tubes (two measurements were needed in order to take the average value between them);
- on the ICE plant: two PT100 temperature sensors are placed, one at the inlet and one at the outlet, at about 2,0 m from the sample.

Assuming the system adiabatic, the total heat power given to the sample by the arc is equal to the power received by the water. This is true in steady state conditions, but also over a time window including a set of beam ON –beam OFF cycles; in this case it is important to take some seconds of margin after the last pulse.

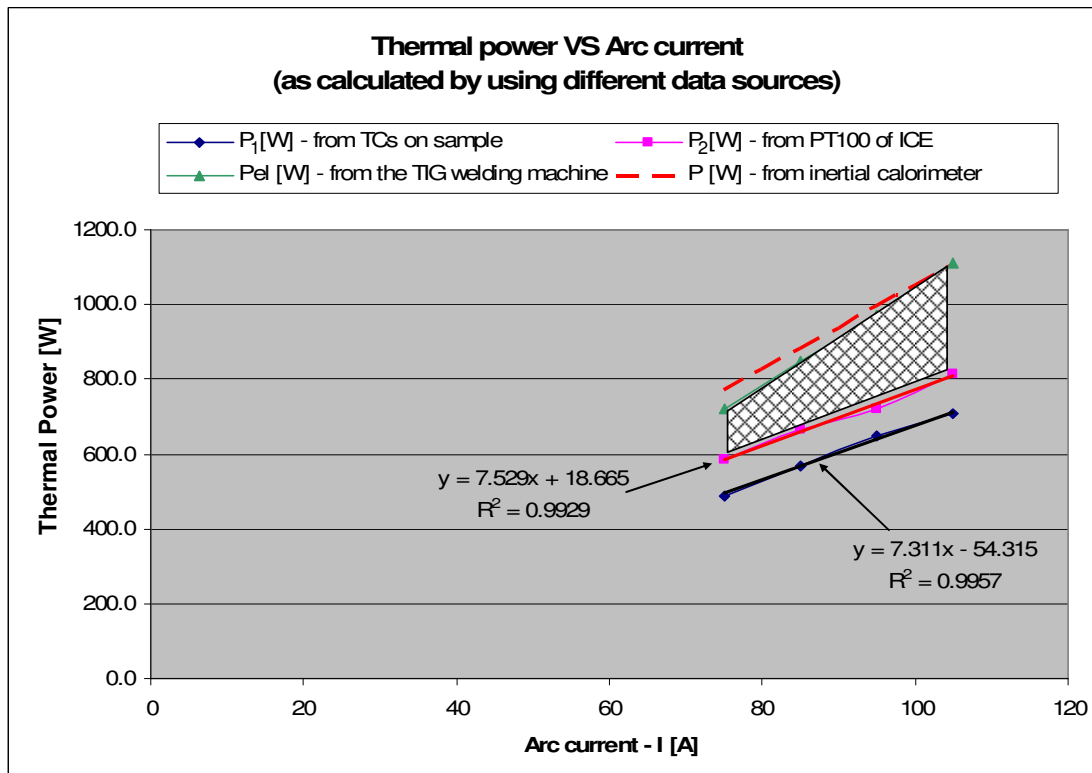


Figure 3.31 – Heat power VS arc current characteristic of the TIG welding machine used for tests calculated by using the different methods

By comparing the results obtained using the temperature T5, T6, T7 on the sample (P_1), with the ones coming from the direct temperature measurements, inside water, of the PT100 of ICE (P_2), a not negligible disagreement can be noted: the power P_2 is constantly higher than P_1 of 10 to 20% (see Figure 3.31). No clear reason was found to explain this incoherence between the two approaches, despite it is probable that the temperatures T5, T6 and T7 are affected by an error due to the fact that their contact pressure towards the copper tube is non controllable and the contact take place in a very restricted area. Since the temperature rise during the test is of about 1.2°C, even a small error in the temperature measurements can cause a relatively high error in the heat power calculations. For this reason it was decided, at the end, to consider more reliable the measurements taken by the PT100, since they are directly placed inside the flowing water. In Figure 3.31 the results obtained by the calorimetric calculations carried out using the described different data sources are shown; in the graph, also the results coming from the previous tests with the inertial calorimeter are shown (in red, dashed line).

Since part of the heating power is lost by radiation towards the environment (the molybdenum surface reaches very high temperatures during the pulse), it is reasonable that the power measured by calorimetry under-estimates of the actual value received by the sample in the arc impinging point. This is why it is possible to say that the actual heat power transferred to sample, in function of the arc current, is enclosed in between the two lines that represent the thermal power calculated by calorimetry using the PT100 sensor temperature measurements (Pt – ICE) and the electrical power delivered by the TIG welding machine (P_{el} – TIG). In Figure 3.31 this “working area” is highlighted by the patterned trapezium.

In Table 3.5 the minimum (Pt – ICE) and maximum (P_{el} – TIG) values of the range inside which the actual value of the power transferred to the sample in function of the arc current (I), are shown.

I [A]	P_2 – ICE [W]	P_{el} – TIG [W]
75	583	718
80	621	783
85	659	848
90	696	913
95	734	978
100	772	1043
105	809	1108
110	847	1173
115	885	1238

Table 3.5 – Thermal shock tests resuming table

3.3.1.4.6 Thermal shock tests

The thermal shock tests had the aim of verifying the capability of the interface between molybdenum and copper to withstand the stresses caused by the different thermal expansion of the two materials.

These tests were performed prior to integrate the control of the TIG welding machine in the ICE control system. It was decided to verify, in advance, that the interface could withstand the thermal shock for some pulses and then go on completing the whole set up for the fatigue tests, as described in paragraph 0.

The thermal shock tests were successfully performed on 3 samples (numbers 1, 2, 4). The main data related to the pulses performed on the three specimens are presented in Table 3.6.

In Figure 3.32 an extract (for a time-window of few seconds) of the temperatures ($T1 \div 7$) and mass flow rate (\dot{m}) recorded during one of the shots at 75 A of arc current is shown

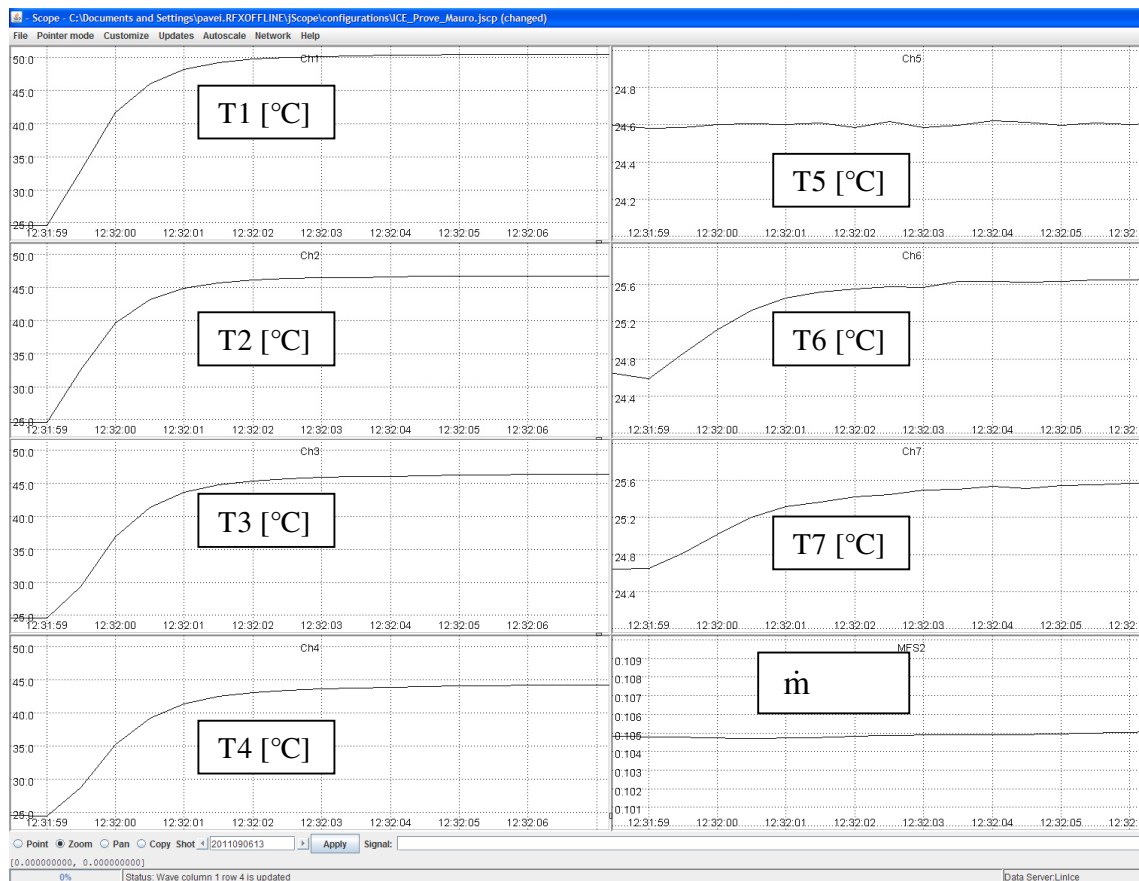


Figure 3.32 – Example of typical temperatures and mass flow rate trends recorded during one thermal-shock test shot (Arc current = 75 A)

Shot #	Time	Current [A]	Pulse duration [s]	Reference filename	Notes	mass flow rate [kg/s]
Sample number 1						
1	16.26.00	50	5			Q=0.05 kg/s
2	16.31.25	50	10	20110505_003.txt		
	16.32.10	50	10			
	16.34.20	50	10			
	16.34.46	50	10			
3	16.35.17	50	10	20110505_004.txt		
	16.37.30	75	10			
	16.38.19	75	10			
	16.38.50	75	10			
4	16.39.20	75	10	20110505_005.txt		
	16.42.40	75	10			
	16.43.07	75	10			
	16.44.03	75	10			
5	16.44.37	75	10	20110505_006.txt	Cleaning of the sample surface	
	16.54.32	75	60			
	16.58.08	75	60			
6	17.04.31	75	60	20110505_007.txt		
	17.14.40	100	60			
	17.18.11	100	60			
7	17.24.11	100	60	20110505_008.txt		
	17.30.38	150	60			
	17.33.14	150	60			
8	17.35.29	150	60	20110505_009.txt	Apparence of deep melting of the molybdenum surface Surface melting Surface melting	
	17.41.10	200	60			
	17.44.29	200	60			
	17.47.00	200	30			
Sample number 2						
1	9.29.03	75	30	20110506_001.txt		Q=0.1 kg/s
	9.29.54	75	30			
	9.30.44	75	30			
	9.32.57	75	30			
	9.34.32	75	30			
	9.36.02	75	30			
	9.37.20	75	30			
Sample number 4						
2	11.26.58	75	30	20110506_002.txt		Q=0.1 kg/s
	11.28.45	75	30			
	11.30.16	75	30			
	11.31.31	75	30			
	11.33.04	75	30			
	11.35.05	75	30			
	11.37.21	75	30			
	11.51.24	75	30			
	11.54.14	75	30			
	11.55.17	75	30			
3	11.58.00	150	30	20110506_003.txt		
	12.00.48	150	30			
	12.02.10	150	30			
	12.03.24	150	30			
	12.04.32	150	30			

Table 3.6 – Thermal shock tests resuming table

After each pulse the molybdenum surface was checked by visual inspection. In Figure 3.33 the molybdenum surface appearance of the 3 specimens tested to thermal shock is shown. Significant (even if limited) surface melting appeared on specimens number 1 and 2. In specimen number 1 melting was recognisable after shots of set #8, with arc current of 200 A, that means thermal power of 2,15 kW (about 2.7 times the one expected in MITICA). The same was confirmed by specimen 4: significant local melting is not evident on the molybdenum surface with shots at current up to 150 A (thermal power of 1.6 kW, about twice the one

expected in MITICA). Only sample number 2 shows some local melting of the molybdenum surface, even if it was exposed only to seven shots with the arc current of 75 A, correspondent to the expected thermal power. Even if the damage found on the surface is not worrying, the anomalous behaviour of sample number 2 is currently being investigated: it could be caused by the presence of local discontinuities in the molybdenum thickness or at the interface.

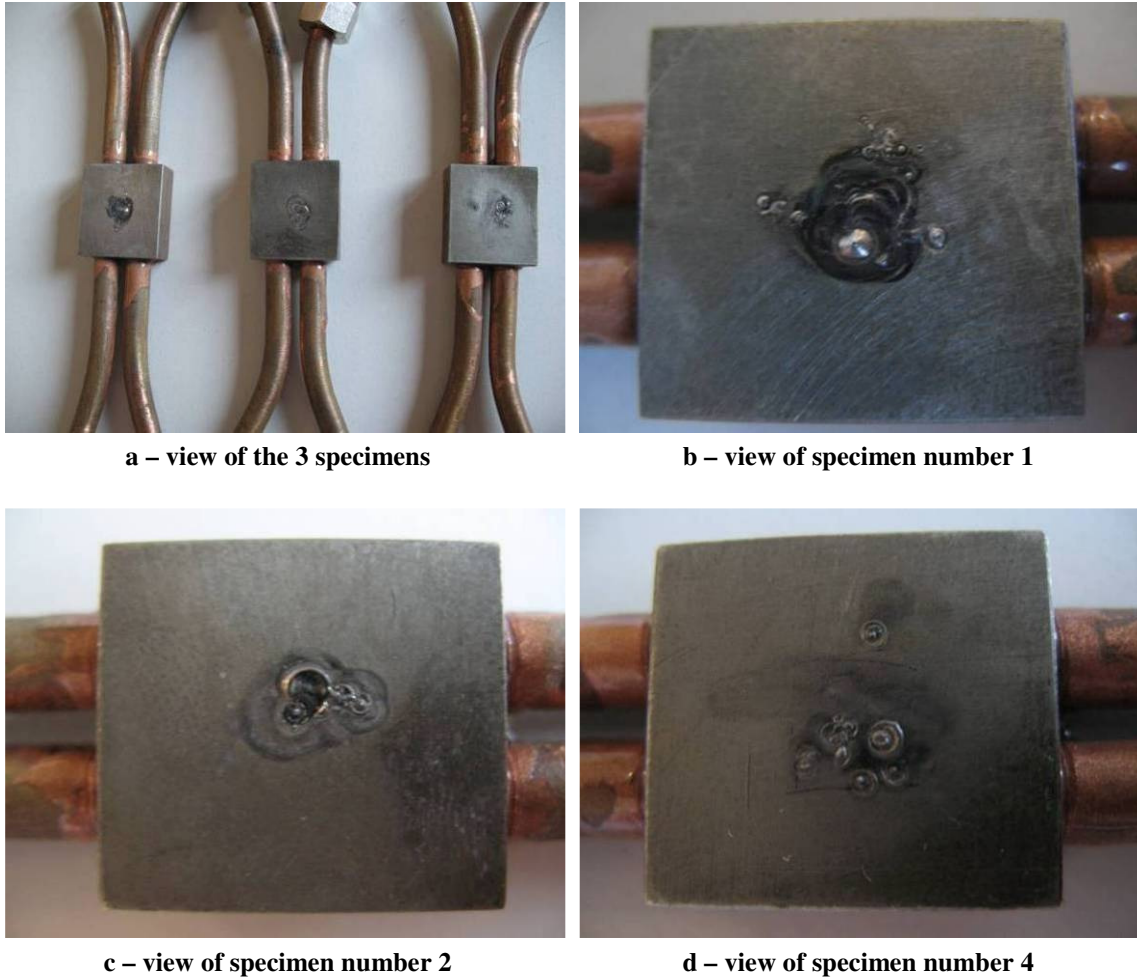


Figure 3.33 – Views of the thermal shock tested specimens after the test

After the test, no macroscopic delamination, nor flaking were found on the specimens. Local melting appeared on the surface, but it is localized and it becomes deep (some tenths of millimetre) only with arc current over 150 A.

The thermal shock test on the 3 specimens was successfully passed; as consequence it was decided to go on with the thermal fatigue tests

3.3.1.4.7 *Thermal fatigue tests*

The thermal fatigue tests had the aim of verifying the capability of the interface between molybdenum and copper to withstand a high number of heating-cooling cycles as it is expected on the Plasma Driver Plate component in MITICA and the future ITER HNB, where 50000 beam-ON/OFF cycles and 450000 breakdowns are foreseen (Paragraph 2.4.2).

After the completion of the set-up of the equipment (integrating the welding machine in the ICE control system, as described in Paragraph 0), the thermal fatigue test was carried out on 2 samples: numbers 5 and 6.

The time-variant Finite Element analyses carried out in Paragraph 2.6 show that the molybdenum-to-copper interface reaches the steady state temperature in less than 1 second. The temperatures recorded during the thermal shock tests, on the copper side of the specimen, had instead a time constant of about 3 seconds, but the measured points were far from the application point of the heating power (see Figure 3.32).

Since the arc ignition of the TIG welding machine is not immediate and sometimes it takes some tenths of second, it was decided to set to 3 seconds the pulse duration and 3 seconds the pause between a pulse and the following one. In this way it was guaranteed that the temperature and the stresses at the interface between the two metals reached the steady state conditions and, at the same time, the duration of the test was acceptable and in the availability time of the ICE plant for the purpose, it was possible to expose 2 specimens to 15000 pulses.

In Figure 3.34 an extract of the temperatures and mass flow rate recorded during the thermal fatigue tests, similar to the one of Figure 3.32, is shown. The inlet water temperature was quite constant around $\approx 25^{\circ}\text{C}$.

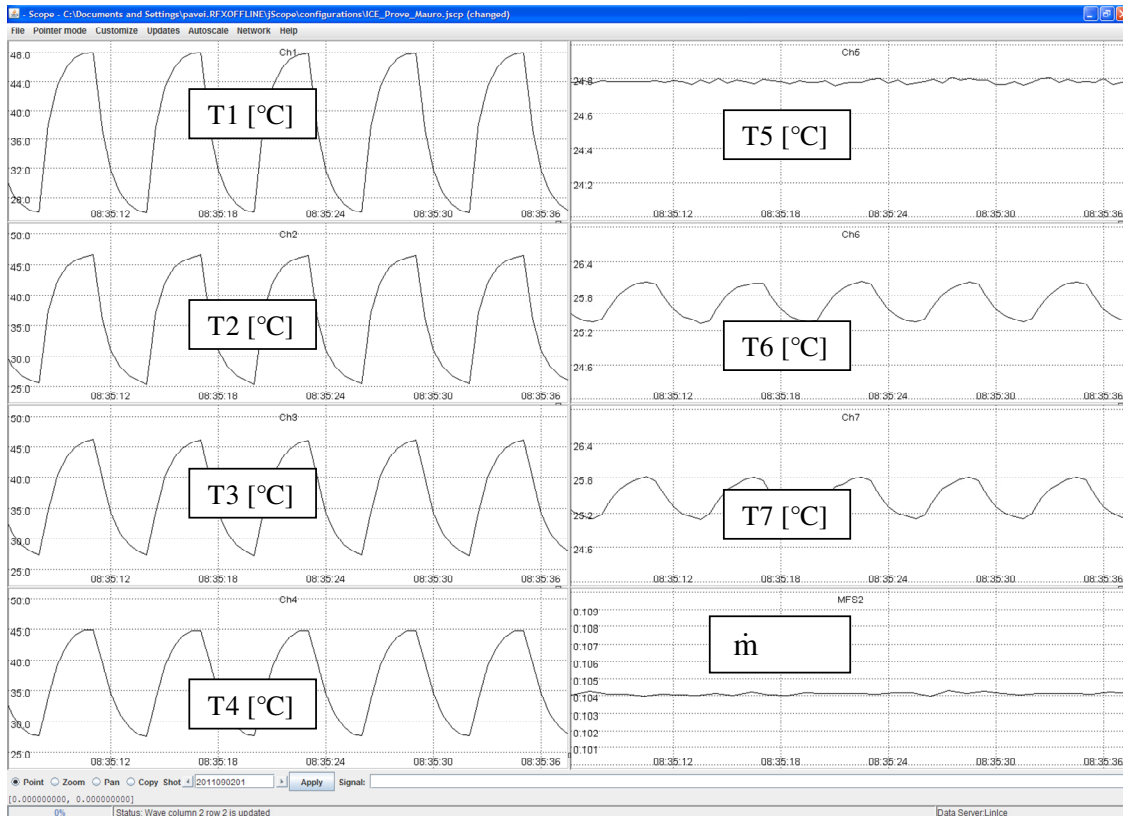


Figure 3.34 – Example of typical temperatures and mass flow rate trends recorded during one thermal fatigue test shot (3s ON / 3s OFF, 75A)

3.3.1.4.7.1 Thermal fatigue test on specimen number 5

Sample number 5 was exposed to a total of 15000 pulses. The data related to the thermal fatigue test on sample number 5 are shown in Table 3.7. All the pulses were performed with arc current of 75 A (actual thermal power to the sample in the range 580÷720W), pulse duration (Beam ON) of 3 s, and pause between consecutive pulses (Beam OFF) of 3 s.

Reference shot number	Current [A]	Beam ON time [s]	Beam OFF time [s]	Initial pulse number	Final pulse number	electrode - sample distance [mm]	Notes	mass flow rate [kg/s]
Sample number 5								
2011082901	75	3	3	1	500	1.0		Q=1.05 kg/s
2011083001	75	3	3	501	1000	1.0		
2011083002	75	3	3	1001	1500	1.0		
2011083003	75	3	3	1500	2000	1.0		
2011083004	75	3	3	2001	2353	1.0	shot interrupted for renewing the TIG torch electrode tip	
2011083005	75	3	3	2354	2648	1.0		
2011083006	75	3	3	2649	3000	0.8	reduced distance between electrode and sample surface	
2011083007	75	3	3	3001	3500	0.8	change of the TIG torch nozzle	
2011083101	75	3	3	3501	4500	0.8		
2011083102	75	3	3	4501	5000	0.8		
2011083103	75	3	3	5001	7000	0.8		
2011083104	75	3	3	7001	8000	0.8		
2011090101	75	3	3	8001	10000	0.6	reduced distance between electrode and sample surface	
2011090102	75	3	3	10001	13000	0.6		
2011090201	75	3	3	13001	15000	0.6		

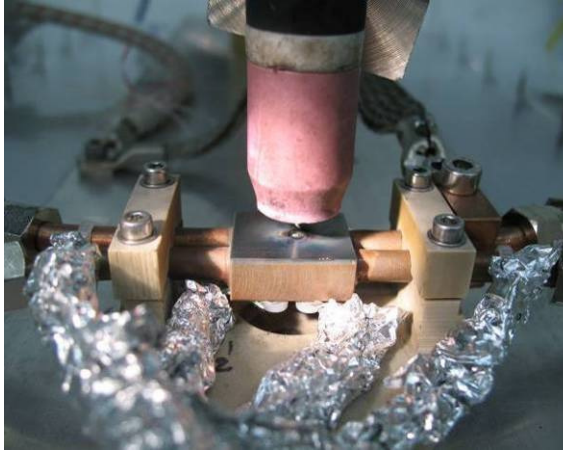
Table 3.7 – Thermal fatigue test parameters for sample number 5

The temperature and mass flow rate were monitored during the test and showed trends similar to the typical ones of Figure 3.34.

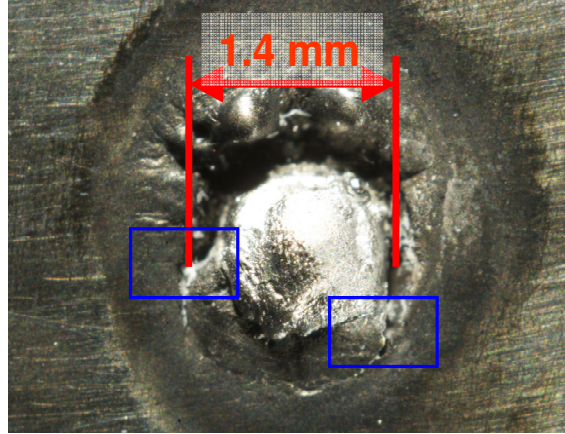
In Figure 3.35 some photos of sample 5 after the fatigue test are shown.

The heat affected area has a diameter of about 3 mm, whereas the real damaged zone is even more restricted. This area appears “recrystallized”, and a crack is visible all around it.

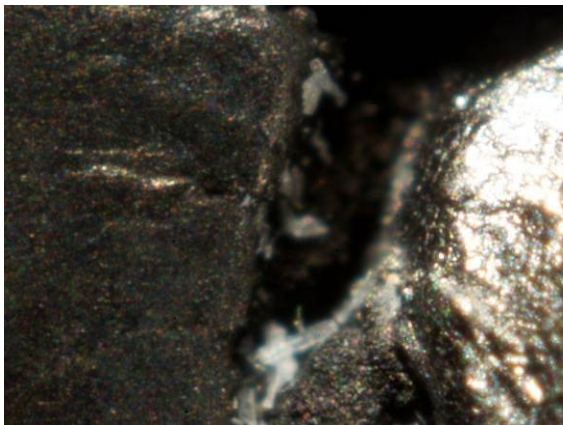
Since no delamination occurred, the result of the thermal fatigue test on sample number 5 is satisfying.



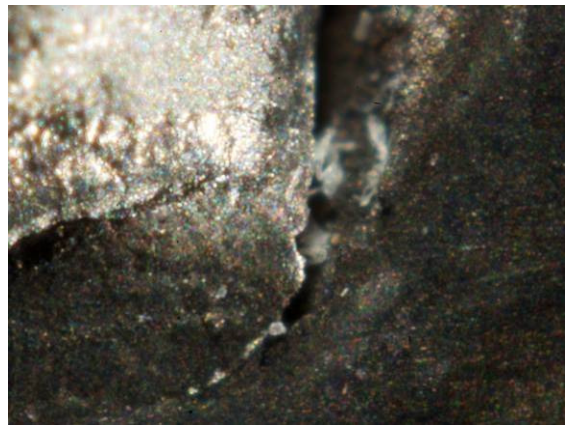
a – view of the specimen after pulse 15000



b – view of the heat power application point of specimen number 5, after 15000 pulses



c – zoom view of the area in the left rectangle of window b in this figure



d – zoom view of the area in the right rectangle of window b in this figure

Figure 3.35 – Pictures of the thermal-fatigue tested specimen number 5

3.3.1.4.7.2 Thermal fatigue test on specimen number 6

Sample number 6 was exposed to a total of 15469 pulses; the test was planned to go on till 20000 pulses, but an anomaly obliged to stop the test.

The data related to the thermal fatigue test on sample number 6 are shown in Table 3.8:

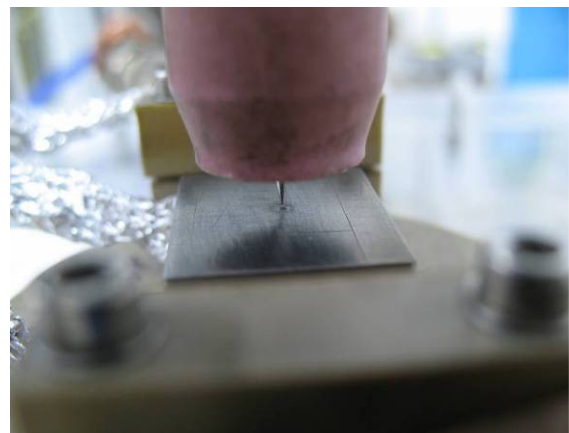
Reference shot number	Current [A]	Beam ON time [s]	Beam OFF time [s]	Initial pulse number	Final pulse number	electrode - sample distance [mm]	Notes	mass flow rate [kg/s]
Sample number 5								
2011090501	75	3	3	1	1290	0.6		Q=1.05 kg/s
2011090502	75	3	3	1291	2500	0.6		
2011090503	75	3	3	2501	4000	0.6		
2011090601	75	3	3	4001	6500	0.6		
2011090602	75	3	3	6501	9000	0.6		
2011090701	75	3	3	9001	10000	0.6		
2011090702	100	3	3	10001	10150	0.6	interrupted for interferences on the temperature acquisition system	
2011090901	115	4	4	10151	11332	0.6		
2011090902	115	4	4	11333	12500	0.6		
2011090903	115	4	4	12501	13500	0.6		
2011091201	115	4	4	13501	15469	0.6	test interrupted for anomaly	

Table 3.8 – Thermal fatigue test parameters for sample number 5

After the first 10000 pulses at 75A (580÷720W) the sample molybdenum surface was checked and found just a little bit “eroded”, but not damaged, so it was decided to increase the arc current to 115A (885÷1240W), after just few pulses at 100A (740÷1050W) in order to perform an intermediate check. In Figure 3.36 a couple of photos of sample number 6 after 10000 pulses at 75A are shown.



a – view of the specimen after pulse 15000



b – view of the heat power application point of specimen number 5, after 15000 pulses

Figure 3.36 – Views of the thermal-fatigue tested specimen number 6 after 10000 pulses at 75A arc current, 3s ON / 3s OFF

After further 3500 pulses with arc current at 115A (with pulse duration and pause extended to 4 seconds in order to let the sample reaching the steady state conditions) a sort of “hole” was visible on the molybdenum, with consequent direct view on the copper subplate. This hole has very little diameter, of about $0.7\div 0.8$ mm, measured on the photos presented in Figure 3.37.

Since the ICE plant was available for further 2 days it was decided to go on with the test, with the goal of reaching 20000 pulses, but the TIG torch was moved of about 3 mm, in order to change arc application point.

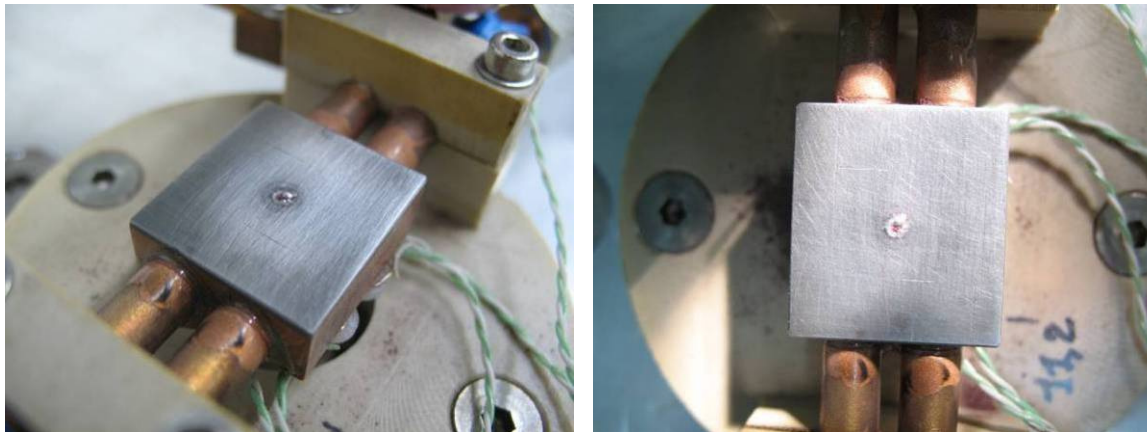


Figure 3.37 – Views of the thermal-fatigue tested specimen number 6 after 10000 pulses at 75 A arc current, 3s ON / 3s OFF and 3500 pulses at 115 A, 4s ON / 4s OFF

During the following shot on sample number 6, around pulses 14500÷15000, the temperature trends started to show, anomalous behaviour, as showed in Figure 3.38: the red rectangle indicates the start of some anomaly that was identified, but not considered dangerous, since it stabilized soon and no visible effects were visible on the specimen molybdenum surface. The blue rectangle shows, instead, the evolution of the anomalous behaviour of the system that obliged to interrupt the test at pulse number 15469.

The test was then interrupted and anomalous damage on the sample surface was recognized. In Figure 3.39 a view of specimen number 6 before the last set of pulses (after pulse number 13500) is shown (a) together with the view of the same sample after the “fault” (b).

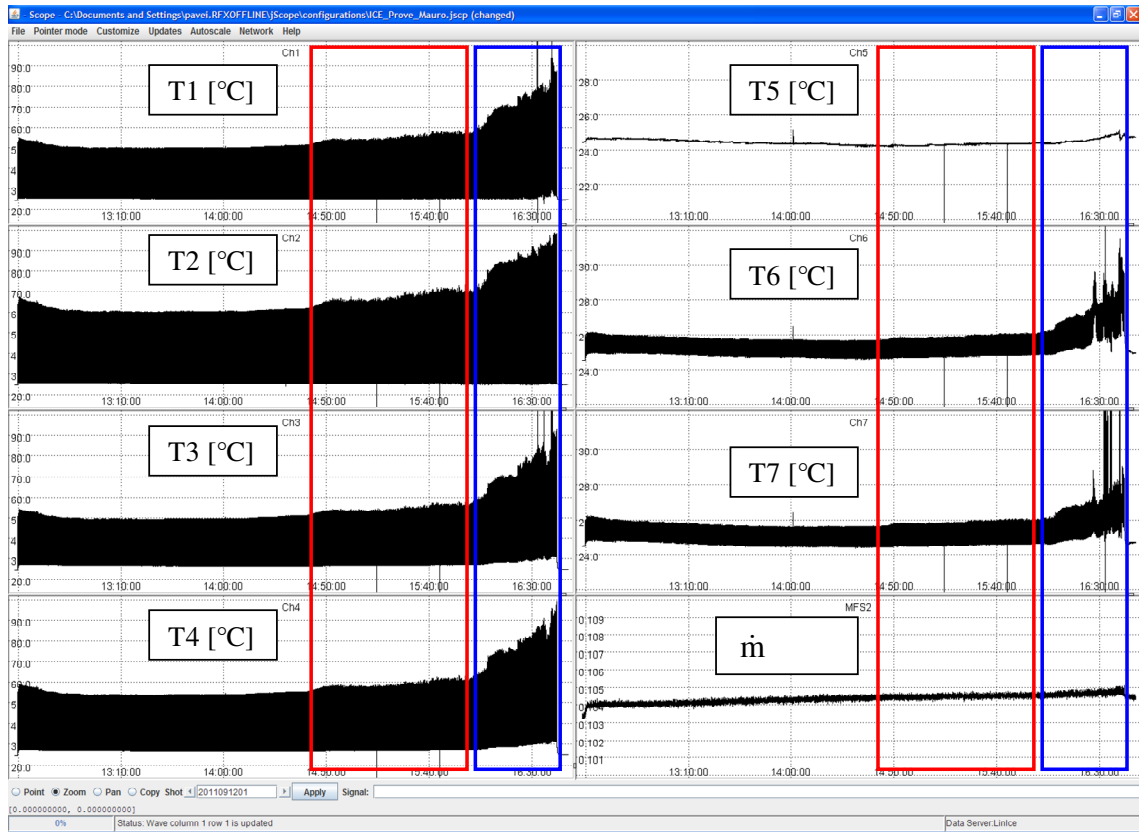
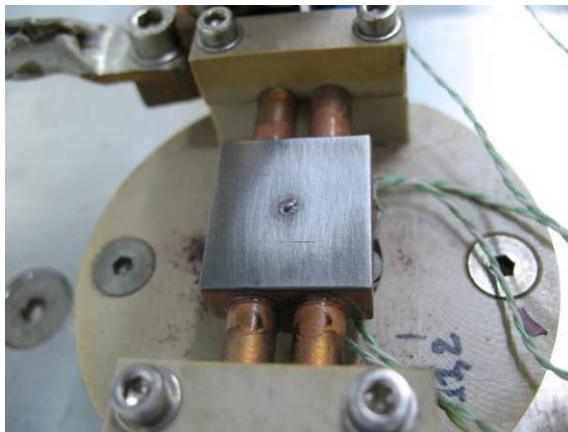
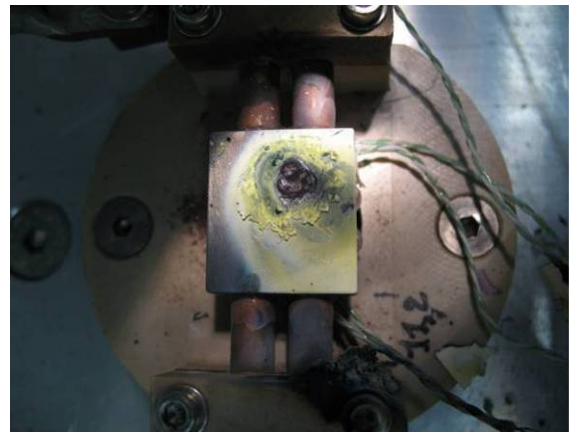


Figure 3.38 – View of the temperatures and mass flow rate trends recorded during the last thermal fatigue test shot (pulse numbers 13500÷15469; 4s ON / 4s OFF, 115A) on sample number 6 showing anomalous behaviour.



a – photo taken after pulse nr 13500



b – photo taken after the fault (pulse nr 15469)

Figure 3.39 – Views of the specimen number 6 after the anomaly that obliged to interrupt the test

Large melting occurred on the molybdenum, but fortunately the damaged area did not affect the zone previously exposed to about 14000 pulses, so the sample was used for the further “post mortem” laboratory analyses.

3.3.1.4.8 Conclusions on thermal shock and fatigue tests

From a macroscopic point of view no serious damages, like delamination in the molybdenum layer thickness, or detachment from the copper substrate were found on the samples after 15000 cycles of 3s beam ON/ 3s beam OFF, with heating power of about 600 W on two tested samples.

Local melting in the most heated area is instead visible, but this was expected, since it is not possible to calculate a priori the distribution of the power density transferred to the molybdenum surface by the arc. Anyway, the area in which the heat power concentrated is visibly restricted in both specimens (few square millimetres); as a consequence, it is possible to calculate the mean power density.

Considering, for example, a power (P) of 600 W (using the case with 75 A) and taking 3.0 mm the diameter (D) of the area heated by the arc (taken measuring the diameter of the visibly affected area of sample number 5 – see Figure 3.35 b), the mean power density (PD) can be simply calculated as follows:

$$PD = \frac{P}{\left(\pi \cdot \frac{D^2}{4}\right)} = \frac{600W}{\left(\pi \cdot \frac{3^2}{4}\right)mm^2} \cong 80 MW/m^2$$

Considering then the effect of the exposure of sample number 6 to 10000 cycles at the same power, it seems that during the test on this sample the heat transfer was much better concentrated, in about 1.0 mm diameter area; in this case the mean power density increase drastically to about 720 MW/m², that is at least an order of magnitude higher than the expected on the source, during operation at nominal conditions.

Since the number of cycles expected in the ITER HNB is at least one order of magnitude higher (see Paragraph 2.4.2) it should be advisable to test (at least) another sample to a higher number of pulses.

3.3.1.5 Post-mortem analyses of the Fatigue Tested samples

The 2 fatigue tested samples have been used for carrying out laboratory analyses with the aim of investigating the materials in the three states:

- before the explosion bonding process;
- after the explosion bonding process;
- after the thermal fatigue test.

These analyses have not been concluded yet and only partial results are hereafter reported, in particular for the molybdenum.

3.3.1.5.1 X-ray diffraction analyses

The phase identification and the crystallites dimensions were achieved by X-ray diffraction (XRD) measurements, performed on samples labelled A, B and C by using a Philips PW 1830 (see Figure 3.40) powder diffractometer in Bragg-Brentano geometry using Cu K α radiation ($\lambda=1.54056 \text{ \AA}$, 30 mA, 40 kV). The detector was a Xe gas proportional counter equipped with a secondary curved graphite monochromator. The patterns were collected in the $35\text{-}135^\circ 2\theta$ range and peak positions were determined with a statistical error $d(2\theta) = 0.005^\circ$ and an instrumental broadening $B_{\text{str}}=0.01^\circ$. Phase identification was performed with the support of standard patterns reported in ICDD database.

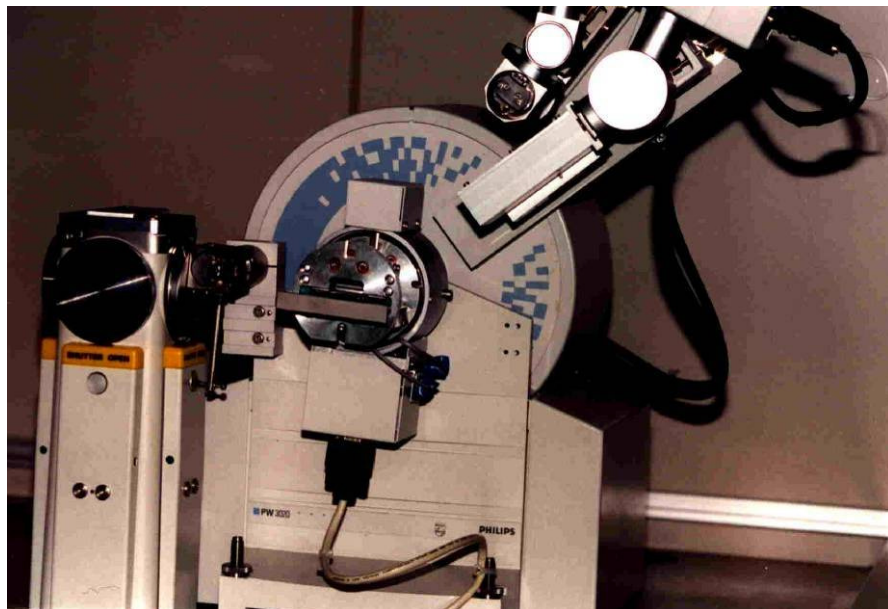


Figure 3.40 – Philips PW 1830 powder diffractometer used for the X-ray diffraction (XRD) measurements

Samples were mounted on custom-made plate that allowed to fix the sample's analyzed surface in contact with the reference plane of the XRD apparatus avoiding the possibility to create any peak artefacts due to incorrect offset estimation.

Preliminary X-Ray diffraction were conducted on Mo samples in order to verify the molybdenum lattice architecture of the bulk material in a typically cubic-structure's significant range of 2θ (10- 100°). Then, taking ICDD 00-001-1205 as reference, acquisitions between the 35-135° in 2θ have been performed to better evaluate the different spatial structural developments.

In order to have an estimation of the crystal domains sizes during the different process conditions the Scherrer-formula (see Equation (3.1)) has been used for the principal Mo peaks at $2\theta = 40.416^\circ$, $58,765^\circ$ and $73,997^\circ$ corresponding to the (110), (200) and (211) Bragg index of plane diffraction respectively [58].

Same methodologies have been performed for Cu XRD peaks contributions using ICDD 00-001-1241 and polymeric fitting at $2\theta = 40.416^\circ$, $58,765^\circ$

The crystallite sizes t have been estimated according to the following Scherrer-formula:

$$t(\text{crystallite-size}) = \frac{K \cdot \lambda}{\cos\theta_B \cdot \sqrt{FWHM^2 - B^2}} \quad (3.1)$$

where λ is the X-ray wave length ($\lambda_{Cu} = 1.54056 \text{ \AA}$), $FWHM$ is the full width at half maximum of the diffraction peak fitted with a 0.5 ratio of Gaussian and Lorentian slope, B that is the instrumental broadening of the peak, θ_B is the diffraction angle in radians, and K is the Scherrer's constant depending on the translating periodic structure modelling the crystal spatial development (in this case we used K equal to 0.9, that corresponds to cubes spatial repetition).

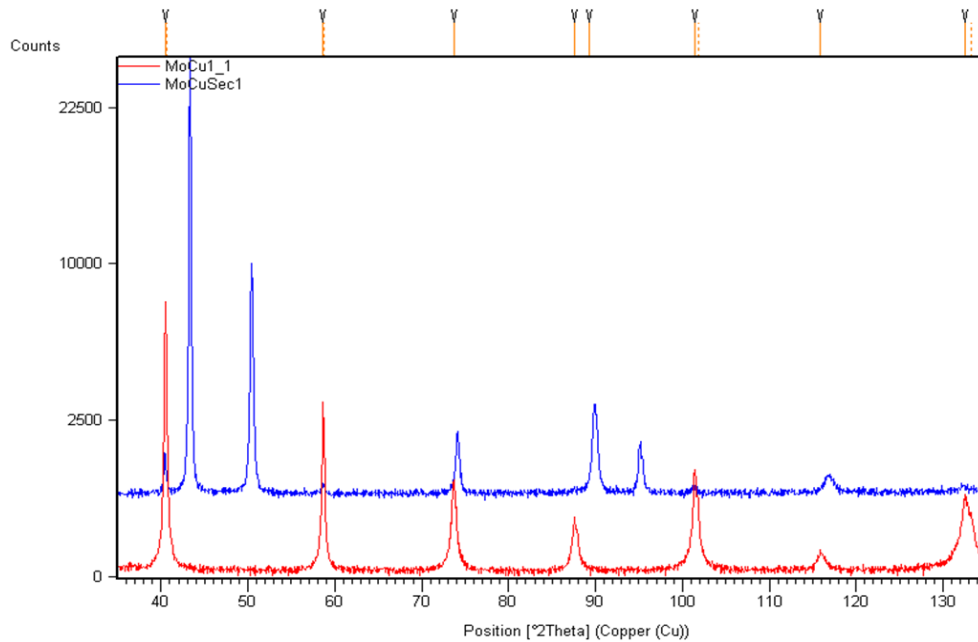


Figure 3.41 – Mo (red slope) and Mo/Cu section (blue slope) XRD plot where even Cu peaks around 43°, 51° and 96° 2Theta are visible

XRD recorded plots are reported in Figure 3.41 .

Mo peaks were fitted using the Im3m (229) spatial group as reference with lattice constant: $a = b = c = 3.144\text{\AA}$; $\alpha = \beta = \gamma = 90^\circ$ [Ref. Code 00-001-1205]; all fitting results have been accepted only in the conditions of R-values ($R_{\text{exp.}}$, $R_{\text{pr.}}$, $R_{\text{wpr.}}$) $< 10\%$.

The t parameter has been calculated on the fitting results regarding the (110) peak at $2\theta = 40.416^\circ$, attributing its intensity as $I = 100\%$. Crystallites dimensions were evaluated for peaks (110), (200) and (211).

Cu peaks, recognizable performing the XRD cross-section analysis of bonded and shaped sample labelled “MoCu_sec” ©, were fitted using the Fm-3m (225) spatial group as reference with lattice constant: $a = b = c = 3.607\text{\AA}$; $\alpha = \beta = \gamma = 90^\circ$ (Ref. Code 00-001-1241); all fitting results have been accepted only in the conditions of R-values $< 10\%$.

The t parameter has been calculated on the fitting results regarding the (111) peak at $2\theta = 43.473^\circ$, attributing its intensity as $I = 100\%$. Crystallites dimensions were evaluated for (111) and (200) peaks.

The starting molybdenum material labelled as “Mo_raw” (A) has shown the largest crystallite domains calculated via Scherrer-formula.

It clearly appears then that the bonding process induces an amorphous contribution in the samples labelled as “MoCu1” (B) and “MoCu_sec” (C): Table 3.9 shows the t sizes for the (110), (200), (211) peaks in the three samples.

Sample	Plane	2 theta (°)	FWHM (°)	<i>t</i> (Å)
Mo_raw (A)	(110)	40,518	0,120	770
MoCu1 (B)	(110)	40,428	0,244	362
MoCu_sec (C)	(110)	40,500	0,299	293
Mo_raw (A)	(200)	58,630	0,105	868
MoCu1 (B)	(200)	58,643	0,184	495
MoCu_sec (C)	(200)	58,568	0,206	442
Mo_raw (A)	(211)	73,667	0,139	714
MoCu1 (B)	(211)	73,653	0,395	251

Table 3.9 – *t* sizes for the (110) plane for the three analyzed samples

It is evident that after having performed the explosion bonding to the Mo-Cu samples crystallites domains have drastically reduced. This could be induced by a crystallite's sizes restrain or by lattice strains introduction.

It immediately appears that structural deformations induced in sample (B) and (C) are present in all the diffraction planes. Furthermore the crystallite sizes change significantly from one peak to another denoting an orientation dependence that is typical of an anisotropic strain presence contribution and cannot be explained only by an isotropic size reduction.

The deformations origin probably can be recognized in the abrupt and impulsive nature of the strain applied to the samples during the “explosion bonding” process. Moreover this amorphous-like improvement can be considered as a critically meaningful feature affecting Mo thermal properties.

3.3.1.5.2 Profilometry

A KLA-Tencor Alpha-Step IQ surface profilometer was used for the film thickness determination and featuring the ability to measure micro-roughness, with up to 1 Å, or less resolution, over short distances with a vertical resolution of 0.24 Å (Figure 3.42).



Figure 3.42 – KLA-Tencor Alpha-Step

Rotating Lapping apparatus model DAP-V by Struers, with single plate, was used to reduce superficial roughness of the specimen.

Pure Mo and Mo/Cu samples were lapped in order to investigate and reduce their mean intrinsic superficial roughness. The procedure described in the following can be positively applied to metallographic preparation of niobium, tantalum, molybdenum tungsten and their alloys.

The process, for each specimen, consisted in three ablations 15 minutes long each at a speed around 200 rpm with 500, 1200, 2400, 3200, 3600, 4000, 6000, 8000, 12000 grinding papers respectively with a cold fresh water jet in order to subtract the remaining powder from the new interface and keeping the processed surface cooled down. Then the specimens were cleaned with a removable tape and finally polished with a nylon 1 micron roughness plate with 1 μ m alumina paste distributed on the surface, cleaned with distilled water and removing-dust tape.

Murakami's reagent was prepared as etchants solution of 15mL HNO₃, 3mL HF, 80mL H₂O according to ASTM 209 and applied for 60 sec on the surfaces in order to emphasize grain boundaries. Samples were then dried in fresh air.

Samples have been analyzed via KLA Profiler in order to evaluate the surface roughness.

The acquisitions were performed with scan rate of 50 micron/sec, sampling rate of 50 Hz, sensor range of 400 microns with load on the tip of 38 mg.

After lapping the mean roughness of the surface was reduced from 0.30 micron (that was the mean roughness of the sample molybdenum surface not exposed to the thermal test) to 0.030 micron. Even though the gaining of such a meaningful result, the molybdenum surfaces were not completely scratch-less: these refractory metals tend to develop disturbed surface that must further removed in order to observe the actual intrinsic structure.

3.3.1.5.3 Microscopy

Observation of samples and identification of elements have been performed by FEI Quanta 200F FEG-ESEM (Field Emission Gun – Environmental Scanning Electron Microscope) instrument. The semi-quantitative elemental analyses were obtained using an Energy Dispersive X-ray Spectrometer (EDS) EDAX Genesys, using an accelerating voltage of 25 keV.

Two ESEM pictures are shown in the following Figure 3.43, at great magnification.

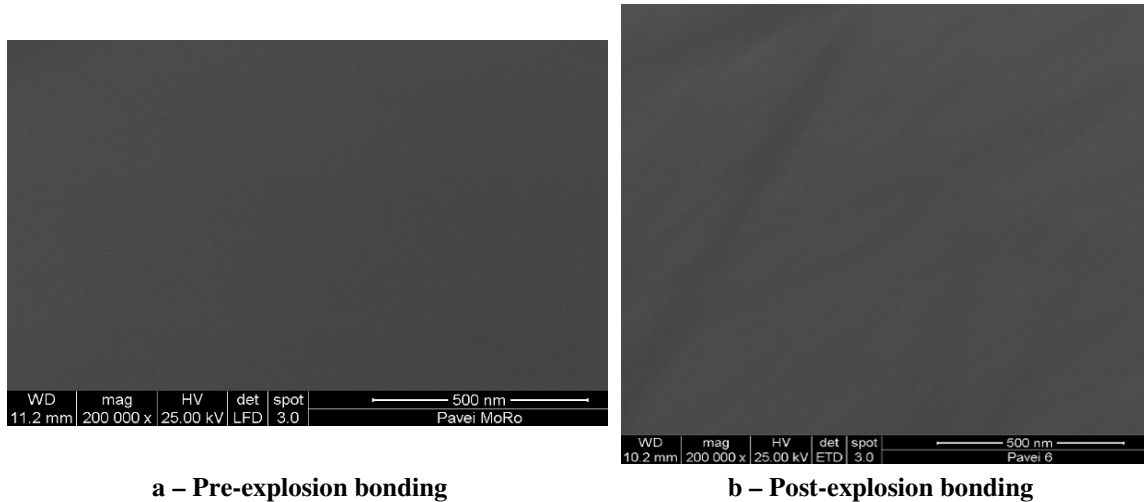


Figure 3.43: Mo surface self generated disturbed surface layer

Unfortunately due to the self-generating disturbed surface layer that Mo develops during polishing it is not possible to have a clear morphological distinction between the pre and post explosion-bonding samples.

A 18 hours polishing treatment alternated with light chemical attaches are suggested in order to lessen this topological self-modification.

3.3.1.5.4 Results of the laboratory analyses on the tested samples

The XRD appears to be the most significant apparatus of investigation for the molybdenum at this study step, since it does not suffer of the previously described presence of surface artefacts, as SEM does.

XRD results show that the explosion bonding process drastically reduces the molybdenum crystallites domains. This could be induced by a crystallite's sizes restrain or by lattice strains introduction: the explosion bonding process introduces defects in the molybdenum sheet causing changes of its mechanical and thermal properties.

These changes of the molybdenum properties, as well as for the molybdenum and copper properties in the interface Cu-Mo, need further analyses, in order to be qualified and quantified and have a complete knowledge of the bimetal plate characteristics.

3.3.2 Second step of R&D activities

The first step of R&D activities for investigating the explosion bonding as suitable technology for the manufacturing of 1 millimetre thick armour layer concluded successfully, demonstrating that it is possible to clad molybdenum on copper obtaining a reliable interface, in terms of both thermal and mechanical properties.

Nevertheless some of the issues arisen during the first stage were not solved (like the delamination within the molybdenum thickness at the hole edge), and a second step of R&D activities was necessary to address them.

3.3.2.1 Main scopes

On the basis of the results obtained within the first step of R&D, further activities were identified in order to solve the still open issues and to define the manufacturing cycle of the Plasma Driver Plate.

A new contract with company 3D METAL FORMING B.V was signed, with the following objectives, mainly aiming at eliminating the delamination at the tip of the finger, after its forming:

1. improve the shape of the formed part of the plasma driver plate (driver hole rim):
 - a. Optimize the shape of the copper cutting prior to forming the “finger”
 - b. Optimize the forming process of the “finger”
2. investigate possible solutions for avoiding delamination in the molybdenum:
 - a. Improve machining process
 - b. Avoid stress concentrations in the molybdenum during pressing
3. increase the ductility in the molybdenum, if possible (for this aspect it is request to discuss together with the sub-supplier):
 - a. Improving heating system with more controllable temperature
 - b. Using the molybdenum as base plate instead of flyer plate
 - c. Explosive bonding in longitudinal direction only
4. verify integration with further manufacturing processes of the PDP

Another important issue for the production of the PDP quarters was related, in fact, to the integration of the electrodeposition phase in the whole manufacturing cycle of the components.

The current manufacturing cycle of the PDP is the following:

- explosion bonding of molybdenum to copper
- machining of the driver holes
- thermal treatment & Flattening of the clad plate
- forming of the driver hole rim
- machining of the cooling channels on the copper side
- electrodeposition of copper for closing the cooling channels and fixing the shaped manifolds to the component
- thermal treatment & Flattening of the clad plate
- final machining and polishing
- final cleaning

The electrodeposition technology has the restriction that it is not efficient with geometries that have hollow sharp edges. For this reason it was decided to study an improvement of the “finger” geometry in order to make it compatible with the electrodeposition.

3.3.2.2 Design and manufacturing of the new prototypes

Accordingly to the requirement identified in Paragraph 3.3.2.1, a new contract has been signed with company 3D Metal Forming B.V. for improving the manufacturing parameters and producing new parameters. The new prototypes are shown in Figure 3.44.



Figure 3.44: New manufactured EB prototypes

The plasma generated into the drivers flows into the RF-source main chamber and has a strong interaction with the edges of the PDP driver holes. As consequence, the molybdenum armour is required to cover over the curved edge of the PDP holes, as well as over the main component plasma facing surface. This design requirement led to introduce a forming step into the first step of R&D activities with the company: the edge of the driver hole was machined, leaving a thin lip (or finger) that was then bent as shown in Figure 3.12.

The main issue that was identified at the end of the first step was the presence of delamination in the molybdenum thickness at the tip of the finger, after the forming. The new prototype geometry and main dimensions were identified in accordance to the scopes listed in Paragraph 3.3.2.1. In particular the new prototypes had:

- inner diameter 275 mm (instead of previous 190 mm);
- modified shapes of the finger and of the tooling (for minimizing deformation in the radius and shear stresses at the tip of the finger)
- the tip of the finger cut by water jet and polished (instead of machined)
- forming performed at 300 °C, with tooling actively heated during pressing

The shape of the new prototypes, with main dimensions are shown in Figure 3.45

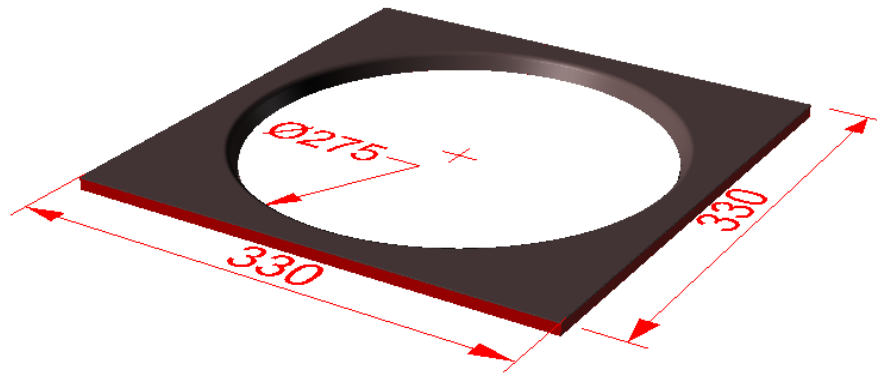


Figure 3.45: Full scale driver hole prototype (dimensions in millimetres)

Figure 3.46 shows an overview of all manufacturing steps for the production of the prototype. Step nr 5 has been performed only on one of the prototypes; instead step nr 6 – the electrodeposition - is only for completeness of information, but was not included in this set of activities.

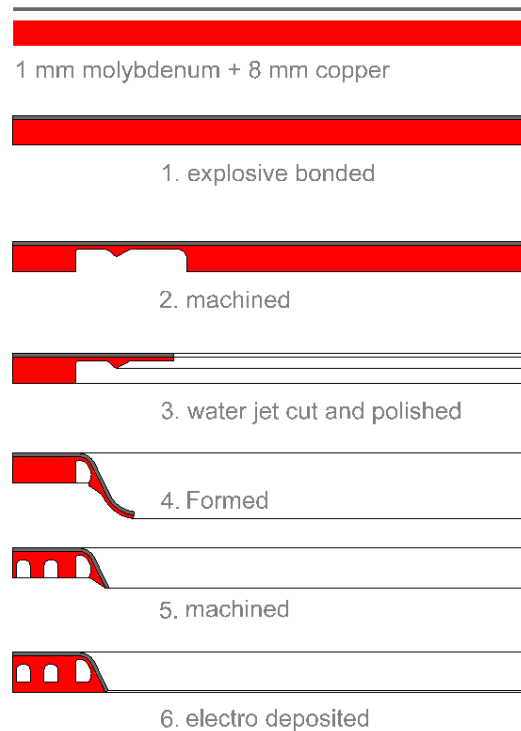


Figure 3.46: Overview of manufacturing operations. Steps nr. 2 and 3 may be reversed. Steps nr. 5 and 6 were not included in the scope of this project

3.3.2.2.1 Materials

The molybdenum sheet was purchased at Plansee. The plate was laser cut according to the scheme of Figure 3.47: 5 plates of 360x350 mm and 6 tensile test specimens (3x longitudinal and 3x transverse) were obtained.

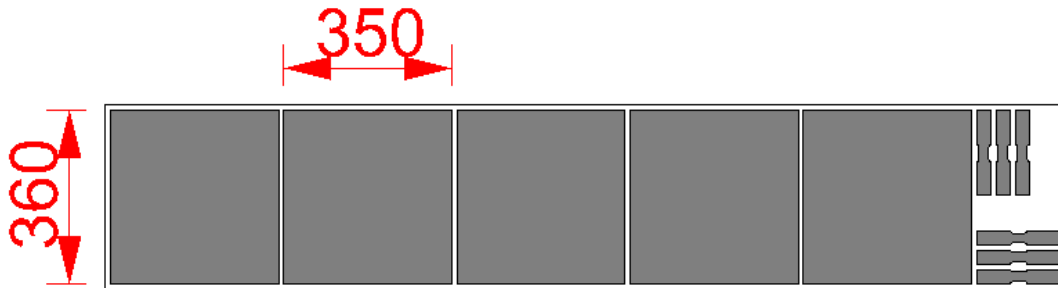


Figure 3.47: Cutting scheme of the molybdenum sheet (dimensions in millimetres)

The tensile test specimens have the dimensions showed in Figure 3.48.

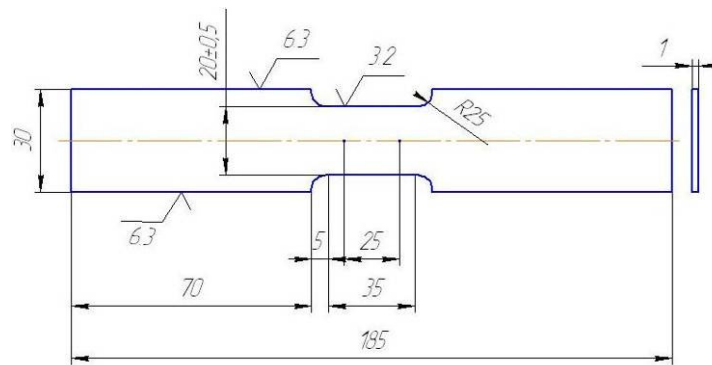


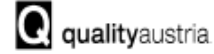
Figure 3.48: tensile test specimen drawing (dimensions in millimetres)

The certificate of the material is plotted in Figure 3.49.

PLANSEE SE
 A - 6600 Reutte
 Tel: +43/5672/600-0
 Fax: +43/5672/600-500
 http://www.plansee.com



RoHS QUALIFIED



SYSTEM CERTIFIED

ISO 9001:2008 NF. 02175/11
 ISO 14001:2004 NF. 01031/11
 OHSAS 18001:2007 NF. 00361/11

Test-Report

acc. to EN 10204 - 2.2

Report No.: **800452940000010**
 Date: **12.10.2011**
 Customer: **3D-Metal Forming B.V. / NL**
 PLANSEE-Order No./Item No.: **8781855 / 10**
 PLANSEE-Material-No.: **Z257249**
 PLANSEE-Segment / PoC. / : **7H / Luke /**
 Customer Order No.: **P110334** dated **28.09.2011**
 PLANSEE-Specification: **PS-IHF 013**

Material / Product: **MO / Mo Blech 1,0 x 380 x 2000mm**
 Condition of material / Quality: **cut with scissors / normal quality**

Dimensions: **1,0 ± 0,04 mm x cut**
 Customer-Material-No.:
 Quantity / Weight: **1,000 PC / KG**
 Batch(es): **0090777843 1,000 KG 0,000 KG**

GUARANTEED MECHANICAL REQUIREMENTS:

Yield Strength EN ISO 6892-1/Methode B: > 590 MPa
 Tensile Strength EN ISO 6892-1/Methode B: > 680 MPa
 Elongation EN ISO 6892-1/Methode B: > 10,0 %
 Hardness HV EN ISO 6507-1: 240 - 280
 Density EN ISO 3369: > 10,2 g/cm³

Luminosity factor DIN 67530: > 230 (Reflektometer REFO 3-D; only bright surface)

GUARANTEED CHEMICAL COMPOSITION: (determined in QA-QR-06-01)

Mo	min. 99,97 %**				
Al	max. 10 µg/g	Cr	max. 20 µg/g	Cu	max. 20 µg/g
Fe	max. 20 µg/g	K	max. 20 µg/g	Ni	max. 10 µg/g
Si	max. 20 µg/g	W	max. 300 µg/g	C	max. 30 µg/g
H	max. 10 µg/g	N	max. 10 µg/g	O	max. 40 µg/g
Cd	max. 5 µg/g	Hg	max. 1 µg/g	Pb	max. 5 µg/g

Cr(VI) + Organic impurities (e.g. PBB, PBDE, PFOS, PFOA)*

The requirements of the EU-directives 2002/95/EG, 2000/53/EG and 2006/122/EG for the restriction of hazardous substances (RoHS) are fulfilled.

*) The presence of Cr(VI) and organic impurities can be excluded definitely because of the production process (multiple heat treatment at temperatures above 1000°C in H₂-atmosphere).

**) Metallic purity without W

Certified that the supplies/services detailed hereon have been inspected and tested in accordance with the conditions and requirements of the contract or purchase order and unless otherwise noted below, conform in all respects to the specification(s), drawing(s) relevant thereto.

This certificate has been generated by computer and need not to be signed for validity according to EN 10204.

PLANSEE SE
 High Performance Materials
 IQM - Certificates

Figure 3.49: certificate of the molybdenum sheet

Tensile tests were in fact carried out in order to verify the actual mechanical properties of the molybdenum sheet, as was done in the previous. The results of the tensile tests are shown in Table 3.10.

Specimen nr.	Yield Strength (MPa)	Ultimate Tensile Strength (MPa)	Elongation (%)
Longitudinal-1	703,6	771,2	22,1
Longitudinal-2	705,3	770,8	22,9
Longitudinal-3	689,3	772,7	24,1
Transverse-1	749,4	814,0	16,3
Transverse-2	772,2	822,9	14,7
Transverse-3	781,5	821,4	10,7

Table 3.10 : Tensile test results on the purchased molybdenum sheet for the second step of R&D activities

The molybdenum sheet was from another batch than the molybdenum that was used in the previous stage. The mechanical properties of different batches of molybdenum can vary; therefore it is important to compare the results from Table 3.10 with the results from the previous step (see Table 3.3).

Comparing the results of the tensile tests performed on the two molybdenum sheets, the conclusion is that the elongation of the second molybdenum sheet is not significantly different from the one of the first plate (24% against 23% average, in the longitudinal direction, and 17% against 14% average, in transverse direction).

The ductility is the most important parameter for explosion bonding: poor ductility can cause cracking in the most deformed zones of the samples. PLANSEE guarantees a ductility of 10% for the molybdenum sheet (see Figure 3.49) but this is usually more, as the results of the tensile tests demonstrate. This means, that there is a theoretical risk that the molybdenum for future projects has poorer ductility than the material purchased till now. The consequence is that it is not possible to guarantee the success of the explosion bonding, plus forming process: material could in fact crack unexpectedly with lower ductility, while cracking was not observed in previous tests.

PLANSEE stated that a special molybdenum batch can be produced for optimal ductility. Than the ductility will be at least as good as the standard quality of molybdenum. This special batch will have a long delivery time and at least 4 plates of 2000x600x1 mm should be purchased. This opportunity was not considered for the current R&D activities (for time and costs reasons), but this option could be evaluated for the manufacturing of the final components.

However, the ductility does not seem to be critical: Figure 3.50 shows the bend test specimens: the one cut in the transverse direction (with respect to the lamination one) cracked after bending at 150°. The deformation that is necessary for forming the driver hole rim is however much lower than the one at which the crack appeared on the transverse specimens. The results of the bend tests with the second molybdenum sheet are similar to the previous ones.



Figure 3.50: bend test specimens: they were 150° bent, without cracking; a crack appeared and developed in delamination in the transverse sample (left) after further bending, up to 180°

The critical parameter for the molybdenum sheet itself is the resistance to self-delamination, or cross-thickness-tensile-strength, as concluded in the previous project. This parameter is very difficult to determine and PLANSEE does not have relevant records on this.

The supplier suggested to perform the forming (and bonding) processes at a temperature of 300°C in order to reduce at minimum the risk of delamination and cracking.

The copper was purchased from Ukrainian manufacturer: OJSC “Artyomovsk non-ferrous metal processing plant”; the certified properties were identical to the ones of the first purchased copper (see Figure 3.13).

3.3.2.2 Explosion bonding

The 5 plates of Figure 3.44 were explosively bonded, using the parameters that were determined in the first stage. There are two main differences that needed to be addressed:

- the size of the prototype: the size of the new plates was now 360x350 mm instead of 300x300 mm; the same heating elements were used, but as a result the temperature was lower, approximately 150 °C (instead of 200 °C with the previous project).
- the explosives that were used: the explosives came from a new batch; therefore the explosives were tested in the bonding process of the first molybdenum plate. The results of this test were, in comparison with the previous project:
 - The shape of the waves at the interface was almost flat
 - The cracks that occurred in the edges of the plate were longer (see Figure 3.51)

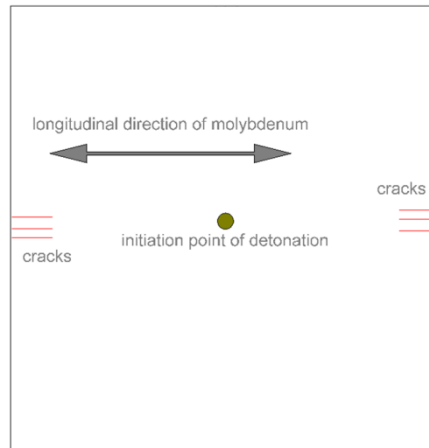


Figure 3.51: Scheme of the cracks that occurred on the edge of the plates

Bend tests and chisel tests were performed on the test plate. The result was good, therefore the other 4 plates were made with the same process parameters.

Apparently the shape of the waves is not relevant. In fact, the absence of strong waves is better when explosion bonding molybdenum and copper, in accordance to [56].

The cracks occur because of deformation during the explosive bonding process.

They were outside the zone that will be formed; therefore no further attention was given to this. Obviously, in future these cracks will be avoided. This can be done by e.g.:

- Making the plate extra large so that the cracks will be outside the net shape;
- Changing the detonation configuration. Now the detonation flowed radially from a central initiation point. This can e.g. be changed by a flat detonation wave that flows in the rolling direction of the molybdenum;
- Improving the heating system of the molybdenum sheet.
-

3.3.2.2.3 Flattening after explosive bonding

The plates were approximately 5 mm unflat after explosive bonding.

In order to make the plates more flat, the plates were first sandwiched in 6 mm steel plates and heated up to 400 °C. Then they were pressed iteratively by changing the positions of metal blocks in the press. As a result, the plates remained about 1 mm unflat.

It should be noted, that this procedure caused dents in the surface of the molybdenum. Most dents were relatively smooth because of the plates in which the explosively bonded plates were sandwiched.

On the first plate, a sharp dent occurred during pressing. The plate was not sandwiched at that time.

This dent had noticeable sharp edges, in contradiction to the dents that occurred later, after the plates were sandwiched.

This first plate was formed nonetheless. The dent was located at the tip of the finger and delamination was clearly visible. This resulted in a crack during the forming process that followed later, so this plate was rejected at the end.

The other (smooth) dents gave no problems in the forming process of the other plates.

Anyway any kind of dents shall be avoided in future, taking care of the molybdenum surface integrity during the flattening process.

3.3.2.2.4 Design for warm pressing

Before starting with the design of the pressing operation, the forming process of the previous project was analyzed by FEM simulations in ANSYS/Autodyn. The results are plotted in Figure 3.52 and gave a reference for the improvement of the forming process.

The shape of the driver hole rim, as defined by the design drawings, has been analyzed and modified accordingly to the aims listed in Paragraph 3.3.2.1, by iterative steps. As consequence of this study the shapes of the press tooling and the workpiece have been finally modified as follows (the letters related to each point of the list are reported in Figure 3.53):

- A. The copper thickness, in the finger, has been reduced to 1 mm instead of 2 mm;
- B. The copper is locally thicker, in the finger, in favour of the following electrodeposition process;
- C. The copper is supported, during forming, by an insert. This insert has smoothing radii in order to reduce the stresses induced by the forming process. The insert must be small enough for keeping the cross section of the hole left by the insert, after forming, below 25 mm^2 (see also Figure 3.58);
- D. The finger will be bent to a radius of approx. 65° instead of 90° , with respect to the plate plane;
- E. The punch is smoothed at the bottom;
- F. A 1 mm stainless steel “dummy plate” (in blue in the picture) has been adopted to protect the molybdenum surface during the forming.

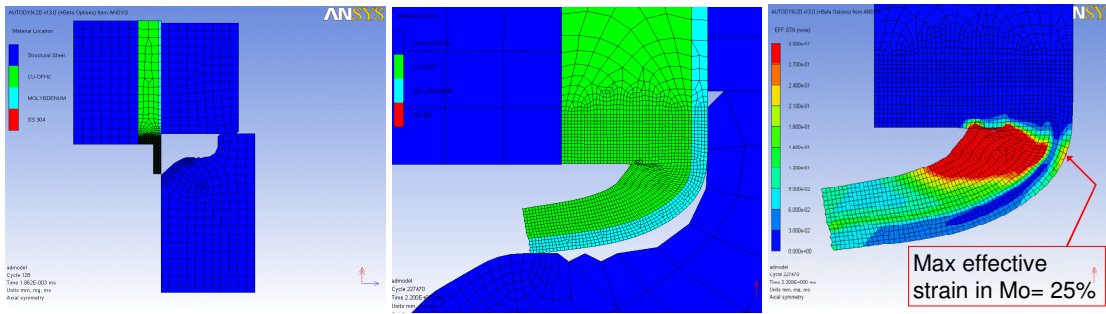


Figure 3.52: Axial-symmetric simulation of last forming test of the first step of R&D activities. The axis is placed horizontally at the bottom of the plots. Left: before forming. Middle: at end of forming. Right: actual strain (red=30%)

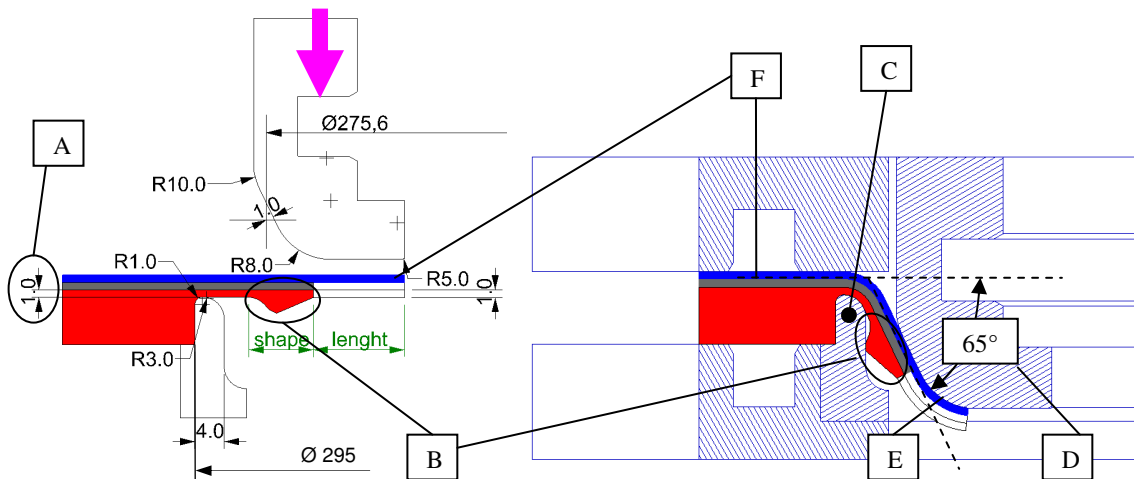


Figure 3.53: shape and main dimensions (in millimetres) of the finger and the tooling for the driver hole rim forming (before-left and after-right)

On the basis of the results obtained from the study of the driver hole rim geometry and the related forming process, most of the significant geometrical parameters of the process itself have been determined and the press tooling has been designed and manufactured. In Figure 3.54 some pictures of the press tooling, with the indication of the heating elements for the active heating and control of the workpiece temperature during the forming process are shown.

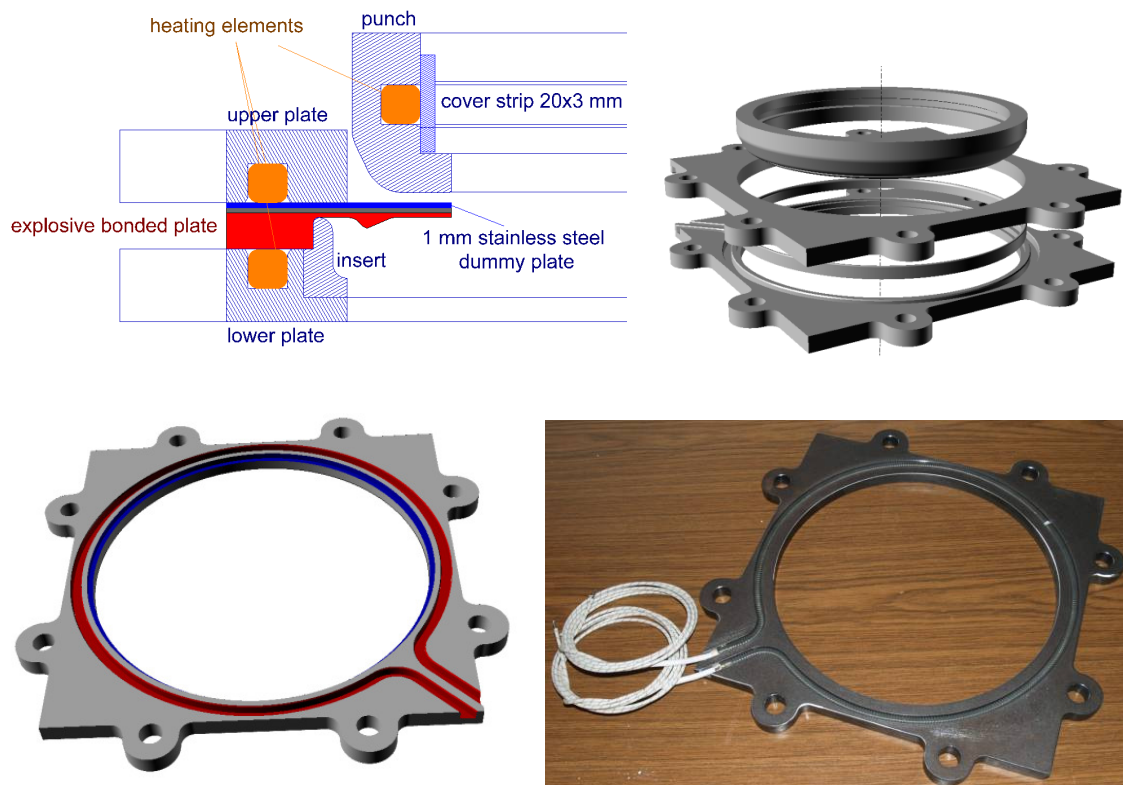


Figure 3.54: design of the press tooling. Top left - cross section of the tooling and workpiece; right - the 4 parts of the tooling; Bottom left - Lower Plate in 3D CAD; right - Bottom plate with heating element

Figure 3.53 shows (text in green colour) the two parameters that remained to be evaluated: the shape of the copper “extra-thickness” in the finger (for improving the following electrodeposition phase) and the length of the finger.

First the optimal value of the over-length of the finger was evaluated by FEM simulations of the sole molybdenum sheet in Autoform. It simulates monolithic sheets only, therefore a sheet thickness of 1,2 mm, with the properties of pure molybdenum, was assumed instead of 1 mm Mo + 1 mm Cu. High values of the over-length cause material draw from the edges, as shown in Figure 3.55. This would actually be an issue, since material draw is not allowed by the presence of the insert for the support of the finger during the forming and consequently heavy local deformation would occur in the copper at the top of the insert.

Figure 3.55 shows the results obtained with different values of the over-length.

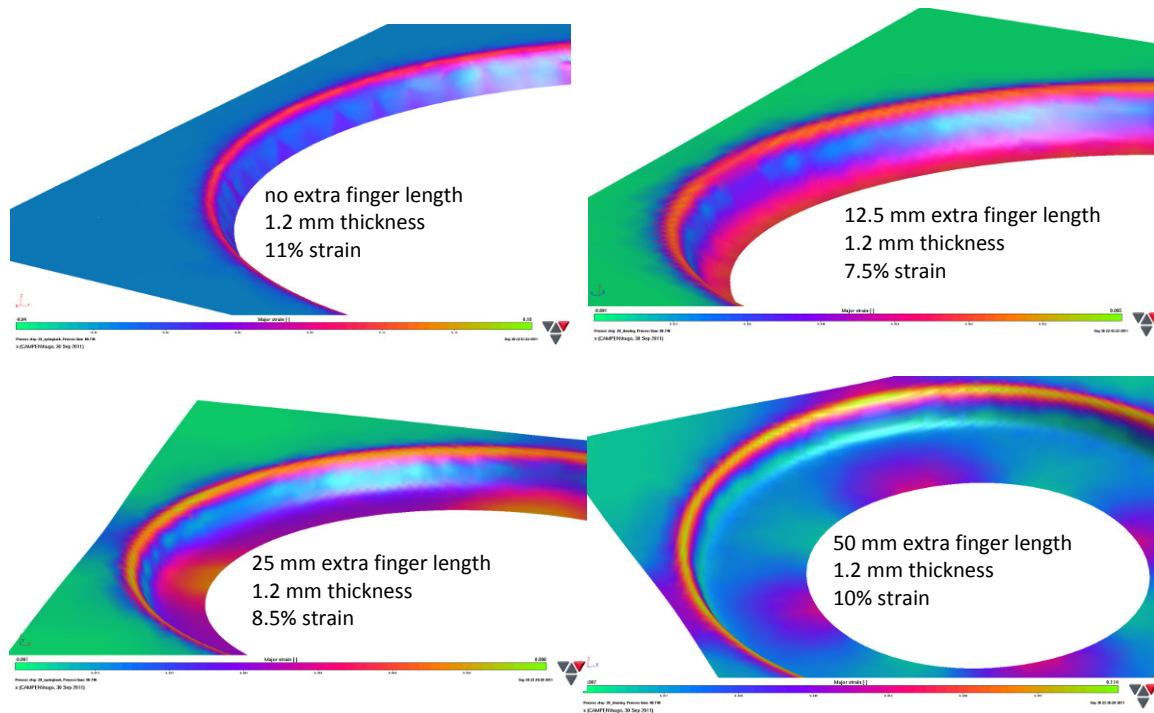


Figure 3.55: Contour plots of strain on the top Mo sheet surface for various values of the finger extra-length. (Note: the colour scale is not the)

The extra finger length has another advantage: the over-length will be cut off after forming, in order to get the required dimensions; if cracks occur, they are expected to start at the top of the edge (see Figure 3.16, on the right) and they will be removed with the cutting.

It was concluded that an extra length of the finger of 12.5 mm is the optimum.

Once the extra finger length was fixed to 12.5 mm, FE simulations were done in ANSYS/Autodyn, in order to take into account the effect of the shape of the copper and the bimetallic composition of the finger.

The first results showed some stress concentrations. This was solved by changing the shapes of the finger and of the tooling. A new FEM simulation was performed and the outcome resulted in further improvement. Figure 3.56 shows the end result of this iterative process; note that the strain in the molybdenum (15%) is now significantly lower than the strain that resulted in the first step (25%), as plotted in Figure 3.52.

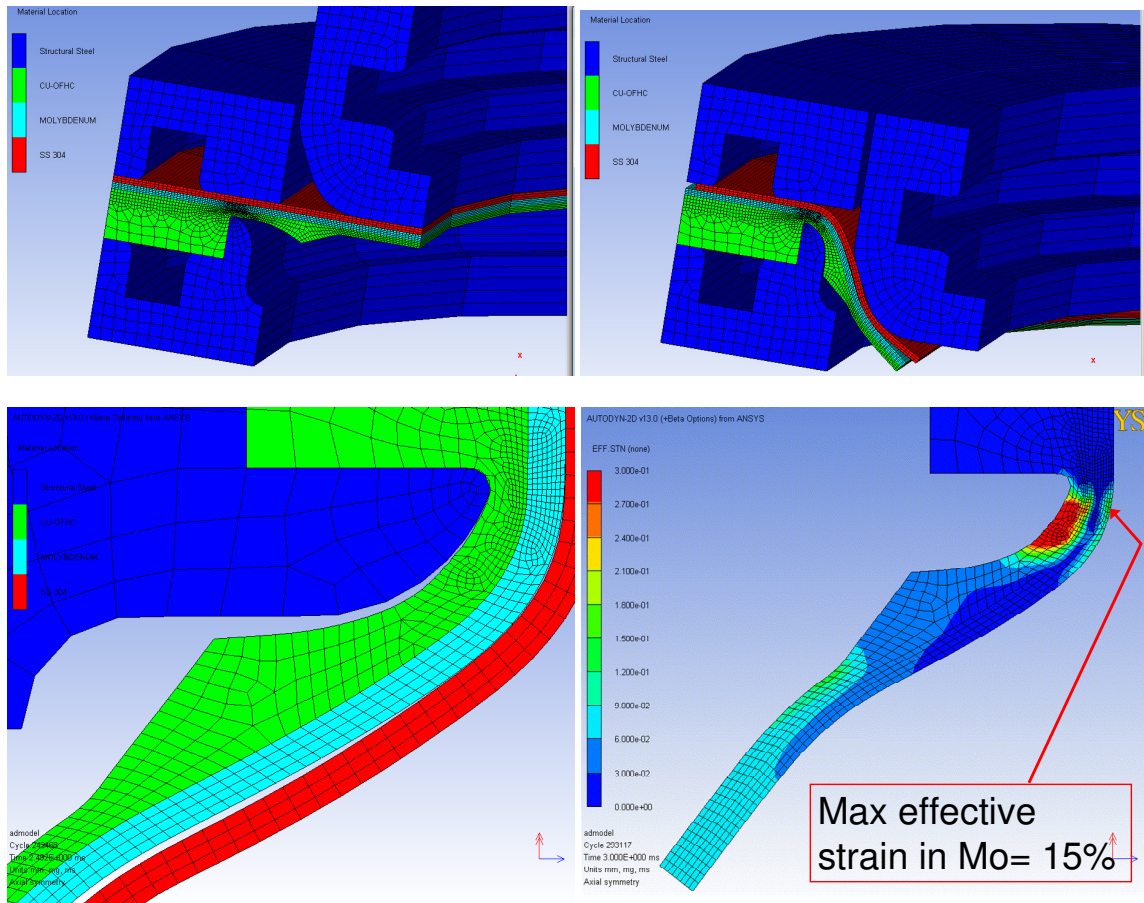


Figure 3.56: Forming simulation in Autodyn. Top left: at start of forming. Top right: at end of forming. Bottom left: after springback. Bottom right: effective strain (red=20%)

Another issue was the springback after forming. The required dimensions are: hole diameter of 275 mm and total thickness of 11,5 mm. The shape of the tooling was designed in order to take into account the springback of the finger after forming.

The springback correction was calculated from the radial expansion as follows:

$$\text{Yield strength: } \sigma_{0,2} = 750 \text{ MPa (see Table 3.10)}$$

$$\text{Elastic modulus: } E = 330 \text{ GPa}$$

$$\text{Elastic strain: } \varepsilon_{\text{elastic}} = \sigma_{0,2}/E = 0,23\%$$

This means, that the insert tool diameter of 275 mm diameter must be increased of 0,23%:

$$\text{Corrected tool diameter: } D^* = 275 \cdot (1 + 0.0023) = 275.6 \text{ mm}$$

In Figure 3.57 a drawing with the final dimensions (in millimeters) of the insert for the forming of the finger is shown.

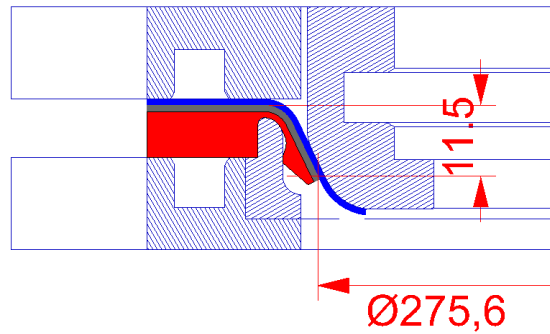


Figure 3.57: Axial-symmetric cross section of the tooling for the forming of the driver hole rim with main dimensions (in millimetres) as resulting from springback correction

Further springback correction could be applied after the first press run, after measuring the actual dimensions of the first formed prototypes, by putting strips on top of the punch (or on top of the upper plate) in order to modify the stroke of the punch (see Paragraph 3.3.2.2.6).

The top of the punch cannot anyway come below the top of the upper plate because the diameter of the punch of the press is bigger than the diameter of the tool punch, realizing a sort of “end-stopper” and guaranteeing the repeatability of the process.

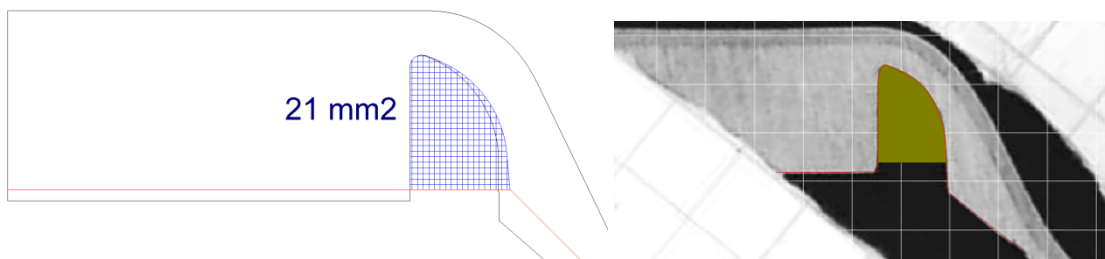


Figure 3.58: Left: theoretical estimation of cross section of cooling channel around the drive hole after springback. The red lines show the shape after machining, before electrodeposition. Right: cross section area measured from a real cross section of prototype nr. 2, showing a cross section area of ~20 mm²

Another improvement of the design was the decision to use the void left by the insert used as support of the finger during the forming step as cooling channel. The area of the cross section of the void must be 25 mm² or less, in order to guarantee an adequate water flow rate in the PDP quarter (since the water flow is governed by the balance of the pressure drops occurring in each of the cooling channels). The picture on the left of Figure 3.58 shows that the expected cooling channel area, considering the 0.3 mm springback and the machining at the required thickness of the plate (before electrodeposition of copper for closing the cooling circuit) is expected to be 21 mm². Measuring the actual cross section (by optical instrumentation on the prototype nr.2, that was cut), the area resulted to be a bit less than 20 mm² (on the right of Figure 3.58). This value

of the channel cross section area is acceptable, since it will cause a water flow rate that will not affect the water distribution in the main cooling circuit of the PDP quarter.

3.3.2.2.5 Preparation of the samples for the forming step

The explosive bonded plates were machined, accordingly to the shape and dimensions described in the previous paragraphs, for the forming step. Firstly a small hole was made in the center and the plates, used for rigidly clamping them on a lathe.



Figure 3.59: Preparation of samples for pressing. Top left: tight fixing in lathe. Top right: water-jet cutting of inner circle (and tensile test specimens). Bottom left: polishing of the finger tip. Bottom middle: close up of the finger. Bottom right: control of the shape of the finger with a laser cut jig

The plates were then machined on the copper side in order to obtain the required shape of the finger (see Figure 3.53); secondly the hole was cut, by water-jet cutting, leaving 12.5mm of over-length on the finger (taking the opportunity of having the water-jet machine, two tensile test specimens have also been cut from the leaving disc at the center of the plates). The finger edge was polished thereafter in order to reduce the probability of crack initiation. The shape of the finger was checked with a laser cut jig. All these steps are shown in Figure 3.59.

The turning of the workpiece will not be possible with the PDP quarter, but the same shape of the finger can be easily obtained by milling with a computerized milling machine.

3.3.2.2.6 *Warm forming of the driver hole rim*

The samples were positioned in the tooling manufactured for the forming (see Figure 3.54). The 3 main parts of the tooling were heated individually with a heating element (see Figure 3.54) and a thermocouple was positioned on each of the three parts.

The assembled tooling, with a plate installed inside it, was positioned in the press and insulated on the top and bottom with pressure resistant insulating material. On both sides, 60 mm blocks were positioned in the press in order to restrict the pressing depth.

The tooling parts were heated until the temperature was $300 \pm 20^\circ\text{C}$.

Figure 3.60 illustrates the equipment for the forming step with pictures.

Four plates were formed: the first one had a crack that was initiated in the flattening process by a dent with sharp edges. The second form was formed successfully. The inner diameter was measured with a jig and the diameter turned out to be slightly too small.

The last two plates were formed with an aluminum plate, 0.5mm thick, positioned on top of the punch, so that it went 0.5mm deeper during pressing. As a result the inner diameter was slightly increased, obtaining the required value of 275mm at 11.5mm of distance from the molybdenum surface.

Apart from the first formed plate, that was previously damaged during the flattening process, with the press, all the other 4 plates were successfully formed: no cracks were visible at the finger tip, nor delamination.



Figure 3.60: The forming step of the plates. Top row: Left-assembled tooling; Middle-ready for pressing; Right-temperature measurement and switches for the 3 tooling parts. Middle row: assembled tooling with insulating material. Bottom row: Left-penetrant test; Right-checking the diameter of 275mm at 11.5 mm depth, with the laser cut jig

3.3.2.3 Prototype and tests for electrodeposition related issues assessment

One of the issues for the production of the final PDP quarters was related to the integration of the electrodeposition phase in the whole manufacturing cycle of the components (see Paragraph 3.3.2.1).

The electrodeposition technology has the restriction that it is not efficient with geometries that have hollow sharp edges. For this reason it was decided to change the geometry of the “finger” to be bent at the driver hole rim in order to avoid a 90° concave angle to be “filled” by copper electrodeposition. The difference between the previous design and the new proposed one is shown in Figure 3.61 (compare step 6 on the left with step 5 on the right)

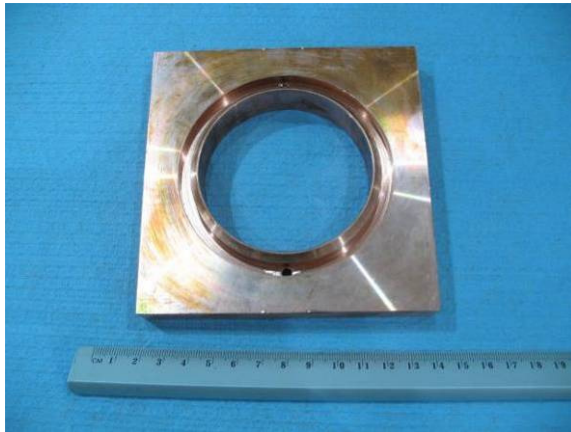


Figure 3.61: Driver hole rim geometries and manufacturing steps

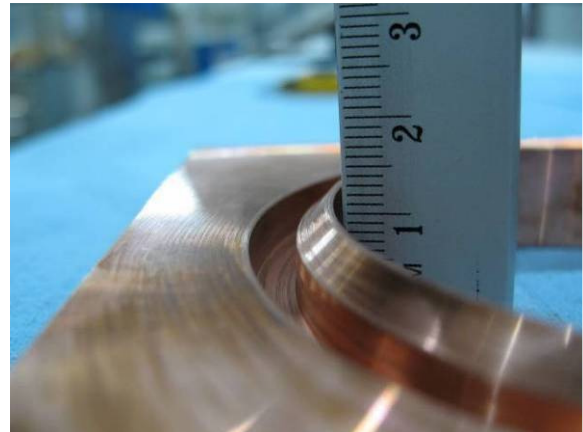
With the new geometry, the angle between the two surfaces that must be covered by electrodeposited copper have an angle between them that is $\geq 135^\circ$ that guarantees a much higher uniformity in the growth of the electrodeposited copper layer.

A small sample reproducing the geometry shown in Figure 3.61.b-step 5 has been manufactured and electrodeposited with 3mm (required) of copper, as test.

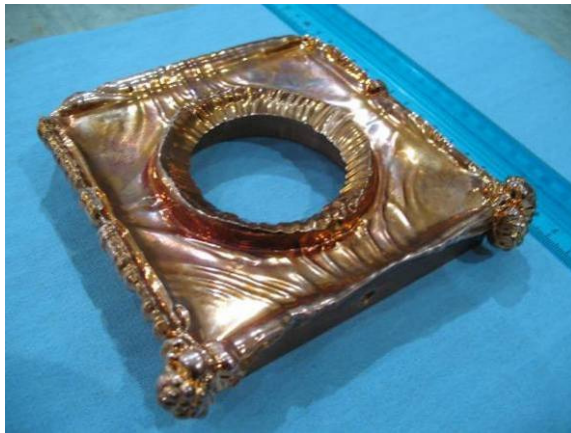
In Figure 3.62 the plate sample is shown: a,b- before the electrodeposition, c- as extracted from the electrodeposition bath, d- after machining at thickness 3,0mm.



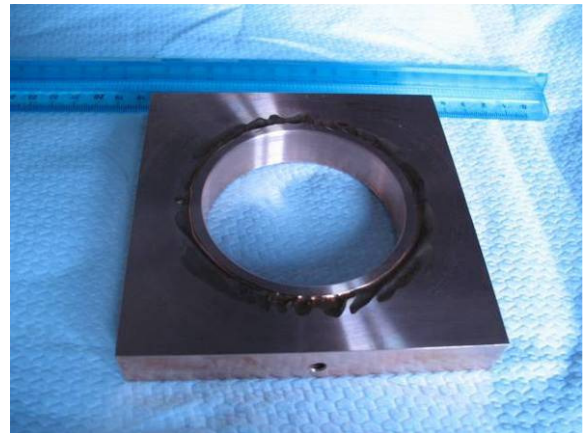
a – before electrodeposition



b – detail of the “edge” geometry



c – as extracted from the bath



d – after machining at final dimensions

Figure 3.62: Copper electrodeposition test on sample reproducing the driver hole rim geometry

Despite the angle between the two surfaces to be electrodeposited was 45° , the growth of the copper was quite slow in correspondence to the edge. At the boundary edges of the plate the thickness was higher, up to 8mm, instead, in the hollow edge, it was thinner, down to 1.7 mm.

After the final machining, the plate resulted to be not completely flat, due to insufficient thickness of electrodeposited copper in correspondence of the groove simulating the cooling channel going around the driver hole.

The plate could have been “repaired”, adding the lacking copper by means of a new electrodeposition phase, but it was decided to accept the plate and to go on with the tests described below.

3.3.2.3.1 Helium leak and pressure tests

In order to assess the acceptability of the electrodeposited layer a helium leak test and a pressure test have been carried out on the plate, accordingly to the procedures requested in [59].

The sample has been cleaned, by immersion in acetone bath with ultrasounds for 30 minutes. In this way residuals of grease and oils can be removed from all the surfaces. Since the acetone has high vapour pressure (that means that it easily evaporates), it also helps to remove residuals of water and does not leave residuals on the surfaces.

After the cleaning with acetone, the sample has been dried fluxing pressurized nitrogen in the channel.

In order to connect the sample to the equipment for the tests two AISI 316L tubes (OD 6mm) have been connected (with threaded joints) to the sample itself. These tubes were previously cleaned with acetone, with the same procedure used for the sample. The vacuum tight between the sample and the tubes was guaranteed by using ARALDITE®.

For both the tests one of the sample tubes has been plugged by means of SWAGELOK® fittings; whereas the other tube has been connected to the test equipment.

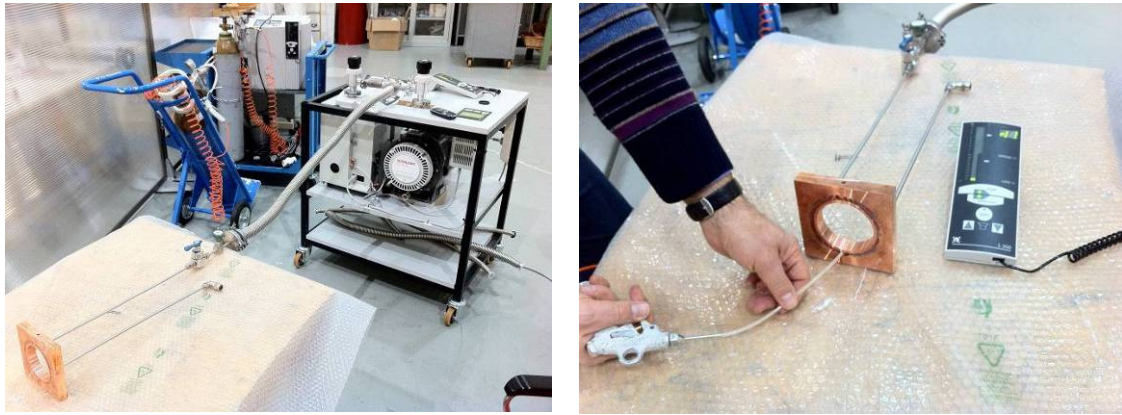
3.3.2.3.1.1 Leak test

The leak test has been carried out connecting the free tube of the sample (by means of a valve and a transition to a DN 40 KF flange) to a leak detector. The leak detector is composed by an internal pumping system and a mass spectrometer (calibrated on mass 4 – He₂). The procedure for the leak test is the following:

- the leak detector equipment pumps the sample volume in the range of “low vacuum” (about 10^{-3} mbar)
- once the required vacuum level is reached, the operator connects the sample volume to the mass spectrometer.
- the operator start to flux helium gas, at low relative pressure, on the junctions to be tested: in presence of micro-cracks, holes, porous structures or other discontinuities the helium gas penetrates in the pumped volume and it is detected by the mass spectrometer.

The leak detector is calibrated by means of “Helium calibrated leaks” that allow to quantify the detected leak: the instrument gives, in fact, a throughput (Q) in mbar*l/s (1 mbar*l/s = 0.1 Pa*m³/s). Consorzio RFX accepts local leaks up to $Q = 1 \cdot 10^{-9}$ mbar*l/s (= $1 \cdot 10^{-10}$ Pa*m³/s) (with Helium).

In Figure 3.63 the leak test equipment and a photo taken during the test are shown.



a – set-up equipment for the leak test

b – Picture taken during the leak test execution

Figure 3.63: Leak test

Following this procedure, the electrodeposited sample has been tested: after the background noise stabilized, the operator tested all the junctions that was not directly interesting for the test (in order to verify the total absence of other leaks and to avoid possible errors) verifying that for all of them the detector did not identify any leak. After that the sample itself was tested, fluxing all the junctions between the base copper and the electrodeposited one. The background noise remained stable at $Q = 3.2 \cdot 10^{-12}$ mbar*l/s during the test, so the test was successfully passed.

After the pressure test described in next paragraph, the leak test has been repeated and it gave successful results, as well.

3.3.2.3.1.2 Pressure test

The pressure test has been carried out according to BS 31.3 ANSI/ASME Code for Pressure Piping.

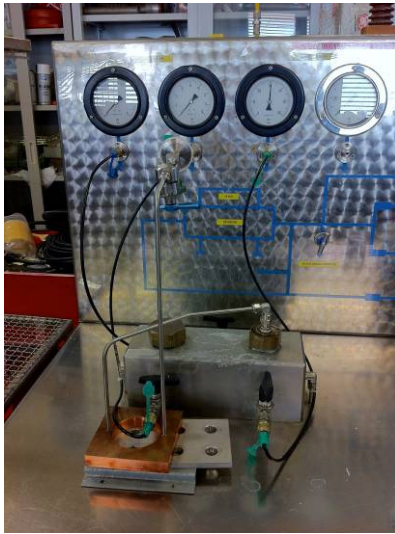
The test consists in repeating for 10 times the following cycle:

- Pressurization of the circuit (with Nitrogen gas – N_2) up to 30 bar (1.4 the nominal operating pressure);
- Permanency in pressure for 60 seconds, verifying that the pressure remains stable;
- Evacuation of the circuit down to atmospheric pressure.

After the 10 cycles, the circuit must be kept in pressure, at 30 bar, for at least 30 minutes, verifying that the pressure remains stable;

The pressure test on the electrodeposited sample plate has been carried out at Consorzio RFX, using a specific test facility. The sample has been connected to it through SWAGELOK® fittings, sealed with LOCTITE® 542. The system was pressurized with Nitrogen gas (N_2) at maximum pressure of 31 bar.

In Figure 3.64 the pressure test equipment and a photo taken during the test are shown.



a – set-up equipment for the pressure test



b – Picture taken during the pressure test execution

Figure 3.64: Pressure test

During the 10 cycles of pressurization and release, no leakages have been detected; after that the system has been pressurized at 31 bar and the valve (along the tube path towards the B14 gas cylinder) closed. The system has been left pressurized for 60 minutes: no change in the pressure inside the sample was detected.

3.3.2.4 Results of the second step of R&D activities

Within the second step of R&D activities (with respect to the scopes listed in Paragraph 3.3.2.1) the following issues have been addressed/solved:

1. The forming process of the driver hole rim has been analyzed and revised as follows:
 - a. improving the shape of the copper cutting prior to forming the “finger”, leaving an over-length on it, helping in reducing stresses;
 - b. improving the forming process of the “finger”, revising the PDP design drawings, reducing the bending angle, designing accurately the tooling used for the forming of the driver hole rim, and performing the process at 300°C;
2. In order to avoid delamination in the molybdenum:
 - a. the machining process has been revised: water jet cut has been adopted, moreover the cut edges have been polished;
 - b. stress concentrations in the molybdenum during pressing have been reduced by improving the shape of the tooling and introducing a “dummy plate” in between the punch and the workpiece during forming;
3. The parameters affecting the ductility of the molybdenum sheet have been discussed with the molybdenum supplier; in particular the temperature for both the explosion bonding and forming steps has been set to 300°C;
4. The integration with further manufacturing processes of the PDP has been considered, in particular with the electrodeposition phase, and the new design of the driver hole rim is now compatible with it.

In total, five molybdenum plates were bonded to copper; the prototypes resulted as follows:

- Sample nr. 1: tested-and-destroyed for checking the quality of the explosive bonding process
- Sample nr. 2: cracked during pressing due to sharp dent caused by erroneous use of the press during flattening operation
- Sample nr. 3: formed, but the diameter of the driver hole was a bit smaller than the 275 mm required (at 11.5 mm from the molybdenum surface);
- Sample nr. 4 and 5: formed (with the punch 0,5 mm deeper during pressing) in order to obtain the required diameter of the driver hole. These two samples completely satisfy the requirements, except the flatness.

The flatness of the prototypes, after forming at 300°C resulted to be an issue. After pressing all prototypes became about 3 mm un-flat after cooling down. This is supposed to be caused by the fact that the shapes consist out of different metals: the coefficient of linear expansion of copper is $\alpha_{Cu} = 16.8 \cdot 10^{-6} K^{-1}$, while the one of molybdenum is $\alpha_{Mo} = 5.0 \cdot 10^{-6} K^{-1}$. The difference in the free expansion of the two metals, at the temperature of 300°C (that has been chosen as the optimum for the forming step, after discussion with the molybdenum supplier) is of about 0.33%, calculated as follows (in terms of strains):

$$\Delta \varepsilon_{Cu-Mo} = (\alpha_{Cu} - \alpha_{Mo}) \cdot \Delta T = (16.8 - 5.0) \cdot 10^{-6} \cdot (300 - 20) = 0.0033 = 0.33\%$$

The elastic strain limit of the copper is approximately of 0.1%, calculated as follows:

$$\Delta \varepsilon_{Cu}^{elastic} = \frac{\sigma_{yield,Cu}}{E_{Cu}} \approx \frac{100 \cdot 10^6}{12.4 \cdot 10^{10}} \cong 0.1\%$$

The consequence is that plastic deformation occurs in any way when the molybdenum - copper plate is heated up to 300 °C and when it cools down. The threshold temperature over which plastic deformation of copper starts is the one at which the difference in the free thermal expansions between molybdenum and copper overcomes the elastic strain limit of the copper subplate; such temperature can be estimated as follows:

$$T_{thr} = T_{env} + \frac{\Delta \varepsilon_{Cu}^{elastic}}{(\alpha_{Cu} - \alpha_{Mo})} = \frac{0.001}{(16.8 - 5.0) \cdot 10^{-6}} + 20 \cong 105^{\circ}C$$

As a consequence the temperature for the forming step of the driver hole rim should be revised in order to guarantee the quality of the forming, without introducing large deformation of the plate itself.

3.3.3 Conclusions

Explosion bonding technology has been investigated for the production of a 1.0 mm thick armour layer on copper substrate. The R&D activities have been conducted in two steps.

In the first step the suitable parameters for explosion bonding molybdenum to copper have been identified. Conventional and non-conventional tests and analyses have been carried out on specimens cut out from the manufactured samples, demonstrating very good qualities of the interface. The interface tensile strength is higher than the one initially required in the technical specifications [Annex 1] and the tests demonstrated that the interface is even stronger than the copper substrate. Thermal shock and thermal fatigue tests have been carried out on specimens manufactured starting from the explosion bonding samples: 5 specimens have been tested (3 at thermal shock and 2 at thermal fatigue). Neither delamination nor flaking were visible on the specimens, only local melting was visible on the molybdenum surface of each specimen in the most heated area. The TIG welding machine, used as heat power generator for these tests, allowed the set-up of the desired value of the thermal power to be applied, but not the surface area of the sample on which the power was applied: the control of the heat power density was not possible. The mean power density has been evaluated to be in the range $0.1\div 0.7$ GW/m² (see Paragraph 3.3.1.4.8), approximately one order of magnitude higher than the expected value in the HNB and MITICA source. The specimens tested at thermal fatigue show, moreover, little cracks in the molybdenum, inside and at the boundary of the most heated area.

Being the results obtained in the first step of R&D activities on explosion bonding very satisfying, in particular for the quality of the molybdenum-copper interface, the second step was focused on the assessment of the other open issues, mainly related to the forming of the driver hole rim of the PDP quarters. The forming process has been studied and analyzed using finite element tools. The plastic deformation of the bimetallic finger occurring during the forming step has been reduced by changing the finger bending angle and thickness. Moreover, during this strong integrated re-design of the driver hole rim geometry and manufacturing process, the subsequent copper electrodeposition process (necessary on the PDP component for closing the cooling channels on the back side) has been considered; the shape of the finger has then been modified in order to satisfy the electrodeposition requirements as well.

Prototypes have been manufactured, producing new explosion bonding molybdenum-copper plates, machining and forming them accordingly to the improved and re-designed geometry and process parameters. These new prototypes, on the contrary of samples manufactured in the first step, showed no delamination, thanks to the introduced improvements, and reproduce the driver hole geometry at full scale, demonstrating eventually the feasibility of the current design.

Flatness of the prototypes resulted to be still an open issue which needs to be further addressed, in view of the manufacturing of the PDP quarters, keeping in mind that:

- dents occurred on the molybdenum surface in the pressing, after explosive-bonding, during the second step of R&D activities, causing the failure of the first prototype during its forming: damages on the molybdenum surface shall be avoided;
- the prototypes become un-flat after warm forming at 300°C, during cooling down;
- there are anyway residual stresses in the workpieces that cause deformations during further machining, due to the stress re-distribution in the material;
- heat treatments and flattening will probably be necessary after the electroplating process which will cause deformations as well.

At present, the most proper actions for guaranteeing the required flatness of the PDP quarter seems to be the following:

- anneal the copper after explosive bonding and roll the plate flat with a 'leveller' (with multiple rolls) continuously, during the cooling down of the plate itself;
- not confine the plate during the forming step, but allow the plate to move freely both during heating up before pressing and cooling down after pressing;
- alternatively, perform the forming at lower temperature ($\leq 100^\circ\text{C}$);
- after electroplating, flatten the plate at room temperature by iterative steps in a press.

4 Overall conclusions

This PhD work has been focused on the development of the ion source design for the ITER Neutral Beam Injectors and their test beds: SPIDER, the Ion Source prototype, and MITICA, the full injector prototype. During the PhD period I managed the engineering design of the SPIDER beam source and of the MITICA plasma source.

Among the components of the ion source, the rear vertical plates (facing the plasma) are the most critical ones, since they are hit by the positive ions that are back accelerated from the accelerator (the Back-Streaming positive Ions, BSI+). The Plasma Driver Plate (PDP), in particular, is the most complex one, having to satisfy a large number of requirements, in terms of heat exhaustion, shape and geometry, resistance to sputtering, surface temperature, etc.: its design has been the most complex and articulated activity of my work.

Different configurations of the cooling circuit have been considered, since the very beginning: the one with the PDP subdivided in four symmetrical quarters has been finally chosen. Analytical calculations of the expected pressure drops in the quarter have been carried out together with the main cooling circuit parameters. After that, detailed finite element simulations of the most stressed areas of the component have been carried out: thermo-mechanical analyses and multi-axial fatigue verifications have been performed, highlighting the critical state of the material subjected to the cyclic heat loads given by the impinging BSI+.

Two different concepts for the PDP have been developed and analyzed. The first one, initially taken as the reference solution, in which the PDP was completely made of CuCrZr alloy, was verified, from the pure mechanical point of view: for this solution the sputtering of copper was evaluated to be too high, with consequent pollution of the plasma. The second configuration, that is the adopted design, foresees the presence of an armour layer of molybdenum, 1.0 mm thick, facing the plasma and the impinging BSI+: the Mo layer is applied on a pure copper sub-plate.

Due to the large mismatch between the copper and molybdenum thermal and mechanical properties, the simulations showed that the interface between the two materials must withstand very high stresses and experiences fatigue damage, the latter overcoming the threshold of 100% during the whole ITER life.

Since the thickness of 1 mm is not an usual value for coatings and the properties at the interface between the two metals strongly depend on the technology used for the production of the joint (it is almost impossible simulate the interface characteristics accurately), dedicated R&D activities have been carried out aimed to identify possible and suitable technological solutions for the production of one millimetre molybdenum layer on copper substrates.

Both Atmospheric Plasma Spray (APS) and Explosion Bonding (EB) techniques have been then investigated.

Specimens manufactured by APS showed insufficient bonding strength to the substrate and relatively high porosity. The outgassing properties of the APS coating have been studied: the main desorbed species at operating temperature (50°C) are CO₂ and N₂. The porous structure of the coating seems to have a role in trapping air and other surface contaminants inside the film. Nevertheless, the initial outgassing flow rate is at least seven orders of magnitude lower than the hydrogen flux during source operations, resulting in a negligible contamination level. Due to the very low bond strength of the interface, the R&D activities on APS technique were stopped at the preliminary stage.

Aimed at assessing the feasibility of Explosion Bonding molybdenum to copper a first stage of R&D activities was launched. Specimens manufactured by EB were tested; the results showed very high quality and strength of the Mo-Cu interface. Thermal shock and thermal fatigue tests have been successfully carried out in order to simulate the expected loading during operations of the parts of the PDP impinged by the BSI+: results confirmed the reliability of the bonding technique. Further tests and analyses are still ongoing in order to complete the study of the properties at the interface between molybdenum and copper, after fatigue loading, and aiming to check the actual behaviour of the molybdenum surface under hydrogen ions bombardment with energy and fluxes comparable with those expected in the source.

In a second step, once assessed the suitable parameters for the explosion bonding and verified the quality of the interface, the activities continued focusing the work on the other engineering issues that needed to be addressed for the manufacturing of the PDP components. Particular attention was paid to the forming step of the edge of the holes placed in correspondence of the drivers, named “driver hole rim”: the proper shape and dimensions of the edge, the shape of the press tool and all the other parameters influencing the forming steps have been analyzed and addressed, carrying to the complete re-design of the driver hole rim and its forming process. A new set of samples have been then manufactured by EB and formed accordingly to the re-designed shape and parameters, obtaining three full scale prototypes of the PDP driver hole, on which neither delamination nor flaking have been detected, even with die penetrant tests.

The flattening of the bimetal plate is still an open issue that is being studied, since the prototypes show large out of plane bending after the forming step.

The solution of this last aspect, together with the manufacturing of a full scale prototype of the whole PDP component, are the last two steps currently under investigation to conclude the roadmap up to manufacturing of the MITICA Plasma Driver Plate.

REFERENCES

- [1] ITER website, www.iter.org
- [2] J.L. Luxon, A design retrospective of the DIII-D tokamak, *Nucl. Fusion* 42 (2002) 614–633
- [3] R. J. Hawryluk et al, Fusion plasma experiments on TFTR: A 20 year retrospective, *Phys. Plasmas* 5, 1577 (1998)
- [4] J. Paméla et al, Overview of JET results, 2003 *Nucl. Fusion* 43 1540
- [5] M. Yoshikawa, AN OVERVIEW OF THE JT-60 PROJECT, *Fusion Engineering and Design* 5 (1987) 3-8
- [6] M. Kikuchi, Overview of Modification of JT-60U for the Satellite Tokamak Program as one of the Broader Approach Projects and National Program, 21st IAEA Fusion Energy Conference (2006), http://www-naweb.iaea.org/naweb/physics/FEC/FEC2006/talks/t_ft_2-5.pdf
- [7] R Aymar et al, 2002 *Plasma Phys. Control. Fusion* 44 519
- [8] Y. Shimomura et al, 1999 *Nucl. Fusion* 39 1295
- [9] T. Inoue et al, Design of neutral beam system for ITER-FEAT, *Fusion Engineering and Design* 56–57 (2001) 517–521
- [10] R. S. Hemsworth et al, Status of the ITER neutral beam injection system, *Rev. Sci. Instrum.* 79, 02C109 (2008)
- [11] R. S. Hemsworth et al, Status of the ITER heating neutral beam system, http://www-naweb.iaea.org/naweb/physics/FEC/FEC2008/papers/it_p7-7.pdf
- [12] R. Hemsworth, et al., Status of the ITER heating neutral beam system, *Nuclear Fusion* 49 (2009), doi:10.1088/0029-5515/49/4/045006
- [13] M. Kuriyama, et al., Operation of the negative-ion based NBI for JT-60U, *Fusion Engineering and Design* 39–40 (1998) 115–121
- [14] D. Marcuzzi, M. Dalla Palma, M. Pavei, B. Heinemann, W. Kraus, R. Riedl, Detailed design of the RF source for the 1 MV neutral beam test facility, *Fusion Engineering and Design* 84 (2009) 1253–1258
- [15] P. Sonato et al., The ITER full size plasma source device design, *Fusion Eng. Des.* 84 (2009) 269-274
- [16] D. Marcuzzi, et al., Detail design of the beam source for the SPIDER experiment, *Fusion Engineering and Design*, 85 (2010), doi:10.1016/j.fusengdes.2010.05.039
- [17] P. Agostinetti, et al., Physics and engineering design of the accelerator and electron dump for SPIDER, *Nucl. Fusion* 51 (2011), doi:10.1088/0029-5515/51/6/063004

- [18] M. Bacal, Physics aspects of negative ion sources, *Nucl. Fusion* 46 (2006), doi:10.1088/0029-5515/46/6/S05
- [19] Yu.I. Belchenko, et al., A powerful injector of neutrals with a surface-plasma source of negative ions, *Nucl. Fusion* 14 (1974), doi:10.1088/0029-5515/14/1/017
- [20] D. Lide, *CRC Handbook of Chemistry and Physics*, 87th Edition, CRC, 2007.
- [21] P. Franzen, H.D. Falter, U. Fantz, W. Kraus, M. Berger, S. Christ-Koch, M. Fröschle, R. Gutser, B. Heinemann, S. Hilbert, S. Leyer, C. Martens, P. Mc-Neely, R. Riedl, E. Speth and D. Wunderlich. - Progress of the development of the IPP RF negative ion source for the ITER neutral beam system. *Nucl. Fusion* 47 (2007) 264-270.
- [22] W. Kraus, H.-D. Falter, U. Fantz, P. Franzen, B. Heinemann et al., Long pulse large area beam extraction with a rf driven H/D source, *Rev. Sci. Instrum.* 79, 02C108 (2008)
- [23] U. Fantz, et al., Spectroscopy—A powerful diagnostic tool in source development, *Nucl. Fusion* 46 (2006) S297
- [24] M Berger, U Fantz, S Christ-Koch and NNBI Team, Cavity ring-down spectroscopy on a high power rf driven source for negative hydrogen ions, *Plasma Sources Sci. Technol.* 18 (2009) 025004
- [25] E. Speth, et al., Overview of the RF source development program at IPP Garching, *Nucl. Fusion* 46 (6) (2006) S220
- [26] ITER Design Description Document 5.3 (N 53 DDD 29 01-07-03 R 0.1), 03/07/2001
- [27] B. Heinemann et al., Design of the “half-size” ITER neutral beam source for the test facility ELISE, *Fusion Engineering and Design* 84 (2009) 915–922
- [28] G. Fubiani, H. P. L. de Esch, A. Simonin, R. S. Hemsworth, Modeling of secondary emission processes in the negative ion based electrostatic accelerator of the International Thermonuclear Experimental Reactor, *Phys. Rev. ST Accel. Beams* 11, 014202 (2008)
- [29] P. Agostinetti et al., Evaluations of the power loads given by electrons on the components downstream of the beam source in MITICA, F4E Grant F4E-2009-GRT32-PMS-H.CD – T6.1/D2, T6.2/D1 - RFX-MITICA-TN-34 (2010)
- [30] R.A. Langley et al., Data compendium for plasma-surface interactions, *Journal of Plasma Physics and Thermonuclear Fusion*, 1984
- [31] P. Agostinetti, *Methods for the Thermo-mechanical Analysis and Design of High Power Ion Beam Sources*, Ph.D. Thesis, University of Padua, 2008
- [32] H. Greuner et al, Design, performance and construction of a 2MW ion beam test facility for plasma facing components, *Fusion Engineering and Design* 75–79 (2005) 345–350
- [33] H. Greuner, High Heat Flux Facility GLADIS at IPP Garching, http://www.ornl.gov/sci/fed/PMTS10/PMTS10_05.pdf
- [34] C. H. Liu, N. K Huang, D. Z. Wang and B. Yang, Microanalyses on Mo films before and after Hydrogen ion irradiation

- [35] W. Eckstein, R. Preuss, New fit formulae for the sputtering yield
- [36] W. Eckstein, J. László, Journal of Nuclear Materials 183 (1991) 19-24, Sputtering of tungsten and Molybdenum
- [37] Communications exchange with Dr. Belchenko, Budker Institute of Nuclear Physics of SB RAS, Novosibirsk, Russia
- [38] J. Lettry, J. Alessi, D. Faircloth, A. Gerardin, T. Kalvas, H. Pereira, S. Sgobba, ICIS 2011, Investigation of the BNL H⁻ Magnetron ion source electrodes after extended operation
- [39] J. Lettry, J. Alessi, D. Faircloth, A. Gerardin, T. Kalvas, H. Pereira, S. Sgobba, ICIS 2011, Investigation of the ISIS Penning ion source electrodes after extended operation
- [40] J. B. Green, The angular distribution of single crystal Molybdenum sputtered by 1-10 keV Cesium ions, Master of Science Thesis, University of California, Berkeley, 1964
- [41] T. Hoshihira, T. Otsuka, T. Tanabe, Journal of Nuclear Materials 390-391 (2009) 1029-1031, A study of Hydrogen blistering mechanism for Molybdenum by Tritium radio-luminography
- [42] Minutes of the meeting between M. Pavei (RFX) and H. Greuner (IPP), November, 25th 2011
- [43] ITER Baseline Documentation. MPH - Material Properties Handbook. In-vessel Materials Database.
- [44] J. Matejicek, Y. Koza, V. Weinzettl, Plasma sprayed tungsten-based coatings and their performance under fusion relevant conditions, Fus. Eng. And Des., 75-79 (2005) 395-399
- [45] S.O. Chwa, D. Klein, H. Liao, L. Dembinski, C. Coddet, Temperature dependence of microstructure and hardness of vacuum plasma sprayed Cu-Mo composite coatings, Surface & Coatings Technology, 200 (2006) 5682-5686
- [46] Sieder E.N., Tate G.E. 1936. Heat transfer and pressure drop of liquids in tubes. Ind. Eng. Chem. 28:1429-35
- [47] Colebrook C.F., White C.M. 1937. Fluid friction in roughened pipes. Proceedings-of-the-Royal-Society-of-London. 1937 Aug. 3. 161A:367-381
- [48] Shah, Sekulic, Fundamentals of heat exchanger design, Wiley, c2003
- [49] ITER SDC-IC, Structural Design Criteria for ITER In-Vessel Components, July 2004 (with Appendixes A, B, C)
- [50] RCC-MR. Design and construction rules for mechanical components of FBR nuclear island. AFCEN edition 2007
- [51] M. Dalla Palma, P. Zaccaria. Procedures for Multiaxial Creep-Fatigue Verifications of Nuclear Components. Oral session at the 14th International Conference on the Fusion Reactor Materials, 6-11 September 2009, Sapporo, Japan. Under review for the publication in the international journal Fusion Science and Technology

- [52] ASME Boiler and Pressure Vessel Code, Sections III and VIII. The American Society of Mechanical Engineers. New York 2001
- [53] M. Dalla Palma, D. Marcuzzi, M. Pavei, RFX_NBTF_TN_055.pdf, RF source Design Description Document, TW6-THHN-NBD1 task report
- [54] F. Fellin et al., Technical specification for the PRIMA Cooling Plant, F4E-2011-GRT-306 – A1/D5 - RFX-PRIMA-TS_001_v7
- [55] S. Dal Bello et al., TECHNICAL SPECIFICATION: SPIDER and MITICA VACUUM AND GAS INJECTION SYSTEMS, F4E Grant F4E-2009-GRT32-PMS-H.CD – T3.6/D2, RFX_SPIDER_TS_011-Rev.2 (2009)
- [56] S. Yano et al., Structural observations of the interface of explosion-bonded Mo/Cu system, JOURNAL OF MATERIALS SCIENCE 33 (1998) 4857 – 4865
- [57] A. Rizzolo et al., Thermo-hydraulic experiments on the Single Channel Prototypes for the SPIDER accelerator, F4E Grant F4E-2009-GRT-032-PMS-H.CD - T7.5/D4 - RFX-SPIDER-TN-128 (2011)
- [58] Patterson, A. (1939). "The Scherrer Formula for X-Ray Particle Size Determination". Phys. Rev. 56 (10): 978–982.
- [59] D. Marcuzzi et al., Beam Source and Vacuum Vessel Technical Specification - Annex B, F4E-2009-GRT-32-PMS-H.CD – Tasks T3.1, T3.2, T3.3, T3.4, T3.7 - Deliverable D1 - RFX-SPIDER-TS-015 (2010)

Annexes

Annex 1: TECHNICAL SPECIFICATION FOR THE RESEARCH AND DEVELOPMENT ACTIVITIES ON THICK MOLYBDENUM COATING – RFX-MITICA-TN-19 (2010)



 <p>CONSORZIO RFX <i>Ricerca Formazione Innovazione</i> Corso Stati Uniti, 4 - 35127 Padova (Italy) Tel. +39.049.8295000 - Fax +39.049.8700718</p>		Page: 1/13			
		RFX Ref.: RFX – MITICA - TN - 19			
		Document type: Technical Specification			
Distribution		RFX: P. Sonato, D. Marcuzzi, P. Zaccaria, S. Dal Bello, F. Degli Agostini, A. Fiorentin F4E: A. Masiello, T. Bonicelli			
Ext Ref.:		F4E Grant F4E-2009-GRT-032-01			
		T 7.8 / D1: Prototypes of thick Mo coating			
<p>TECHNICAL SPECIFICATION FOR THE Research and Development ACTIVITIES ON THICK MOLYBDENUM COATING</p>					
0	FIRST ISSUE	M.Pavei, F.Degli Agostini, D. Marcuzzi	S. Dal Bello	P.Sonato	24/06/2010
Rev.	Description	Author(s)	Checked by	Approved by	Date
Reference author: Mauro Pavei (mauro.pavei@igi.cnr.it , +39 049 829 5845)					

TABLE OF CONTENTS

1.	BACKGROUND INFORMATION.....	3
2.	DESCRIPTION OF THE SUPPLY.....	3
2.1.	General aspects	3
3.	Prototype requirements	4
3.1.	Material requirements.....	4
3.1.1.	Copper	4
3.1.2.	Molybdenum.....	5
3.2.	Technology requirements.....	5
3.3.	Vacuum compatibility requirements	5
3.4.	Finishing compatibility requirements	5
3.5.	General tolerances	6
4.	IDENTIFICATION AND TRACEABILITY REQUIREMENTS.....	6
5.	MANUFACTURING	6
5.1.	MANUFACTURING DESIGN AND APPROVAL.....	6
5.2.	MANUFACTURING RECORDS.....	6
6.	EXAMINATIONS AND TESTS	7
6.1.	Non destructive examinations	7
6.1.1.	General requirements	7
6.1.2.	Ultrasonic Examination	8
6.1.3.	Radiographic Examination	8
6.1.4.	Surface Examination.....	9
6.2.	Destructive tests.....	9
6.2.1.	Grain size measurement test.....	9
6.2.2.	Hardness test.....	9
6.2.3.	Tensile test.....	10
7.	CLEANING	10
8.	PACKAGING AND DELIVERY REPORT.....	11
9.	DELIVERABLES.....	11
10.	QUALITY ASSURANCE	12
10.1.	General Requirements	12
10.2.	Hold Points	12
10.3.	Documents and Records.....	12
10.4.	Control of monitoring and measuring equipment	13
11.	ACCESS	13
12.	DISSEMINATION	13
	ANNEXES.....	13

1. BACKGROUND INFORMATION

One of the most technically challenging components of the MITICA (Megavolt ITER Injector & Concept Advancement) injector is the Plasma Driver Plate (PDP), whose main function is to support the eight drivers of the Radio-Frequency plasma source, to confine the source plasma and to dump down the back-streaming positive ions generated into the 1MV accelerator. It is subdivided in four symmetric “quarters”.

The PDP is actively cooled and it has to sustain the heat and particle fluxes during normal and transient operations (breakdowns among grids).

The PDP consists of a plasma-facing material, the armour, which is made of molybdenum (Mo) or tungsten (W). The armour is joined onto an actively cooled substrate, the heat sink, made of pure copper. During operation at nominal conditions, the back-streaming ions impinge on the PDP reproducing on it the print of the 1280 plasma grid apertures. The power load on the PDP is then localized in 1280 points. The heat load for each hot spot has a Gaussian profile with a peak estimated up to 60 MW/m² and some millimetres in diameter. Such concentrated heat loads on the surface of the molybdenum layer cause very high stresses at the interface between the armour and the copper sub-plate.

Moreover, the impinging of the ions against the PDP causes sputtering of the surface material and consequently the pollution of the plasma. Calculations of the total amount of sputtering occurring during the ITER life (International Tokamak Experimental Reactor, www.iter.org) led to fix the requirement of having pure Molybdenum facing the plasma with minimum thickness of the layer of 0,5 mm.

The first stage of the R&D activity aims to examine, qualify and compare different technologies available for the final production of the PDP quarters.

2. DESCRIPTION OF THE SUPPLY

2.1. General aspects

- A. The Supplier is asked to manufacture the qualification prototype(s) and a set of specimens, as defined in this technical specification and in the drawings in Annex B. At least six specimens (two for the tension test and four for other possible tests) must be taken (cut away) from the same semifinished product from which each prototype is obtained. Therefore, the semifinished product dimensions shall be bigger than the prototype ones. In Annex B, drawings GRT032-T7.8_01 and GRT032-T7.8_03, give a qualitative representation of the prototype, of the semifinished product and of the places from where the specimens have to be taken off.
- B. The Supplier is asked to carry out a feasibility study, in collaboration with Consorzio RFX (process FMEA is recommended), in order to evaluate its capability to manufacture the armour layer for the PDP quarter, as described in the drawing GRT032-T7.8_02 named “PLASMA DRIVERS PLATE QUARTER ASSEMBLY”. The aim of the study is to demonstrate that the qualification prototype is representative of the final PDP in terms of:
 1. technical feasibility, with particular care to:
 - a. the double curvature required to the armour layer (in correspondence of the driver’s hole).

- b. the fact that the cooling channels are realized by electro-deposition of copper. The Supplier must take it into account when it designs the manufacturing procedure and processes. The stainless-steel manifolds attached on the rear surface of the PDP quarters are kept by the same electro-deposited copper layer that closes the cooling channels of the component.

- 2. manufacturing equipment, machines and process parameters;

3. Prototype requirements

The Supplier is asked to manufacture and deliver to Consorzio RFX the number of prototypes specified in the order. The prototype dimensions are given in Annex B - drawing GRT032-T7.8_01 named “MITICA THICK COATING PROTOTYPE”.

The Supplier can propose any modification of the geometry, any procedure, or alternative technology he deems appropriate to obtain the specified component with the required quality, in an efficient, economic and timely manner.

3.1. Material requirements

Molybdenum is the reference design material for the armour layer, due to its low sputtering yield and due to the fact that molybdenum has been chosen for the plasma grid coating.

The Supplier is also asked to express in advance, in the offer, if tungsten, as alternative material to molybdenum for the armour layer, is preferable for some technical reasons. In this case the Supplier is request to give evidence of such reasons to Consorzio RFX, together with the alternative possible solution.

The nominal required thickness of the pure Mo layer is 1,0 mm. The porosity of the Mo armour layer shall be <1% (density of armour layer > 99% of density of pure metallic Mo).

The reference material for the base plate is copper.

All the materials required to manufacture the components are provided by the Supplier. ASTM standards shall be used. However, other internationally recognized standards may be adopted subject to the prior Consorzio RFX’s approval.

3.1.1. Copper

The material for copper components shall be “OFXLP C10300” or “OF UNS C10200” according to the ASTM B152M-00 standards, or an equivalent material having physical properties that comply with the limits listed below.

- a) Chemical composition in percent according to standards ASTM B170-99 and B152M-00.
- b) State of the copper: state H01 (hardness 1/4) is proposed;
- c) The following mechanical characteristics are required:

Yield stress (deviation from the proportionality of 0.2%)	min	205 MPa
tensile strength at break	min	235 MPa
ultimate elongation	min	25%
modulus of elasticity or Young's modulus		115-130 GPa

3.1.1.1. Copper certificates

The Supplier shall provide the following documentation for this material:

- Certificate of conformity to a national or international standard
- Certificate of the measurements of the chemical composition
- Report on the measurements of the grain size
- Report on the measurements of the tensile properties (at least yield strength, ultimate strength, ultimate elongation)
- Certificate of the hardening state (heat treatment procedure)
- Report on the measurements of the hardness
- Certificate of fatigue tests according to international standards (if already issued by the material Supplier)

3.1.2. Molybdenum

Pure molybdenum (>99,99% Mo) shall be used as reference material for the armour layer.

3.1.2.1. Molybdenum certificates

The Supplier shall provide the following documentation for this material:

- Certificate of conformity to the national or international standard
- Certificate of the measurements of the chemical composition
- Report on the measurements of the grain size, when applicable
- Report on the measurements of the tensile properties, when applicable (at least yield strength, ultimate strength, ultimate elongation)
- Report on the measurements of the porosity (or volume density) of the armour layer, when applicable

3.2. Technology requirements

The core technology required to the Supplier for the production of the prototypes is explosion bonding and/or welding.

3.3. Vacuum compatibility requirements

The prototype shall be compatible with an operation in an ultra-high vacuum environment.

After the final cleaning procedure, each part shall be handled with care and using appropriate gloves for possible in-vacuum tests to be carried out at Consorzio RFX site (out of this supply).

The typical out-gassing rate of the prototype must be the same of the unbaked copper used for the heat sink. If the Supplier needs to set up a test for measuring the outgassing rate of the prototype(s), such test shall be agreed with Consorzio RFX.

3.4. Finishing compatibility requirements

The finishing of all the external metallic surfaces shall be $R_a = 1.6 \mu\text{m}$ (ISO N7) or finer except when non-destructive examinations or tolerances require better values or explicitly specified in the drawings. The molybdenum surface(s), shall have approx. $R_a = 0.8 \mu\text{m}$ (ISO N6) or finer.

3.5. General tolerances

Unless otherwise specified in the drawings, all the dimensions shall satisfy ISO 2768 - mK.

4. IDENTIFICATION AND TRACEABILITY REQUIREMENTS

The Supplier shall ensure that each material is properly identified, each batch of material being assigned a unique traceable number.

Traceability of each material shall be maintained throughout all manufacturing processes. Traceability documentation which cross-references component parts to material certificates shall be included in the Final Report.

In order to have the traceability of the parts, the following identification method is given for the prototype(s) and the specimens for tests:

- A capital letter (A, B, C, ...) indicates each prototype (if more than one is requested according to the order);
- A number from 1 to 6 indicates the position of the specimen on the semifinished product as shown in drawing GRT032-T7.8_03, then the names of the specimens taken from each semifinished product shall be A1 to A6, (B1 to B6, C1 to C6, ...).

These marks shall be written with an electrical pen, in order to be sure that they are not cancelled during the tests (or the heat treatments).

5. MANUFACTURING

5.1. MANUFACTURING DESIGN AND APPROVAL

Before manufacturing can start the drawings of the prototype, specimens and of the semifinished product shall be issued to Consorzio RFX for prior written approval.

A detailed report describing all the manufacturing processes and the parameters shall also be issued to Consorzio RFX for prior written approval. The acceptance of the specifications for all the manufacturing steps and their qualification represents a Hold Point.

Consorzio RFX's approval of the manufacturing process is only aimed at checking whether the Supplier's proposal is ITER relevant and whether it is consistent with the scope of the prequalification phase. Consorzio RFX's approval does not relieve the Supplier from any of his responsibility. The Supplier has the sole responsibility in the success or failure of the proposed manufacturing process.

Other equivalent national or international standards (if applicable) than those mentioned in this Technical Specification may be acceptable with prior written Consorzio RFX's approval.

5.2. MANUFACTURING RECORDS

The Supplier shall record the process operations (with their parameters) for each part and record any deviation from the designed process.

If the Supplier foresees any stress relieving heat treatment in the normal manufacturing procedure, the optimized temperature and time values shall be reported to Consorzio RFX. The actual heat treatment parameters shall be specified and reported by the Supplier.

The measuring and the record of the semifinished product(s) dimensions (before the specimens and the prototype are cut off) represent a hold point and must be reported to Consorzio RFX.

The measuring and the record of the dimensions of each prototype(s) dimensions represent a hold point and must be reported to Consorzio RFX.

The measuring and the record of the dimensions of each tensile test specimen (L_0 , L_C , cross section) represent a hold point and must be reported to Consorzio RFX.

6. EXAMINATIONS AND TESTS

In case the manufacturing process includes a final heat treatment, samples number 1, 2 and 3 must be cut from the semifinished product before the execution of such heat treatment; they shall not be treated. Samples number 4, 5 and 6 shall be subjected exactly to the same manufacturing process followed by the relative prototype(s), including heat treatments.

All the tests described in this section shall be executed at the end of the manufacturing process (with the distinction made between prototypes 1, 2, 3 and 4, 5, 6).

6.1. Non destructive examinations

6.1.1. General requirements

Following any non destructive examination in which any foreign substance enters in contact with the product, the piece shall be thoroughly cleaned. The applicable standards are those specified below for each examination. Other equivalent national or international standards may be acceptable with prior written Consorzio RFX's approval.

The minimum required examinations and the examination procedures are given hereinafter. They shall be carried out by experienced and qualified personnel. The Supplier is recommended to envisage all the additional examinations he deems to be necessary to detect possible non-conformities at an early stage of the manufacturing process and thus to be able to perform suitable and timely corrective actions.

The non-destructive examinations to be applied shall be performed in accordance with a written procedure that shall include, as a minimum, the following information in addition to the requirements of the applicable standards:

- Scope of examination and stage of manufacture at which it is conducted;
- Surfaces on which examination will be performed: drawings may be used to indicate areas of examination for each procedure, and any limitations due to size, shape or other physical characteristics;
- Data to be recorded.

The written approval of all the non-destructive testing protocols represents a Hold Point.

The Supplier shall prepare a report for each non-destructive examination carried out to be included in the Final Report. All reports shall contain, as a minimum, the following information in addition to the requirements of the applicable standards:

- All procedural, equipment and calibration parameters shall be identified and recorded sufficiently to provide a basis for comparison with later examinations guaranteeing the repeatability and reproducibility of the measurements and tests;
- A marked up drawing or sketch indicating the part examined, the item or piece number, the datum points and co-ordinate conventions used for location, and other necessary identification information;
- The dimensions of each detected, identified and recorded defect.

6.1.2. Ultrasonic Examination

6.1.2.1. Extent of the Examination

The ultrasonic examination shall be carried out on:

- the copper base-plate (if allowed by the manufacturing process);
- the Mo armour plate (if allowed by the manufacturing process);
- the final prototype(s);
- the specimens.

6.1.2.2. Examination Procedure

Ultrasonic examination shall be in accordance with the ASME V Art. 5 (*Ultrasonic Examination Methods for Materials and Fabrication*) together with the requirements of Art. 1 (*General Requirements*) and of any other part of the ASME code referenced in these Articles.

The use of other standards may also be acceptable subject to the written Consorzio RFX's approval. The conformity with ASME Code shall be demonstrated.

The capability to detect a 2,0 mm diam. circular defect in each material and at the interface shall be demonstrated by means of *ad hoc* calibration samples. The report of the test of calibration defects shall be prepared and included in the supporting documentation and delivery.

6.1.3. Radiographic Examination

6.1.3.1. Extent of the Examination

The radiographic examination shall be carried out on:

- the copper base-plate (if allowed by the manufacturing process).
- the Mo armour plate (if allowed by the manufacturing process).
- the final prototype(s);
- the specimens.

6.1.3.2. Examination Procedure

The radiographic examination shall be performed in accordance with the ASME V Art. 2 (*Radiographic Examination*) together with the requirements of Art. 1 (*General Requirements*) and of any other part of the ASME code referenced in these Articles.

The use of other standards may also be acceptable subject to the Consorzio RFX's approval. The conformity with ASME Code shall be demonstrated.

The capability to detect a 2,0 mm diam. circular defect in each material and at the interface shall be demonstrated by means of *ad hoc* calibration samples. The report of the test of calibration defects shall be prepared and included in the supporting documentation and delivery.

6.1.4. Surface Examination

6.1.4.1. Extent of the Examination

Surface examination shall be carried out on all the visible surfaces of:

- the final prototype(s);
- the specimens.

6.1.4.2. Examination Procedure

Visual examination shall be in accordance with the ASME V Art. 9 (*Visual Examination*) together with the requirements of Art. 1 (*General Requirements*) and of any other part of the ASME code referenced in these Articles.

The use of other standards may also be acceptable subject to the Consorzio RFX's approval. The conformity with ASME Code shall be demonstrated.

6.2. Destructive tests

6.2.1. Grain size measurement test

Specimens 2 and 5 (see drawing GRT032-T7.8_03 – Annex B) shall be subjected to grain size measurement (according to ASTM E112 or equivalent) on a section orthogonal to the plate. The grain size measurements shall be done on the molybdenum layer and on the copper sub-plate; the measuring points on the copper thickness are:

1. at the interface with molybdenum
2. at 1.0 mm from the interface
3. at 2.0 mm from the interface
4. at 8.0 mm from the interface

6.2.2. Hardness test

Specimens 2 and 5 (see drawing GRT032-T7.8_03 – Annex B) shall be subjected to hardness measurement (according to EN ISO 6507, or equivalent) on a section orthogonal to the plate. The hardness measurements shall be done on the molybdenum thickness and on the copper sub-plate; the measuring points on the copper are:

1. at 0.1, 0.2, 0.3, 0.5 mm from the interface (microhardness Vickers test)
2. at 1.0 mm from the interface
3. at 2.0 mm from the interface

4. at 8.0 mm from the interface

6.2.3. Tensile test

6.2.3.1. Specimens for tensile tests

The reference standard for specimens' dimensions, geometry and tolerances is EN 10002-1 (or ASTM E8).

The dimensions are reported in drawing GRT032-T7.8_04, titled “MITICA THICK COATING PROTOTYPE – TENSILE TEST SAMPLE”.

The initial section of the calibrated area is:

$$S_0 = 10 \cdot 10 = 100 \text{mm}^2$$

The initial distance between the references must be:

$$L_0 = k \cdot \sqrt{S_0} = 56.5 \text{mm}$$

where the value given by the norm of $k=5.65$ is used, in order to obtain "proportional" specimens.

The minimum calibrated length is:

$$L_{C,\min} = L_0 + 1.5 \cdot \sqrt{S_0} = 71.5 \text{mm}$$

The value of L_C is then approximated to 72 mm.

The upper and lower main surfaces shall satisfy a parallelism tolerance of 0.04 mm.

The roughness specifications is $Ra < 1.6 \mu\text{m}$.

6.2.3.2. Test specifications

The tension tests shall be made at room temperature. The temperature must be constant during the test and uniform across the specimen volume. The actual temperature at which each test is made shall be recorded.

The outputs of the test shall be: Young's Modulus, Yield Tensile Strength, Ultimate Tensile Strength, Elongation, Reduction of area, Stress-Strain curve.

7. CLEANING

Final cleaning shall ensure effective cleaning without damage to the surface finish, material properties or metallurgical structure of the materials.

All scales or flakes shall be removed.

The surfaces shall be polished with clean and well dry clothes that shall not deposit particles and downs on the surfaces.

Acetone is recommended for degreasing.

Ultrasonic cleaning in demineralised water is requested for each part.

After the cleaning operations the objects shall be dried by means of hot dry air flow, having care of filtering dusts, powders and oils.

The Supplier shall submit to Consorzio RFX the proposed cleaning procedure for approval.

Consorzio RFX may, if they consider it necessary, instruct the Supplier to repeat or carry out a special cleaning process on any item.

8. PACKAGING AND DELIVERY REPORT

The prototype(s) shall be properly packed in order to prevent any kind of damages and properly fixed inside a box. This box shall be rigid enough in order not to deform appreciably under the component weight. The supports have to avoid extra loading on the components due to sudden movements or accidental drop, in this respect a shock absorbing material shall be used.

The prototype(s) shall be enclosed just after the cleaning in a sealed envelope in dry atmosphere or under vacuum.

Delivery of the components to their final destination is done under the Supplier's full responsibility.

Prior to packing each prototype(s), a "Release Note" shall be prepared by the Supplier, stating as a minimum:

- The packaging date
- The full address of the place of delivery and the name of the person responsible to receive the package
- The enclosed documentation
- The declaration of conformity of the package

9. DELIVERABLES

All communication between the Supplier and Consorzio RFX shall be in English language and all measures shall be given in the metric system SI. This includes all reports, documentation, correspondence and labelling. All the reports shall be properly bound. The deliverables of the contract are the following:

Del. 1 : The Quality Plan.

Del. 2 : The prototypes specified in the order

Del. 3 : The samples (six each prototype) obtained from the semifinished product(s)

Del. 4 : Initial Report. It shall include:

- Del. 4.1: The detail drawings of the prototype.
- Del. 4.2: The detail drawings of the semifinished product with the indication of the prototype, samples profiles and traceability marks.
- Del. 4.3: The detail drawings of the samples for the tests.
- Del. 4.4: The description of the manufacturing process and parameters.
- Del. 4.5: The testing protocols.

Del. 5 : Final Report. It shall include:

- Del. 5.1: The material certificates described in this specification.
- Del. 5.2: The “as-built” drawings of the prototypes.
- Del. 5.3: A comprehensive and detailed report of the manufacturing process, including the manufacturing/process records, parameters and critical issues.
- Del. 5.4: The tests certificates and reports.
- Del. 5.5: A feasibility study, to be carried out with Consorzio RFX, of the applicability of the process to the PDP quarter taking into account the results on the prototypes (process FMEA is recommended).

All the documents shall be delivered both in paper and electronic format (text, tables and images)

10. QUALITY ASSURANCE

10.1. General Requirements

The Management Specification in Annex A, with RFX comments applies.

10.2. Hold Points

A Hold Point is a point of defined circumstances beyond which an activity must not proceed without the approval of Consorzio RFX.

In the Control Plan the Hold Points given in (a) through (e) shall be included:

- (a) the acceptance of the detailed drawings of the semifinished product, prototype and samples as proposed by the Supplier;
- (b) the acceptance of the design of the manufacturing processes;
- (c) the measurements of each semifinished product dimensions, before the prototype and the samples are cut off;
- (d) the acceptance of the non-destructive and destructive testing protocols (Sect. 6);
- (e) the demonstration of the capability to fulfil the requirements on the ultrasonic, radiographic and surface examinations (Sect. 6.1.2, 6.1.3, 6.1.4);

10.3. Documents and Records

In advance of their intended use, the Supplier shall obtain Consorzio RFX’s written acceptance of the documents for which the Consorzio RFX’s approval is required by this technical specification.

Documents and records issued by the Supplier in connection with the contract shall be:

- uniquely identified, including subsequent revisions,
- reviewed before being sent to Consorzio RFX for acceptance. Evidence of review status shall be readily identified.

Changes to previously approved documents shall be governed by control measures commensurate to those applied to the original document.

The latest issue of applicable documents shall be directly accessible to those carrying out the work.

Consorzio RFX's acceptance of documents and records shall not relieve the Supplier of any contractual obligations and responsibilities.

10.4. Control of monitoring and measuring equipment

Requirement 7.6 of ISO 9001:2008 applies.

11. ACCESS

The Consorzio RFX shall at reasonable notice have the right to check at the Supplier's premises or at those of his sub-contractor the progress and status of the work forming the subject matter of the procurement and to witness specified tests.

The Supplier shall hold at the disposal of the Consorzio RFX and make available to it such information and documents as are necessary to determine the progress and status of the work.

12. DISSEMINATION

All the information regarding the manufacturing process and parameters shall not be given outside Consorzio RFX. The results will be used for scientific publications, guaranteeing that the Supplier know-how is protected.

Dissemination to the scientific community will be agreed between the Supplier and Consorzio RFX.

ANNEXES

- Annex A: Management Specification (*here omitted*)
 - GRT32_Management_Spec_Task7-8.pdf

- Annex B: Drawings (*here omitted*)
 - GRT032-T7.8_01_PROTOTYPE.pdf;
 - GRT032-T7.8_02_MITICA_PDP_QUARTER.pdf;
 - GRT032-T7.8_03_SEMIFINISHED_PRODUCT.pdf;
 - GRT032-T7.8_04_TENSILE_TEST_SAMPLE.pdf